Università degli studi di Roma "Tor Vergata"
Facoltà di Scienze Matematiche, Fisiche e Naturali
Dottorato di Ricerca in Astronomia
XVII ciclo (A. A. 2001/2002–2003/2004)

SuperAGILE: an X-ray monitor for a gamma mission

Ettore Del Monte

Coordinatore

Prof. Roberto Buonanno
(Università di Roma "Tor Vergata")

Relatore

Dott. Enrico Costa
(IASF CNR/INAF)

Contents

Introduction **vii**

1 AGILE in the context of the High Energy Astrophysics **1**
1.1 Introduction . . . 1
1.2 Gamma Ray Bursts . . . 1
1.2.1 The discovery of the prompt and afterglow emission . . . 1
1.2.2 Observational properties of the Gamma Ray Bursts . . . 5
1.2.3 Theoretical models . . . 6
1.2.4 The AGILE contribution . . . 7
1.3 Compact Galactic Sources . . . 8
1.3.1 High-mass X-ray binary stars . . . 9
1.3.2 Low-mass X-ray binary stars . . . 11
1.3.3 Black hole candidates . . . 12
1.3.4 Gamma ray pulsars . . . 12
1.3.5 The EGRET unidentified sources . . . 13
1.3.6 The AGILE contribution . . . 15
1.4 Active Galactic Nuclei . . . 17
1.4.1 The properties of the Active Galactic Nuclei . . . 17
1.4.2 The AGN classification and the Unified Model . . . 17
1.4.3 The X-ray emission from AGN . . . 19
1.4.4 The gamma ray emission from AGN . . . 21
1.4.5 The blazar class . . . 21
1.4.6 The AGILE contribution . . . 22
1.5 Gamma ray Diffuse Galactic Emission . . . 24
1.5.1 The AGILE contribution . . . 27
1.6 AGILE and GLAST . . . 27
1.7 Conclusions . . . 28

2 The AGILE mission and the SuperAGILE instrument **31**
2.1 The AGILE mission . . . 31
2.2 The GRID . . . 33
2.2.1 The Silicon Tracker . . . 33
2.2.2 The Mini-Calorimeter . . . 34

2.2.3 The GRID scientific performances 36
2.3 The SuperAGILE instrument 38
2.3.1 The coded mask and the collimator 38
2.3.2 The silicon microstrip detector 39
2.3.3 The SuperAGILE scientific performances 42
2.4 The Anti-Coincidence system 44
2.5 The Payload Data Handling Unit 46
2.6 The AGILE mission scientific objectives 47
2.6.1 Active Galactic Nuclei 47
2.6.2 Gamma ray Bursts 47
2.6.3 Compact Galactic Sources 48
2.6.4 Diffuse emission 48

3 The SuperAGILE electronics **49**
3.1 Introduction 49
3.2 The SuperAGILE front-end electronics 49
3.3 The XAA1.2 chip 50
3.4 Sources of noise in silicon microstrip detectors 55
3.5 The XAA1.2 acquisition system 57
3.5.1 The XA-DAQ acquisition board 57
3.5.2 The XA-DAQ acquisition software 58
3.6 The SAFEE Test Equipment acquisition system 58
3.6.1 The SAFEE Test Equipment hardware 60
3.6.2 The SAFEE Test Equipment software 61
3.7 The interface and conditioning electronics 62
3.8 The PDHU and SuperAGILE 63
3.9 The SuperAGILE criticalities 64
3.9.1 Thermal stability 65
3.9.2 Effects due to the cosmic rays interactions 65
3.9.3 Threshold uniformity and signal to noise ratio in the sky images 66
3.9.4 Dead and hot pixels 66
3.9.5 Mechanical assembly and alignment 67

4 The XAA1.2 performance measurements **69**
4.1 Introduction 69
4.2 The XAA1.2 input charge linearity 70
4.3 Gain and threshold uniformity 72
4.3.1 Gain and offset uniformity 72
4.3.2 Threshold uniformity 75
4.4 Thermal stability of the address signals 81
4.5 Supply voltage stability 82
4.6 Conclusions 86

5 The XAA1.2 resistance to the cosmic rays interaction **91**
5.1 Introduction . . . 91
5.2 The interaction of cosmic rays in electronic devices . . . 92
5.3 Radiation-induced effects measurements . . . 94
5.3.1 The SIRAD irradiation facility . . . 95
5.3.2 XAA1.2 acquisition and control system . . . 96
5.3.3 Experimental set-up and strategy . . . 97
5.4 Latch-up measurements . . . 99
5.5 SEU measurements . . . 102
5.6 Total Dose Effects measurements . . . 105
5.7 The expected effects on-orbit and the recovery strategy . . . 108
5.7.1 Heavy ions interactions . . . 108
5.7.2 Proton interactions . . . 111
5.8 Conclusions . . . 112

6 The SuperAGILE data analysis programs **115**
6.1 Purpose and requirements . . . 115
6.2 The SuperAGILE data architecture . . . 116
6.2.1 The DISCoS archiving system . . . 117
6.2.2 The SAFEE TE data format . . . 118
6.2.3 The SAIE TE data format . . . 119
6.2.4 The TE independent L2 data format . . . 120
6.3 Analysis of electronic pulse measurements . . . 121
6.3.1 Analysis of electronic calibrations . . . 121
6.3.2 Analysis of parameter scans . . . 125
6.3.3 Analysis of threshold scans . . . 126
6.4 Analysis of photons acquisitions . . . 126
6.4.1 Address reconstruction and amplitude correction . . . 127
6.4.2 Analysis of spectra . . . 127
6.4.3 Analysis of detector images . . . 128
6.5 The `SADAS` package . . . 130

7 The SAFEE performance measurements **131**
7.1 Assembly and testing of the SuperAGILE proto-flight model . . . 131
7.2 Performances of the SAFEE before the detector integration . . . 134
7.2.1 Linearity and electronic noise . . . 134
7.2.2 The background and the threshold . . . 142
7.3 Verification of the performances stability after the burn-in process . . . 143
7.4 Performances of the SAFEE after the detector bonding measured with the electronic calibration . . . 145
7.4.1 Linearity and electronic noise . . . 145
7.4.2 The background and the threshold . . . 154
7.5 SuperAGILE "first light" . . . 154
7.5.1 Identification of hot pixels . . . 156

7.5.2 Analysis of the X-ray sources spectra 157
7.6 Optimization method of the SAFEE performances 165
7.7 Discussion and conclusions 165

8 Impact of the SAFEE features on the SuperAGILE scientific performances 167
8.1 Introduction 167
8.2 Measurement of the threshold non uniformity 168
8.3 The SuperAGILE background 170
8.3.1 Monte Carlo simulation of the SuperAGILE background features 172
8.3.2 Semi-analytic background estimations 175
8.4 Overview of the imaging algorithm 175
8.5 Analysis of the SuperAGILE images and correction techniques 177
8.5.1 Replica of the measured threshold values 177
8.5.2 Threshold cut-off technique 182
8.5.3 Threshold digital fine regulation technique 184
8.6 Discussion and conclusions 186

Conclusions and future perspectives 189

Acknowledgements 193

A Selected list of publications 195
A.1 The AGILE mission and the SuperAGILE instrument 195
A.2 The XAA1.2 ASIC performances 197
A.3 Radiation-induced effects on ASIC 198
A.4 Software for SuperAGILE Data Analysis 198

B List of acronyms and abbreviations 201

List of Figures 203

List of Tables 211

Bibliography 213

Introduction

This thesis describes the study of the performances of the SuperAGILE instrument, with a particular attention to the most important criticalities of the front-end electronics. The research work has been developed in the "Astrofisica delle Alte Energie e Tecnologie Relative" research group of the Istituto di Astrofisica Spaziale e Fisica Cosmica (IASF) CNR (now INAF) in Rome.

SuperAGILE is the hard X-ray monitor of the AGILE satellite mission, the first small scientific mission of the Italian Space Agency (ASI), which is composed by two instrument, sensitive in the $15 \div 40$ keV and 30 MeV $\div$ 50 GeV energy bands respectively, and will be launched in late 2005. For the first time a gamma ray and a hard X-ray monitor are mounted in series and designed to work together, improving the mission scientific capabilities. In order to achieve a wide field of view and high angular resolution in the selected energy band, SuperAGILE is designed as a coded aperture instrument, with a silicon microstrip detector and a tungsten coded mask.

An overview of the most important classes of sources in the High Energy Astrophysics, Gamma Ray Bursts, Compact Galactic Sources, Active Galactic Nuclei and Gamma Ray Diffuse Galactic Emission, is reported in chapter 1. Of each class a summary of the distinctive features and emission mechanisms is given and the expected AGILE contribution to the source nature knowledge is introduced.

The description of the instruments composing the payload of the AGILE mission is given in chapter 2. Since most of the SuperAGILE scientific performances are due the features of its electronics and since most of my research work concerns the laboratory measurements of the front-end electronics performances, a description of the SuperAGILE electronics and particularly the XAA1.2 read-out chip, is presented in chapter 3. The research work contained in this thesis deals with some of the most important criticalities of the SuperAGILE instrument, that are discussed at the end of chapter 3.

Chapter 4 contains the results of laboratory measurements performed on the XAA1.2 read-out chip in order to evaluate its linearity, the uniformity of the linearity parameters, its thermal stability, that is a key parameter for the SuperAGILE images production, and finally its stability against variation of the supply voltage.

The XAA1.2 is not designed as a radiation-resistant component for space application. On orbit the integrated circuits built using the CMOS technology, as the XAA1.2, are affected by the interaction of the cosmic rays, that can produce single particle effects, such as the latch-up, that is the sudden increase of the supply currents and can permanently damage the chip because of the overheating, or the Single Event Upset (SEU), a

bit flip in the chip memory producing unpredictable changing in the device operations, or integrated effects, known as total ionizing dose, degrading the chip performances.

An overview of the effects produced by the cosmic rays interaction in integrated circuits is reported in chapter 5. Part of my research work involves a dedicated measurement campaign, performed at the SIRAD facility of the Laboratori Nazionali INFN in Legnaro near Padova in Italy, in order to evaluate the cosmic rays effects on the XAA1.2 chip and described in chapter 5. After measuring the latch-up and SEU cross sections, the expected rate on orbit is evaluated estimating the cosmic ray flux at the AGILE orbit and using an approximated method to estimate the rate of the proton induced effects.

My research work includes the development of data analysis programs, to process the data acquired in the laboratory measurements. Because SuperAGILE is composed of a large number of pixels, each one considered as an independent detector, the main requirement of the analysis software is the capability to process automatically data from all the pixels and to produce the statistics summary of the results. The problems and the algorithms are described in chapter 6, with the aid of block diagrams and screen shots. The general philosophy of SuperAGILE is to use the same software to analyse calibrations, simulations, laboratory tests and flight data. Therefore a large part of the programs developed during my research work will be integrated in the SuperAGILE standard data analysis software.

The building and assembly of the SuperAGILE proto-flight model started at the end of August 2004 and is presently in progress. In a solid state detector based instrument the front-end electronics dominates all the scientific performances. For this reason, a great effort is made in measuring the front-end electronic performances during all the stages of the instrument development.

Chapter 7 contains the measurements of the front-end electronics performances during all the development stages. The system linearity is measured by means of an electronic pulse generator and X-ray calibration sources, that are also used to evaluate the energy resolution. A dedicated technique has been developed in order to measure the energy threshold.

Coded aperture systems are background dominated wide field of view instruments and any instrumental feature affecting the background uniformity among the pixels has serious effects on the background accumulation and thus on the imaging capabilities. In case of SuperAGILE the background uniformity is dominated by the threshold uniformity. The study of the effect of the measured threshold non uniformity on SuperAGILE imaging is evaluated by means of semi-analytic techniques and are described in chapter 8.

The Appendix A contains a list of papers, sorted by topic, concerning this research work and published in the years 2001–2004. The list of acronyms and abbreviations is contained in Appendix B.

Chapter 1

AGILE in the context of the High Energy Astrophysics

1.1 Introduction

In this chapter an overview of the most important classes of sources in the High Energy Astrophysics that will be observed by the AGILE mission is presented. Of the main classes of sources a short description is given aiming to overview the emission mechanisms and the most important observational features matching the AGILE scientific performances, without pretending to report the matter in a complete and exhaustive presentation.

In sec. 1.2 the main features of the Gamma Ray Bursts are described, an overview about the Compact Galactic Sources is in sec. 1.3, the Active Galactic Nuclei are reviewed in sec. 1.4 and the Galactic Diffuse Emission of gamma rays is described in sec. 1.5. At the end of each section the AGILE contribution to the study of the just described class of sources depending on the class features and the AGILE scientific performances is given. Finally sec. 1.7 contains the conclusions of this chapter.

1.2 Gamma Ray Bursts

1.2.1 The discovery of the prompt and afterglow emission

Gamma Ray Bursts (GRB) are brief transients of high-energy photons appearing at random in the sky and emitting the bulk of their energy between 100 keV and 500 keV. One to three events are recorded every day and they do not show repetitions.

The first GRB have been detected between July 1969 and July 1972 by the four Vela class satellites (Vela 5A, 5B, 6A and 6B), launched in a joint program of the Advanced Research Projects of the U.S. Department of Defense and the U.S. Atomic Energy Commission, managed by the U.S. Air Force to monitor the nuclear explosions in the atmosphere, forbidden by the nuclear test treaties. The four satellites, flying in a circular orbit with radius about $1.2 \cdot 10^5$ km, were equipped with scintillation detectors

sensitive to X-rays ($6 \div 12$ keV) and gamma rays ($150 \div 750$ keV). Only nearly three years after the discovery the information about this new class of sources was unclassified and the first paper about sixteen events was published in 1973 (see Klebesadel et al. (1973)). The four Vela satellites recorded 73 gamma ray bursts in the ten years interval July 1969 – April 1979.

In the next step a system of satellites was set-up, the first interplanetary network (IPN), started with the launch of the Helios-2 satellite, carrying the first experiment purposefully built for GRB studies as described in Cline et al. (2001). The IPN was then completed by late 1978 with the NASA launch of Pioneer Venus Orbiter and the Soviet Launches of Venera-11 and Venera-12. The IPN can localize GRB with triangulation techniques based on the detection of more than one distant satellite. Continuously some satellite left the IPN and are replaced by new spacecraft. The IPN is still working and can now localize GRB to a single error box whose typical size is ten square arcminutes, as in Hurley et al. (2001).

After these first pioneering detections, the Burst and Transient Source Experiment (BATSE, see Fishman et al. (1989) for details about the instrumentation) on board the NASA Compton gamma ray Observatory (CGRO) was launched in 1991 and was dedicated to the study of the GRB to reveal its nature and origin. The most striking result of the nine years BATSE activity, summarized in a catalogue (Paciesas et al. (1999)) containing 2704 GRB, is the discovery of the high degree of isotropy of the Gamma Ray Bursts location (see also Meegan et al. (1992)), that can be seen in the plot in galactic coordinates in fig. 1.1. No dipole or quadrupole moments have been detected in the location distribution (detailed analysis in Briggs et al. (1996)). This degree of isotropy can be achieved only by phenomena originating near Earth (within the Solar System) or at cosmological distance (on the gigaparsec scale).

One of the major breakthrough in the field was achieved in 1997 by the Italian-Dutch BeppoSAX satellite (details in Boella et al. (1997a) and Piro et al. (1995)), including an all-sky Gamma Ray Burst Monitor (GRBM, see Costa et al. (1998) and Frontera et al. (1997) for further information) sensitive in the $40 \div 700$ keV energy range, two Wide Field Cameras (WFC, described in Jager et al. (1997)) covering about 5 % of the sky in the $2 \div 26$ keV energy range with a pixel size of 5', and a set of Narrow Field Instruments (NFI), designed for observations in the $0.1 \div 10$ keV energy band (Low-energy concentrator spectrometer (LECS, see Parmar et al. (1997) for details) with a 37 arcmin field of view and an imaging resolution of 1 arcmin) and in the $1.3 \div 10$ keV energy band (Medium-energy concentrator spectrometer (MECS, see Boella et al. (1997b) for further information) with a field of view of 28 arcmin radius and an angular resolution about 100 arcsec).

On 28 February 1997 the GRBM was triggered by a GRB event (hereafter GRB970228) and a counting excess was also present in one WFC. Images produced with the WFC before and after the event showed that the source was transient and simultaneous with the burst. Only eight hours after the GRBM trigger the observation with the Beppo SAX NFI started in the WFC error box and one X-ray transient source was found, whose flux decreased of nearly a factor of twenty in about three days (see fig. 1.2) and whose position was missing in the Rosat all-sky survey (Boller et al. (1997)). This

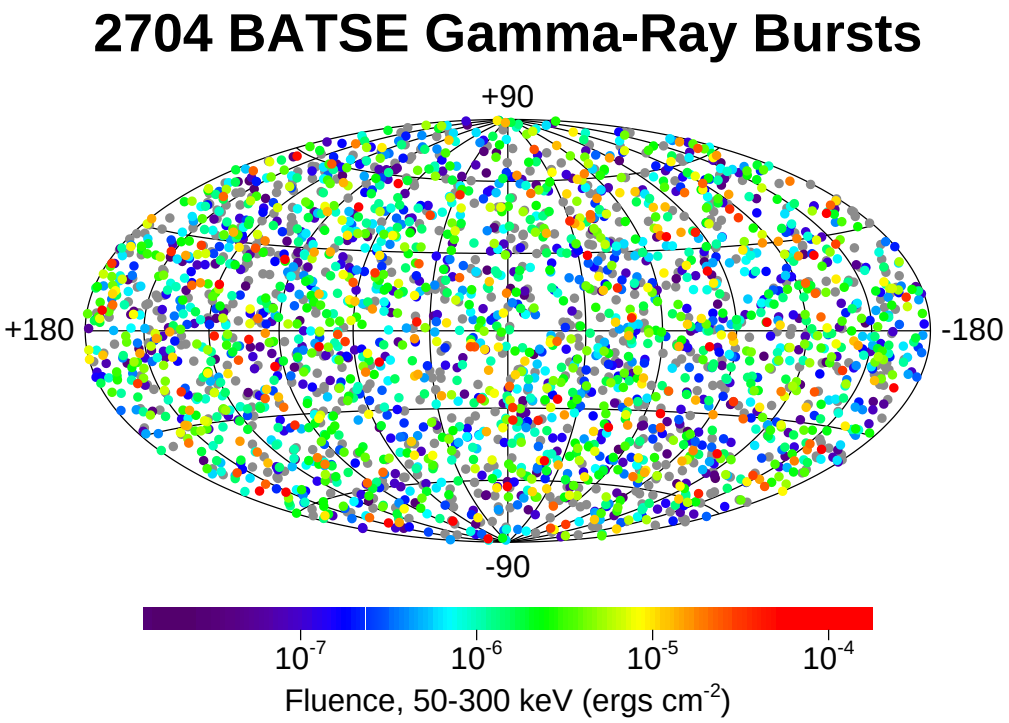

Figure 1.1: Final map showing the location in galactic coordinates of the 2704 GRB recorded with the Burst and Transient Source Experiment (BATSE) on board NASA's Compton gamma ray Observatory (CGRO) during the nine-year mission (from `http://gammaray.msfc.nasa.gov/batse/grb/skymap/`).

X-ray transient source is the first example of a GRB "afterglow". More details about this observation can be found in Costa et al. (1997).

On 28 February 1997, about 21 hours after GRB970228 occurred, an object in the error box of the WFC was detected in the V and I band images with the Prime Focus Camera of the 4.2 m William Herschel Telescope at La Palma (more details in van Paradijs et al. (1997)). During this observation the magnitudes of the object were $V = 21.3 \pm 0.1$ and $I = 20.6 \pm 0.1$. A second pair of images in the same configuration was exposed on 8 March 1997 and the object was not detected ($V > 23.6$ and $I > 22.2$).

Further images were obtained with the ESO New Technology Telescope (NTT) on 13 March and show a faint and extended object, probably a galaxy, at the position of the transient. Known types of optical transients, such as novae, supernovae, dwarf novae and flare stars, are unlikely to account for the optical transient because of the amplitude and short timescale of its variability. From a rough estimate of the galaxy redshift a value between 0.2 and 2 was found. With a spectroscopic campaign at Keck observatory (described in Bloom et al. (2001)) the redshift of the host galaxy was measured and was found that $z = 0.6950 \pm 0.0003$, in agreement with the previous result.

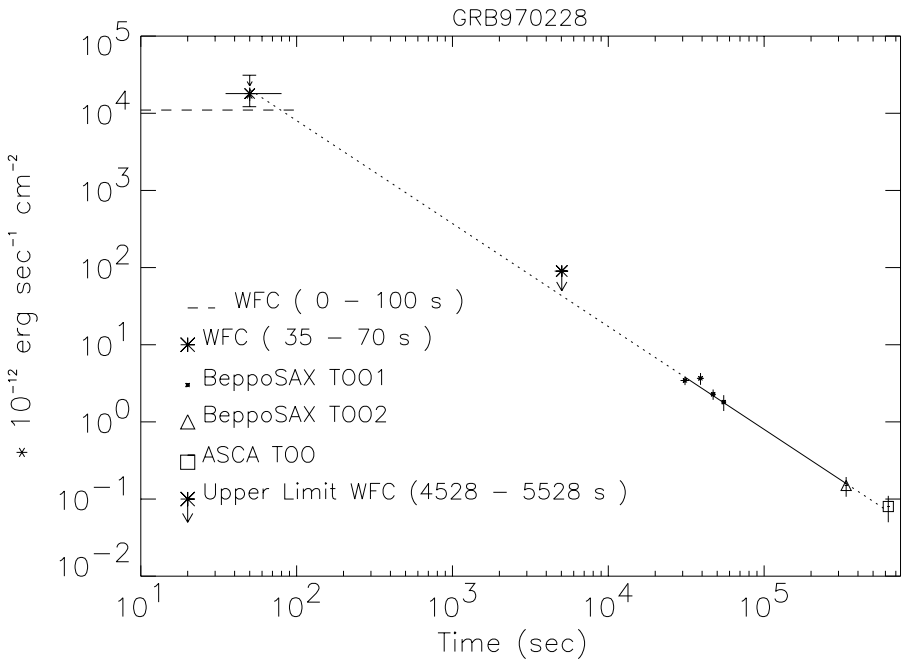

Figure 1.2: Source flux with time in the 2-10 keV range from Costa et al. (1997). The zero time is taken at the GRBM trigger time. Data are fitted by a power law ($\propto t^{-1.32}$), shown as a solid sloping line at lower right.

The first radio afterglow was detected for the gamma ray burst of 8 May 1997 (GRB970508): a variable radio source was found in the error box of GRB970508 and coincident with the optical transient (see Frail et al. (1997) for more information). The radio afterglow emission shows a frequency dependent rise time (about ten days at 8.46 GHz, about three weeks at 4.86 GHz), remains steady for about two months and then starts to decrease. From the observed fluctuations in the radio emission of the source, an angular size $\theta \simeq 3$ μarcsec can be estimated two weeks after the burst. The measured redshift $z = 0.835$ (see Metzger et al. (1997) for the complete analysis) gives a distance $D \simeq 10^{28}$ cm and, at that distance, the angular size θ corresponds to a linear size $R \simeq 10^{17}$ cm. For a relativistic fireball, $R = f\gamma^2 ct$ with γ Lorentz factor and f factor ranging between 2 and 14 depending on the dynamical details of the expansion. Thus $f\gamma \simeq 4$ implying a mildly relativistic shell two weeks after the burst.

Started with GRB970228, the observation of the optical counterparts of Gamma Ray Bursts detected in the X-ray band and the determination of their redshift continues to play a crucial role in the understanding of the GRB physics. Recent examples are in Castro et al. (2003) giving $z = 2.038$ for GRB 000926, Andersen et al. (2000) discussing $z = 4.50$ of GRB 000131 and Bloom et al. (2003) with $z = 1.30658$ for GRB 990506 and $z = 1.1181$ for GRB 000418. The measured redshift gave the first unambiguous evidence of the GRB cosmological origin.

1.2.2 Observational properties of the Gamma Ray Bursts

The GRB observed fluence on Earth is $10^{-8} \div 10^{-4}$ erg $\cdot$ cm^{-2}, the lower limit depending on the detector sensitivity and on the log N-log S curve. If the emission is isotropic the total energy is of the order $10^{51} \div 10^{54}$ erg while this value decreases of about two orders of magnitude if the emission is beamed.

The overall energy emitted in the GRB afterglow ranges from a few per cent to a consistent fraction of the energy in the main burst. Moreover, while the measurements of the energy of the burst includes the peak of the emission and is "more or less" bolometric, the measurement of the afterglow is limited by the band of the optics. As the spectrum is flat in νf_ν, we do not really know yet how much energy is in the afterglow. The afterglow light curve decays, in most cases, as a single power law, $F_\nu \propto t^{-\alpha}$ with $1 \leq \alpha \leq 2$.

The GRB spectrum is nonthermal and can be fitted using a Band function,

$$N_E(E) = \left\{ \begin{array}{ll} A \left(\frac{E}{100 \text{ keV}}\right)^{\alpha} \exp(-E/E_0) & \text{if } (\alpha-\beta)E_0 \geq E \\ A \left[\frac{(\alpha-\beta)E_0}{100 \text{ keV}}\right]^{\alpha-\beta} \exp(\beta-\alpha) \left(\frac{E}{100 \text{ keV}}\right)^{\beta} & \text{if } (\alpha-\beta)E_0 < E \end{array} \right\} \qquad (1.1)$$

introduced in Band et al. (1993), and representing a power law with an exponential cut-off at energy E_0. From the 54 spectra reported in Band et al. (1993), typical values of the parameters are $-1.5 \leq \alpha \leq 0$ and $-2.5 \leq \beta \leq -2$. There does not appear to be a clear relationship between α and β so the linear correlation coefficient of the two parameters is nearly zero. The distribution of the cut-off energy as detected by BATSE peaks at $E_0 \simeq 150$ keV but extends to much higher values, up to 1000 keV.

Bright X-ray transient events with fluence in the range $10^{-8} \div 10^{-7}$ erg $\cdot$ cm^{-2} $\cdot$ s^{-1}, duration ranging from 10 s to 200 s and single power-law photon spectrum in the $2 \div 25$ keV energy band with cut-off energy at about $30 \div 50$ keV have been discovered by the BeppoSAX WFC and called X-ray flashes. New observations of the High Energy Transient Explorer 2 (HETE-2, see Ricker and HETE Science Team (2001) for details) satellite show that some X-ray flashes have observed peak energy smaller than 5 keV without photon detection above 10 keV, as in Sakamoto et al. (2004).

Most striking is the morphological diversity of the GRB lightcurves and the large range of the event durations. The approximate Gamma Ray Burst duration range spans from about 30 ms to more than 100 s. Two groups of GRB can be identified basing on duration, for which the T_{90} (the time during which 90 % of the fluence is accumulated) is smaller or larger than 2 s (see Kouveliotou et al. (1993) for a complete analysis). Each group exhibits an acceptable bimodal log-normal ("two gaussian") fit with a third gaussian needed at 99.98 % significance level. In Horváth (2002) this analysis is performed on the 1929 GRB of the BATSE catalogue that have duration and peak flux information. As a result three duration classes are found, the short bursts with average duration $\log T_{90} = -0.25$ (corresponding to $T_{90} = 0.6$ s), standard deviation $\sigma(\log T_{90}) = 0.53$ and weight $w = 0.26$, the intermediate bursts with $\log T_{90} = 0.63$ (corresponding to $T_{90} = 4.3$ s), $\sigma(\log T_{90}) = 0.20$ and $w = 0.06$ and finally the long bursts with $\log T_{90} = 1.55$ (corresponding to $T_{90} = 35.5$ s), $\sigma(\log T_{90}) = 0.42$ and

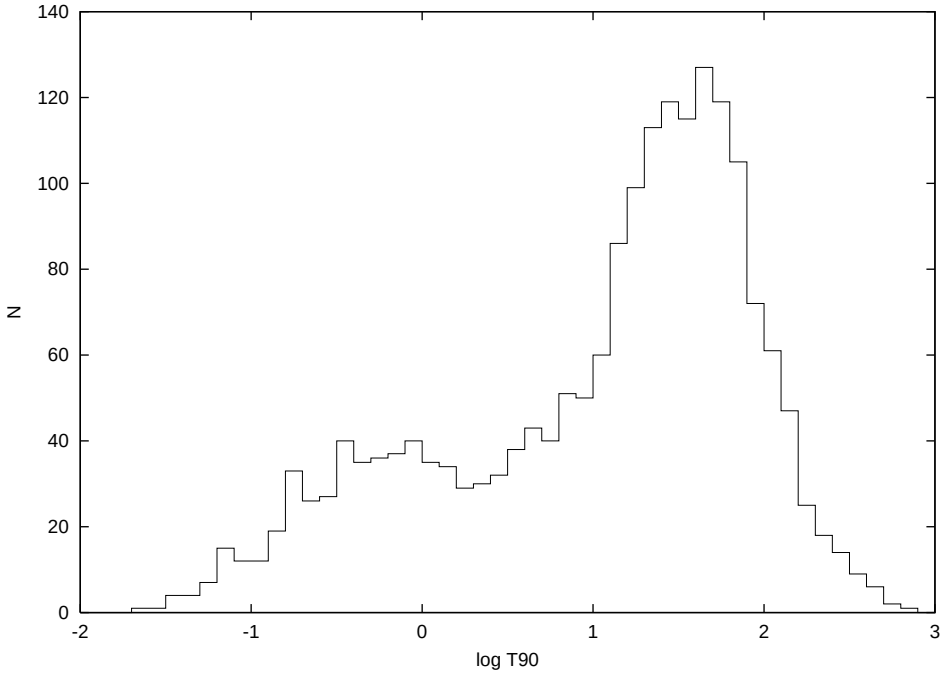

Figure 1.3: Histogram of the GRB duration T_{90} from Horváth (2002).

$w = 0.68$. The histogram of the GRB duration from Horváth (2002) can be seen in fig. 1.3.

A correlation between the GRB peak energy and the total energy emitted in the prompt emission has been found (see Amati et al. (2002)). The relation is in the form $E_{peak} \propto E_{iso}^{1/2}$ where E_{peak} is the peak energy and E_{iso} is the total energy (calculated assuming isotropy). Such a correlation is not yet firmly established and is debated by other authors (see for example Friedman and Bloom (2004)).

1.2.3 Theoretical models

The nonthermal GRB spectrum (1.1) indicates that the observed emission emerges from an optically thin region. However the observed small temporal variability $\delta t \simeq 10$ ms implies that the size of the source is $c \cdot \delta t \simeq 3 \cdot 10^8$ cm (see Piran (1997)). Such a small source must be optically thick to photons, because of the $\gamma\gamma \to e^+e^-$ reaction that has an opacity $\tau_{\gamma\gamma} \gg 1$, so it cannot emit nonthermal emission. This fact is known as the Compactness problem.

The simplest way to overcome this problem is considering the source as moving relativistically toward us, in the frame of the so called "fireball model" (see Piran (2000) for details). In this scenario an extremely relativistic shock with Lorentz factor Γ between 100 and 1000 accelerates electrons that emit gamma rays via synchrotron or synchrotron self Compton processes so producing the Gamma Ray Burst prompt emission. The interaction of the relativistically accelerated matter with the surrounding material

(interstellar medium or circumstellar wind emitted earlier) generates an external shock producing the observed afterglow.

The fireball model predicts an emission likely to be beamed within a cone of aperture $\theta \simeq 0.1$. This fact implies a beaming factor of about 100, so reducing the energy of the burst to about $10^{51} \div 10^{52}$ erg. Such an amount of energy is a significant fraction of the binding energy of a solar mass compact object. Also the millisecond variability time scale suggests that a solar mass compact object is involved in the emission process. The GRB duration (from 10 s to 100 s) suggests a prolonged activity, much longer than the gravitational time scale of the source.

All these considerations (reported in Piran (2000)) suggest that the GRB are powered by accretion of a 0.1 $M_{\odot}$ disk onto a compact object, most likely a black hole. Such a system can be produced by the merging of a binary neutron star, of a neutron star and a black hole, of a neutron star and a white dwarf or, finally, by a collapsing star of large mass ("failed supernova" or "hypernova" introduced in Paczynski (1998)) producing a rotating massive black hole surrounded by an accreting torus. Alternative models include the explosion/implosion of a supramassive neutron star, a neutron star with a larger baryon number than any normal neutron star deriving part of its support against self-gravity from the centrifugal force and taking place through mass and angular momentum transfer from a close companion, as in Vietri and Stella (1999), or the Poynting-flux driven outflow from a magnetar, an ultramagnetized neutron star with a magnetic field of about $10^{14} \div 10^{15}$ G, as explained in Lyutikov and Blackman (2001).

1.2.4 The AGILE contribution

Gamma Ray Bursts are one of the most important scientific goals of the AGILE mission. In the wide field of view of the two instruments 25 events per year are expected in the hard X-ray band and $5 \div 10$ events per year in the gamma ray band. The GRB prompt emission will be detected mainly with the Mini-Calorimeter and the SuperAGILE hard X-ray monitor. SuperAGILE sensitivity is not enough to detect the faint X-ray afterglows after the very first start.

The angular resolution of SuperAGILE for sources as intense as the GRB ranges from about 1 arcmin to 2 arcmin. Such a resolution, together with the high expected fluence, can help to reconstruct the position of the events in the gamma ray band where the angular resolution is about 1°, so allowing to study this class of sources in a wide energy range ($15 \div 40$ keV and 30 MeV $\div$ 50 GeV).

Between 1991 April 22 and 1994 August 29, five GRB coincident with a trigger from the BATSE instrument have been detected in the EGRET spark chamber (see Jones et al. (1996) for details). The lack of redshift measurement for these events does not allow to know their fluence. Similar events can be detected by the Gamma Ray Imaging Detector (GRID) and, since they are expected to be faint (see for example Schneid et al. (1995) for a detailed analysis), the timing and position from the SuperAGILE observation can be used to constraint the search for GRB in the GRID data.

Furthermore, SuperAGILE can image intense sources, as the GRB, directly on-board so reducing the total time needed to obtain the source position. Using the ORB-

COMM satellite constellation[1], the GRB information from the on-board processing will be rapidly transmitted to the ground station (within one to ten minutes) and from there will be delivered as short text messages. In this way the GRB coordinates can be distributed to optical, infrared and radio observers so allowing a rapid and efficient follow-up. The trigger to SuperAGILE can also be given by the Mini-Calorimeter, whose energy band best fits the energy peak of the GRB emission although it cannot produce images.

As all the high variable sources, the GRB lightcurves show small scale variations. The analysis of twenty GRB reported in Walker et al. (2000) shows that all bursts have low-level flickering on timescales from 256 μs to 33 ms, in the majority of them the rise times are faster than 4 ms, 30 % have rise time faster than 1 ms and finally two GRB reveal isolated flares with timescales from 256 μs to 2048 μs. For this reason a high temporal resolution of the GRB prompt emission is an important tool to understand their nature. Thanks to the low dead time of the front-end electronics in all the AGILE instruments (time tag is about 2 μs in SuperAGILE and dead time is about 100 μs in the GRID), the initial impulsive phase of GRB can be studied with high temporal resolution.

1.3 Compact Galactic Sources

The first X-ray source discovered outside the Solar System is Sco X-1, detected in 1962 and located in 1966 in the Scorpio constellation (details in Gursky et al. (1966a)). This source, the most powerful in the X-ray band, has an optical counterpart of only $V \simeq 13$ magnitude (Gursky et al. (1966b)) with a peculiar optical spectrum showing a smooth blue continuum with superposed weak emission lines of hydrogen and ionised helium, similar to the cataclismic variables and without absorption features (Charles and Seward (1995)). The absence of absorption features indicates that only a small fraction of the observed spectrum is coming from a main sequence star and the presence of ionized helium indicates that the source of excitation of the lines is very hot and probably connected with the X-rays. Since the discovery there were clear indications that the X-ray emission was due to a binary system.

Theoretical speculations about the nature of the energy source in Sco X-1 involved the presence of white dwarfs, neutron stars and black holes within the binary system. Few months after the launch of the Uhuru satellite (12 December 1970) two more sources were discovered (Her X-1 and Cen X-3), showing regular pulsations with extremely precise periods. In observations over longer time intervals both sources showed X-ray eclipses, a clear indication of the presence of a binary system, so these objects are grouped as X-ray binaries. The compact object contained in the binary system cannot be a white dwarf since the measured period is so short that the white dwarf would break up with centrifugal forces. For this reason the X-ray emitting object must be a rapidly spinning neutron star or, in some cases, a black hole.

[1]Web site `http://www.orbcomm.com`

The short binary period indicates that the two components of the system are interacting and exchanging mass. The X-ray emission is due to the heating because of the gravitational energy released by the matter transferred from the non collapsed component to the compact object, that is said to "accrete" the material. The accretion phenomenon produces an energy release with luminosity

$$L \simeq \frac{GM\dot{M}}{R} \tag{1.2}$$

where G is the gravitational constant, M is the mass of the compact object, R its radius or the radius of the last marginally stable orbit in case a black hole is present and $\dot{M}$ is the mass accretion rate. The corresponding efficiency is $\eta = L/\dot{M}c^2 \simeq 10 \div 40$ %, rather high if compared to the efficiency of the nuclear reactions ($\eta \simeq 1$ %).

The mass transfer within a binary system can be caused by the stellar wind from a massive OB star or from the matter flow through the inner Lagrangian point. Since in the first case the non collapsed object is a massive star, these objects are classified as high mass X-ray binaries (HMXB) while the second type of objects contain a small mass star and are called low mass X-ray binaries (LMXB). The stellar wind from a massive star carries very little angular momentum and falls directly onto the compact object while the material from a low-mass star is directed into the gravitational field of the compact object and dissipates its angular momentum forming an accretion disk. More details about the classification of the X-ray emitting binary systems can be found in Charles and Seward (1995).

HMXB and LMXB are sources of X-ray emission but do not emit gamma rays. Other classes of compact galactic sources can be found that emit gamma rays, mainly the Gamma ray pulsars, that can be detected also in other energy band, especially at radio wavelengths. Of great importance between the Compact Galactic sources are the Unidentified EGRET sources, so called because their gamma ray emission have been detected by the EGRET experiment on board CGRO but their counterparts have not been found in other energy bands.

1.3.1 High-mass X-ray binary stars

In high mass X-ray binary systems the material transferred onto the compact object is provided by a powerful stellar wind, emitted by an early type massive star. Only the massive star can be detected in the optical band because it is so luminous even compared to the X-rays emitted by the compact object.

Most of the HMXB show X-ray pulsations, with periods of order of seconds and orbital periods of order of days and are found associated with bright stars of spectral type earlier than B2. From the Doppler shift of the spectral lines emitted by the primary component and from the binary system inclination, that can be measured if the system shows eclipses, the mass of the compact object can be evaluated. In binary systems where this evaluation is possible neutron stars with masses from 0.98 $M_\odot$ (for Her X-1) to 1.8 $M_\odot$ (for 4U1538-52) have been found.

Following the model developed by Davidson and Ostriker (1973), the compact object accretes matter from the companion stellar wind, ranging typically between $10^{-6}\ M_{\odot} \cdot \mathrm{year}^{-1}$ and $10^{-4}\ M_{\odot} \cdot \mathrm{year}^{-1}$ and is energized by the UV emission. The mass loss occurs in all directions from the surface of the star and the orbiting neutron star must pass through it.

The accreted material from the stellar wind probably forms an accretion disk because of its angular momentum. In case a neutron star is present in the binary system, the gas spirals downward and, at the star magnetospheric radius, it moves along the magnetic field lines toward the magnetic polar caps. As the material hits the neutron star surface, a very hot shock is formed in which X-rays are produced. The X-ray emission is not uniform because of the column of material above the polar cap and is shadowed into a kind of fan beam. These magnetic pole caps are displaced from the rotation axis, so they modulate the X-rays emission at the neutron star spin period producing a kind of lighthouse effect. The angular momentum of the accreted material is transferred to the neutron star, producing the so called "spin up" effect, i. e. the decrease of the pulsing period.

Some compact galactic sources show X-ray transients, flaring up suddenly and then fading into invisibility after only a few weeks. These systems can be divided into two class: Be stars and soft X-ray transients.

Be stars are mid B giant or main sequence stars with peculiar spectra showing emission lines, variable in both intensity and profile on short and long timescales (hours to days). The outbursts are produced in these systems by episodes of mass ejection, probably from the equator, that form a ring of material. The mass ejection can be connected with the fast rotating speed of these stars, often close to the break-speed. The compact object encounter the ring so producing an increase in the X-ray emission.

The peculiar system PSR B1259-63, composed of a radio pulsar orbiting around a massive Be star companion emitting $L_X \simeq 10^{34}\ \mathrm{erg} \cdot \mathrm{s}^{-1}$ in the band $1 \div 10$ keV (Kaspi et al. (1995) and Hirayama et al. (1996)) and $L_X \simeq 3 \cdot 10^{34}\ \mathrm{erg} \cdot \mathrm{s}^{-1}$ in the band $30 \div 200$ keV (Grove et al. (1995)), is of special interest for AGILE. The X-ray emission is due to the interaction of the wind from the radio pulsar with the mass outflow of the Be companion, as explained in Tavani and Arons (1997). PSR B1259-63 is expected to emit in the gamma ray band although only upper limits have been detected by EGRET, as described in Tavani et al. (1996). The same source has been recently detected at TeV energy above about 200 GeV, see Beilicke et al. (2004).

The soft X-ray transients, on the other hand, are low-mass systems with non collapsed stars of usually K-M spectral type and brighten during outbursts showing softer X-ray spectra. Cen X-4, for example, shows intensity variations of about 300 times producing outburst approximately every ten years. This source is a binary system composed of a red dwarf K3V star and a neutron star. The mechanism causing the outbursts is probably connected with episodes of mass transfer onto the neutron star which produces the strong X-ray emission and is still unknown.

1.3.2 Low-mass X-ray binary stars

The model of low-mass X-ray binary stars is an evolved late-type star transferring material through its inner Lagrangian point into the gravitational field of a compact object (white dwarf, neutron star or black hole). The accreted material orbits around the compact object, so forming an accretion disk. The secondary star is generally too faint to be detected apart from observation in the infrared and during the eclipses. In these cases it is possible to find that the secondary star is generally of low mass and evolved.

The type of the compact object can be inferred depending on the luminosity, the light curve and the spectrum of the binary system. If the luminosity is smaller than $10^{33}\,\mathrm{erg}\cdot\mathrm{s}^{-1}$, the compact object is likely to be a white dwarf while, if the luminosity is bigger, the compact object is almost surely a neutron star or a black hole. If the system shows X-ray bursts, it contains a neutron star while, if the X-ray spectrum is soft, it may contain a black hole.

The binary behaviour of a LMXB is difficult to be detected in X-ray observations because of the nature of the X-ray emitting region. In fact an eclipse can happen when the mass-losing star is found between the compact object and the observer but, in this case, the optical thickness of the disk itself prevents us from detecting the X-ray emission. Eclipses in X-rays can be found in some sources, like EXO0748-676 and, from the shape of the light curves, the characteristic dimension of the compact object can be inferred.

Characteristic of some LMXB systems is the periodic emission of X-ray bursts, short (about 10 s duration) and intense (about 10^{39} erg) flares with a black-body like time profile and a time decay shorter at high energy and longer at small energy. The sources emitting X-ray bursts are generally distributed in the galactic bulge and seem all of the same population. Furthermore, the radius of the sphere required to radiate the observed black body falls in the range $10 \div 15$ km, the characteristic radius of a neutron star.

As explained by Maraschi and Cavaliere (1977) and independently by Woosley and Taam (1976), the X-ray bursts can be considered as a thermonuclear flash due to the unstable helium nuclear burning on the surface of a neutron star. The X-ray bursts repeat periodically because the accretion by the neutron star from the companion star produces a hydrogen layer that steadily burns forming helium. When the density and temperature of the helium layer reach a critical point it starts burning into carbon. The accretion then continues producing helium until the unstable nuclear burning happens again and a new burst is produced. The X-ray bursts are clearly surface effects and can be produced only by LMXB systems containing a neutron star. Moreover the X-ray burst emission is characteristic of a small mass transfer rate, in fact at high mass transfer rates the helium burning instability does not occur and the bursting behaviour is suppressed.

As seen in sec. 1.3.1 above, the HMXB systems contain neutron stars showing pulsating emission of X-rays while the LMXB systems contain neutron stars showing bursting emission of X-rays. The difference between these two emission behaviours can be explained in terms of the neutron star magnetic field, strong during the initial star collapse producing the neutron star and slowly decaying over time. Since a strong

magnetic field is needed to channel the material onto the poles of the neutron star, X-ray pulsations are expected only in young neutron stars, associated with young and massive stellar companions. On the other hand, the small magnetic field of the older neutron stars associated with old and less massive stellar companions lets the accreting material fall onto the neutron star surface producing the X-ray bursts.

1.3.3 Black hole candidates

The emission of X-rays from a binary system reveals the presence of a compact object. Since the system luminosity depends on the gravitational potential of the compact object, from the luminosity measurement it is possible to notice only if we are dealing with a white dwarf or a more massive object like a neutron star or a black hole. Distinguishing between a neutron star and a black hole requires precise mass measurements, obtainable from the optical spectroscopy using the mass function,

$$f(M) = \frac{M_x^3 \sin^3 i}{(M_n + M_x)^2} = \frac{P K_n^3 \sin^3 i}{2\pi G} \tag{1.3}$$

where M_x and M_n are the mass of the compact object and the normal star respectively, P is the period, and $K_n \sin i$ is the velocity amplitude of the normal star with i inclination angle of the orbit to our line of sight (from Charles and Seward (1995)). M_n and i must be accurately known in order to find M_x.

About twenty black holes have been discovered and studied in our Galaxy during the last two decades (Ziólkowski (2003) contains a detailed table with orbital periods, masses and references). These black holes can be found preferentially in low-mass binary systems, associated to a companion of $M \leq 1\ M_\odot$. Black holes in LMXB are transient sources, displaying month-long outbursts with luminosity $7 \div 8$ orders of magnitude bigger than their $L < 10^{31}\ \mathrm{erg \cdot s^{-1}}$ quiescence luminosity. Black holes can also be found associated with high mass stars and the first example of such a system is Cygnus X-1, whose mass function gives $M_x \geq 15\ M_\odot$.

Peculiar sources containing a black hole and emitting two-sided relativistic jets are the so called "microquasars" for the similarity of their features with the quasar class of Active Galactic Nuclei. The characteristics of these systems can be explained considering a stellar mass black hole surrounded by a gas torus and accreting matter from that. The collimated jets are composed of relativistic plasma and the emission mechanism is still unclear. An example of microquasar is the X-ray source GRS 1915+105, see for example Castro-Tirado et al. (1994).

1.3.4 Gamma ray pulsars

Six gamma ray emitting pulsars have been detected by EGRET (see Nolan et al. (1996)): Crab, Vela, Geminga, PSR B1706-44, PSR B1055-52 and PSR B1951+32, although PSR B1951+32 is not included in the Third EGRET Catalogue. A pulsed emission of gamma rays at ultra-high energy (E > 500 GeV) from Vela pulsar has been observed by atmospheric Cerenkov detectors (see Bhat et al. (1980)).

As shown in Nolan et al. (1996), in the EGRET energy range, the spectra of the pulsars can be fitted by a simple power law and the fitted spectral indices range from -2.07 for the Crab to -1.39 for Geminga. Four out of six pulsars have spectral indices harder than -1.6. Three spectra show a drop in flux above few GeV while two others have large uncertainties in flux in the $4 \div 10$ GeV band and cannot exclude the existence of a similar dropoff. Only the Crab is inconsistent with a significant dropoff above 4 GeV.

The most evident feature of the pulsar light curves is that four of them (Crab, Vela, Geminga and PSR B1951+32) have two roughly equal peaks separated by $0.4 \div 0.5$ in phase while the other two (PSR B1706-44 and PSR B1055-52) show a single broad peak, that might really be double or even triple. Observations with higher counting statistics may improve the understanding of the last two pulsars. Only the Crab has a gamma ray light curve matching fairly well with the radio pulsation, although the radio emission has a third peak below 600 MHz that does not match any gamma ray feature. PSR B1055-52 has a similar triple-peaked radio pulse but without any correlation with the gamma ray peaks and the other radio pulsars have single radio peaks which do not line up with the gamma ray peaks.

A detailed model of the pulsar beaming geometry is not yet stated so the luminosity of the source cannot be calculated exactly. From a rough estimate and assuming that the observed radiation is concentrated in two conic beams, however, a luminosity about $2 \cdot 10^{35}$ erg $\cdot$ s^{-1} between 50 MeV and 10 GeV can be estimated (see Bignami and Hermsen (1983)).

1.3.5 The EGRET unidentified sources

The third and last EGRET catalogue of high-energy gamma ray sources (Hartman et al. (1999)) contains 271 objects, including the single solar flare detected in 1991, the Large Magellanic Cloud, five pulsars, one probable radio galaxy detection (Cen A), 66 high confidence and 27 low confidence blazar identifications and 170 sources not yet identified, generally known as EGRET unidentified sources. The search of the counterpart of such unidentified sources is one of the most interesting problems in today gamma ray astronomy and is one of the scientific objectives in the next gamma ray astronomy missions, such as AGILE and GLAST (see for example Torres and Nuza (2003)).

The point spread function of the EGRET telescope is about 6° at 100 MeV and smaller at higher energies (more details in Thompson et al. (1993)). As explained in Hartman et al. (1999), the source location is estimated using the maximum likelihood method and constructing likelihood test statistics maps at different energies ($E < 100$ MeV, $300 < E < 1000$ MeV and $E > 1000$ MeV). A source is defined as unidentified if no known source can be associated with the EGRET error box. Since more than 60 % of the sources contained in the EGRET catalogue are classified as unidentified, there is great interest in the nature of these sources, whether they be pulsars, blazars or representatives of new classes of gamma ray sources.

As shown in Mukherjee et al. (1995), the longitude distribution of the unidentified

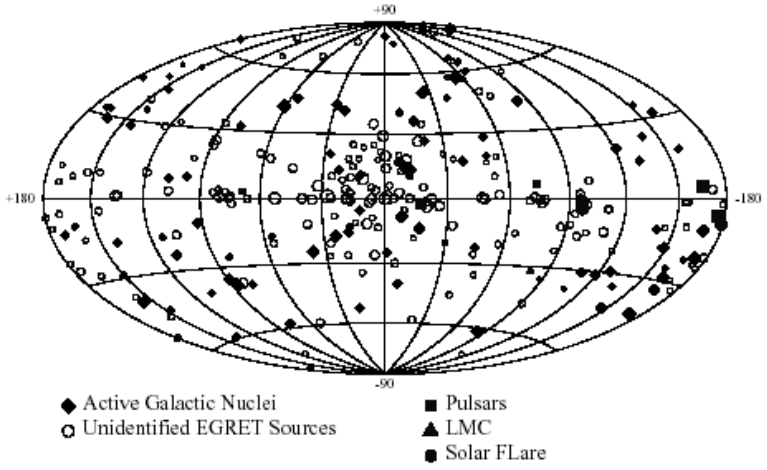

Figure 1.4: Final map showing the location in galactic coordinates of the 271 sources recorded in the Third EGRET catalog (from Hartman et al. (1999)). The unidentified sources are plotted with open circles

sources is not uniform and shows a broad peak centered approximately on the galactic disk and with a dispersion of $71.3^\circ \pm 11.9^\circ$, indicating a concentration of sources toward the inner part of the Galaxy. The absence of a strong concentration in longitude within 30° of the Galactic center suggests that the sources are rather uniformly distributed along the disk. The longitude distribution suggests that the unidentified sources are not distant objects, with an upper limit at about 6 kpc. The lower limit can be estimated from the latitude distribution of the sources with $|b| < 10^\circ$, giving a standard deviation of $1.9^\circ \pm 0.3^\circ$. From the observed latitude distribution a minimum distance of about 2.6 kpc can be inferred.

Assuming a beaming angle of about 1 sr and a distance in the range $2.6 \div 6$ kpc, the luminosity range of the unidentified EGRET sources close to the Galactic plane is $(0.3 \div 1.33) \cdot 10^{33}$ erg $\cdot$ s^{-1}, higher than the typical luminosity of the pulsars. Basing on these arguments, Mukherjee et al. (1995) conclude that the unidentified sources cannot be explained as representing a population of older and low luminosity pulsars like Geminga because their predicted luminosity would be too low to account for the unidentified sources at their estimated distances.

In Kaaret and Cottam (1996) the position of 16 over 25 unidentified EGRET sources lying near the Galactic plane (Galactic latitude $|b| < 5^\circ$) is correlated with the position of the OB associations from the catalog in Mel'Nik and Efremov (1995). The authors found that four sources are well within OB associations, five sources have 95 % position contours overlapping with OB associations boundaries and seven sources lie within 1° from the boundary of an OB association. Several classes of sources emitting gamma rays occur near OB associations, mainly Supernova remnants and high-mass X-ray binaries. Once the correlation of gamma ray sources and OB associations is stated, from the known distances of the OB associations the luminosity of the unidentified sources can

inferred. In Kaaret and Cottam (1996) it is found that the estimated pulsar luminosity is about 10^{35} erg $\cdot$ s^{-1} and their distribution is consistent with that of the known gamma ray pulsars.

An alternate method of determining the source class is the study of the flux variability, as in Wallace et al. (2000) for example. In this paper the variability index V is used, defined starting from the light curve χ^2. If Q is the probability of obtaining a value of χ^2 equal or greater than the empirical χ^2 from an intrinsically non variable source, the variability index is defined as $V \equiv -\log Q$ and light curves with $V \geq 3$, corresponding to $Q \leq 10^{-3}$, are considered to manifest source variability. Pulsars are believed to be stable on timescales of about one day (see for example Ramanamurthy et al. (1995)) while blazars are strongly variable on the same timescale (see for example Mattox et al. (1997)). Since the statistics of the data are limiting, especially on the one day timescale, EGRET is sensitive to only the most dramatic short term variations. In Wallace et al. (2000) the study of the variability index V of eight sources, two identified and six unidentified, is reported. The variability index of the unidentified sources is smaller than the value of the AGN and the unidentified sources are not characterized by strong variability on one and two days timescale.

1.3.6 The AGILE contribution

Pulsars are a major topic of investigation of AGILE and this new mission will improve photon statistics for searches of gamma ray pulsars offering the first possibility, before the launch of GLAST mission, of detecting several young and energetic radio pulsars, discovered since the end of CGRO mission.

As shown in Tavani et al. (2004), addressing and resolving fundamental questions regarding the gamma ray emission processes of Galactic sources require a substantial improvement in detecting performances. Three are the major areas of improvement: optimal angular resolution in a large field of view (improving EGRET error boxes by at least a factor of four), microsecond-level timing and simultaneous X-ray and gamma ray detection with on-board triggering and alert capabilities for fast transients.

The large field of view of AGILE allows simultaneous monitoring of many sources and could cover the whole sky with only six pointings. Furthermore, AGILE will continuously observe pulsars for long periods (one to two months) avoiding typical timing analysis problems arising from merging many short observations at different times.

As reported in Pellizzoni et al. (2004), a typical AGILE exposure on the galactic plane is about $2 \cdot 10^9$ cm$^2 \cdot$ s for $E > 100$ MeV and the expected pulsar counts at these energies (about 7000 counts from Geminga and about 17000 counts from the Vela pulsar) are comparable or slightly better than the corresponding values for EGRET and give, after folding at the known periods, a sensitivity of about $5 \cdot 10^{-8}$ photons $\cdot$ cm$^{-2} \cdot$ s^{-1} at $E > 100$ MeV.

As can be seen in Pellizzoni et al. (2004), 35 radio-pulsars are likely to have fluxes detectable by AGILE ($F_{\min > 2 \cdot 10^{-8}\ photons \cdot cm^{-2} \cdot s^{-1}}$) even in the absence of coincidence with EGRET sources. Furthermore, 11 radio pulsars are coincident with EGRET unidentified sources and have expected fluxes near AGILE sensitivity. These estimates give a

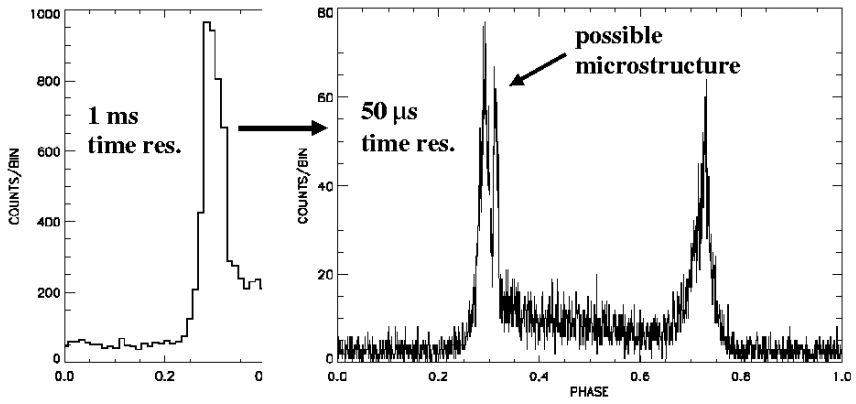

Figure 1.5: Simulation of an AGILE observation of the Vela pulsar from Pellizzoni et al. (2004). Timing analysis with resolution $10 \div 50\,\mu$s can reveal possible microstructures within the peaks of the light curve.

preliminary number of about fifty pulsars detectable by AGILE. Particularly interesting are the about thirty new young pulsars discovered in the Galactic plane by the Parkes survey (see for example D'Amico et al. (2001)). Unfortunately, the X-ray flux of the gamma ray pulsars is about 1 mCrab, too small to be detected by SuperAGILE.

AGILE will have the first opportunity to observe pulsars with time resolution better than EGRET, looking for possible microstructures in folded gamma ray light curves such as those seen in radio pulses from Vela. A simulation of the observation of the Vela pulsar light curve with different microstructure templates is reported in Pellizzoni et al. (2004) and shown in fig. 1.5. The analysis shows that a resolution better than about 50 μs can be achieved with good signal to noise ratio so allowing to discover microstructures not resolved with lower resolution.

Some of the galactic black hole sources (such as Cyg X-1, GRS 1915+105, GRO J1655-40 and others) can produce gamma ray emission for favorable accretion states and geometries. Particularly important in this class are the so-called microquasars, accreting black holes of several solar masses showing a complex phenomenology and moderately relativistic jets. The expected gamma ray flux of these sources is faint compared to the known X-ray flux, that can be used to single out the timing and the position of the transient emission. In this way the detection of the outbursts from these sources is

improved by the capability of simultaneous hard X-ray and gamma ray observations.

New galactic sources emitting hard X-rays and showing a highly absorbed spectrum below about 10 keV, with very strong fluorescent emission lines (for example Fe Kα, Fe Kβ and Ni Kα) have been recently discovered by INTEGRAL, especially in the galactic plane (see for example Walter et al. (2003)). AGILE can monitor this type of sources in an effective way and alert the community for hard X-ray outbursts.

Finally, some pulsars exhibit "giant pulses", consisting in large and power-law distributed flux and rare emission occurring in restricted phase windows, observed in radio in Cairns (2004). For example, the Crab pulsar shows giant pulses with integrated flux exceeding ten times the average pulse-integrated flux, discovered by Staelin and Reifenstein (1968). The Crab giant pulses have been jointly studied in the radio and gamma ray bands in Lundgren et al. (1995) in order to compare the flux in the two bands during giant and weak pulses. Since, from the radio data, pulses with width of the order $20 \div 100$ μs have been detected (see Hankins (1992) for details), high resolution timing gamma ray observations are required in order to compare the pulsar emission in different energy bands.

1.4 Active Galactic Nuclei

1.4.1 The properties of the Active Galactic Nuclei

Active Galactic Nuclei (AGN) are some of the most interesting astronomical objects that can be studied in the X-ray band. One of the important features of this class of sources is their emission in different energy bands, from the radio wavelengths to the IR, optical, UV and X-rays. A peculiar class of AGN, known as blazars and described in sec. 1.4.5, emits gamma rays up to the GeV/TeV range.

In a small volume (even the nearest AGN are unresolved by the Hubble Space Telescope) the AGN produce very large luminosity (up to 10^{48} erg $\cdot$ s^{-1}, about three orders of magnitude greater than a normal galaxy) with a broad spectrum and fast (down to tens of seconds in X-rays) and large amplitude variability. All these features implies that the emission cannot be of stellar origin.

As reported in Mushotzky et al. (1993), the X-ray emission is a defining characteristic of the active galaxies. In fact, in the $2 \div 10$ keV band, there are more X-ray emitting Seyfert 1 galaxies per unit volume than found in surveys conducted in any other wavelength band and, in the $0.2 \div 2$ keV band, the surface density of X-ray discovered quasars is equal or larger than that of the optically discovered objects. Furthermore, the X-ray flux emitted in Active Galactic Nuclei shows the fastest variability in any of the wavelength ranges, as if it is emitted in a small region close to the central object.

1.4.2 The AGN classification and the Unified Model

The AGN can be empirically classified basing on the observed properties, as reported in Urry and Padovani (1995). A table summarizing the AGN classification and correlating the observed features with the central nucleus properties is shown in fig. 1.6.

TABLE 1
AGN Taxonomy

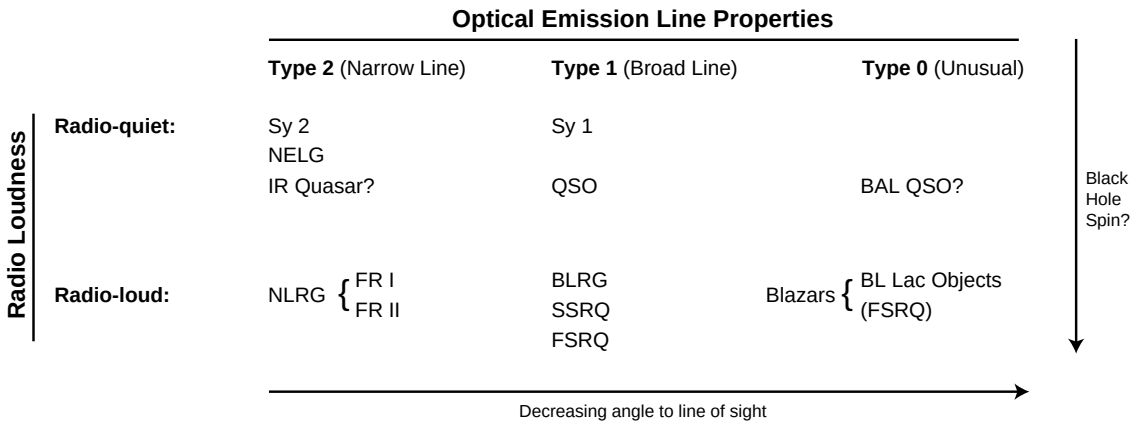

Figure 1.6: Principal classes of AGN (from Urry and Padovani (1995)), organized according to their radio-loudness and their optical spectra, i.e., whether they have broad emission lines (Type 1), only narrow lines (Type 2), or weak or unusual line emission (Type 0). Within each of the groupings, different types of AGN are listed by increasing luminosity.

About $15 \div 20$ % of the AGN are radio-loud, meaning their ratio of radio (5 GHz) to optical (B band) flux is $F_{5\,GHZ}/F_B \geq 10$. The radio loudness itself can be related to the host galaxy type, which might enable the formation of relativistic jets. Basing on the features of the optical and ultraviolet spectra, the AGN can be divided in three broad classes, as shown in fig. 1.6.

Type 1 AGN show bright continua with broad emission lines from hot and high-velocity gas, presumably located deep in the well of the central black hole. Radio-quiet type 1 AGN include Seyfert 1 galaxies and radio-quiet quasars (QSO), while in radio-loud type 1 AGN Broad-Line Radio Galaxies (BLRG), Steep Spectrum Radio Quasars (SSRQ) and Flat Spectrum Radio Quasars (FSRQ) are grouped.

Type 2 AGN have weak continua and only narrow emission lines, meaning either that they have no high-velocity gas or that the line of sight to the gas is obscured by a thick wall of absorbing material. Seyfert 2 galaxies belong to the Radio-quiet type 2 class while the radio-loud type includes the Narrow-Line Radio Galaxies (NRLG), both Fanaroff-Riley type I and Fanaroff-Riley type II radio galaxies.

A small number of AGN have peculiar spectra and can be grouped into a third Type 0 class. This class does not seem to include radio-quiet objects and, among the radio-loud objects, BL Lacertae (BL Lac) objects and some FSRQ are grouped. Collectively, BL Lacs and FSRQ are called blazars.

In a deeper study of the AGN, some of the observed features can help understanding the emission mechanisms of these objects. The continuum and line spectrum, producing the classificaton summarized above, is due to the obscuration of the central nucleus by

the accreting torus. Moreover the radio-loudness can be related to the angle between the relativistic jet and the line of sight. These considerations lead to the formulation of a unified model, including all classes of AGN and allowing to explain the observed features in terms of the angle between the relativistic jet emitted by the central nucleus and the line of sight.

The Unified Model of the AGN is composed of a supermassive black hole ($10^6\ M_\odot \leq M \leq 10^8\ M_\odot$) surrounded by a toroidal accretion disk. The gas falling from the accretion disk into the black hole produces the object luminosity. Two collimated jets, initially at relativistic speed and detectable in the radio wavelength, emanate from the region near the black hole in the orthogonal direction with respect to the accretion disk and can reach distances from 10^{17} cm to 10^{24} cm from the central object. Broad emission lines are produced in clouds orbiting above the disk (at a distance about $(2 \div 20) \cdot 10^{16}$ cm from the black hole) and perhaps by the disk itself. A thick and dusty torus obscures the broad-line region from transverse line of sight. Narrow lines can be produced in clouds much farther from the central source (at a distance about $10^{18} \div 10^{20}$ cm from the black hole).

Following the Unified Model, the AGN classification depends on the angle between the observer line of sight and the radio jets. The blazars are AGN observed directly along the line of sight, such that one of the radio jets points toward the observer. Increasing the angle between the radio jet and the line of sight, the Seyfert 1 galaxies, in which only part of the central region is obscured by the torus, and finally the Seyfert 2 galaxies, with the central region completely obscured by the torus, are found. A picture of the unified model from Urry and Padovani (1995) is reproduced in fig. 1.7.

1.4.3 The X-ray emission from AGN

The X-ray emission can be considered as a defining characteristic of the AGN and is a major component of the total luminosity, typically between 5 % and 50 % of the bolometric luminosity for radio-quiet AGN with $L(x) < 10^{44}\,\mathrm{erg \cdot s^{-1}}$. Furthermore, in the X-ray band large amplitude ($\delta I/I \sim 1$) and rapid ($\Delta T < 1$ day) variability can be detected. This combination of large luminosity and variability of the X-ray emission provides the strongest support to the identification of the central object with an accreting black hole.

An interesting review of the spectral and variability feature of the AGN can be found in Mushotzky et al. (1993). In particular, the X-ray spectrum accounts for the emission mechanisms in AGN and the study of the X-ray variability can be used to constrain the size, the mass and the efficiency of the central source.

In the $2 \div 50$ keV energy band the spectrum of the AGN Seyfert 1 Galaxies (in photons $\cdot\ \mathrm{cm^{-2} \cdot s^{-1} \cdot keV^{-1}}$) can be described by a simple power law $F(E) = AE^{-\Gamma}$ with $\Gamma \simeq 2$. The spectral index increases to $\Gamma \simeq 2.2$ for radio-quiet quasars and $\Gamma \simeq 2.5$ for radio-loud quasars in case $E < 3$ keV.

The strongest feature in the $0.1 \div 100$ keV range is the photoelectric absorption at low energy ($E < 0.6$ keV) due to the cold or partly ionized material in the line of sight, that can be described by a column density $n_H \sim 3 \cdot 10^{20}$ atoms $\cdot\ \mathrm{cm^{-2}}$. Particularly Seyfert

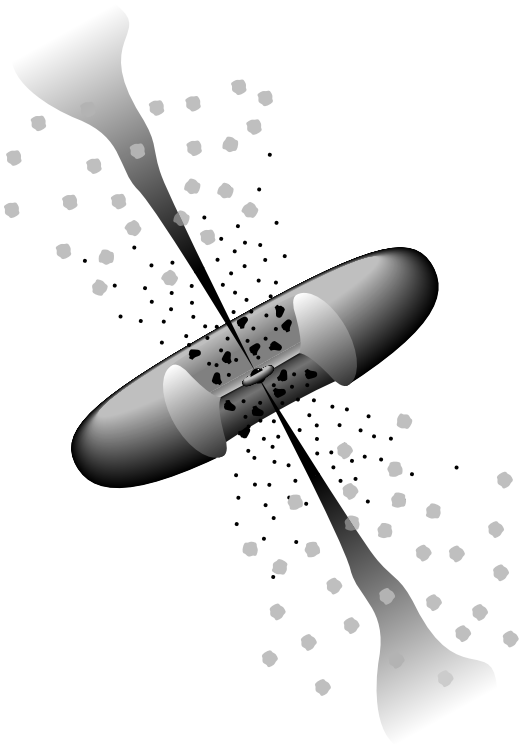

Figure 1.7: A schematic diagram of the current paradigm for radio-loud AGN (not to scale) from Urry and Padovani (1995).

2 Galaxies show significant X-ray absorption by cold material since, as explained by the unified model, the central region is obscured by cold material along the line of sight.

The spectrum flattens at high energy (above $10 \div 20$ keV) and a possible explication is that this feature is due to X-rays "reprocessed" or "reflected" in optically thick material subtending a substantial solid angle to the source (Compton reflection model). Another important spectral feature is the Fe fluorescence emission at 6.4 keV from near-neutral or cold material with equivalent width ranging between 50 eV and 350 eV. Also the brightest quasars and the majority of the Seyfert 2 Galaxies show significant Fe line emission.

The X-ray emission shows the shortest timescale for AGN variability than in any other wavelength band. Since the variability cannot be observed on timescales shorter than the light crossing time of the source, an upper limit on the size $R < c\delta t$ can be found. Assuming, as in Mushotzky et al. (1993), that the source size R is five Schwarzschild radii, a limit mass $M < 2 \cdot 10^6 \cdot \delta t_{100}\ M_\odot$ is found with $\delta t_{100} \equiv \delta t/100$ s. The variability can also be used to derive the efficiency η of the source in converting accreting matter to luminosity and $\eta = 0.05 \cdot \delta L_{43}/\delta t_{100}$ where $\delta L_{43} \equiv \delta L/10^{43}$. Since the maximum efficiency of nuclear reactions is $\eta \sim 0.007$ while the efficiency of accretion processes ranges from $\eta = 0.057$ for Schwarzschild metric up to $\eta = 0.32$ for extreme Kerr metric,

the estimated efficiency supports the idea that AGN are powered by accretion.

About 40 % of AGN from a hard X-ray selected sample show variability on a timescale less than one day. On scales of weeks to months about 97 % of AGN show variability. There is no agreement on how the X-ray variability is produced. Probably long-term variability is caused by changes in the global accretion rate. The rapid variability cannot be given by the viscosity in the accretion disk since the viscosity timescale is longer. The most commonly used model assumes that the variability is given by the superposition of many similar events.

1.4.4 The gamma ray emission from AGN

Some radio-loud AGN show gamma ray emission extending up to GeV and TeV energy. This gamma ray emission can be observed particularly from a subset of radio-loud objects, called blazars and described in sec. 1.4.5 below, whose jet emission is so intense to completely outshine the disc radiation. Examples of gamma ray emitting AGN are Mkn 421 (observed above 250 GeV by the Cherenkov imaging telescope CAT in Piron et al. (2001)), Mkn 501 (studied with the HEGRA experiment in Krawczynski et al. (2001)), PKS 0208-512 (observed from MeV to GeV energy by EGRET and Comptel in Stacy et al. (2003)) and 3C273 (studied between 3 MeV and 10 GeV by Comptel and EGRET in Collmar et al. (2000)).

The gamma ray emission in AGN can be explained in terms of Inverse Compton scattering of high energy electrons, coming from the blob of a jet, on the optical UV photons produced by the broad line clouds and the accretion disc. A model is shown in Ghosh et al. (1999).

1.4.5 The blazar class

As reported in Cavaliere and D'Elia (2002), the main features of the blazar class include the strong radio emission at high frequency from compact cores, the gamma ray emission up to 10 GeV, the rapid multiwavelength variability and the high and variable optical polarization. The radiation from this class of objects is likely to be produced by a collimated and relativistic jet of particles with bulk Lorentz factor $\Gamma \sim 5 \div 20$ observed at small angles of the order of Γ^{-1} (see Begelman et al. (1984) for details).

Two type of sources are grouped in the blazar class: BL Lac objects and FSRQ. The distinctive properties of the BL Lac objects are the lack of emission lines with EW ≥ 5 Å and of blue-UV bump, luminosity smaller than 10^{46} erg $\cdot$ s^{-1}, spectral energy distributions peaking at frequencies from optical to X-rays and in the gamma rays at 10 GeV, while the FSRQ are characterized by a luminosity greater than 10^{46} erg $\cdot$ s^{-1}, spectral energy distributions peaking at far IR to optical frequencies and around 0.1 GeV and strong evolution.

Basing on the observational properties, Cavaliere and D'Elia (2002) predict that all the blazars are similar sources and explain the differences between BL Lac and FSRQ objects considering a blazar main sequence in terms of the accretion rate

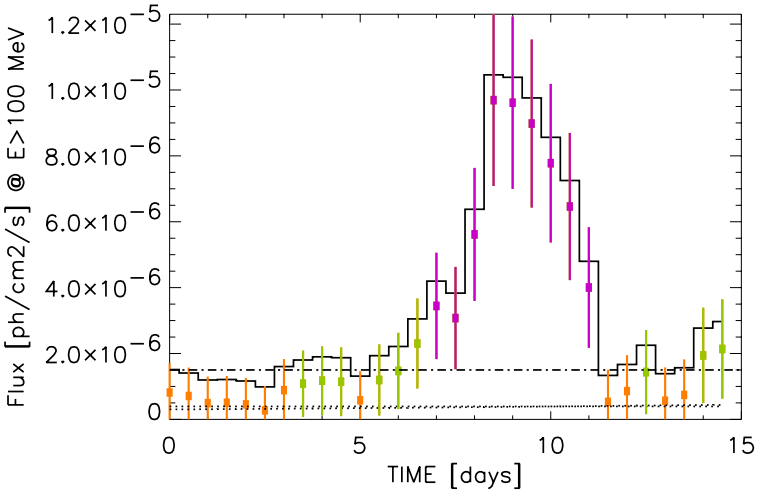

Figure 1.8: Reconstructed light curve of a simulated flare of PKS 1622-297 (similar to the 1995 event reported in Mattox et al. (1997)).

$$\dot{m} \equiv \frac{\dot{M}c^2}{L_{Edd}} \tag{1.4}$$

with $\dot{M}$ accretion mass and $L_{Edd} \equiv 4\pi cGMm/\sigma_T = 1.3 \cdot 10^{38}(M/M_\odot)$ erg $\cdot$ s^{-1} Eddington luminosity (c is speed of light, G is gravitational constant, M is accreting object mass, m is proton mass and σ_T is Thomson cross section). The FSRQ are energized by accretion rates $\dot{m} \simeq 1 \div 10$ while the BL Lac by $\dot{m} \leq 10^{-2}$. In this scheme either the optical-UV bumps and the prominence of the emission lines in FSRQ are consistent with $\dot{m} \simeq 1 \div 10$ while the weakness of absence of such features in BL Lac can be understood if $\dot{m} \leq 10^{-2}$.

1.4.6 The AGILE contribution

The AGILE capabilities in observing the blazar class is studied in Vercellone et al. (2003), where the simulation of an observing strategy of a whole Sky coverage, composed of six pointings lasting sixty days each, is reported. About $10 \div 20$ gamma ray emitting AGN can be monitored simultaneously, out of which $2 \div 6$ might be detectable by SuperAGILE. At the end of this all Sky observation, at high galactic latitude a typical flux limit of $F_{E>100\ \mathrm{MeV} \simeq 3 \cdot 10^{-7}\ photons \cdot cm^{-2} \cdot s^{-1}}$ can be achieved.

The reconstructed light curve of a simulated flare of PKS 1622-297 (similar to the 1995 event reported in Mattox et al. (1997)) is shown in fig. 1.8. Assuming a peak flux $F_{E>100\ \mathrm{MeV} \simeq 1.8 \cdot 10^{-5}\ photons \cdot cm^{-2} \cdot s^{-1}}$, the quick-look analysis should be able to report such a flare about one or two days after the event onset and with error boxes $15 \div 30$ arcmin.

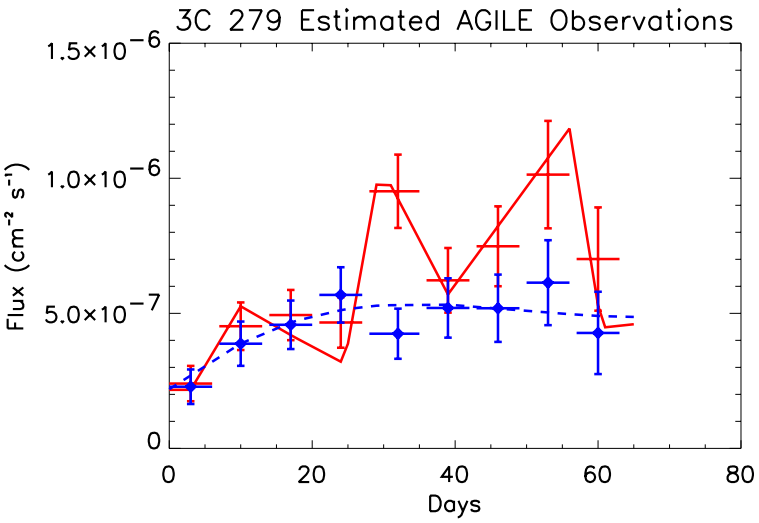

Figure 1.9: Reconstructed light curve of the 3C 279 AGILE simulated observation with two possible models (steady emission, dashed blue line and flaring emission, solid red line) from Vercellone et al. (2003).

The light curve of 3C 279 with a sixty days long observation is shown in fig. 1.9. In the EGRET observation of this source in 1993 (see Hartman et al. (1999)) a steady emission (dashed blue line in the plot) or a flaring emission (solid red line) could not be distinguished. As seen in the plot, AGILE observation can determine the time sequence of the flaring and quiescent emission so finding the correct emission model.

The joint observations in hard X-ray and gamma ray bands will add crucial broad band information on blazars. An example of the AGILE energy bands superimposed on the Spectral Energy Distribution (SED) of several blazars can be seen in fig. 1.10. Simultaneous observation of the synchrotron (hard X-ray) and inverse Compton (gamma rays) spectral bands of high-energy peaked BL-Lac objects will provide invaluable information on the physics of the emitting regions.

AGILE will give emphasis to multi-wavelength campaigns by means of coordinated observation with ground-based and space observatories. An example of a possible coordinated multi-wavelength observation of known blazars by AGILE and observatories located in the Northern Hemisphere can be seen in fig. 1.11.

From simultaneous radio and gamma ray blazar observations, tight constraints can be set on the emission sites along the jets and the correlation between radio plasmoid ejection in jets and gamma ray flares, still a debated issue because of the EGRET sparse data, will be extensively studied during the AGILE mission. SuperAGILE will provide both hard X-ray monitoring of bright AGN and a prompt alert to TeV ground-based observatories.

AGILE is expected to discovery about 100 new AGN, improving our knowledge of gamma ray duty cycles and of blazar Spectral Energy Distribution with simultaneous

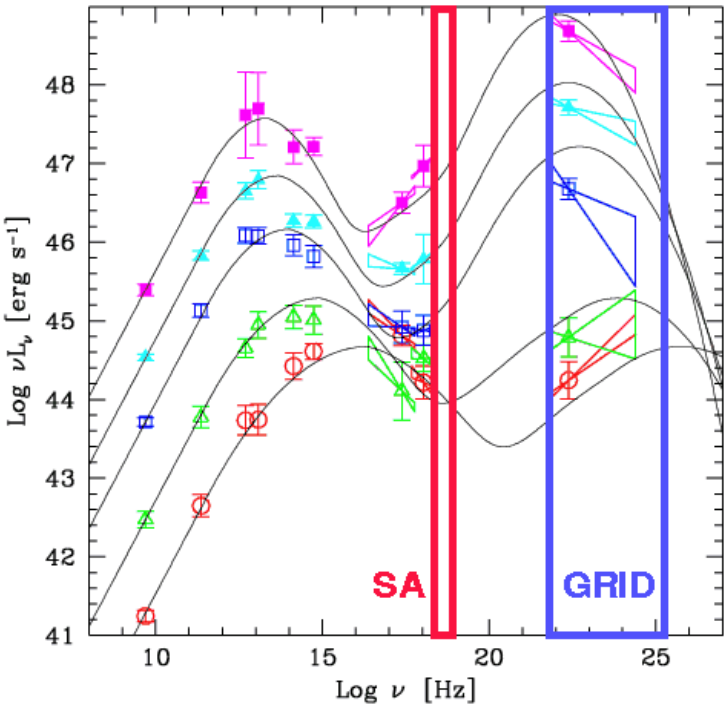

Figure 1.10: AGILE energy bands superimposed on the Spectral Energy Distribution of several blazars

gamma ray and hard X-ray data. Depending on source intensity and spectrum, AGILE is expected to locate blazars within $6 \div 20$ arcmin for moderately intense AGN at high Galactic latitudes.

1.5 Gamma ray Diffuse Galactic Emission

The dominant feature of the high-energy gamma ray sky is the narrow band of intense emission along the Galactic plane ($|b| \leq 10°$), whose luminosity above 100 MeV is about 10^{39} erg $\cdot$ s^{-1}. This extended area of diffuse emission was first seen by the OSO-3 satellite, confirmed by the SAS-2 and COS-B observations and recently studied by EGRET.

As reported in Hunter et al. (1997), the diffuse galactic emission of gamma rays is particularly strong in a region about 100° wide centered on the inner galaxy and is generally correlated with spatial structures seen at other wavelengths such as the tangents of the spiral arms. Two examples of the spiral arm tangents are the Carina arm at $l \simeq 285°$ and the Crux or Centaurus arm at $l \simeq 315°$. Both features can be detected in the integrated 21 cm emission, CO emission, radio continuum and at $E > 100$ MeV. The minima between the arms are the interarm regions, where the atomic and molecular gases are particularly lacking.

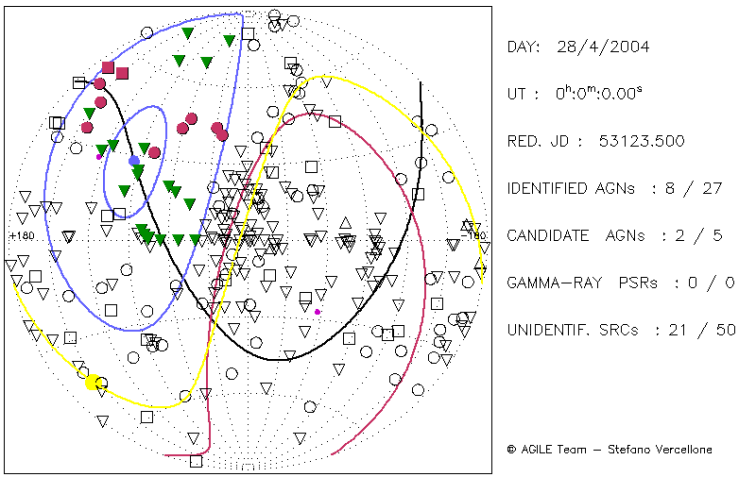

Figure 1.11: Example of simultaneous gamma ray and hard X-ray observations of known AGN by AGILE: red circles and squares are identified and candidate EGRET AGN respectively, green triangles are identified sources, blue circles are GRID and SuperAGILE field of view respectively, the black line is the time-dependent AGILE allowed pointing direction, the red line is the accessibility limit (dec $\leq 15°$) for northern observatories, finally the filled symbols are the sources that could be monitored simultaneously by AGILE and ground based observatories.

One interarm region lies at $60° \leq l \leq 70°$ between the Sagittarius arm and the Cygnus region while the other at $210° \leq l \leq 60°$ between the Vela pulsar and the anticenter. The emission from the inner galaxy is more intense and characterized by a smaller latitude distribution than elsewhere in the galactic plane, corresponding to the distribution of the interstellar medium in a thin disk along the galactic plane.

The spectrum of the galactic isotropic emission is fairly well described by a power law with spectral index -2.1 and integral flux $1.17 \cdot 10^{-5}$ photons $\cdot$ cm$^{-2} \cdot$ s$^{-1} \cdot$ sr^{-1} above 100 MeV, as can be seen in fig. 1.12.

The gamma ray emission observed from the galactic plane is a combination of a diffuse emission from Galactic cosmic rays origin, a diffuse emission probably of extragalactic origin, the emission from resolved point sources and an uncertain additional component from unresolved point sources. The most important contribution to the galactic emission of gamma rays originates from the interaction of cosmic rays with gas and photons in the interstellar medium (see Bloemen (1989) for a review). In the 50 MeV $\div$ 5 GeV energy range three are the dominant emission effects producing gamma rays: π^0-mesons decay, bremsstrahlung and inverse-Compton scattering. The electron bremsstrahlung dominates below about 100 MeV while the emission from the π^0 decay, forming a bump at $E \simeq 68$ MeV which is the only spectral feature, is dominant above 100 MeV. The synchrotron emission from electrons in the magnetic field can also produce gamma rays but it is estimated not to be significant.

Cosmic rays with energies between 1 GeV and few tens of GeV interacting with

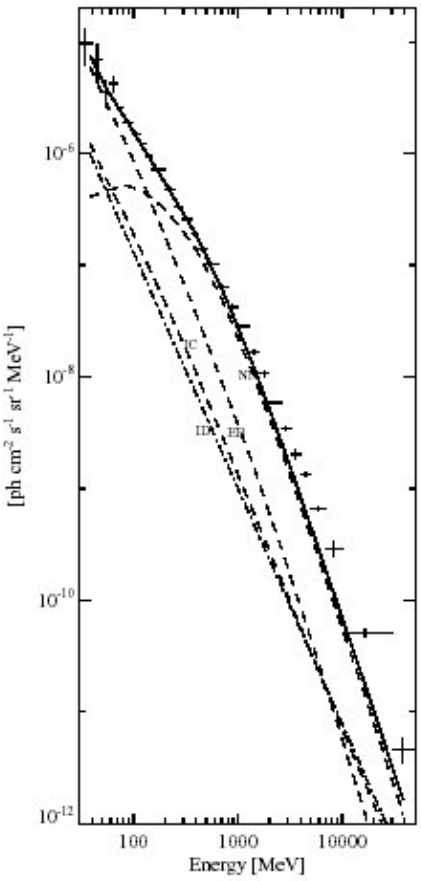

Figure 1.12: Average diffuse gamma ray spectrum of the inner Galaxy region, ($300° < l < 60°$, $|b| \leq 10°$), from Hunter et al. (1997).

nuclei in the interstellar gas can produce π^0-mesons via various nuclear decay chains. The π^0 decays in about 10^{-16} s following the reaction $\pi^0 \rightarrow \gamma\gamma$. In the π^0 rest frame each photon has an energy of $m_{\pi^0}c^2 \simeq 68$ MeV, which transforms in a broad distribution centered on 68 MeV in the observer reference system. The interaction of cosmic rays and matter can also produce charged pions that decay giving as final products electrons and positrons which annihilate producing photons with 0.511 MeV energy.

The Coulomb scattering of cosmic rays on nuclei and electrons of the interstellar gas leads to the production of gamma rays via the bremsstrahlung emission process. If E_e is the electron energy, the energy of the bremsstrahlung emitted photon is $E_\gamma \simeq E_e/3$.

High energy electrons ($E_e > 10$ GeV) can accelerate photons of energy $\varepsilon \ll m_e c^2$ (photons in the optical and infrared band and from the 2.7 K Cosmic Microwave Background) via the so called "inverse-Compton effect" up to gamma ray energy. The resulting mean photon energy is $\overline{E}_\gamma \simeq 4\gamma^2\overline{\varepsilon}/3$ where $\gamma \equiv E_e/m_e c^2$.

From the observations, below about 4 GeV the spectrum of the diffuse emission

with $|b| \leq 10^\circ$ does not vary significantly with longitude or latitude, indicating that the variation of electron to proton ratio in cosmic rays is small. Above about 4 GeV, the spectrum is uniform with longitude if $2^\circ < |b| < 10^\circ$ while at $|b| < 2^\circ$ there is a weak evidence for softening of the spectrum in the direction of the outer Galaxy ($135^\circ < l < 225^\circ$ while at $|b| < 2^\circ$).

From the observations a model can be built predicting the distribution of cosmic rays in the galaxy and the variation along both latitude and longitude. A first model was built basing on SAS 2 and COS B results (see Bertsch et al. (1993) for details) and then it was improved using the EGRET data (more information in Hunter et al. (1997)). This model contains just two adjustable parameters: the molecular hydrogen mass calibrating ratio, $X \equiv N(H_2)/W_{CO}$ and the scale of the cosmic ray coupling to the interstellar matter, r_0. From the observations at $E > 100$ MeV, the model predicts that the cosmic rays are coupled to the interstellar matter density on the scale of $r_0 = (1.8 \pm 0.2)$ kpc and are in dynamic balance with it. The Galactic average values of the X ratio are $N(H_2)/W_{CO} = (1.56 \pm 0.05) \cdot 10^{20}$ mol $\cdot$ cm^{-2} $\cdot$ (K $\cdot$ km $\cdot$ s^{-1})$^{-1}$.

1.5.1 The AGILE contribution

The galactic gamma ray diffuse emission is produced in interactions of cosmic rays with gas and ambient photon field and thus provides us with an indirect measurement of cosmic rays in various locations of the Galaxy, as explained in Longo et al. (2003). The study of the Diffuse gamma ray Emission reveals a spectrum which is not compatible with the assumption that the cosmic ray spectra measured locally hold throughout the Galaxy. Above 1 GeV energy, where the emission is supposedly dominated by the π^0 decay, the spectrum is harder than that derived from the local cosmic ray proton spectrum and this fact is known as the GeV excess.

Thanks to its good angular resolution and large average exposure, AGILE will further improve our knowledge of cosmic ray origin, propagation, interaction and emission processes. AGILE can obtain larger exposures (compared to EGRET) of complex regions such as the Cygnus and Orion regions in addition to the Galactic Center. A joint study of gamma ray emission from MeV to TeV energy is possible by special programs involving AGILE and new generation TeV observatories of improved angular resolution.

1.6 AGILE and GLAST

GLAST (Gamma ray Large Area Space Telescope) is a satellite-borne mission devoted to the study of the celestial sources in the 10 MeV $\div$ 100 GeV energy band, as described in Ritz et al. (2004). The GLAST project is funded in the United States by NASA and the Department of Energy and by government agencies in France, Italy, Japan, and Sweden. GLAST launch is foreseen in 2007.

The GLAST payload contains a Large Area Telescope (LAT), composed of a tracker and a calorimeter, complemented by the GLAST Burst Monitor (GBM), an instrument for studying Gamma Ray Bursts between 5 keV and 25 MeV. LAT peak effective area is about 8000 cm^2 (more than ten times the GRID effective area), the field of view is

2 sr, the angular resolution is about 3.5° at 100 MeV and 0.15° at 10 GeV (similar to AGILE).

GLAST scientific objectives are the same of AGILE: Compact Galactic Sources, Active Galactic Nuclei, Gamma Ray Bursts and Diffuse Galactic Emission. With its increased effective area and angular resolution, GLAST will detect new point sources at flux levels about three times lower then EGRET and AGILE. The first year of the GLAST activity will be devoted to the gamma ray sky survey and, after that time, the instrument will start performing observations.

Despite its large effective area if compared with AGILE, GLAST does not contain a hard X-ray monitor. For this reason the joint observations in gamma rays and X-rays, that are one of the most important features of the AGILE mission, can be performed by GLAST only using data from other observatories, that is commonly a difficult task.

Moreover, the Gamma Ray Burst localization is performed using the GBM, an instrument composed of 12 Sodium Iodide (NaI) scintillation detectors and 2 Bismuth Germanate (BGO) scintillation detectors, similar to BATSE with about one twelfth effective area and about 3° angular resolution. Better localization can be achieved using the LAT if the GRB is found within the LAT field of view, but in this case the statistic is extremely low. The GBM angular resolution does not allow to perform the GRB follow up observations to detect the event afterglow. Consequently the GLAST capability to obtain the localization accuracy required to detect the optical afterglow and the redshift is based on the LAT Gamma Ray Burst detection only for events with a significant number of gamma ray photons.

1.7 Conclusions

The High Energy Sky is populated by sources belonging to many different classes but all characterized by nonthermal emission, often involving accretion on a collapsed object and jet emission, and high variability, frequently producing transient emission. Collapsed objects such as white dwarfs, neutron stars and black holes play a crucial role in the sources nature. The AGILE mission is designed in order to effectively study all the different classes of High Energy emitting sources.

The instruments wide field of view together with a good angular resolution allows to efficiently monitor the known sources, to improve the position of the unidentified sources and to discover possible new objects. SuperAGILE field of view and angular resolution are an important tool to detect GRB and to help the reconstruction of the events position in the gamma ray band, where EGRET showed that the detection is possible. The coordinates of the detected GRB will be reconstructed directly on-board and will be provided to optical, infrared and radio observers so allowing a rapid and efficient follow-up. Finally, also the study of the gamma ray diffuse emission, involving the cosmic ray origin, propagation, interaction and emission processes, will be improved.

The high temporal resolution is an important tool in the study of GRB, showing small scale variability and low-level flickering, and compact galactic sources, where microstructures in the gamma ray light curves are expected and "giant pulses" occur.

The joint observations in the hard X-ray ($15 \div 45$ keV) and gamma ray (30 MeV $\div$ 50 GeV energy bands is an important tool to study broad-band emitting sources such as the AGN blazar class. AGILE will emphasize multi-wavelengths campaigns by means of coordinated observations with ground-based radio, optical and ultra high-energy (TeV) observatories. Moreover the detection of X-ray transients from some of the accreting compact galactic sources, such as the microquasar, can be used to single out the timing and the position of the expected faint gamma ray transients.

Chapter 2

The AGILE mission and the SuperAGILE instrument

2.1 The AGILE mission

AGILE (Astrorivelatore Gamma ad Immagini LEggero, Light Imager for Gamma ray Astrophysics) is a satellite-borne mission devoted to the study of the High-Energy Astrophysics in the hard X-ray and gamma ray energy bands. AGILE is the first small scientific mission of the Agenzia Spaziale Italiana (ASI). The mission was proposed in 1997, the Phase A study was conducted during 1998, the mission was finally selected by ASI in 1999 and the launch is planned in late 2005. Main properties of a typical small scientific mission, as defined from the NASA SMEX requirements[1], are a spacecraft of mass from 180 to 250 kg with orbit-average power consumption of 50 to 200 W.

The AGILE scientific payload consists of two instruments: the Gamma Ray Imaging Detector (GRID), sensitive to photons in the 30 MeV to 50 GeV energy range, and SuperAGILE, that can detect X-rays of energy between 15 keV and 40 keV. The GRID is composed of a Silicon Tracker, with tungsten converters and silicon microstrip position-sensitive detectors, complemented by a Mini-Calorimeter with CsI(Tl) scintillator bars. SuperAGILE is a coded mask instrument with a silicon microstrip detector and a tungsten coded mask. The two instruments are built in series and are designed as a single experiment. Because of dimensional and budget constraints, both the instruments share part of the constructing materials, for example the silicon microstrip detector tiles. All the payload is enclosed inside a plastic scintillator Anti-Coincidence system. A schematic of the AGILE payload is shown in fig. 2.1: from top SuperAGILE, the Silicon Tracker and the Mini-Calorimeter can be seen.

The AGILE payload size is $63 \times 63 \times 58$ cm^3, the weight is about 100 kg and the planned budget is about 50 million euros. The payload total power budget is 122 W, of which 11 W allocated to SuperAGILE, 25 W to the Silicon Tracker, 6 W to the Mini-Calorimeter, 2 W to the Anti-Coincidence system and 26 W to the data handling system. AGILE will fly on an equatorial low-Earth orbit with about 560 km altitude

[1] information from `http://sunland.gsfc.nasa.gov/smex/`

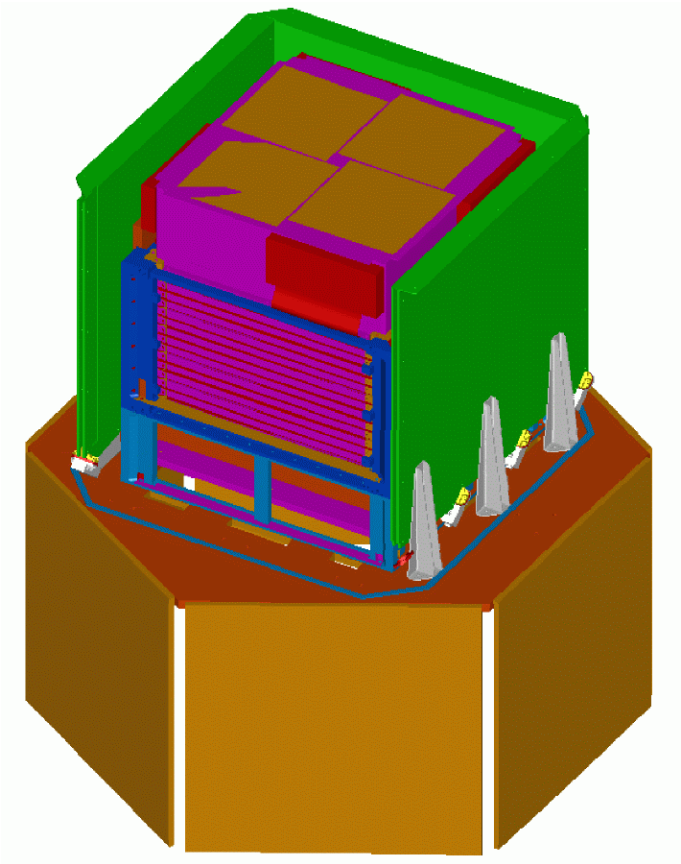

Figure 2.1: Schematic of the AGILE payload: from top SuperAGILE (in brown the coded mask, in purple the collimator and in red the electronics boxes), the Silicon Tracker (in purple the converter-detector planes), the Mini-Calorimeter (in purple and red the scintillator bars), the Anti-Coincidence (in green with photomultiplier tubes in yellow) and the bus (in brown).

and less than 10° inclination with a resulting orbital period of nearly 100 minutes. The satellite will point using a three-axis attitude stabilization with an accuracy near $0.5^\circ \div 1^\circ$. An attitude reconstruction of about 1 arcmin will be obtained using star sensors. The downlink telemetry rate is 500 kbit $\cdot$ s^{-1} and is adequate for both AGILE and SuperAGILE for a single contact per equatorial orbit. More details on the mission features can be found in Tavani et al. (2004).

AGILE is a collaboration involving the University of Roma "Tor Vergata", the University of Roma "La Sapienza", the University of Trieste, the CNR/INAF Istituto di Astrofisica Spaziale and Fisica Cosmica (IASF) of Roma, Bologna and Milano and the INFN sections of Roma "Tor Vergata", Roma "La Sapienza" and Trieste.

In this chapter a short overview of the two experiments composing the AGILE payload is given. In sec. 2.2 the GRID is described while the SuperAGILE description is in

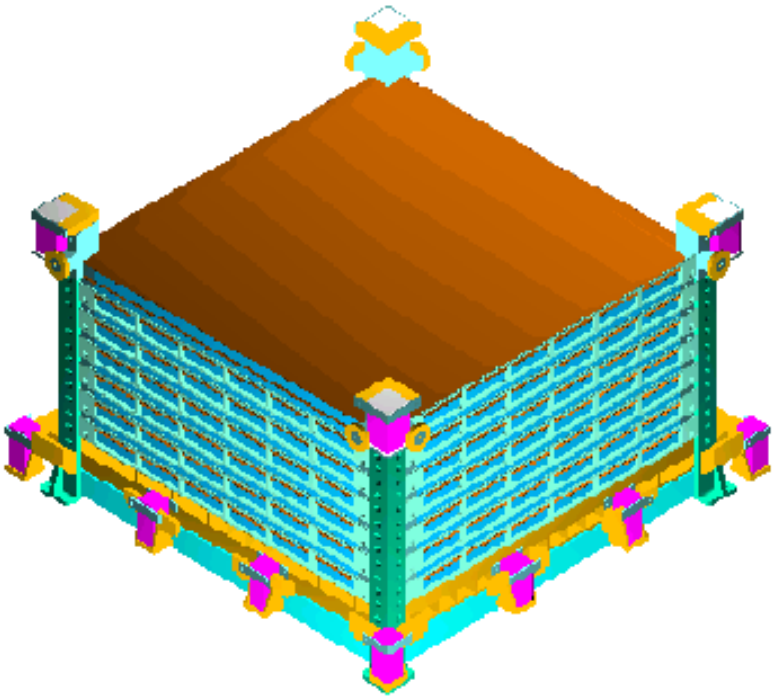

Figure 2.2: Schematic view of the Silicon Tracker assembly.

sec. 2.3. At the end of each section an overview of the scientific performances of each instrument is given. The Anti-Coincidence system is described in sec. 2.4 and finally the data handling system is described in sec. 2.5.

2.2 The GRID

2.2.1 The Silicon Tracker

The Silicon Tracker converts the gamma ray photons into e^+e^- pairs and reconstructs the direction of the gamma rays tracking the position of the pair particles. For this purpose the Silicon Tracker is composed of ten planes, each one containing a tungsten converter layer (of 245 μm thickness) and two one-dimension silicon microstrip detector layers, with strips oriented in orthogonal directions. Since the GRID trigger algorithm requires at least three planes to be activated, two more planes with the silicon detector layers and without the tungsten layer are inserted at the instrument bottom. A schematic view of the Silicon Tracker can be seen in fig. 2.2.

Each silicon microstrip layer is a single-sided, AC-coupled, position sensitive detector of 410 μm thickness and 38×38 cm^2 surface, composed of 16 tiles of 9.5×9.5 cm^2 dimensions each. The two detector layers in each plane have the strips oriented in orthogonal directions in order to locate the particles position. Each layer has a 121

μm strip pitch and is read-out using the "floating readout strip" system, consisting in reading one strip every two, with readout pitch equal to 242 μm and a total of about 38000 readout channels. In this way if a particle crosses a floating strip, image charges are induced on the two adjacent read-out strips through capacitive coupling and an interpolation algorithm can thus be used to improve the detector spatial resolution.

The on-axis thickness of each tungsten layer corresponds to 0.07 radiation lengths X_0, thus the total on-axis radiation length is 0.7 X_0. The distance between the planes is 1.6 cm and is optimized by extensive Monte Carlo simulations. A description of the Silicon Tracker assembly and the CERN tests can be found in Prest et al. (2003).

The Silicon Tracker read-out electronics is composed of three TA1 chips per silicon tile, with a total number of 480 chips. The TA1 is a Very Large Scale Integration (VLSI) low-noise and low-power commercial chip produced by Ideas ASA[2]. Each TA1 is composed of 128 input channels, with a folded cascode charge sensitive preamplifier, a CR-RC shaper, a sample and hold circuit and a level sensitive discriminator. The discriminator threshold is unique for the 128 channels with a 3-bit trimming DAC per channel to obtain a threshold uniformity better than 10 %.

2.2.2 The Mini-Calorimeter

Under the Silicon Tracker planes the Mini-Calorimeter is positioned, so called because, due to dimensional and weight constraints, its thickness is only 1.5 radiation lengths on axis. This instrument is designed to improve the energy reconstruction of the incident photons imaged by the Silicon Tracker (GRID mode) and can be used as a stand-alone gamma ray detector, without imaging capabilities, in the energy range 250 keV $\div$ 250 MeV (BURST mode). In BURST operating mode this instrument can be used to detect transients, such as Gamma Ray Bursts, and to evaluate fluctuations of the gamma ray background. The features of the Mini-Calorimeter and its scientific performances are reported in Celesti et al. (2004).

The Mini-Calorimeter is composed of two planes of fifteen CsI(Tl) bars, each one of $2.3 \times 1.5 \times 37.5$ cm^3 size. The two planes contain bars disposed in orthogonal directions. The Mini-Calorimeter has a sensitive surface of about 40×40 cm^2 and a total volume of 4416 cm^3. A schematic view of the Mini-Calorimeter assembly, from Celesti et al. (2004), is shown in fig. 2.3.

The bars exhibit low light attenuation combined with high light output. The readout of the scintillation light from each bar is accomplished by two custom PIN photodiodes (with area 1.5×2.3 cm^2, 2 mm thickness and active area about 256 mm^2), coupled at the bar sides by means of a siliconic glue. To maximize the light output and to keep the light attenuation within an optimal range of values, the bars surfaces are polished and the bars are wrapped with a thin reflective coating.

Signals from the photodiodes are collected by means of low noise charge preamplifiers, and then conditioned by a dedicated front-end electronic, composed of sixty analogue electronic channels, one for each photodiode. Each electronic chain is composed of

[2]Web site: www.ideas.no

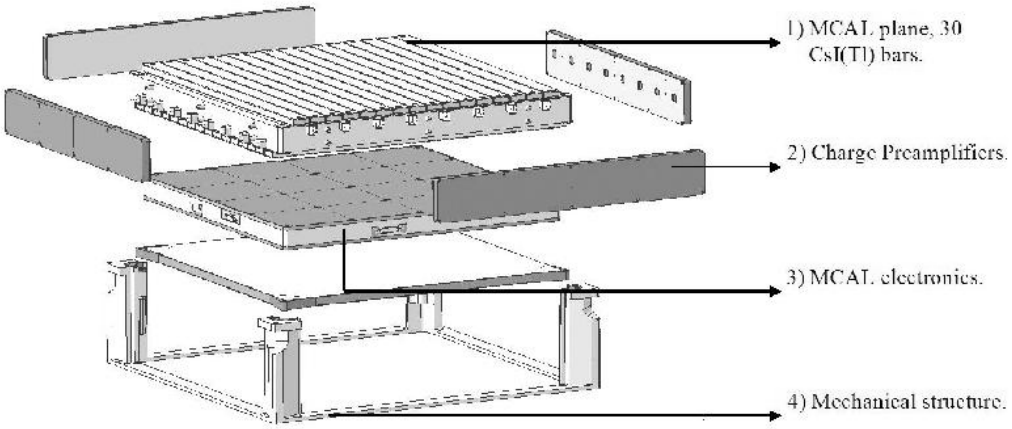

Figure 2.3: Schematic view of the Mini-Calorimeter assembly from Celesti et al. (2004).

an amplification stage, a signal shaper (with shaping time of about 3 ms), a baseline restorer, a programmable threshold discriminator and two signal stretchers, one for the GRID chain and one for the BURST chain. The output signal from the stretchers is multiplexed separately for the BURST and GRID chains and is provided to different ADC with 12 bit precision. GRID and BURST chains can acquire data simultaneously. The rms noise of the electronic chains is about 800 e^-.

Each bar, complete with its own two photodiodes, is hosted in a dedicated carbon fiber housing 1 mm thick, that provides rigidity and modularity to the instrument detection plane. As shown in fig. 2.3, all the housings are mounted on to an aluminum frame, fifteen in the upper side and fifteen in the lower side. The frame containing the detection plane is joined to the lower part of the Mini-Calorimeter main frame and, below the detector plane, the two front-end electronics (FEE) boards are placed, contained in an aluminum box.

When used in conjunction with the Silicon Tracker, signals are converted when a trigger from the data handling system is received. Moreover, a trigger pulse is generated by the readout electronics when the total energy released in the whole instrument exceeds a selected threshold (starting from 10 MeV and programmable via tele-command). In fact such an amount of energy released in the Mini-Calorimeter could produce a backsplash of particles triggering the Anti-Coincidence system, that in this case will be momentarily disabled.

When the Mini-Calorimeter is used as a stand-alone instrument, the triggers generated by signals above threshold are provided to an FPGA. In case the acquisition is not inhibited by a veto signal from the Anti-Coincidence, this FPGA sends a conversion command to the stretchers of the triggering bars.

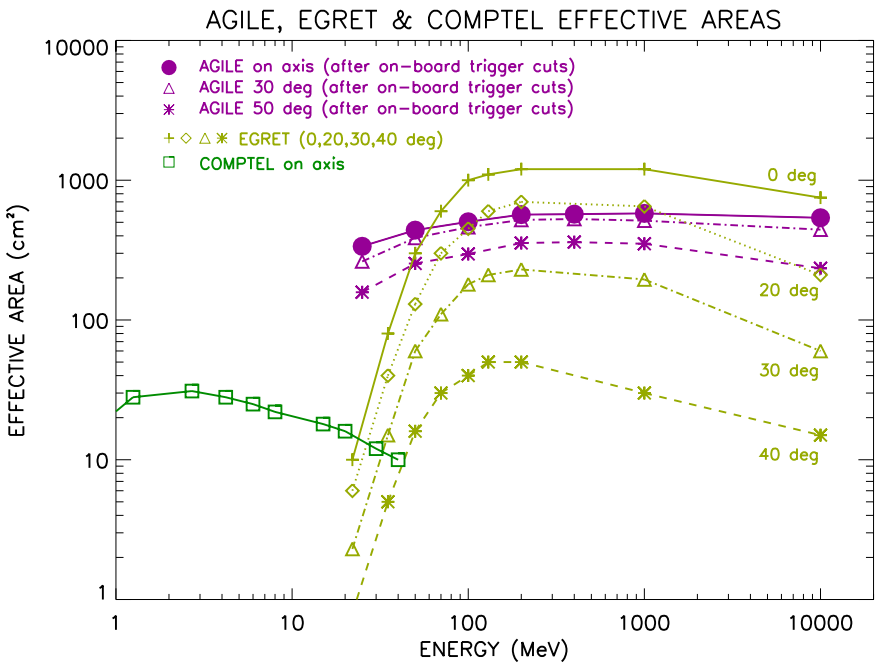

Figure 2.4: A comparison between the effective areas of AGILE, EGRET and COMPTEL at different inclinations off axis, from Tavani et al. (2004).

2.2.3 The GRID scientific performances

The Silicon Tracker effective area, given by the product of the geometric surface times the detection efficiency, is about 550 cm^2 on axis and about 350 cm^2 at 50° off axis for energies between 200 MeV and 10 GeV. Since the interaction probability is significant also for the side coming photons, the effective area does not rapidly decrease off axis.

A comparison between the effective areas of AGILE, EGRET and COMPTEL (from Tavani et al. (2004)) can be seen in fig. 2.4. As can be seen in the plot, the AGILE effective area, about one half of EGRET on axis, decreases of only 10 % at 20° off axis (comparable with EGRET) and is bigger than EGRET effective area at off-axis angles above 30°. Since the fixed solar panels configuration of the satellite imposes some constraints on the pointing strategy and during AGILE observations the sources drift within the field of view of about $1° \cdot day^{-1}$, the off axis performances are extremely important for the instrument.

The point source Silicon Tracker sensitivity is the smallest flux that can be detected and depends on the significance level, the background flux, the effective area, the energy band and the exposure time. Taking into account the intensity and the spectrum of the extragalactic diffuse background and considering a significance level of 5σ and an exposure time of 10^6 s, a sensitivity between about $6 \cdot 10^{-9}$ photons $\cdot cm^{-2} \cdot s^{-1} \cdot MeV^{-1}$ at 100 MeV, approximately $4 \cdot 10^{-11}$ photons $\cdot cm^{-2} \cdot s^{-1} \cdot MeV^{-1}$ at 1 GeV and about $3 \cdot 10^{-12}$ photons $\cdot cm^{-2} \cdot s^{-1} \cdot MeV^{-1}$ at 10 GeV can be achieved. As a comparison,

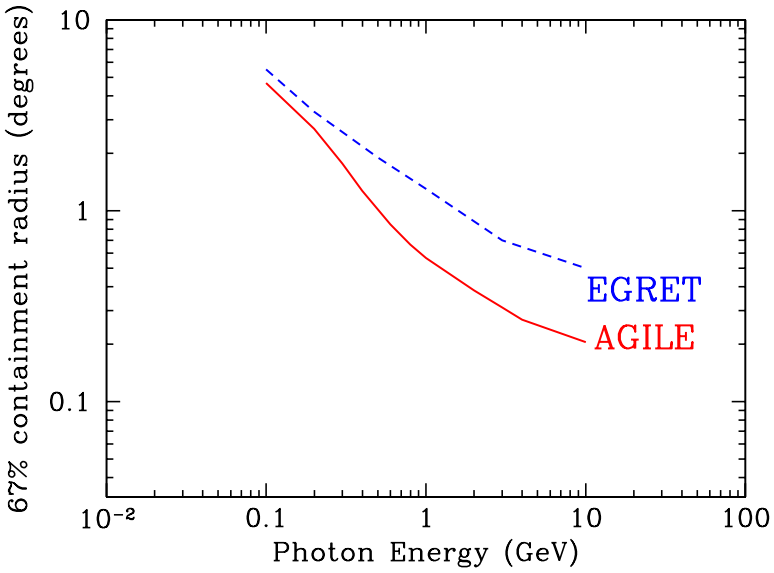

Figure 2.5: A comparison between the angular resolution of AGILE (in red) and EGRET (in blue), from Tavani et al. (2003).

the Crab flux (from Zombeck (1990)) is about $3 \cdot 10^{-5}$ photons $\cdot$ cm$^{-2} \cdot$ s$^{-1} \cdot$ MeV^{-1} at 1 GeV.

The Silicon Tracker field of view is delimited by the instrument geometric dimensions and the trigger criteria and is about 2.5 sr, approximately one fifth of the sky. In this field of view many sources can be simultaneously observed and a wide fraction of the sky can be monitored looking for transient sources.

In gamma ray Astrophysics experiments based on the pair production, the photon direction is reconstructed from the electrons and positrons tracks. The indetermination on such tracks produces a distribution of the incoming directions and the instrument angular resolution is given by the standard deviation of this distribution. Particularly, the multiple scattering of the electrons and positrons produced by photons of energy smaller than about 500 MeV decreases the reconstruction of the incident photon direction. The GRID angular resolution ranges from about 4.7° at 100 MeV and about 0.2° at 10 GeV (from Tavani et al. (2003)) and is plotted in fig. 2.5 compared to the EGRET angular resolution.

The instrument imaging capability is then different from the angular resolution because it is connected to the accuracy in localizing the centroid of the photon incoming direction distribution. With a spatial resolution reaching 40 μm, the source location accuracy of intense sources ranges between 5 arcmin and 20 arcmin depending on source intensity.

The GRID timing capability is based on the smallest ever obtained deadtime for

single gamma ray detection, about 100 μs for the Silicon Tracker and about 20 μs for each of the individual CsI bars.

Since the Mini-Calorimeter can only partially stop the electrons and positrons produced in the Silicon Tracker, the gamma ray energy will be reconstructed basing on the kinematics of the interactions in the Silicon Tracker and on the energy deposited in the Mini-Calorimeter. This technique is studied by means of Monte Carlo simulations and the expected spectral resolution is $\Delta E/E \simeq 1$.

2.3 The SuperAGILE instrument

SuperAGILE is the X-ray monitor of the AGILE mission and is designed in order to operate together with the GRID to observe the same objects in the sky with similar instrumental capabilities. For this reason both the field of view and the time resolution of SuperAGILE and the GRID are matched. In order to have a wide field of view with a good angular resolution in the hard X-ray range, SuperAGILE is a coded mask instrument. The basic principles of the coded-mask imaging process and the main properties of the SuperAGILE coded mask are reported in sec. 2.3.1. The SuperAGILE detector shares the same silicon microstrip tiles of the Silicon Tracker and is described in sec. 2.3.2. As shown in sec. 3.4, the noise in the SuperAGILE experiment is dominated by the electronic noise of the front-end electronics. The conditioning and interface electronics are then described in sec. 3.7

As shown in fig. 2.1, the SuperAGILE instrument is positioned above the GRID. This arrangement is efficient in order to house two experiments observing the same field in the sky in a small and compact payload, but SuperAGILE can stop some of the gamma ray photons so reducing the GRID detection efficiency. In order to avoid this inconvenience, as a designing requirement the opacity to gamma rays of all SuperAGILE instrument must not exceed the opacity of 1 cm of plastic scintillator. This tight requirement has been satisfied selecting a 410 μm thin silicon microstrip detector and a 120 μm thin tungsten coded mask.

The arrangement of SuperAGILE and GRID produces a great advantage while observing sources, such as the GRB, bright in X-rays and faint in gamma rays. In this case the source can be located basing on the X-ray observations and with the estimated position it is possible to single out the faint flux of gamma rays.

2.3.1 The coded mask and the collimator

Coded mask instruments allow to produce images in a wide field of view when a focusing device cannot be used. The grazing incidence technique (see for example the BeppoSAX satellite optics in Citterio et al. (1986)) is efficient below 10 keV but using this technique only small field (about 50 arcmin $\times$ 50 arcmin) telescopes can be produced. Other focusing techniques, such as the grazing incidence on multilayers of different materials (see Mao et al. (1997) for a detailed description) or the Bragg diffraction on mosaic crystals (see Pareschi et al. (1997) for further information), are efficient above 20 keV but may be used only to produce small field instruments (5 arcmin $\times$ 5 arcmin

and 40 arcmin $\times$ 40 arcmin respectively). Wide field imaging instruments in the hard X-ray band can be produced only using the coded mask imaging principle, introduced in Fenimore and Cannon (1978).

The coded mask imaging principle is a two step process and requires a plate with a pattern of pixels transparent and opaque to the electromagnetic radiation of interest, called "coded mask", coupled to a position sensitive detector. In the first step of the process photons are accumulated on the detector, so producing a "detector image", consisting in the mask pattern shifted of the source off-axis angle with respect of the instrument optic axis. The "detector image" is then decoded applying proper algorithms in order to produce the "sky image", showing the position of the sources. More details on the mathematical algorithms required to decode the sky images can be found in in't Zand (1992).

Using the coded mask imaging process both one dimension and two dimensions images can be produced depending on the system properties. This imaging method is particularly efficient for hard X-rays and gamma rays sources. For example the payload of the INTEGRAL satellite-borne mission, launched in october 2002 by the European Space Agency and devoted to the X-ray and gamma ray astronomy (see Winkler et al. (2003)), is composed of three instruments, JEM-X (see Budtz-Jørgensen et al. (2004) for details), IBIS (described in Ubertini et al. (2003)) and SPI (see Vedrenne et al. (2003)) all based on the coded mask imaging principle.

SuperAGILE coded mask is divided into four one-dimension modules, two oriented along one direction and two along the orthogonal one. Each module contains a tungsten mask of 19 $\times$ 19 cm^2 surface composed of 787 opaque and 787 transparent pixels of 242 μm width each. The distance between the mask and the detector is 14.1 cm and the corresponding angular pixel size is 6 arcmin.

The mask is composed of a single tungsten layer of 120 μm thickness, whose transparency to X-rays is lower than 10 % below 40 keV, glued on a 500 μm thick carbon fiber support whose transparency is greater than 95 % above 10 keV. The mask is manufactured by Contraves company and the transparent pixels are opened in the tungsten layer by means of chemical etching of a single tungsten plate. A picture of the coded mask is shown in fig. 2.6.

The coded mask is positioned on a collimator, that both provides mechanical sustain and delimits the field of view of each module. The collimator is in turn composed of four square modules of 19 cm side and 14.1 cm height, each one subdivided by one sect in two cells of 9.5 $\times$ 19 cm^2 surface. From the geometry of the collimator the resulting SuperAGILE field of view is 107° $\times$ 68°. The collimator is manufactured by Contraves using a 100 μm thick tungsten layer glued on a 500 μm thick carbon fiber support. A picture of the collimator can be seen in fig. 2.7.

2.3.2 The silicon microstrip detector

The SuperAGILE detector is composed of four modules, each one constituted of four silicon microstrip tiles of 410 μm thickness and 9.5 $\times$ 9.5 cm^2 surface and coupled to a coded mask module. The strip pitch is 121 μm and the strips are co-aligned to the

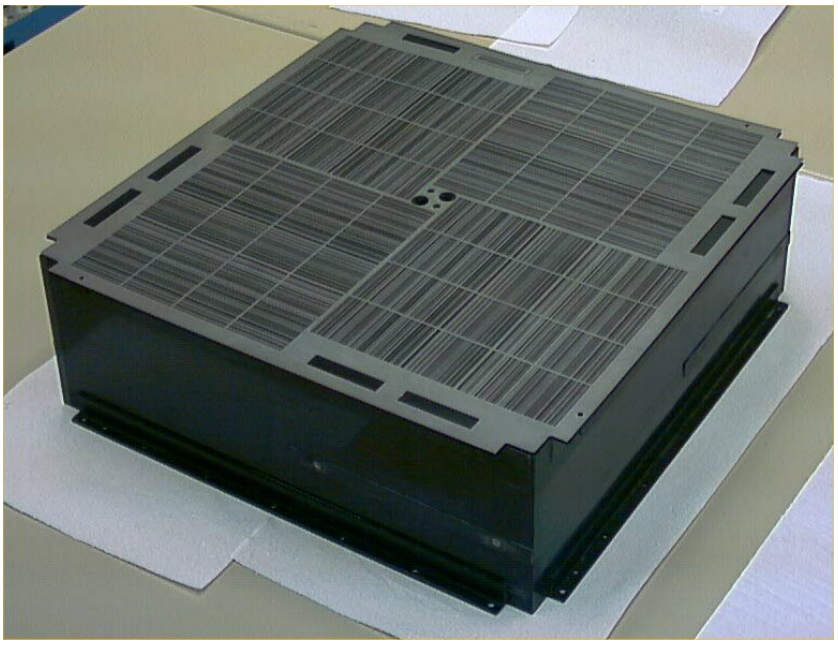

Figure 2.6: Picture of the SuperAGILE coded mask.

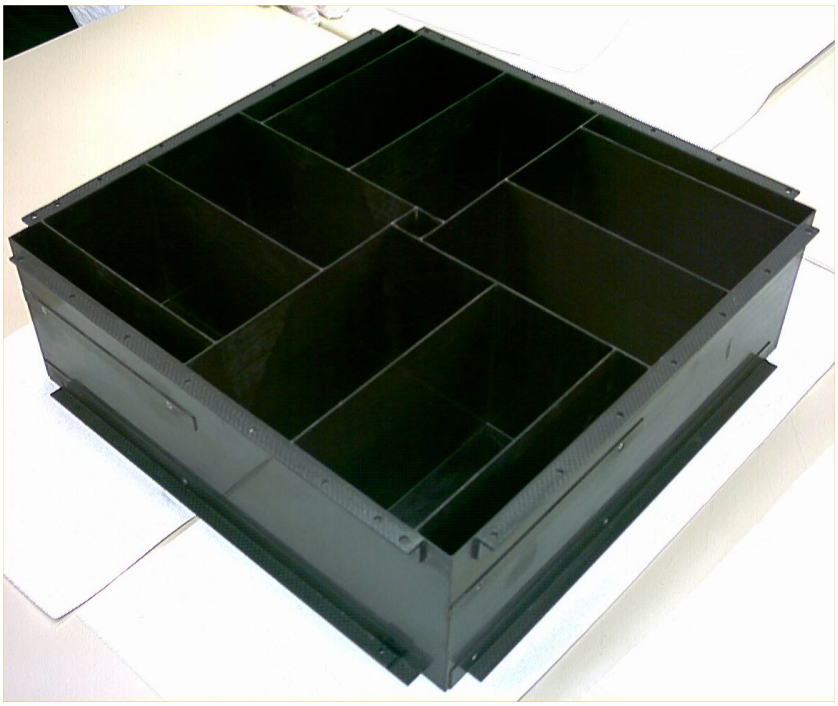

Figure 2.7: Picture of the SuperAGILE collimator.

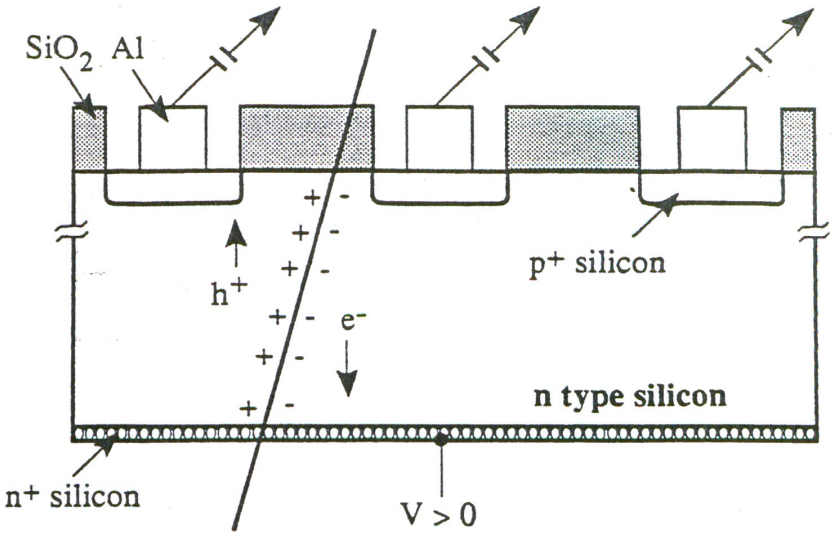

Figure 2.8: Section of the silicon microstrip detector together with a schematic view of its working principle from Peisert (1992).

coded mask pixels. Two tiles, containing 768 strips each, are connected edge-on in order to form a ladder of 19×9.5 cm^2 dimensions. Two ladders constitute a detector module with a resulting surface of about 19×19 cm^2. The surface of a single detector strip is 19 cm $\times$ 121 μm. The silicon tiles are manufactured by Hamamatsu company and are the same used for the GRID.

A section of the silicon microstrip detector together with a schematic view of its working principle (from Peisert (1992)) is shown in fig. 2.8. The detector bulk is made of n-type silicon (doped with donor atoms) and the pixels are p^+-type silicon obtained by the ion implantation technique (see Peisert (1992) for details). The detector is biased applying a +80 V voltage to the lower side and can be seen as a $p-n$ junction reversely biased and fully depleted. All the 410 μm detector thickness can be approximately considered as fully depleted.

In the picture the working principle is shown in case a charged particle (solid line) crosses the detector ionizing the silicon bulk. A photon, in turn, can be absorbed inside the silicon volume by means of the photoelectric or the Compton effect and, in this case, it is the resulting electron that crosses the detector ionizing the silicon bulk. The ionization produces electron-hole pairs (h^+ and e^- in the picture, one pair each 3.62 eV deposited in the bulk by the incident photon) that move in opposite directions under the effect of the bias electric field. In the SuperAGILE detector the positive voltage applied to the lower face forces the holes to move upward where they are gathered in aluminum electrodes, deposited above the p^+-type zone, and are provided to the readout

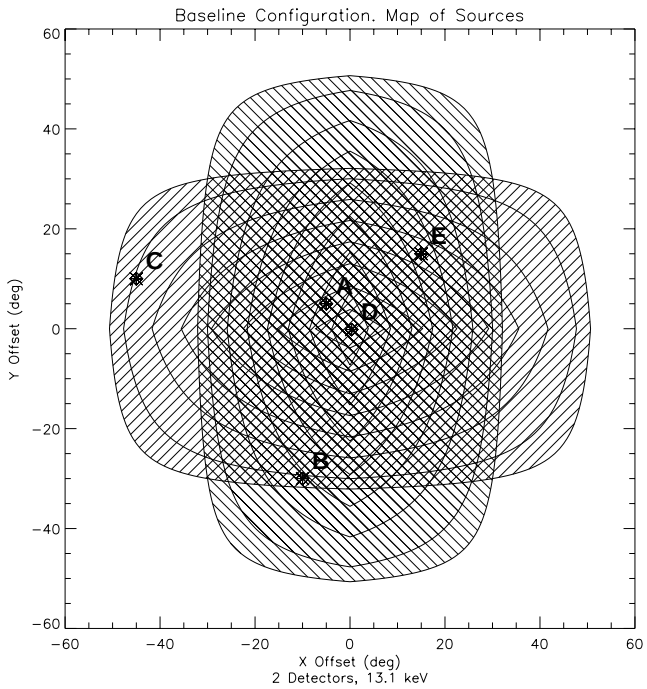

Figure 2.9: Picture of the SuperAGILE field of view. The region between $-30°$ and $+30°$ is fully coded while in the remaining four "wings" only one coordinate is coded.

electronic.

Each strip represents a pixel, can be seen as a separate detector and is individually connected to an input channel of the front-end electronic circuits. Since most of my research work concerns the measurements of the SuperAGILE electronic performances, chapter 3 is devoted to the description of the instrument electronics.

2.3.3 The SuperAGILE scientific performances

The SuperAGILE field of view is defined by the geometry of the collimator and is selected as a trade-off between the observed field in the sky and the instrumental background. The resulting field of view is composed of two $107° \times 68°$ orthogonal areas. Within one area sources can be located only in one direction because each mask module is one-dimension coded. The two areas overlap at the center of the field of view, where both coordinates are coded, while in the remaining four "wings" only one coordinate is coded. A plot of the SuperAGILE field of view is shown in fig. 2.9.

The angular resolution is also defined by the mask and collimator geometry and the resulting pixel size is 6 arcmin. A better resolution of the order $1 \div 2$ arcmin can be achieved for intense sources from the position of the barycenter in the image.

In an X-ray instrument the effective area is given by the product of the geometric area and the efficiency and gives the effective capability of detecting photons. The SuperAGILE efficiency is dominated by the Anti-Coincidence transparency and the sil-

icon detector opacity. The transparency of a material corresponds to the ratio between the number of transmitted photons I and the number without an absorber I_0 and, as explained in Knoll (1989), is given by

$$\frac{I}{I_0} = e^{-\mu \cdot t} \tag{2.1}$$

where t is the material thickness and μ is the linear attenuation coefficient,

$$\mu = \tau(\text{photoelectric}) \ + \ \sigma(\text{Compton}) \ + \ \kappa(\text{pair production}). \tag{2.2}$$

It is only the linear attenuation coefficient that depends on the photon energy, $\mu = \mu(E)$. Since the linear attenuation coefficient varies with the density of the absorber, even though the material is the same, the absorption coefficients μ are generally divided by the material density ρ in order to give the mass attenuation coefficient,

$$\text{mass attenuation coefficient} \equiv \frac{\mu}{\rho} \ . \tag{2.3}$$

Substituting the (2.3), the (2.1) becomes

$$\frac{I}{I_0} = e^{-(\mu/\rho) \cdot \rho t}. \tag{2.4}$$

A plot of SuperAGILE effective area is shown in fig. 2.10. At energies lower than about 15 keV the effective area is limited by the Anti-Coincidence transparency while above about 20 keV it is limited by the silicon detector efficiency.

Given the same effective area, the sensitivity of an X-ray instrument is mainly determined by the background counting rate. In case of SuperAGILE, the most important background contribution is the Cosmic X-ray Diffuse Background, whose spectrum, as shown in Zombeck (1990), is composed of two power-laws with different spectral indices joining at about 21 keV energy.

From Monte Carlo simulations, the SuperAGILE expected background counting rate is about 600 cts $\cdot$ s^{-1} corresponding to about 0.1 cts $\cdot$ s^{-1} $\cdot$ strip^{-1}. The expected overall on-axis sensitivity is about 10 mCrab in $5 \cdot 10^4$ s integration. Plots of the expected sensitivity in the three energy bands $15 \div 20$ keV, $20 \div 30$ keV and $30 \div 40$ keV can be seen in fig. 2.11 (in units of photons $\cdot$ cm^{-2} $\cdot$ s^{-1} $\cdot$ keV^{-1}) and in fig. 2.12 (in units of mCrab).

The dead time in the SuperAGILE front-end electronics is about 4 μs per daisy chain, depending on the time required to empty the XAA1.2 buffers and on the ADC conversion rate. The photon time tag is provided as a differential time with respect to the on board time, that is synchronised every second with 1 μs precision with the absolute time UTC.

The SuperAGILE energy resolution is dominated by the electronic noise introduced by the front-end electronic. A discussion of the most important sources of noise in silicon microstrip detectors is reported in sec. 3.4, where an overall energy resolution of about 7.8 keV FWHM is expected.

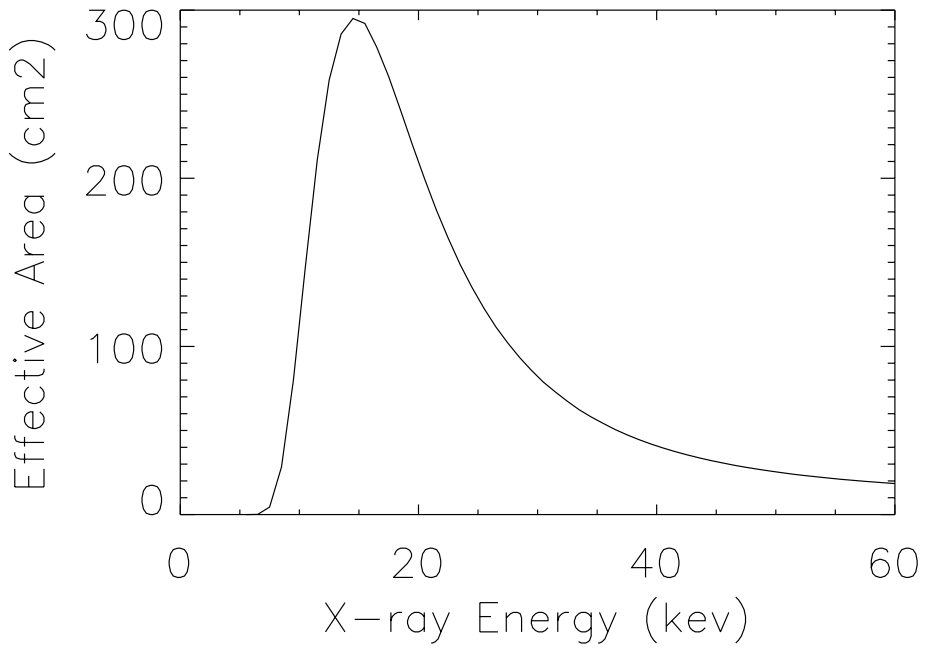

Figure 2.10: Plot of the SuperAGILE effective area below 60 keV.

2.4 The Anti-Coincidence system

On orbit at energy higher than 100 MeV, the ratio between the charged particles and the gamma ray photons number is greater than about 10^4. It is so necessary to inhibit the processing of the signals produced by the charged particles in the GRID detector to avoid the data handling and telemetry overflow.

The charged particles rejection is performed by the Anti-Coincidence system, composed of plastic scintillator (Bicron BC404) 5 mm thick layers coupled to phototubes. One scintillator layer covers the AGILE payload top plane and each side is covered using three layers. Only the payload bottom face is not enclosed in the Anti-Coincidence system.

Charged particles such as cosmic ray protons crossing the payload produce a signal in the plastic scintillator layers. The signal is provided to the data handling electronics and inhibits the processing of the corresponding signal in the detector. SuperAGILE does not need any anticoincidence system since the particle background is extremely low (about 1 particle $\cdot\, \mathrm{cm}^{-2} \cdot \mathrm{s}^{-1} \cdot \mathrm{sr}^{-1}$ except in the South Atlantic Geomagnetic Anomaly region, located between 80° W and 40° E longitude and the Equator and 55° S latitude, where this value can increase of three orders of magnitude) and because, at these energy values, the charged particles release about 150 keV in the silicon detector. An upper

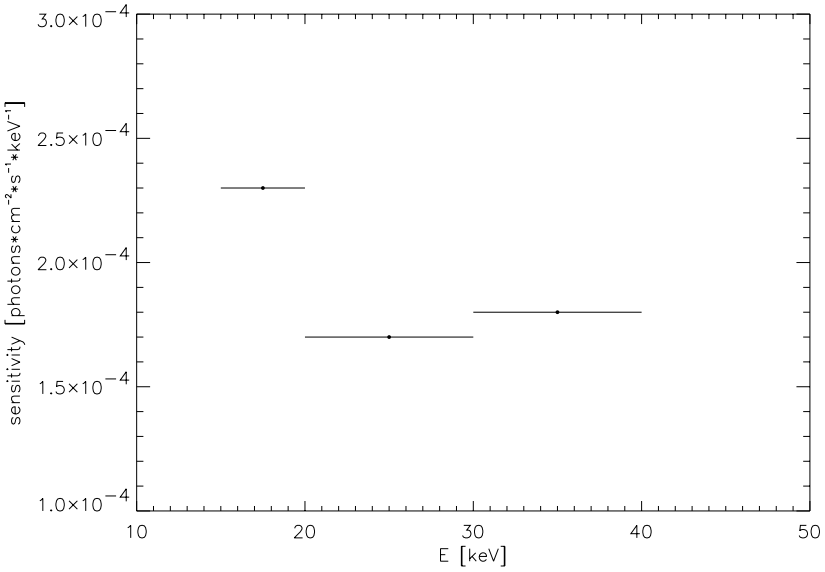

Figure 2.11: On-axis sensitivity curves for SuperAGILE with $5 \cdot 10^4$ s integration time at 5σ significance level in units of photons $\cdot$ cm^{-2} $\cdot$ s^{-1} $\cdot$ keV^{-1}.

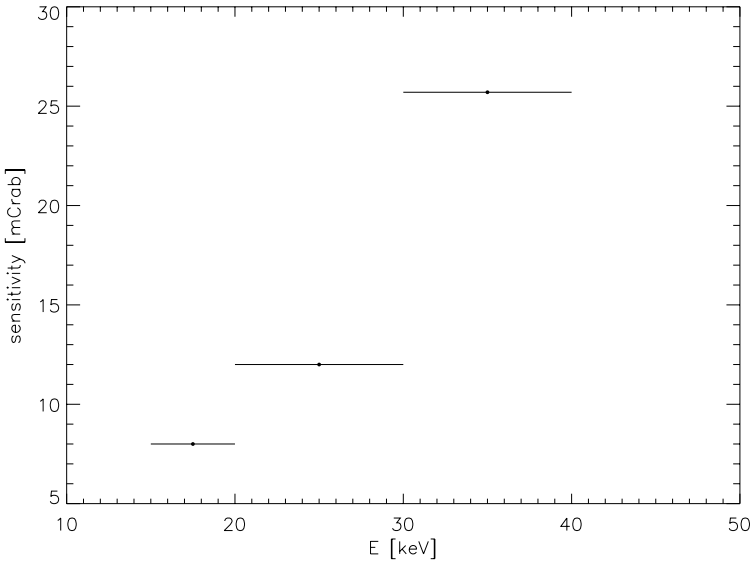

Figure 2.12: On-axis sensitivity curves for SuperAGILE with $5 \cdot 10^4$ s integration time at 5σ significance level in units of mCrab.

threshold inhibiting the processing of the events with energy above this value is enough to reject the charged particles.

The Anti-Coincidence inefficiency, i.e. the fraction of charged particles crossing the plastic scintillator layers without producing any signal, is about 10^{-4}. Since the AGILE background particle flux ranges between $4 \cdot 10^3$ cts $\cdot$ s^{-1} and $8 \cdot 10^3$ cts $\cdot$ s^{-1}, only 0.4 to 0.8 cts $\cdot$ s^{-1} do not produce any Anti-Coincidence signal and cannot be rejected.

The dimensions of the top plastic scintillator plane are 51×51 cm^2 and the side planes have trapezoidal shape with a major base 44 cm long, a minor base 42 cm long and a 17.5 cm height. The trapezium shape avoids the mechanical interference between the photomultiplier tubes coupled to each side. The top plane is inserted within a composite materials protective panel and optically connected to four photomultiplier tubes (Hamamatsu R7400) placed at its corners. The scintillation photons coming from the side panels are gathered by optical fibers and are delivered to the photomultiplier tubes.

2.5 The Payload Data Handling Unit

The Payload Data Handling Unit (PDHU), described in Morselli et al. (2000), is the AGILE on board data handling electronics. The main tasks of the PDHU are the acquisition and processing of the data delivered by the AGILE payload instruments and by the Anti-Coincidence veto signals, the switch of the payload operative modes, the housekeeping (HK) generation, the telecommand management and the telemetry processing.

Since within the GRID energy band the charged particle rate is between $4{\cdot}10^3$ cts $\cdot$ s^{-1} and $8 \cdot 10^3$ cts $\cdot$ s^{-1} and the gamma ray photons rate is between 0.01 cts $\cdot$ s^{-1} and 3 cts $\cdot$ s^{-1}, the charged particle rejection is a crucial task to perform gamma ray observations. To this charged particle background, mainly due to cosmic ray protons, the gamma ray background is added, produced principally by the mirror effect of the Earth atmosphere on the cosmic gamma rays and increasing the total background. The background gamma rays and particles rejection is a major problem since the background rate can decrease the GRID sensitivity and can fill the telemetry band.

Considering a maximum data transmission rate of about 500 kbit $\cdot$ s^{-1} and a transmission time duration between AGILE and the Malindi ground station of about ten minutes, about 300 Mbit of data maximum can be stored during one orbit. Since one event, given by a photon or a charged particle, produces about 2 kbits of data, the memory required to store all the events is above two times higher than the available memory. Thus the main PDHU task is the on-board discrimination between the charged particles and the photon events, performed by means of two fast hardware (response faster than 25 μs) and one software asynchronous rejection procedures.

Between the data processing tasks, a specific Gamma Ray Burst search procedure based on the SuperAGILE and Mini-Calorimeter triggers is introduced. The PDHU continuously integrates the SuperAGILE ratemeters on different time scales (from less than 1 ms to about 100 s) and, if a statistically significant intensity increase is found,

a sky image is produced so allowing to find the direction of the transient source. The transient coordinates are then sent to Earth via the ORBCOMM satellite constellation.

The PDHU provides also information about the satellite position, reconstructed by a GPS (Global Positioning System) transceiver with about 50 m accuracy, and attitude, provided by the attitude and star sensors. Basing on this information the incoming direction of the detected photons can be reconstructed.

The PDHU is composed by seven electronic boards, contained in an aluminum box of $25 \times 20 \times 15.7$ cm^3 and 6.65 kg mass, fixed in the payload bottom side, under the Mini-Calorimeter. Four boards are dedicated to the Silicon Tracker data analysis, one contains the on-board DSP, one the electronics to interface all the experiments and the last board the payload memory (80 Mbits, of which 30 Mbits dedicated to SuperAGILE). The PDHU power consumption is about 26 W.

2.6 The AGILE mission scientific objectives

2.6.1 Active Galactic Nuclei

From a conservative estimation, in a three year programme AGILE will detect a number of AGN about two or three times larger than EGRET. For the first time the brightest objects can be simultaneously monitored in the hard X-ray band. Moreover a programme for joint AGILE and ground-based observations is being planned.

For the first time in the AGILE Field of view simultaneous monitoring of a large number of AGN will be possible. The main topics of the AGILE observations will be the study of transients and low-level gamma ray emission and duty cycles, the relationship between the gamma ray variability and the radio, optical, X-ray and ultra high-energy (TeV) emission, the correlation between relativistic radio plasmoid ejections and gamma ray flares and finally the hard X-ray/gamma ray correlation.

SuperAGILE will provide X-ray flux measurements of the brightest blazars simultaneously with the GRID gamma ray observations. Moreover SuperAGILE will provide periodic measurements of the brightest Seyfert 1 and 2 Galaxies, leaving open the possibility to discover new objects thanks to the wide field of view.

2.6.2 Gamma ray Bursts

The expected number of Gamma Ray Bursts detected by AGILE is 25 events per year in the hard X-ray band and $5 \div 10$ events per year in the gamma ray band. The GRID detection can allow to study the Gamma Ray Bursts in the gamma ray energy band where only some events were detected by EGRET. Moreover the GRID is expected to be highly efficient in detecting photons above 10 GeV because of limited backsplashing.

SuperAGILE will locate Gamma Ray Bursts at a few arcmin level. The SuperAGILE data handling procedure includes the on-board location of the GRB and the transmission of the event coordinates by means of the ORBCOMM satellite constellation in order to be distributed to optical, infrared and radio observers, so allowing a rapid and efficient

follow-up. Moreover the joint observation by the GRID and SuperAGILE will allow the study of the interplay between hard X-ray and gamma ray emissions.

Special emphasis is given to fast timing, allowing the detection of sub-millisecond GRB pulses independently detectable by the Silicon Tracker, the Mini-Calorimeter and SuperAGILE.

2.6.3 Compact Galactic Sources

AGILE will contribute to the study of gamma ray pulsars improving photon statistics for gamma ray period searches, detecting possible secular fluctuations of the gamma ray emission from neutron star magnetospheres and studying unpulsed gamma ray emission from plerions in supernova remnants searching for time variability of pulsar/wind interactions, for example in the Crab Nebula.

A large number of gamma ray sources near the Galactic plane are unidentified (also known as Unidentified EGRET sources) because no counterpart has been detected. The angular resolution of both GRID and SuperAGILE will improve the location of such sources in order to find possible counterparts.

The typical hard X-ray flux of black hole candidates and binary emitting X-ray systems makes this class of sources a primary scientific objective to SuperAGILE for the purposes of flux monitoring, period monitoring and search and phase resolved spectroscopy. Special emphasis is given to the broad band energy observation of Galactic X-ray jet sources (like for example Cyg X-3, GRS 1915+105, GRO J1655-40 and others) in order to search for gamma ray emission in peculiar jet geometries.

While the steady X-ray counterparts of Soft Gamma-Ray Repeaters are usually too faint to be detected by SuperAGILE, four out of five sources (SGR 1900+14, SGR 1806-20, SGR 1627-41 and SGR 1801-23) displayed an intense activity over the past years, emitting recurrent and short bursts. At this purpose the wide field of view and the energy range of SuperAGILE are perfectly matched. SuperAGILE will not only detect these sources in their active states, but it will also produce accurate and likely time resolved energy spectra. Since the discovery of Soft Gamma-Ray Repeaters is limited by the instrumental coverage in the proper energy range, SuperAGILE is expected to discover new sources in this so far small class.

2.6.4 Diffuse emission

The AGILE good angular resolution and large average exposure will further improve the study of cosmic ray origin, propagation, interaction and emission processes. A joint study of gamma ray emission from MeV to TeV energies is possible by dedicated programs involving AGILE and new-generation TeV observatories of improved angular resolution.

Chapter 3

The SuperAGILE electronics

3.1 Introduction

In an experiment with a solid state detector, as SuperAGILE, most of the scientific performances depend on the features of the front-end electronic circuits. From the electronic point of view, in fact, the detector (actually each strip) can be simply considered as a current generator, providing a pulse of current after a photon is detected. The detector also contributes to the noise as a source of leakage current and as a resistor at the input. All the resulting signal features, such as the shape, the dynamic range and the duration depend on the front-end electronics properties.

In this chapter the electronic of the SuperAGILE instrument is described and the most important features affecting the scientific performances of the experiment are discussed. The chapter starts with the description of the SuperAGILE front-end electronics (in sec. 3.2), followed by the report of the most important features of the XAA1.2 read-out chip (in sec. 3.3). Then a short overview of the noise sources in the experiments involving silicon microstrip detectors is reported in sec. 3.4. The XAA1.2 can be interfaced to a custom acquisition system, described in sec. 3.5, provided by the chip manufacturing company and allowing to perform functional and performance tests. To bias, configure and read-out the SuperAGILE front-end electronic a dedicated instrumentation has been developed, described in sec. 3.6. The output signals from the front-end electronics are fed to the interface electronics, that performs signal conditioning and digitization, as reported in sec. 3.7. The data are then processed by the PDHU, described above in sec. 2.5, whose tasks concerning SuperAGILE are shown in sec. 3.8. Data, organised in packets, are eventually downloaded through telemetry. At the end of this chapter, in sec. 3.9, I report a discussion of the most important and critical features of SuperAGILE, with specific reference to the topics included in my research work.

3.2 The SuperAGILE front-end electronics

Each of the four SuperAGILE detector modules is separately coupled to a board of the SuperAGILE front-end electronics (SAFEE), containing 16 XAA1.2 chips, for a total

number of 48 chips. The SAFEE is in charge of the analogue processing of the signals produced by the detector and by a calibration electronic pulse generator included in the instrument. For this reason the SAFEE contains all the electronic devices needed to supply, bias and configure the XAA1.2 front-end chips. A block diagram of the SAFEE board can be seen in fig. 3.1.

Within each board the XAA1.2 are arranged in daisy chain of three chips, sharing the power supply, the serial control bus and the bias voltages and currents and providing parallel output signals. From the electronic point of view a daisy chain can be considered as a single circuit and in this arrangement a simpler schematic and a smaller board can be produced.

In the SAFEE configuration only seven XAA1.2 biases out of eleven can be adjusted (the currents *prebias*, *shabias*, *Trigdelbias*, *TrigWbias* and *ResWbias* and the voltages *Vfs* and *Vfp*, all described in the next section), generated by four AD8842 DAC, one per daisy chain. Each AD8842 DAC provides also the reference voltage.

Because of the small room available on the detector tray, the SAFEE boards are manufactured on two multilayer printed circuit boards (PCB), internally connected with a flexible kapton part. The PCB with the smallest area (horizontal SAFEE) is placed on the detector tray and contains the XAA1.2 and all the ancillary components. The PCB with the widest area (vertical SAFEE), containing the DAC and other conditioning devices, is enclosed in a dedicated box fixed to the collimator outer walls. Such a configuration can be arranged because the flexible kapton connection between the two parts can be bent. A picture of the SAFEE PCB equipped with the XAA1.2 chips can be seen in fig. 3.2: from top the vertical SAFEE section, the flexible kapton connection (in red) and the horizontal SAFEE section with the XAA1.2 chips.

The XAA1.2 read-out circuits proves to be extremely sensitive to the temperature variations. Specific measurements of the thermal stability of some performances of this circuit are reported in sec. 4.4. Due to this sensitivity to temperature variations, SuperAGILE includes 32 AD590 thermometers, distributed on the SAFEE and SAIE PCB, on the detector tray, on the collimator walls and on the coded mask plate.

Since the detector strip pitch is 121 μm and the XAA1.2 input pad pitch is 91 μm, ceramic pitch adapters are manufactured in order to connect the chips to the detector via 17 μm (lower side) and 25 μm (upper side) thin wire bondings. A microscopy picture of the pitch adapter is shown in fig. 3.3.

3.3 The XAA1.2 chip

The XAA1.2 is an application specific integrated circuit (ASIC) designed using very large scale integration (VLSI) technology by the Norwegian company Ideas ASA[1] as a front-end electronic chip for silicon microstrip detectors. The chip is manufactured with a 0.8 μm complementary metal oxide semiconductor (CMOS) double-poly and double metal technology on epitaxial layer. As specified in Yokoyama et al. (2001), a feature size of 0.8 μm corresponds to a 16 nm gate oxide thickness.

[1] Web site: www.ideas.no

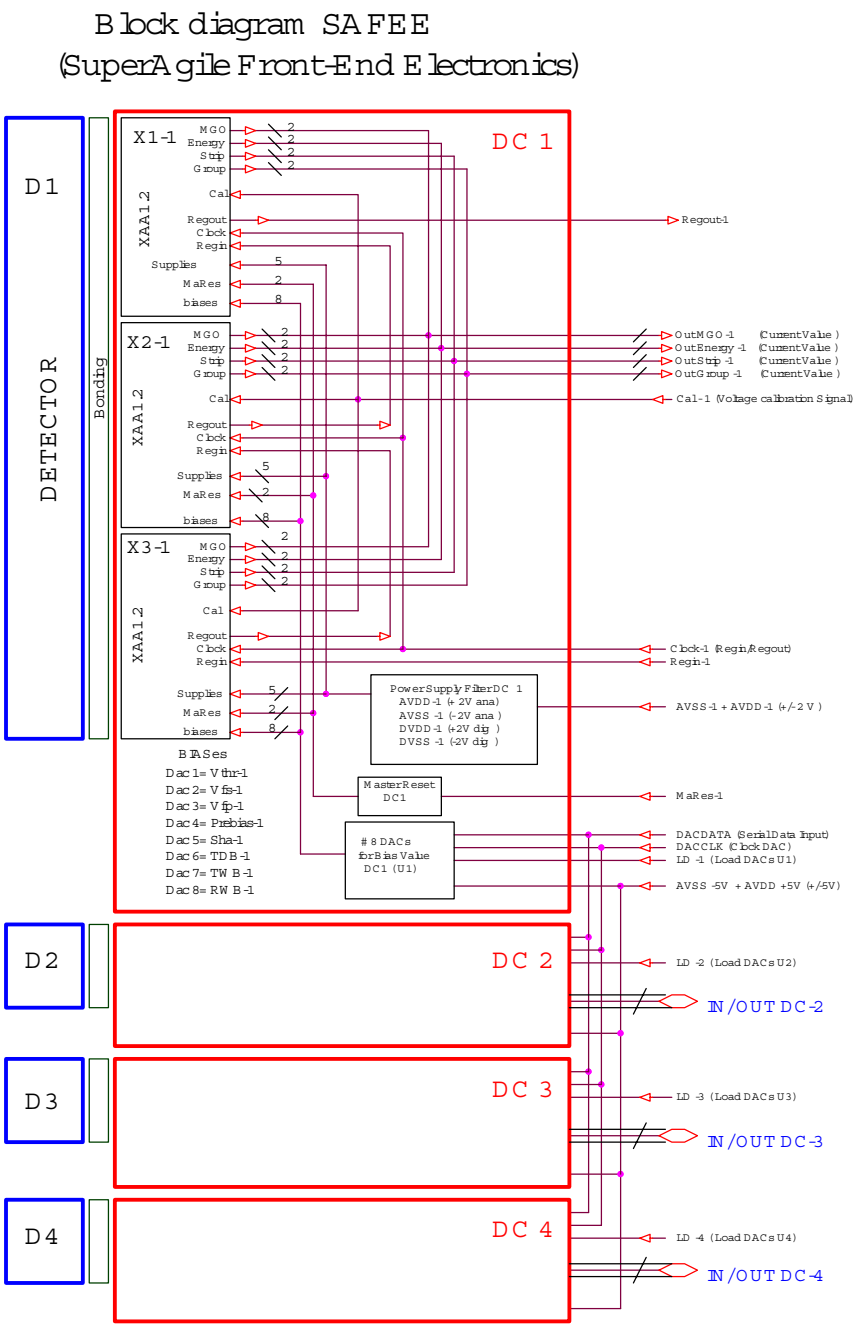

Figure 3.1: Block diagram of the SAFEE board.

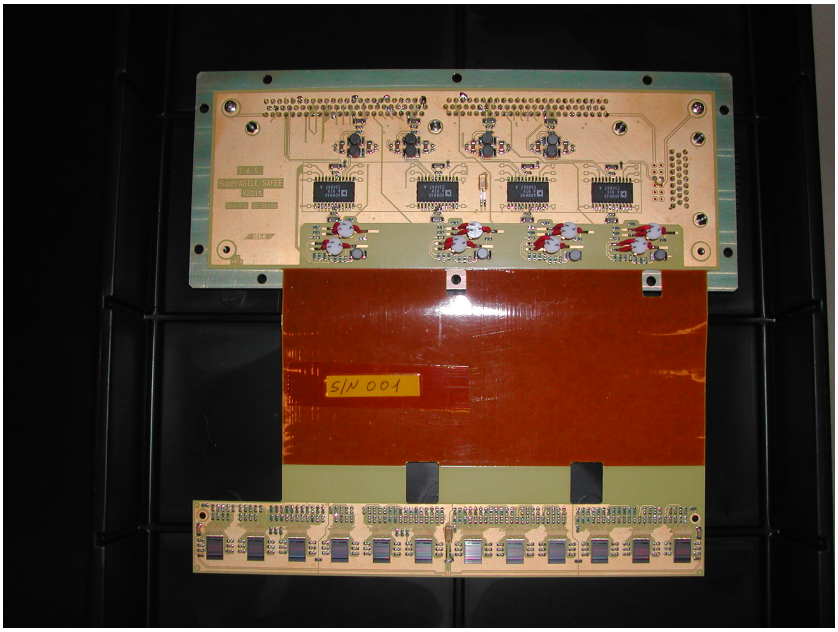

Figure 3.2: Picture of the SAFEE PCB: from top the vertical SAFEE section, the flexible kapton connection (in red) and the horizontal SAFEE section with the XAA1.2 chips.

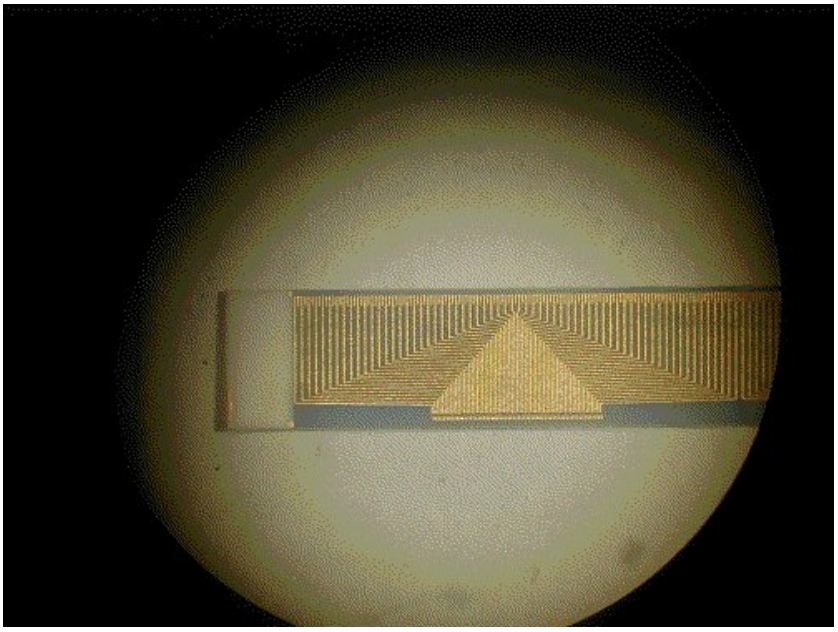

Figure 3.3: Microscopy picture of the ceramic pitch adapter. The detector is bonded to the top side in the picture (121 μm pitch) and the XAA1.2 input pads are bonded to the lower side (91 μm pitch).

The XAA1.2 has a 6×8 mm^2 surface and a 600 μm thickness, is divided in 128 data driven and self-triggering input channels, consisting of an analog and a digital part, and is designed to detect single hit events with sparse readout. The main features of this chip as a front-end electronic circuit for silicon microstrip detectors are reported in Soffitta et al. (2000). The XAA1.2 is a custom ASIC chip designed starting from the Ideas ASA commercial device XA1.3 after making design modifications aiming to improve the performance in term of noise, power consumption and thermal stability by means of an extensive laboratory testing, as reported in Del Monte et al. (2000).

Each analogue signal processing chain is turn composed of a charge sensitive preamplifier, a CR-RC shaper and a peak store unit, that contains a peak stretcher, as shown in the schematic in fig. 3.4. The peak stretcher can be excluded and bypassed changing the digital configuration of the ASIC, thus reducing the overall power consumption.

The digital section can be programmed with a 646 bit long register, built inside the chip and serially loaded. The register contains a 646 bit stream, referred to as configuration mask or "register in", encoding all the information needed to configure the chip: 128 bit specifying the enabled channels in test mode (to measure the chip linearity as described in section 5.3.2), 384 bit configuring the threshold fine regulation (3 bit per channel), 128 bit specifying the disabled channels, 4 bit containing the address offset (to connect more than one XAA1.2 in daisy chain), 1 bit enabling the stretcher and 1 bit enabling the chip in test mode. By sending twice this configuration string the actual value contained in the memory, referred to as "register out", is provided and can be read out.

The XAA1.2 chip is supplied using four voltages, two for the analogue section ($AV_{DD} = +2.0$ V and $AV_{SS} = -2.0$ V) and two for the digital section ($DV_{DD} = +2.0$ V and $DV_{SS} = -2.0$ V). Since the power consumption of the digital part is negligible, the currents of the analogue part can be considered as the chip supply currents (I_{DD} and I_{SS}).

The chip functionality and performance are controlled via eleven biases and a reference voltage, all set to the XAA1.2 chip using Digital to Analog Converters (DAC) units. The tunable bias currents are the *prebias* and the *shabias*, controlling the source and the drain current of the preamplifier and the shaper respectively, the *otabias*, bias current of the discriminator, the *IbDAC*, that controls the current-voltage buffer converters, the *strbias*, controlling the peak stretcher and the *Vthrbi*, controlling the digital fine regulation of the threshold, the *TrigDelbias*, controlling the trigger delay, the *TrigWbias*, defining the trigger width and the *ResWbias*, affecting the width of the reset signal after an event is read-out. The tunable bias voltages are the *Vfs* and *Vfp*, DC voltages for the gate of the feedback MOS resistor in the preamplifier and the shaper respectively. The nominal values of the bias currents and voltages are shown in tab. 3.1.

The power supply currents of the XAA1.2 chip in nominal conditions and stretcher-on configuration are $I_{DD} \simeq 14$ mA and $I_{SS} \simeq 24$ mA. The power consumption of a single chip can be calculated from

$$P = \frac{I_{DD} \cdot V_{DD} + I_{SS} \cdot V_{SS}}{128} \tag{3.1}$$

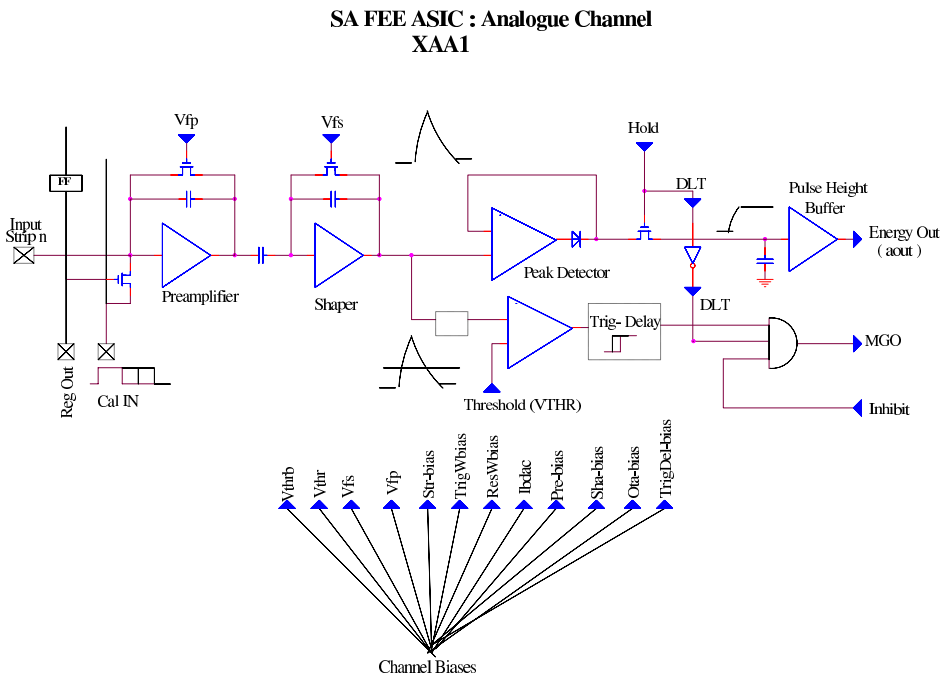

Figure 3.4: Schematic of a XAA1.2 analogue channel. From left the preamplifier, the shaper, the peak stretcher and the discriminator.

and, in nominal conditions, $P \simeq 0.5$ mW/ch. Further details on the XAA1.2 are available at www.ideas.no/products/ASICs/pdf/XAA1.pdf.

Table 3.1: Nominal values of the XAA1.2 bias currents and voltages. I_{bias} is the bias current while V_{bias} is the bias voltage.

Bias name	I_{bias} [μA]	V_{bias} [mV]
prebias	50	
shabias	22	
otabias	10	
strbias	90	
Vthrbi	20	
IbDAC	60	
TrigDelbias	8	
TrigWbias	20	
ResWbias	4	
Vfp		-200
Vfs		501

The XAA1.2 is developed as a front-end electronic chip for 1-D position sensitive solid state detectors. On trigger, the XAA1.2 returns as analogue current differential outputs (to reduce the pick-up noise) the following information: amplitude, address and multiplicity of the triggering signal. The address is provided in terms of analogue currents corresponding to the MSB (group, 2 bit plus 4 offset bit to connect up to 16 chips in daisy chain) and LSB (strip, 5 bit). Since the internal chip logic is not able to provide information on more than one hit at a time, the switch of a threshold inhibits all the other inputs in a few nanoseconds time range. For this reason the chip delivers an output current by a multiplicity generator output (MGO), thus allowing to reject multiple hit events.

The analog chains of the XAA1.2 can process charge pulses produced by an external generator and replicating the output pulses from a detector. For this purpose the chip contains a test charge input where voltage pulses can be provided. Such voltage signals are then converted into charge pulses in a 0.5 pF capacitor contained in the XAA1.2. The linearity measurement by means of the charge pulse generator is called "electronic calibration", has been extensively used during this research work and will be used in orbit to evaluate the linearity (gain and intercept) of the SAFEE channels. Linearity calibration will be essential during the mission. They will allow to accumulate photons of the wished energy intervals and to update the look-up tables for the identification of the strip from two analog signals.

The amplitude of the test pulse is selected considering that a hole-electron pair is created for every $E_0 = 3.62$ eV absorbed inside the detector. Consequently the equivalent energy E of a pulse of charge q is given by

$$E = \frac{q}{e} \cdot E_0 \tag{3.2}$$

where $e = 1.6 \cdot 10^{-19}$ C is the electron charge.

The voltage threshold is set attenuating of a factor 11 the output voltage from a 8-bit DAC, giving the same reference value for all the input channels. Moreover the XAA1.2 analogue channels contain a 3-bit digital fine regulation circuit that allow to compensate the inequalities in the reference value of all the channels.

3.4 Sources of noise in silicon microstrip detectors

The main sources of noise in ASIC circuits coupled to silicon microstrip detectors are the shot noise given by the leakage current in the detector, the thermal noise from the biasing resistors of the detector, the noise produced by the metal strips and the electronic noise in the readout circuit. The electronic noise is far dominant over the other contributions. All other noise components in the input transistor, such as the flicker noise and the bulk-series resistance noise, are negligible if compared to the four ones given above. In this section an overview on the main sources of noise is given and each contribution in the case of the XAA1.2 chip is evaluated. An extensive review about the most important sources of noise in silicon microstrip detectors can be found in Barichello et al. (1998).

The noise figures are generally expressed using the Equivalent Noise Charge (ENC), a parameter connecting the root mean squared (RMS) noise voltage at the output of the shaper with the signal input and generally measured in e^-. Considering that in silicon the mean energy needed to create a hole-electron pair is $E_0 = 3.62$ eV, the mean number of electron-hole pairs produced by a photon of energy E is

$$N_e = \frac{E}{E_0}. \tag{3.3}$$

The fluctuation on the number of charge carriers produced by the interacting photon increases the noise contribution of the detector. Considering that the number of electron-hole pairs follows the Poisson statistics and that only the holes are processed, the contribution is

$$ENC_{det} = \sqrt{N_h \cdot f} \tag{3.4}$$

where N_h is the number of detected holes from the (3.3) and f is the Fano factor of the material, correcting the Poisson statistics. Since in silicon $f = 0.14$ as in Knoll (1989), at 15 keV $ENC_{det} \simeq 24$ e^- and at 40 keV $ENC_{det} \simeq 40$ e^-.

All the noise sources increase the width of a monochromatic energy line following a gaussian distribution. For this reason, the ENC can be converted into the FWHM of a spectral line taking into account the equation connecting the FWHM of a spectral line and the signal RMS,

$$FWHM = 2.35 \cdot RMS \tag{3.5}$$

and from (3.3) and (3.5), the FWHM in keV produced by a noise ENC is given by

$$FWHM = 8.51 \cdot 10^{-3} \cdot ENC. \tag{3.6}$$

Applying the (3.6), the fluctuation of the charge carriers in (3.3) gives noise contributions of $FWHM_{det} \simeq 0.2$ keV (at 15 keV) and $FWHM_{det} \simeq 0.3$ keV (at 40 keV).

In case of the XAA1.2 chip, the shot noise given by the leakage current in the detector can be written as

$$ENC_{leak} = 107 \cdot \sqrt{I_L(T) \cdot T_P} \tag{3.7}$$

where I_L is the strip leakage current (in nA), T_P is the peaking time (in μs) and T is the temperature (in K). Considering that at room temperature (300 K) the detector leakage current is $I_L = 2$ nA $\cdot$ cm^{-2} and the signal peaking time is $T_P = 2$ μs, the contribution is $ENC_{leak} \simeq 100$ e^- and $FWHM_{leak} \simeq 0.9$ keV.

The thermal noise in the detector bias resistors can be written as

$$ENC_{bias} = 45 \cdot \sqrt{\frac{T_P \cdot T}{R_{bias}}} \tag{3.8}$$

with $R_{bias} = 20$ $M\Omega$. Substituting the numeric values the estimated noise is $ENC_{bias} \simeq 240$ e^- and $FWHM_{bias} \simeq 2.0$ keV.

The ENC contribution of the detector metal strips is

$$ENC_{ms} = 2.58 \cdot 10^{-2} \cdot C_{IN} \cdot \sqrt{\frac{R_{ms} \cdot T}{T_P}} \tag{3.9}$$

and since $C_{IN} = 30$ pF $\cdot$ strip^{-1} and $R_{ms} = 72\ \Omega$, $ENC_{ms} \simeq 80$ e$^-$ and $FWHM_{ms} \simeq 0.7$ keV.

The XAA1.2 electronic noise at the *prebias* nominal value of 50 μA is given by the semiempyrical formula

$$ENC_{el} = 171 + 23.5 \cdot C_{IN} \tag{3.10}$$

(from Sundal (2001)) where the contribution proportional to the input capacitance is the transistor channel noise and the constant term takes into account the internal capacitance. Without bonding the chip to the detector ($C_{IN} = 0$) the electronic noise is $ENC_{el} \simeq 170$ e$^-$, corresponding to $FWHM_{el} = 1.5$ keV, and taking into account the capacitance of the detector ($C_{IN} = 30$ pF $\cdot$ strip^{-1}) the resulting noise is $ENC_{el} \simeq 880$ e$^-$ and $FWHM_{el} = 7.5$ keV. A method to reduce the electronic noise is the increase in the preamplifier bias current (*prebias*). Since a variation of this bias changes the output signal shape, a corresponding adjustment of the *Vfp*, *shabias* and *Vfs* is required. The electronic noise reduction method by means of the bias voltages and currents variation is outlined in sec. 7.6.

From the discussion above, the electronic noise is by far the most important noise source in the XAA1.2. Without detector the noise is given only by the transistor channel component so $ENC_{total} \simeq 170$ e$^-$ and $FWHM_{total} \simeq 1.5$ keV while, in case of a 30 pF $\cdot$ strip^{-1} capacitance detector is present, the resulting ENC from the quadratic sum of the previous contributions is $ENC_{total} \simeq 920$ e$^-$ and $FWHM_{total} \simeq 7.8$ keV.

3.5 The XAA1.2 acquisition system

3.5.1 The XA-DAQ acquisition board

All the operations needed to supply, configure and control the XAA1.2 chip can be performed using a dedicated acquisition board, the XA-DAQ, manufactured by Ideas ASA. The XA-DAQ is interfaced to the parallel port of a PC and all its functions are controlled using a custom software, developed in LabView environment under Windows98 operating system and provided by the manufacturer. The interface to the test board containing the XAA1.2 chip is via a 50-pin f ERNI connector. Only one chip at a time can be connected to the acquisition board. More information about the XA-DAQ can be found in Sundal (1999).

The ± 2 V power supply of the XAA1.2 chip is generated by a dedicated module in the XA-DAQ. The board contains a power supply monitor designed to measure the supply voltages V_{SS} and V_{DD} with about 200 μV accuracy and the corresponding currents I_{SS} and I_{DD} with about 1 mA accuracy. A dedicated circuit provides the bias currents and

voltages to the chip. The system can generate 12 biases, all monitored for both voltage and current.

The digital part of the XAA1.2 can be programmed by means of a dedicate module, that sends the 646-bit of the configuration mask to the digital input. By sending twice the bit stream and using a specific monitor, the content of the digital part can be read out in order to verify that the configuration is stored correctly.

Using the XA-DAQ board some of the chip performances can be measured, particularly the linearity and the threshold. The board contains a voltage pulse generator used to calibrate the XAA1.2. The voltage signals produced in the board are converted into charge in a 0.5 pF capacitor contained in the XAA1.2 and are then provided to the chip input channels. For each channel the results of the electronic calibration are the output amplitude of the input charges, the MGO and the two address signals (strip and group).

By means of the same voltage pulse generator also the chip threshold can be measured, producing a so called "threshold scan". In this procedure a reference voltage is selected, a fixed number of charge pulses of the same amplitude is provided to each input channel and the number of triggers (due to signals with amplitude above the selected threshold) is recorded. The voltage value is then changed and the acquisition software evaluates the threshold finding (using a linear interpolation) the value at which the ratio between the number of acquired pulses and the number of sent pulses equals 1/2. By means of a pulse charge variation the threshold as a function of the input charge can be evaluated, representing the characteristic curve of the discriminator.

3.5.2 The XA-DAQ acquisition software

The XA-DAQ acquisition board is controlled by a dedicated software developed in the LabView environment and running under Windows98 operating system. The instrument driver is implemented as a C-code program linked to LabView and all other controlling functions are developed as libraries interfaced to the instrument driver.

Main XA-DAQ software functions include board initialization and calibration, generation of the XAA1.2 supply and biases, protected chip connection via a software controllable relay, electronic calibration, threshold scan and detector read-out. A screen capture of the XA-DAQ software main menu can be seen in fig. 3.5.

3.6 The SAFEE Test Equipment acquisition system

In order to supply, control and run the SAFEE boards, a custom Test Equipment (TE) has been developed, based on a VME acquisition system and a VME-PCI bridge interface. The SAFEE TE is controlled using a dedicated acquisition software, developed under Linux operating system. In this section a brief overview of the acquisition system is given, describing both hardware and software tools. More details about the hardware and software of the SAFEE TE can be found in Pacciani et al. (2004).

The data produced by the SAFEE TE are archived using the Detector Independent Science Console Subsystem (DISCoS), connected to the acquisition via TCP/IP, and then converted into FITS format by dedicated processors. Both tasks are described in

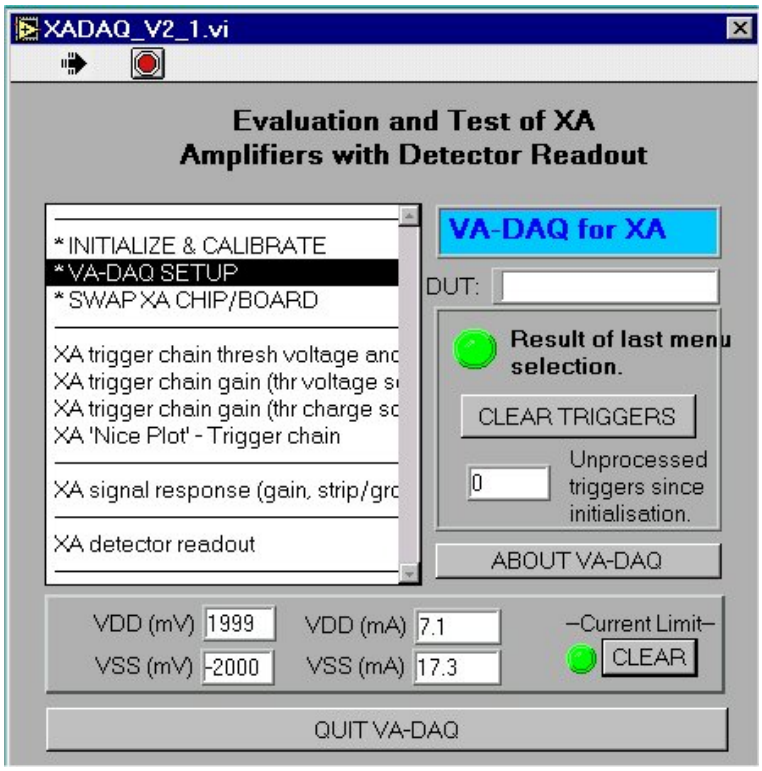

Figure 3.5: Screen capture of the XA-DAQ software main menu.

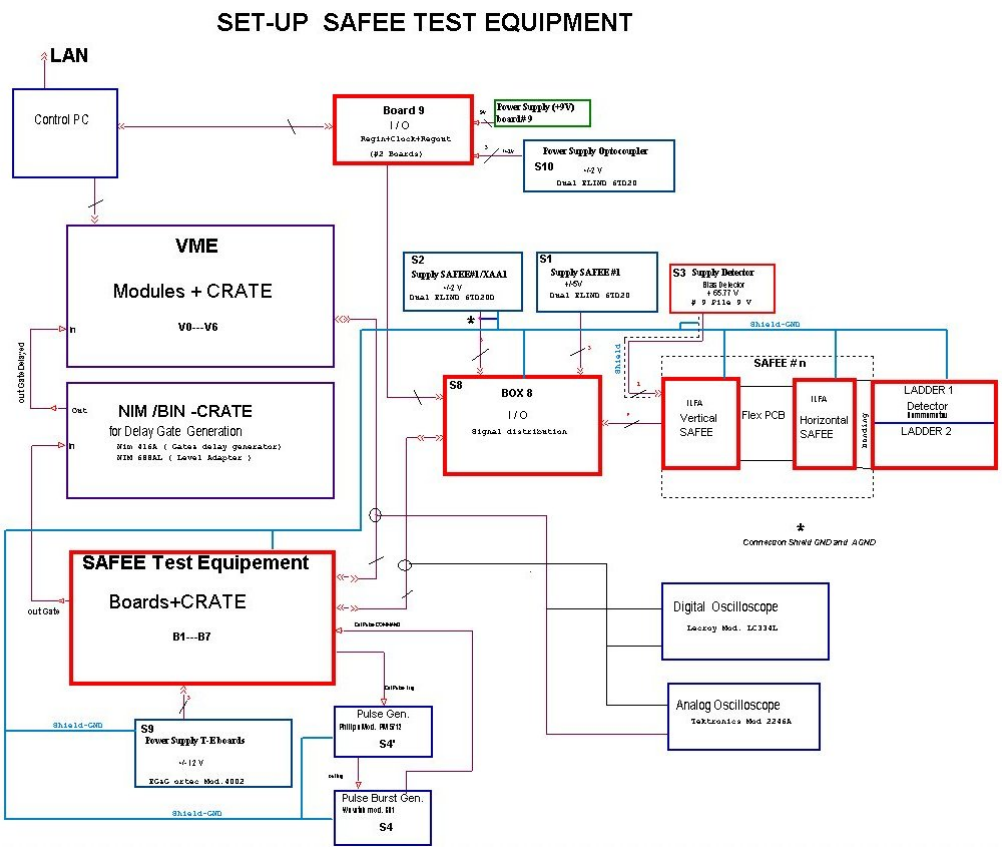

Figure 3.6: Simplified scheme of the SAFEE TE from Pacciani et al. (2004).

sec. 6.2.1. The archived data are accessed and analysed by means of dedicated programs developed in the Interactive Data Language (IDL) environment. Since the development of this analysis software is part of my research work, these programs are described in dedicated sections, 6.3 and 6.4.

3.6.1 The SAFEE Test Equipment hardware

The SAFEE TE is based on commercial VME modules and laboratory developed custom boards. The VME bus guarantees high reliability and high acquisition rates. A simplified block diagram describing the different parts of the SAFEE TE (from Pacciani et al. (2004)) is shown in fig. 3.6.

Peculiar functions of the TE are provided by dedicated laboratory developed boards: current-voltage conversion and signal conditioning of all analog outputs, trigger system for the VME acquisition, event timing (with about 1 μs resolution), event mark, I/O interface to configure all chips and DAC contained in the SAFEE boards, conditioning of the housekeeping signals (such as the temperature of the SAFEE measured using eight AD590 thermometers per board) and ratemeters.

The XAA1.2 outputs are differential current signals. From the circuit specifications, the address analog outputs are in the $0 \div 480$ μA range, the amplitude signal ranges between -200 μA and $+200$ μA and the MGO current is given by 60 μA times the multiplicity of the signal (described in sec. 3.3). All these current signals are converted into voltage in a I/V converter board before being acquired.

An event is marked in the analog bus by the MGO signal and a trigger signal is generated when a MGO corresponding to a single multiplicity event (selected using a window discriminator) is detected. On trigger the voltage converted MGO, amplitude and address (strip and group signals) are digitized using a 12-bit ADC, and the time tag, the event mark and the daisy chain number are added to the data. The time tag is generated by means of a 1 MHz clock and 32-bit latch.

The housekeeping signals consist in sixteen counters, mainly the number of MGO signals acquired by each daisy chain (four counters giving the ratemeter per daisy chain), the total number of acquired MGO (giving the whole SAFEE ratemeters), the "good event" number (counter of the ADC gates), two time counters (12-bits MSB and 12-bit LSB) and eight spare counters, plus sixteen AD590 temperature sensors voltmeters.

The SAFEE TE is also in charge of the electronic calibration pulse generation, performed using a 12-bit DAC unit, a commercial digital pulse generator and a dedicated board. The digital pulse generator can produce bursts of charge pulses (2 kHz frequency and 130 μs duty cycle) and the measurements are generally performed with bursts of $4 \div 5$ pulses each.

The 646-bit XAA1.2 programmation is provided by a specific board based on a MC68 processor, interfaced to the control PC by an RS232 port. The programmation is controlled by a two lines serial bus, composed of a 1 MHz clock and a data line (the register in defined in sec. 3.3). An additional line can be used to retrieve the register out in order to check the chip functionality and to verify that the configuration did not change since the last update.

The DAC AD8842 generating the chip bias voltages and currents are controlled via a six lines low frequency serial bus. This bus is interfaced to the six output lines of a VME parallel port with serial communication protocol fully implemented in software.

3.6.2 The SAFEE Test Equipment software

The primary requirement of the SAFEE TE software is the acquisition of the SAFEE data, the transmission to the DISCoS archiving system and the display of the quicklook results with the smallest delay even possible.

A single event is described by twenty words of 4 bytes each. Since the SuperAGILE expected background is about 700 $\mathrm{cts} \cdot \mathrm{s}^{-1}$, the transient events can produce a rate as high as $5 \cdot 10^4$ $\mathrm{cts} \cdot \mathrm{s}^{-1}$ and the clock frequency of the electronic calibrations will be up to 20 kHz, the acquisition software has to operate with an acquisition rate up to 2 $\mathrm{Mbytes} \cdot \mathrm{s}^{-1}$. To assure the requirement of the high rate acquisition efficiency, the core of the data acquisition system has been developed as a module of the linux kernel, building VME interrupts, building events and putting them in a circular buffer readable from the user space. More details about the system architecture and development can

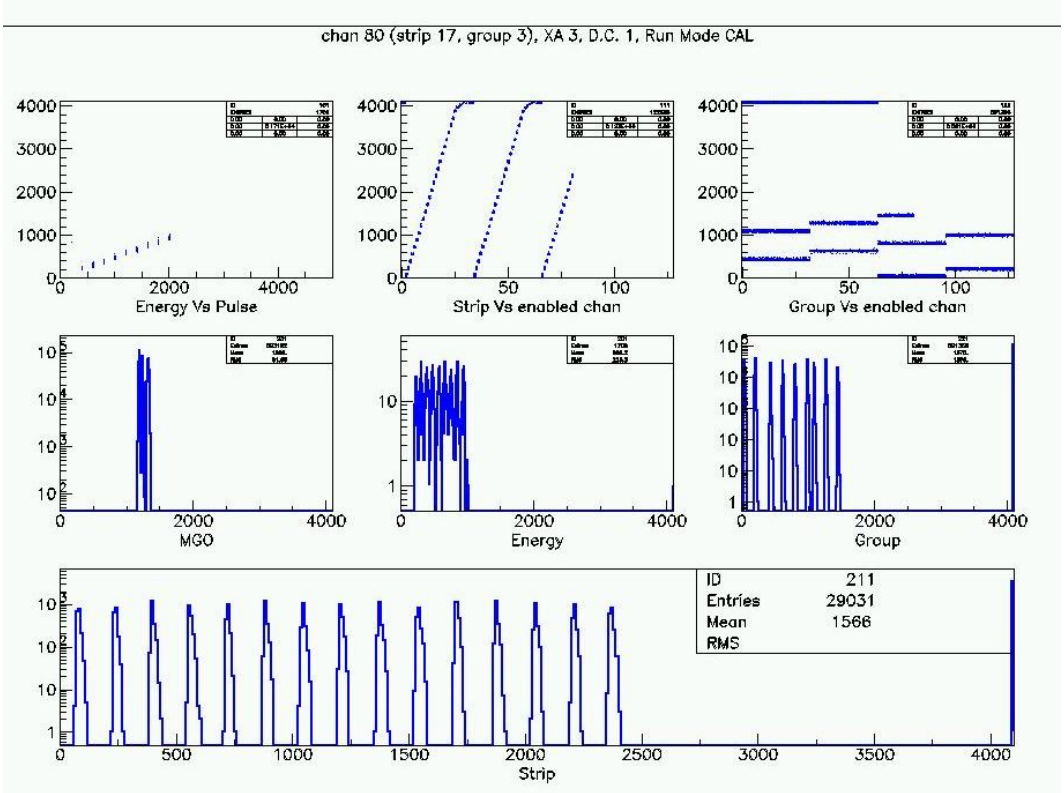

Figure 3.7: Example of the SAFEE TE quicklook screen capture.

be found in Pacciani et al. (2004).

The acquisition software is complemented by a quicklook monitor, developed using CERNLIB and cfortran interface, providing online histograms of scientific data and showing the housekeeping counters. An example of the quicklook screen capture can be seen in fig. 3.7.

3.7 The interface and conditioning electronics

The SuperAGILE Interface Electronics (SAIE) performs the conditioning of the SAFEE output signals and is the interface between the front-end and the data handling electronics (represented by the PDHU, whose tasks involving the SuperAGILE instrument are summarized in sec. 3.8 below). Two SAIE boxes of $30 \times 15 \times 2$ cm^3 dimensions and 2.7 kg mass each are placed on the sides of the Silicon Tracker. A block diagram of the SAIE main tasks is shown in fig. 3.8.

The main tasks of the SAIE are the digital conversion of the SAFEE output signals (by means of a 12-bit ADC), the event timing (based on a 1 MHz clock), the event generation (60 bit each), the control of the SAFEE configuration (biases and digital configuration of the XAA1.2 chips) and electronic calibration (using a voltage pulse

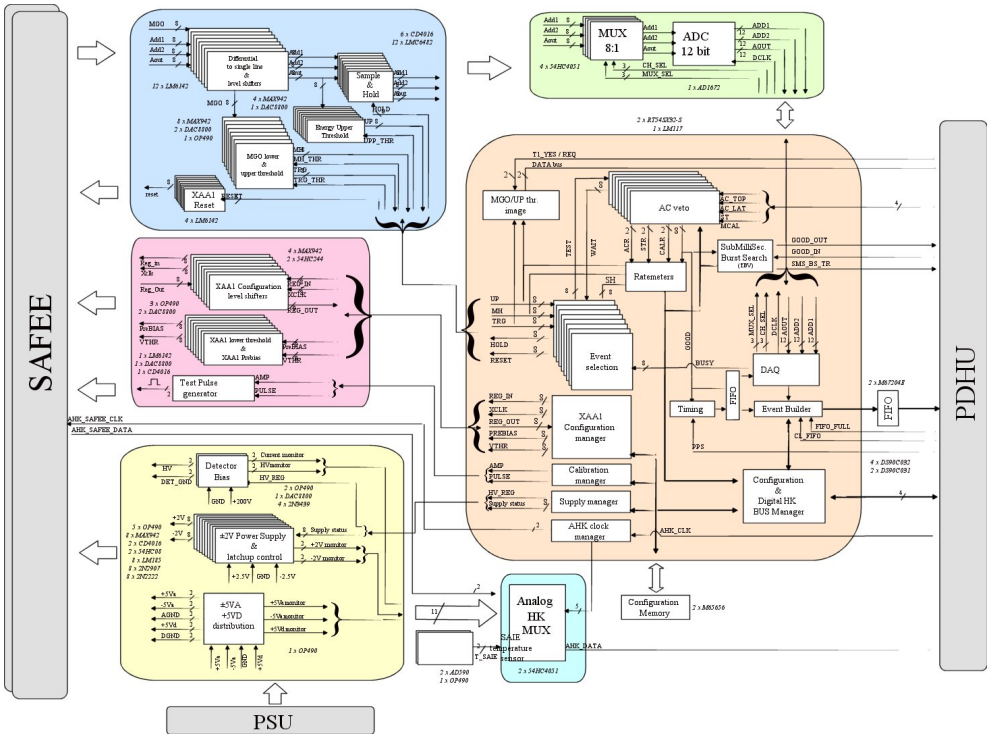

Figure 3.8: Block diagram of the SAIE board.

generator) and finally the generation of the functional ratemeters.

The bidirectional communication between SAIE and PDHU is provided through two dedicated LVDS serial data buses at 5 MHz frequency. A SAIE Test Equipment, also in this case based on a VME bus, has been developed in order to control the SAIE, send commands and receive data from it.

3.8 The PDHU and SuperAGILE

The PDHU is the payload computer and, as described in sec. 2.5, performs on-board data processing tasks aiming to select the events to be sent to the telemetry and to perform specific transient search procedures. Furthermore, the PDHU is in charge of the telemetry transmission of the events detected by the AGILE instruments. The main PDHU tasks are shown in fig. 3.9.

The PDHU is programmed to perform specific tasks involving SuperAGILE data in order to reconstruct the photon position from the address signals, produce on-board SuperAGILE images of the sky if a Gamma Ray Burst trigger is detected by SuperAGILE or the Mini-Calorimeter and finally accumulate images to be sent to the ground station as a backup procedure, for example in case the counting rate exceeds the telemetry quota.

The address reconstruction of the detected photons is performed by means of an ad-

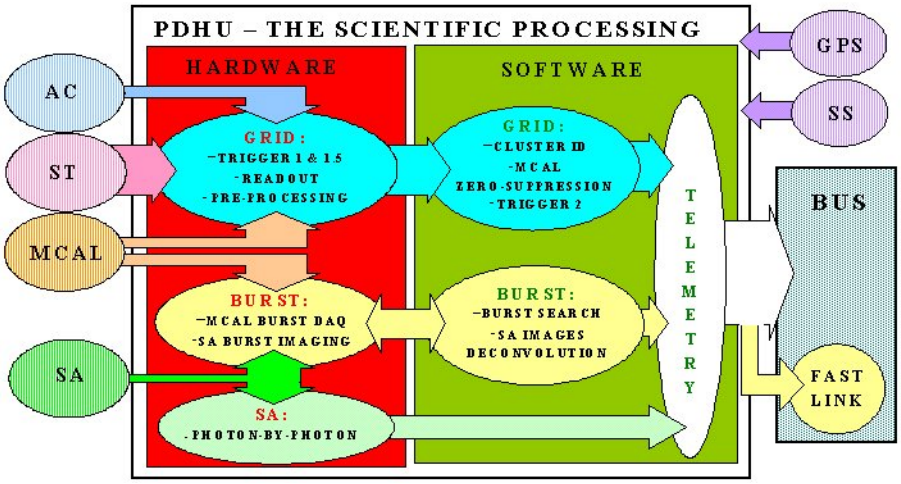

Figure 3.9: Main functions of the PDHU.

dress look-up table (LUT), containing the digitized value of the group and strip address signals of the whole SuperAGILE. Of each channel the strip and group range recorded during the electronic calibration is stored and the photon position is reconstructed comparing its address signals with the ranges stored in the LUT. Up to four such LUT can be stored in the payload memory. Since the address signals show variations depending on the thermal drift on about 10° C scale (as described in sec. 4.4), four of such tables can cover the whole 40° C operative thermal range of the instrument.

Moreover in the PDHU software a specific Gamma Ray Burst search procedure in SuperAGILE data is introduced. The SuperAGILE ratemeters are continuously integrated on time scales from less than 1 ms to about 8 s and, in case a statistically significant intensity increase is found, an image of the Sky is produced. The transient coordinates are extracted directly on-board from the image and are then transmitted to Earth via the ORBCOMM satellite constellation.

The accumulation of detector images is also used as a backup data transmission procedure, for example in case SuperAGILE counting rate is higher than the allocated quota. In this case the accumulated detector images are sent to the telemetry instead of the event by event data.

3.9 The SuperAGILE criticalities

SuperAGILE is an innovative instrument under many points of view. It is the first time that a silicon microstrip detector is used to detect X-rays in a space experiment, the coded mask has one of the smallest pixel size ever manufactured and the front-end ASIC chip is designed in order to achieve a high signal to noise ratio with a small power consumption. In this section a discussion of the most innovative and critical features of SuperAGILE is presented in order to investigate the instrument peculiarities. Since

my research activity concerns most of these topics, of each one a description of my contribution is given with reference to the chapter of this thesis where the work is described.

3.9.1 Thermal stability

As described in sec. 2.3, the SuperAGILE imaging process is a two step task, involving the accumulation of the photon position on the detector and its decoding by means of specific algorithms. As for all the coded mask instruments, the reconstruction accuracy of the sources position in the Sky depends on the accumulation accuracy of the detector image. Of paramount importance in the image accumulation is the address reconstruction because the decoding algorithms are based on the correlation between the photon position and the mask pattern and serious mistakes are made if the photons are assigned to the wrong pixel. For this reason all sources of confusion in the address reconstruction have to be carefully studied and corrected, otherwise the resulting sky image can be confused and the existing X-ray sources cannot be identified.

The identification of the photon position on the detector, the first step of the detector image accumulation, is based on the address signals of each event. The correspondence between the pixel position and the bonded channel address signals is set recording the address output of each channel during the electronic calibrations. Every effect producing variations in the XAA1.2 address signals has to be studied, taken under control and corrected.

A possible reason of change in the address signals of the channels is the temperature variation. Most of the electronic components features change as a function of temperature and similarly the address signals of the channels may change. For this reason I have studied the thermal stability of the address signals by means of electronic calibrations at different temperatures. This work is reported in chapter 4 and specifically in sec. 4.4.

3.9.2 Effects due to the cosmic rays interactions

All the devices in orbit outside the Earth atmosphere are exposed to the cosmic rays flux, composed of high energy charged particles (mostly protons, electrons and ions) crossing the payload materials and producing ionization in them. Particularly sensitive to the cosmic rays ionization are the electronic devices and, most of all, the circuits manufactured with CMOS architecture as the XAA1.2. A wide literature is available about the effects produced by the cosmic rays ionization on the electronic devices, some examples are referenced in sec. 5.2.

While the SAFEE board are manufactured using cosmic rays resistant passive components, the XAA1.2 chip, which is not developed as a radiation hard device, needed to be specifically tested and qualified. The test of the radiation-induced effects on the XAA1.2 chip is part of my research work and includes either the study of the possible effects, the measurement of the ASIC sensitivity to the charged particle interactions performed in a dedicated facility, the evaluation of the radiative environment at the AGILE orbit using dedicated codes and finally the estimation of the expected rates on

orbit. All these topics are described in chapter 5.

3.9.3 Threshold uniformity and signal to noise ratio in the sky images

The coded mask instruments decoding algorithms introduce the so called "coding noise" in the sky image, that depends on the selected reconstruction technique and can be estimated and corrected. All other sources of noise in the sky image depend on the background in the detector image. The background in the detector is produced mainly by the X-ray diffuse background and, in an ideally uniform case, this background is the same in all the detector pixels apart from geometrical factors that can be evaluated and easily removed.

All sources of non uniformity between the pixels in the detector can decrease the signal to noise ratio in the sky image because they can affect the uniformity of the background among the pixels and this noise contribution cannot be corrected after the image reconstruction. For this reason the non uniformity of the pixels must be reduced to the minimum when accumulating the detector images. The most important source of background non uniformity in SuperAGILE instrument is the threshold non uniformity. The measurement of the flight model SAFEE threshold non uniformity is reported in chapter 7 and specifically in sec. 7.4.2.

The effect of the threshold non uniformity on the SuperAGILE imaging is studied in sec. 8.5. In particular the X-ray background is generated with a semi-analytic method and the effect of the threshold non uniformity in the background events accumulated by the detector (detector image) is introduced. The analysis is performed considering three different threshold non uniformity models: a replica of a permutation of the measured values, a simple correction performed by integrating the background only above a fixed energy and the digital equalization of the threshold in the read-out circuit. Then the images of the background are extracted using the SuperAGILE imaging algorithm and the standard deviation is evaluated in order to estimate the effect of each threshold model on the background and consequently on the sources detection. In this way the impact of the electronic performances on the SuperAGILE imaging capability can be estimated.

3.9.4 Dead and hot pixels

Another possible source of confusion in the detector image is the lack of signal in some pixels ("dead pixels") or the abnormally high counting rate in some other pixels ("hot pixels").

Dead pixels can result from manufacturing defects or damages in the detector, resulting in non working strips, or in the front-end electronic circuit, giving channels that do not produce any output signal, or in the wire bondings between microstrips and input channels, in case a wire bonding is broken and the current signal cannot be transmitted. A dead pixel can be also intentionally produced by excluding a pixel with a noise too high.

Hot pixels can result from manufacturing defects or damage in the detector or in

the front-end electronic circuit giving low threshold channels with a resulting high background counting rate. Another possible reason of hot pixels is the low threshold in the front-end input channels.

After decoding the detector image, both dead and hot pixels produce a non uniformity in the sky image baseline, so decreasing the signal to noise ratio and decreasing the statistics significance of the detected sources.

3.9.5 Mechanical assembly and alignment

In coded mask instruments the reconstruction of the sources position is based on the measurement of the angular shift of the photon position on the detector with respect to the on-axis position of the mask pattern. For this reason the angular accuracy depends on the accuracy of position measurements on the detector and on the mutual alignment of coded mask and detector.

In the case of SuperAGILE, the mask pixel size is 242 μm and the detector pixel size is as small as 121 μm. To obtain a good accuracy in the reconstruction of the sources position an alignment accuracy of about half a pixel (60 μm for SuperAGILE) is required.

The alignment of the mask and the detector is guaranteed at 30 μm level and is performed by Contraves, manufacturing also the coded mask and the collimator, using an optical system and mechanical reference targets on the detector and the mask plane. Since this topic is not involved in my research work, I will not investigate it further.

Chapter 4

The XAA1.2 performance measurements

4.1 Introduction

Most of the SuperAGILE criticalities are due to the front-end electronics and mainly to the XAA1.2 chip. As shown in sec. 3.9, the variation of some of the chip performances, for example the address signals, as a function of various environmental parameters, such as the temperature or the power supply, is one of the source of criticalities. Other criticalities are due to the non uniformity of the chip parameters, for example the linearity and the threshold of the analogue chains since, from the electronic point of view, on one side each channel is a different and independent circuit, on the other side the channels share common supplies and common thresholds so a noisy channel can interfere with all the others.

This chapter is devoted to the description of the laboratory tests performed on the XAA1.2 chip in order to measure its performances and study its compliance to the peculiar space conditions before designing the SAFEE boards. This study is complemented by the measurement of the radiation-induced effects and the space qualification of the component, reported in chapter 5.

Since the SuperAGILE front-end electronics contains 48 chips, with 128 input channels each and a total number of 6144 channels, the linearity of the electronic chains, that is a key feature in a read-out circuit, cannot be measured on-orbit using X-ray sources. Moreover the compact geometry would not allow for a uniform irradiation of individual strips. In fact the integration time needed by a complete linearity measurement with X-ray sources would be huge and unaffordable, so the linearity will be measured using the pulse charge generator, described in sec. 3.3, by means of the so called "electronic calibrations". The measurements of the XAA1.2 linearity using the "electronic calibrations" are reported in sec. 4.2, where both results of the XAA1.2 alone and the XAA1.2 bonded to a single tile of 9.5×9.5 cm^2 size and 15 pF $\cdot$ strip^{-1} capacitance, also known as Constructive Technical Model (CTM) are shown.

The uniformity of the electronic chains is an important property of the instrument

affecting also the imaging capability, as explained in sec. 3.9. For this reason in sec. 4.3 the measurements of the linearity and threshold uniformity among the input channels are reported for both the XAA1.2 and the CTM.

On-orbit the planned temperature within the AGILE payload ranges between $-20°$ C and $+40°$ C and the SuperAGILE instrument will be at an estimated temperature of about $30°$ C. The performances of the electronic devices, both active and passive, are expected to vary as a function of temperature. For this reason in sec. 4.4 the measurements of the thermal stability of the address signals, which are the most critical features, are reported. In fact, as discussed in sec. 3.9, the address signals are key parameters to reconstruct the images of the sources in the Sky and all variation of these signals must be measured and corrected.

The payload Power Supply Unit (PSU) provides the supply voltage and current from the spacecraft solar panels to the SAFEE boards via the SAIE boards. Since the power supply voltage value may change on orbit, the functionality and performances of the XAA1.2 have been studied as a function of the voltage and the results are reported in sec. 4.5.

Finally in sec. 4.6 the conclusions of this chapter are given discussing the results of the measurements in the context of the instrument criticalities.

4.2 The XAA1.2 input charge linearity

The measurements of the XAA1.2 linearity are performed using the XA-DAQ board, described in sec. 3.5.1, for both the input charge generation, by using the internal test pulse generator, and the data acquisition. Charge pulses ranging from 0.41 fC, corresponding to about 10 keV following the (3.2), to 5.64 fC, corresponding to about 127 keV, are fed to the chip input channels and the output signals (digitized by the ADC in the acquisition board) are recorded. For each charge amplitude fifty pulses are fed to every input channel to increase the data statistics.

The mean value $\bar{A}_{XA}$ of the digital output signal of the XAA1.2 non connected to the detector, averaged over the 50 pulses and the 128 input channels, is shown as a function of the input charge q in fig. 4.1. The same measurement $\bar{A}_{CTM}$ in case the XAA1.2 is connected to the detector is shown in fig. 4.2. Since 2 channels of the CTM do not work at all, 89 channels over 128 show a noise level much higher than the remaining 37, only data from these last 37 channels are shown in the plot. In both plots the error bars on the amplitude values are the standard deviation over the 128 channels, $\sigma(A_{XA})$ and $\sigma(A_{CTM})$. As can be seen in both plots, the chip is linear for input charge pulses at least up to 120 keV of equivalent energy.

From the data it is now possible to evaluate the uniformity of the system linearity. The uniformity among the input channels of the XAA1.2 linearity curve can be defined as

$$\frac{\sigma(A_{XA})}{\bar{A}_{XA}} = 5\ \% \tag{4.1}$$

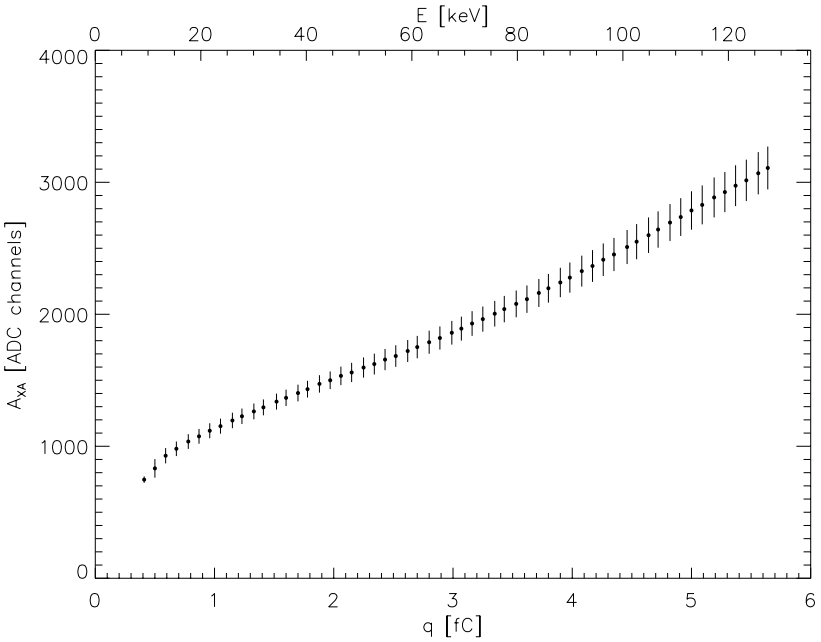

Figure 4.1: Linearity curve of the XAA1.2 chip non bonded to the detector evaluated with charge pulses from 0.41 fC (corresponding to about 10 keV) to 5.64 fC (corresponding to about 127 keV).

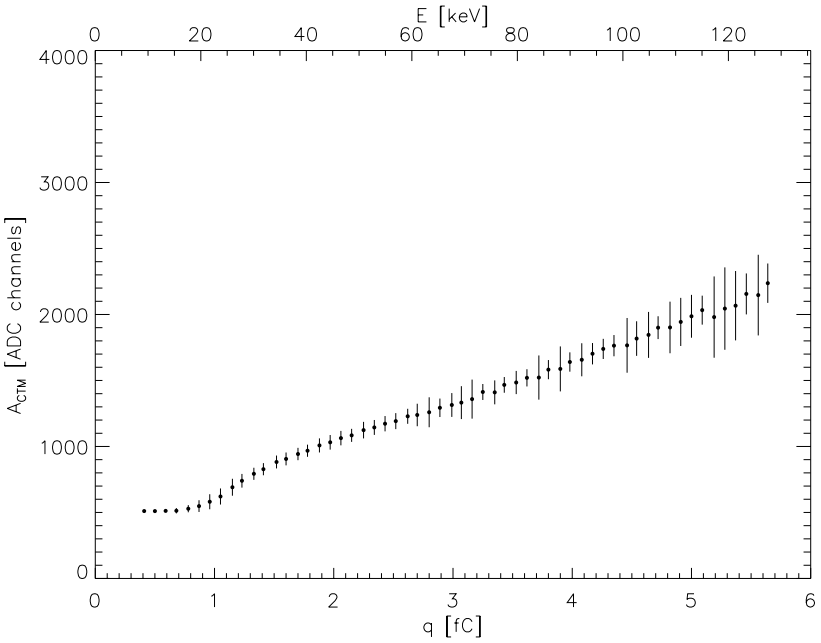

Figure 4.2: Linearity curve of the CTM evaluated with charge pulses from 0.41 fC (corresponding to about 10 keV) to 5.64 fC (corresponding to about 127 keV. Only data from the less noisy 37 channels are shown in the plot.

while the uniformity of the CTM linearity is

$$\frac{\sigma(A_{CTM})}{\bar{A}_{CTM}} = 7\ \% \ . \tag{4.2}$$

When the chip is bonded to the detector the linearity uniformity is lower than in the chip alone condition because of the noise introduced by the detector, increasing the amplitude spread among the channels.

4.3 Gain and threshold uniformity

The XAA1.2 chip is composed of 128 input channels and, from the electronic point of view, each channel is a different and independent circuit. In this section the uniformity among the input channels of the chip main performances, the offset, the gain and the threshold is measured and discussed.

4.3.1 Gain and offset uniformity

From the linearity curves shown in sec. 4.2 above, the gain g and offset f of each input channel can be evaluated applying a linear fit to the output mean amplitude A as a function of the input charge q,

$$A = f + g \cdot q. \tag{4.3}$$

The XAA1.2 offset and gain values are plotted in the lower panels of the fig. 4.3 and 4.4 respectively. The CTM offset and gain values are plotted in the lower panels of the fig. 4.5 and 4.6 respectively.

From the linear fit in the chip alone condition, the offset mean value is $\bar{f}_{XA} = 670.6$ ADC while the offset standard deviation is $\sigma(f_{XA}) = 46.8$ ADC and the gain mean value is $\bar{g}_{XA} = 415.8$ ADC/fC while the gain standard deviation is $\sigma(g_{XA}) = 26.1$ ADC/fC. As a measure of the parameters uniformity the ratios $\sigma(f_{XA})/f_{XA} = 7\ \%$ and $\sigma(g_{XA})/g_{XA} = 6\ \%$ can be considered. The offset and gain histograms are plotted in the upper panels of the fig. 4.3 and 4.4 respectively.

In case the chip is bonded to the detector, the linear fit results are $\bar{f}_{CTM} = 354.1$ ADC, $\sigma(f_{CTM}) = 77.0$ ADC, $\bar{g}_{CTM} = 323.9$ ADC/fC and $\sigma(g_{CTM}) = 41.2$ ADC/fC respectively. Since, as reported in sec. 4.2 above, 2 channels do not work, 89 channels over 128 show a noise level much higher than the remaining 37, only data from these less noisy 37 channels are considered in this analysis. The offset and gain histograms are plotted in the upper panels of the fig. 4.5 and 4.6 respectively. The system gain is lower when the XAA1.2 is bonded to the detector because of the charge subdivision due to the detector capacitance and the gain ratio is $\bar{g}_{CTM}/\bar{g}_{XA} = 0.78$. In this case the parameters uniformity is $\sigma(f_{CTM})/f_{CTM} = 22\ \%$ and $\sigma(g_{CTM})/g_{CTM} = 13\ \%$.

From the offset and the gain values the amplitude uniformity of a 0.88 fC pulse, corresponding to a 20 keV photon energy, can be evaluated. In case of the XAA1.2 alone, the mean amplitude is $\bar{A}_{20,\ XA} = 1036.5$ ADC channels and the standard deviation is

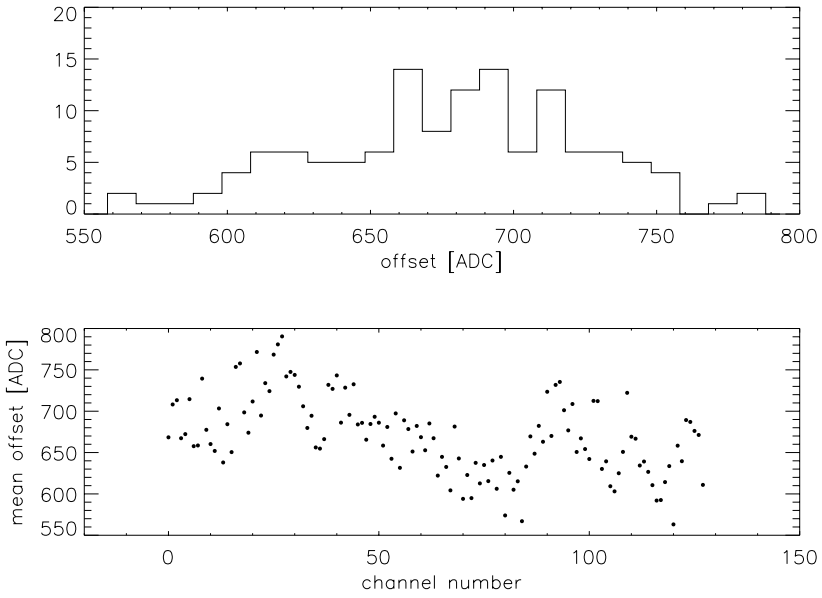

Figure 4.3: Histogram of the XAA1.2 offset (upper panel) and offset value of each input channel (lower panel).

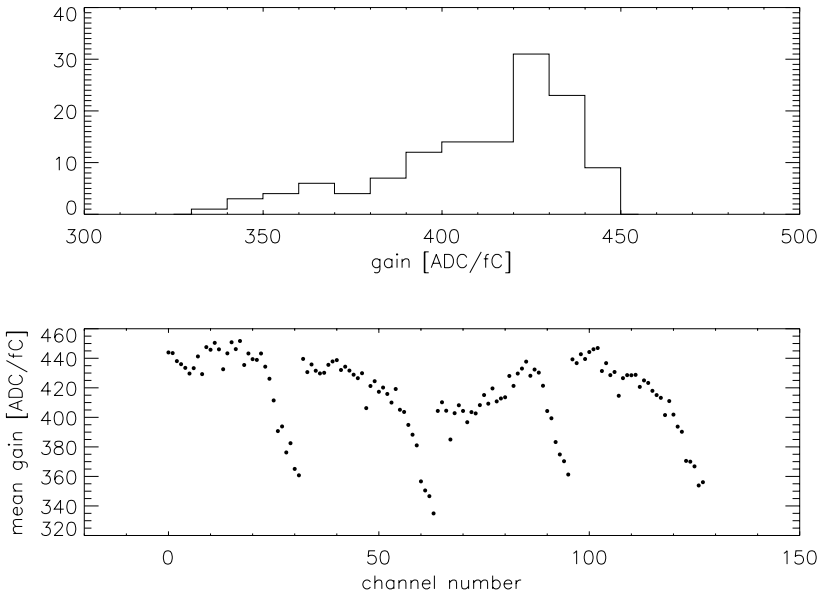

Figure 4.4: Histogram of the XAA1.2 gain (upper panel) and gain value of each input channel (lower panel).

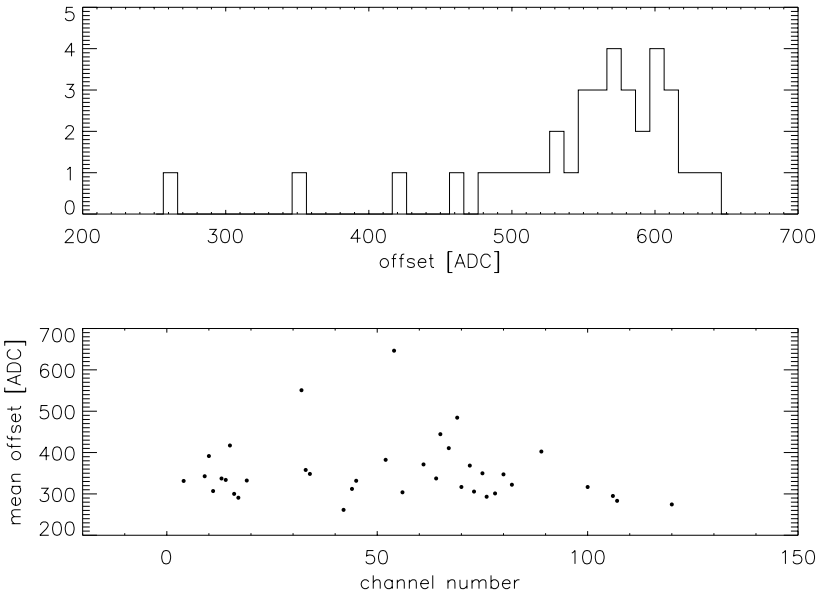

Figure 4.5: Histogram of the CTM offset (upper panel) and offset value of the 37 less noisy input channel (lower panel).

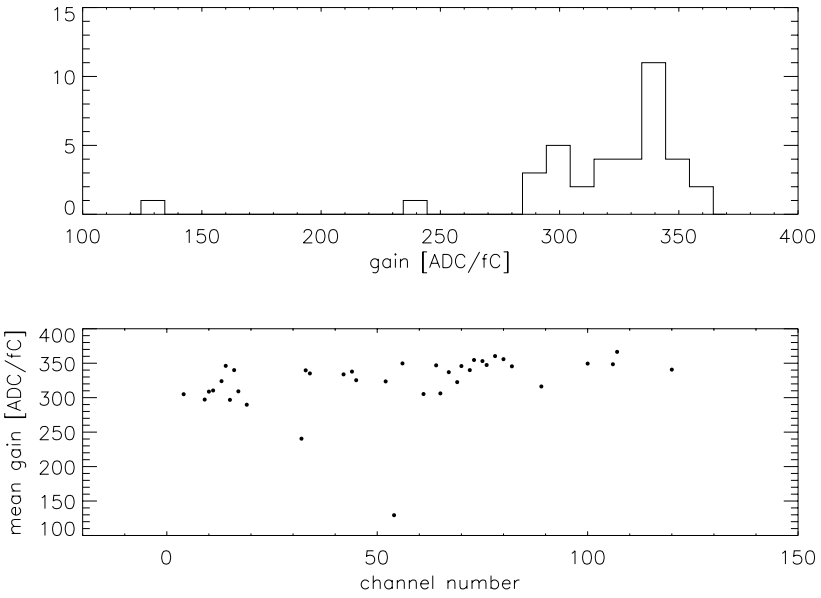

Figure 4.6: Histogram of the CTM gain (upper panel) and gain value of the 37 less noisy input channel (lower panel).

$\sigma(A_{20,\,XA}) = 52.8$ ADC channels. Considering the chip bonded to the detector, the corresponding values are $\bar{A}_{20,\,CTM} = 639.2$ ADC channels and $\sigma(A_{20,\,CTM}) = 52.5$ ADC channels.

As a uniformity measure the ratio between the amplitude standard deviation and the mean amplitude can be considered: $\sigma(A_{20,\,XA})/\bar{A}_{20,\,XA} = 5.1$ % without the detector and $\sigma(A_{20,\,CTM})/\bar{A}_{20,\,CTM} = 8.2$ % in case the chip is bonded to the detector. The 20 keV equivalent energy amplitude histograms are plotted in the upper panels of fig. 4.7 and 4.8 respectively. The amplitude value for each input channel (only the 37 less noisy channels of the CTM) is plotted in the lower panel of the same plot.

4.3.2 Threshold uniformity

As specified in sec. 3.3, the threshold is set to the XAA1.2 chip using a 8-bit DAC, that gives the same reference value V_{ref} to all the input channels. The reference voltage value is selected considering the counting rate of the events due to the electronic noise. The lower the reference value the higher the electronic noise counting rate. For example, considering the XAA1.2 chip not connected to the detector, the mean counting rate of the electronic noise events is 160 cts $\cdot$ s^{-1} $\cdot$ strip^{-1} if $V_{ref} = -7.9$ mV, clearly a saturated value, and decreases down to 0.003 cts $\cdot$ s^{-1} $\cdot$ strip^{-1} in a single DAC step variation when $V_{ref} = -4.6$ mV.

The reference value can be converted from voltage into charge and then into energy by means of a threshold scan, explained in section 3.5.1, and a set of background acquisitions. In the threshold scan the characteristic curve of the discriminator in each channel is evaluated in term of a linear fit

$$V_{ref} = a + b \cdot q \; . \tag{4.4}$$

By means of a linear interpolation of the counting rate at different reference voltage values, the V_{thr} voltage is evaluated such that the electronic noise increases the background counting rate of 0.01 cts $\cdot$ s^{-1} $\cdot$ strip^{-1}, that is 10 % of the SuperAGILE background on-orbit. Lowering the threshold produces an increase in the background counting rate due to both the electronic noise and the environmental background. Since the electronic noise is catastrophic and its counting rate is more than two orders of magnitude above the environmental background, this last contribution can be neglected when measuring the threshold.

The interpolated voltage threshold V_{thr} is then converted into the charge threshold value q_{thr} applying the linear fit parameters in (4.4) and finally into the energy threshold value E_{thr} using the (3.2).

From the linear fit in (4.4), the XAA1.2 parameters mean values are $\bar{a} = -19.3$ mV and $\bar{b} = 39.3$ mV/fC while the parameters standard deviation values are $\sigma(a) = 1.6$ mV and $\sigma(b) = 0.9$ mV/fC. The linear fit in (4.4) is directly performed by the acquisition board software and the fit parameters are provided without any error. The a and b histograms are plotted in the upper panels of the fig. 4.9 and 4.10 respectively while the parameter values for each input channel are in the lower parameters of the same figures.

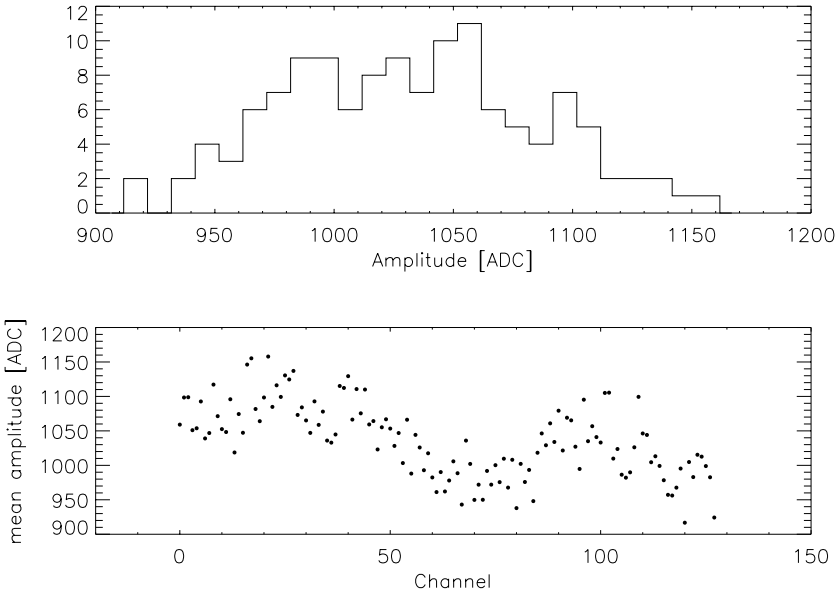

Figure 4.7: Histogram of the 0.88 fC output amplitude (corresponding to 20 keV energy) acquired with the XAA1.2 alone (upper panel) and output amplitude value of each input channel (lower panel).

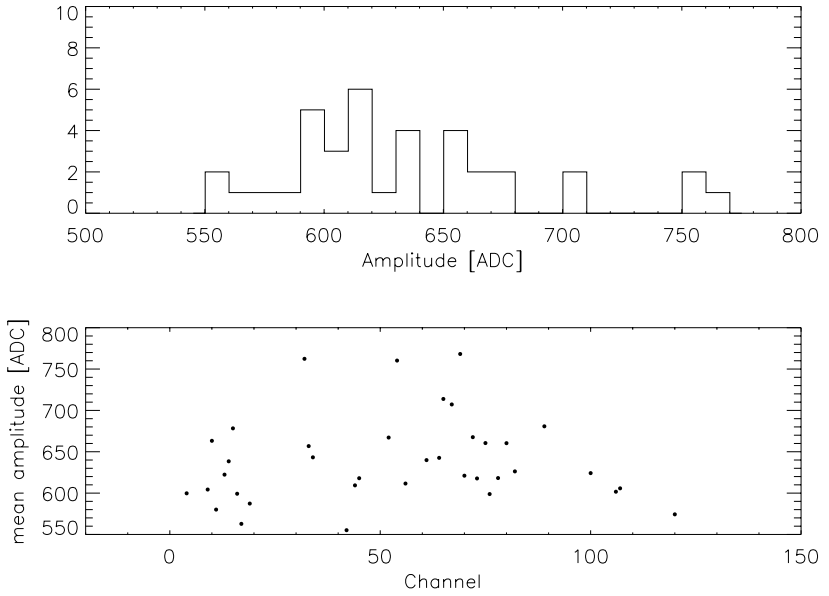

Figure 4.8: Histogram of the 0.88 fC output amplitude (corresponding to 20 keV energy) acquired with the CTM (upper panel) and output amplitude value of the 37 less noisy input channel (lower panel).

In case the XAA1.2 is bonded to the 9.5×9.5 cm^2 size, 410 μm thickness and 15 pF $\cdot$ strip^{-1} capacitance detector, the parameters are $\bar{a} = -20.5$ mV and $\bar{b} = 30.1$ mV/fC while the parameters standard deviation values are $\sigma(a) = 2.6$ mV and $\sigma(b) = 2.6$ mV/fC. In this case the a and b histograms are plotted in the upper panels of the fig. 4.11 and 4.12 respectively while the parameter values for each input channel are in the lower panels of the same figures.

Inverting the linear fit in (4.4) the threshold charge q_{thr} can be obtained as a function of the voltage threshold V_{thr},

$$q_{thr} = c + d \cdot V_{thr} \tag{4.5}$$

where $c = -a/b$ and $d = 1/b$. The XAA1.2 mean parameter values in (4.5) are $\bar{c} = 0.49$ fC and $\bar{d} = 2.5 \cdot 10^{-2}$ fC/mV. The CTM mean parameter values are $\bar{c} = 0.68$ fC and $\bar{d} = 3.3 \cdot 10^{-2}$ fC/mV.

Considering the relation (3.2) between charge and energy, the law connecting the threshold energy E_{thr} and the reference voltage V_{thr} can be finally written,

$$E_{thr} = f + g \cdot V_{thr} \tag{4.6}$$

and the mean parameters are $\bar{f} = 11.1$ keV and $\bar{g} = 0.575$ keV/mV for the XAA1.2 alone and $\bar{f} = 15.4$ keV and $\bar{g} = 0.757$ keV/mV for the CTM.

Basing on MonteCarlo simulations, the expected counting rate of the SuperAGILE background on-orbit, mainly due to the diffuse X-ray background, is about 0.1 cts $\cdot$ s^{-1} $\cdot$ strip^{-1}. For this reason, as threshold the reference voltage value that increases of 0.01 cts $\cdot$ s^{-1} $\cdot$ strip^{-1} (10 % of SuperAGILE background) the limiting background value is selected.

Considering for the XAA1.2 chip the threshold voltage $V_{thr} = -4.6$ mV, that gives about 0.003 cts $\cdot$ s^{-1} $\cdot$ strip^{-1}, the energy threshold can be evaluated from the (4.6) and is $\bar{E}_{thr} = 8.5$ keV and its standard deviation among the input channels is $\sigma(E_{thr}) = 0.9$ keV. The corresponding threshold uniformity is $\sigma(E_{thr})/\bar{E}_{thr} = 11$ %. In the upper panel of fig. 4.13) the energy histogram is shown while in the lower panel the value for each input channel is shown.

Interpolating with the same procedure the background counting rate of the CTM as a function of the threshold voltage, $V_{thr} = 4.9$ mV is found and the corresponding energy threshold is $\bar{E}_{thr} = 19.1$ keV with spread $\sigma(E_{thr}) = 1.2$ keV. The corresponding threshold uniformity is $\sigma(E_{thr})/\bar{E}_{thr} = 6$ %. In the upper panel of fig. 4.14 the energy histogram is shown while in the lower panel the value of the different channels is shown. As for the CTM linearity, this analysis is performed only on the 37 less noisy channels.

The mean value of the energy thresholds of both the XAA1.2 and the CTM are rather high compared with the required scientific performances of SuperAGILE (shown in sec. 2.3.3) and need to be reduced. The main explanation of these threshold values is that most of the background is due to the electronic noise introduced by the XA-DAQ acquisition board and moreover the system is not optimized in order to reduce the noise. However the measurements reported in this section aim only to evaluate the threshold

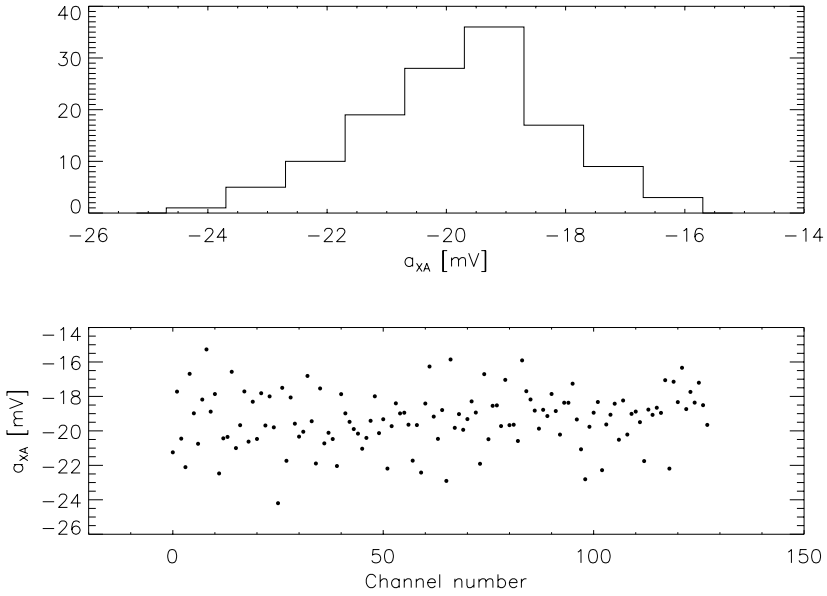

Figure 4.9: Histogram of the intercept a in the XAA1.2 threshold scan (upper panel) and intercept value of each input channel (lower panel).

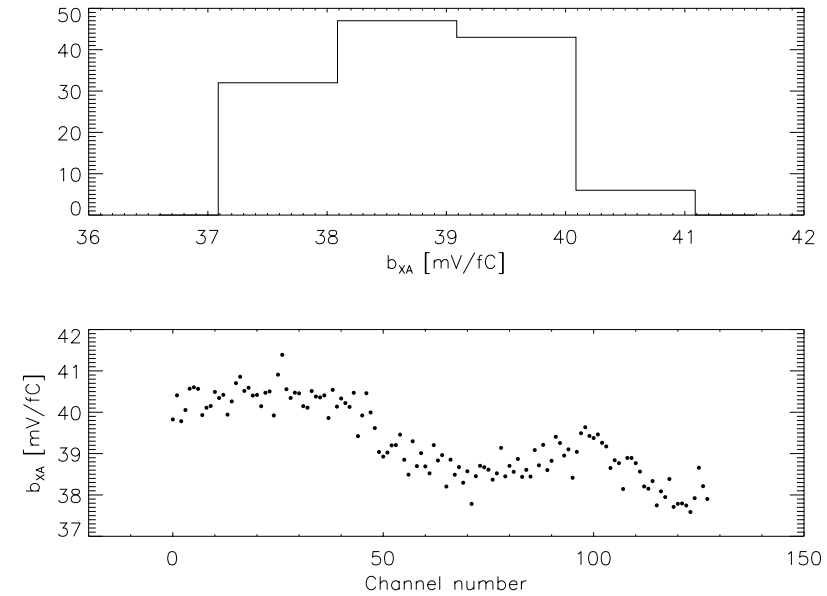

Figure 4.10: Histogram of the slope b in the XAA1.2 threshold scan (upper panel) and intercept value of each input channel (lower panel).

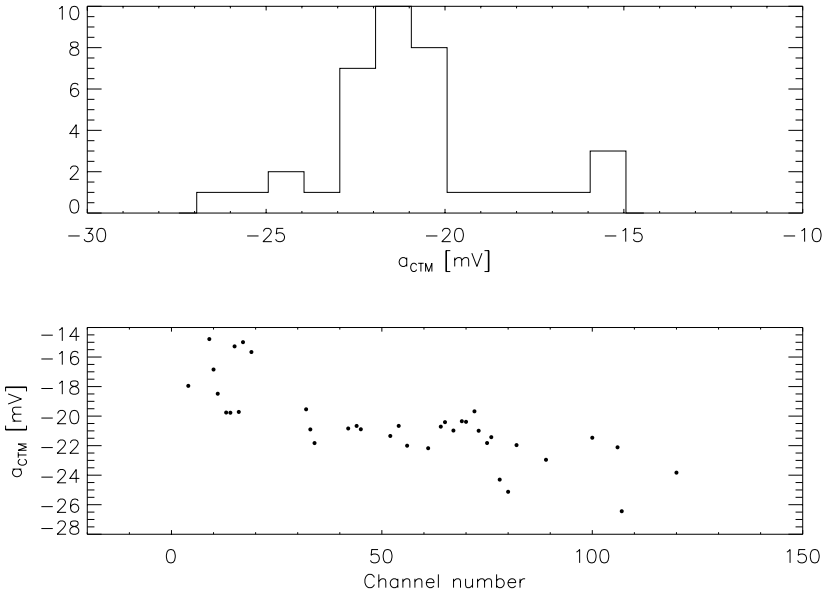

Figure 4.11: Histogram of the intercept a in the CTM threshold scan (upper panel) and intercept value of the 37 less noisy input channels (lower panel).

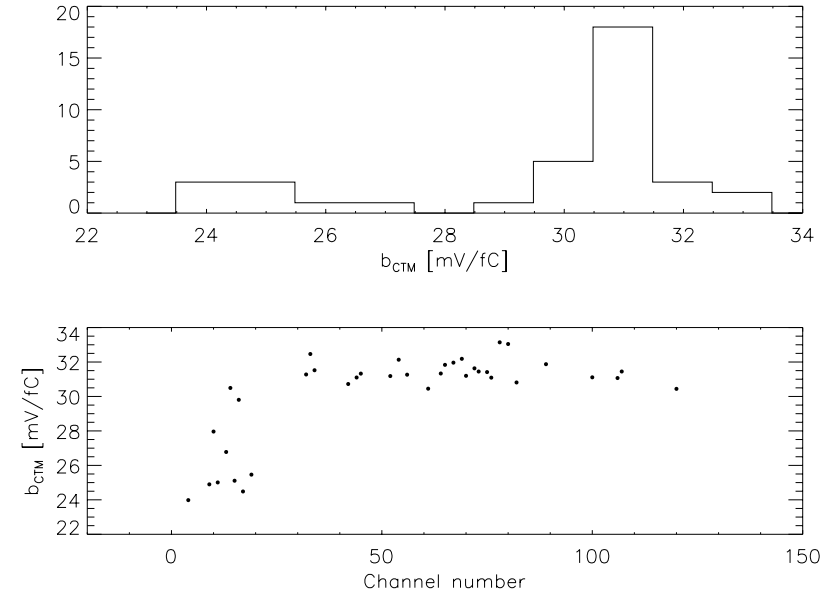

Figure 4.12: Histogram of the slope b in the CTM threshold scan (upper panel) and slope value of the 37 less noisy input channels (lower panel).

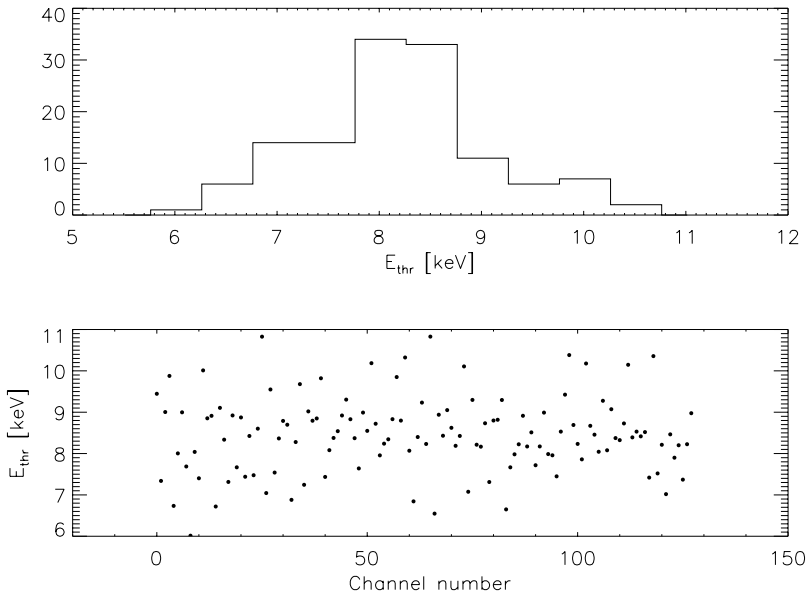

Figure 4.13: Histogram of the XAA1.2 energy threshold (upper panel) and energy threshold value of the input channels (lower panel). The energy threshold is evaluated basing on the threshold scan and the background counting rate.

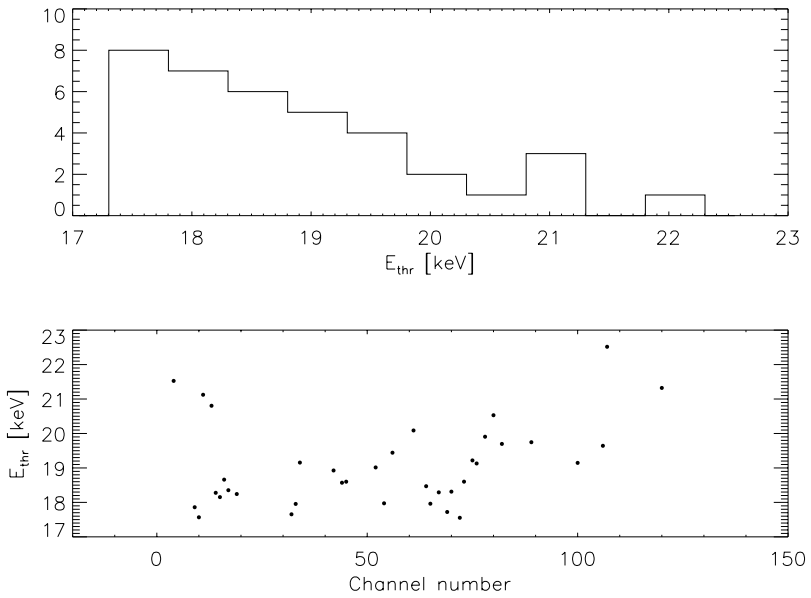

Figure 4.14: Histogram of the CTM energy threshold (upper panel) and energy threshold value of the input channels (lower panel). The energy threshold is evaluated basing on the threshold scan and the background counting rate.

uniformity and the noise is reduced in designing the SAFEE boards. The measurements of the SAFEE energy threshold are reported in sec. 7.2 and 7.4.

4.4 Thermal stability of the address signals

From thermal model evaluations, the maximum variation range of the internal temperature in the AGILE payload on orbit is between $-20°$ C and $+40°$ C, although the temperature variation during the AGILE observations ranges between $0°$ C and $+30°$ C. From the same thermal models SuperAGILE will be probably at about $+30°$ C because the heat dissipated by the Silicon Tracker electronic is conducted by the main frame up to the SuperAGILE stage. Moreover, due to the power dissipation, in vacuum the temperature of the XAA1.2 is about $10°$ C higher than the environment, as measured with an infrared thermometer in a thermo-vacuum facility.

The performances of most electronic devices, both active and passive, show variations as a function of temperature. For this reason in a space instruments components with extended range of functionality (typically from $-55°$ C up to $+85°$ C) are selected. Since the XAA1.2 is not developed as a component for space applications, its thermal stability has to be measured. Particularly the thermal stability of the address signals, needed to reconstruct the position of the detected photons, is studied. In fact, as discussed in sec. 3.9, a wrong reconstruction of the photon position produces a detector image without correlation with the position of the Sky sources, so resulting in a completely incomprehensible and useless sky image.

As specified in sec. 3.3, the XAA1.2 encodes the number of triggering channel with two signals: group (MSB, 2 bit plus 4 offset bit to connect up to 16 chips in daisy chain) and strip (LSB, 5 bit). For this purpose the 128 channels are subdivided in four groups of 32 channels each. The group signal indicates in which subdivision the triggering channel is found and the strip indicates which one is among the 32 channels. Both strip and group are provided as analogue differential currents, are converted into voltage signals in the I/V converters and are then digitized by the ADC.

The thermal stability of the XAA1.2 address signals is measured between $-20°$ C and $+40°$ C (the AGILE non operative temperature range) inserting the XAA1.2 PCB in a thermal chamber. Inside the thermal chamber (BM model TH125) temperatures between $-70°$ C and $+180°$ C can be set. The temperature is measured with a thermocouple[1], sensitive in the range $-70°$ C $\div$ $175°$ C and fixed on the XAA1.2 PCB at a distance of about 5 cm from the chip. The XAA1.2 is interfaced to the XA-DAQ acquisition board, located outside the thermal chamber, and the measurements are performed by means of the electronic calibration, recording the address signals of each channel.

Because of the power dissipation, in vacuum the temperature of the XAA1.2 is about $10°$ C higher than the environment, as measured with an infrared thermometer in a thermo-vacuum facility. Since on orbit the temperature is measured using 32 AD590 thermometers (located on the SAFEE and SAIE PCB, on the detector tray, on the collimator walls and on the coded mask plate) and the actual temperature of the XAA1.2

[1] Omega SA1-T, with copper-constantan sensor and teflon insulator

chip cannot be measured, the thermal stability of the address signals is measured as a function of the environment temperature.

The superposition of group signals in the range -20° C $\div$ 40° C is shown in fig. 4.15. As can be seen in the plot, a temperature variation of about 10° C produces a group signal shift of about 50 ADC channels. A temperature variation of about 50° C produces a superposition in the group signals of two consecutive groups, that can cause the wrong reconstruction of the triggering channel.

A similar shift as a function of temperature can be seen in the strip signal. A plot of the strip digitized signal of the first group (first 32 channels) is shown in fig. 4.16. As can be seen in the plot, the strip variation with temperature depends on the channel under test, being negligible between channel 10 and 20 and important under channel 5 and above channel 25. Particularly, under channel 5 a shift of one channel is seen with a temperature variation of about 60° C while above channel 25 the same shift is produced by a temperature variation of $10 \div 20^\circ$ C.

Considering the most conservative results, significant shifts in the address signals can be seen depending on temperature variations on the scale of 10° C.

As outlined in sec. 3.8, the address reconstruction is performed by the PDHU by means of an address LUT. Since significant address shifts are seen with a temperature variation of about 10° C and up to four of such LUT can be stored in the payload memory, a LUT covers a temperature variation of 10° C. In this way a SuperAGILE temperature variation range up to 40° C can be compensated without uploading different LUT from the ground station, that is a time consuming operation and can introduce substantial delays from the diagnosis of the problem to the corrective action because of the expected operating hours of the AGILE ground station (eight hours a day on five days a week).

4.5 Supply voltage stability

In the SAFEE design the supply voltages V_{SS} and V_{DD} are provided by the flight model Power Supply Units (PSU) via the SuperAGILE Interface Electronics (SAIE) boards. Generally the variability range of the integrated circuits supply voltage is small around the nominal values and the chip performances are expected to show a dependence on the supply voltage. In order to fix the requirements on the stability of the PSU in providing V_{DD} and V_{SS}, I studied the XAA1.2 functionality and performance as a function of the supply voltage. In these measurements I evaluated the XAA1.2 performances by means of the electronic calibrations.

In the XA-DAQ and SAFEE circuits the biases to the XAA1.2 chip are set using Digital to Analog Converters (DAC) components and the V_{DD} and V_{SS} voltages are used as the reference values of these DAC units. If the supply voltage changes, the biases also change because of the reference voltage variation.

In the measurements the XAA1.2 performance variations are measured as a function of the supply voltage with equal absolute value of V_{DD} and V_{SS}. As described in sec. 3.2, in the SAFEE boards only seven XAA1.2 biases out of eleven can be adjusted

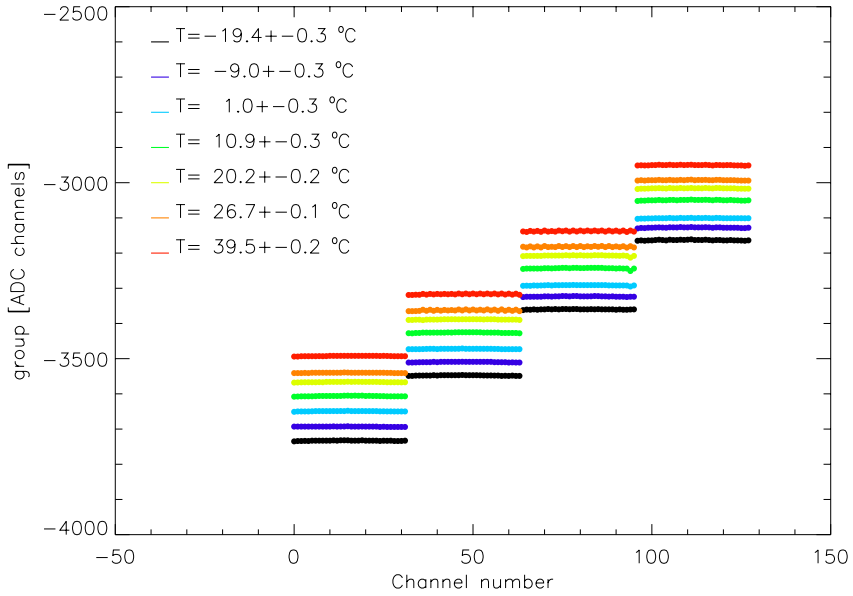

Figure 4.15: Superposition of group signals at different temperatures between −20° C and +40° C.

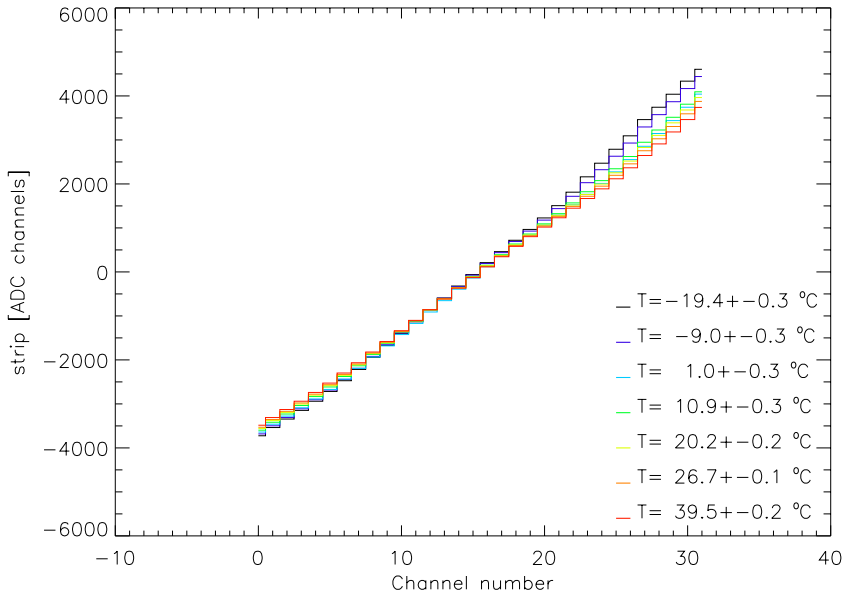

Figure 4.16: Superposition of strip signals in the first group at different temperatures between −20° C and +40° C.

Table 4.1: XAA1.2 bias values fixed during the test

bias name	bias voltage [mV]	bias current [μA]
prebias	-904.1	44.2
shabias	-541.8	21.1
Vfs	501.5	0.3
Vfp	-4.1	0.2

(the currents *prebias*, *shabias*, *TrigDelbias*, *TrigWbias* and *ResWbias* and the voltages *Vfs* and *Vfp*). Unfortunately, among these tunable biases only *prebias*, *Vfs*, *Vfp* and *shabias* can be adjusted using the XA-DAQ while *ResWbias*, *TrigWbias* and *TrigDelbias* cannot. For this reason, in the measurements the XAA1.2 conditions on-orbit, where a bias adjustment can compensate a voltage variation, are reproduced by fixing the *prebias*, *Vfs*, *Vfp* and *shabias* (using the XA-DAQ DAC adjustment units) to the values shown in tab. 4.1.

The XAA1.2 functionality is tested measuring the supply currents I_{DD} and I_{SS} (shown in fig. 4.17) and the power consumption (in fig. 4.18) as a function of the supply voltage. Among the XAA1.2 performances, the stability of the linearity is studied from a superposition of the electronic calibration results (plotted in fig. 4.19) with a particular stress on the output amplitude corresponding to a 20 keV equivalent charge (shown in fig. 4.21). The offset and the gain are evaluated from the electronic calibration linear fit and shown in fig. 4.20. Finally, the group and strip address signals are studied and plotted in fig. 4.22 and 4.23 respectively.

In the results the variation of the measured quantities with respect to the nominal 2000 mV supply voltage value is stressed. Among the supply currents, the I_{DD} variations are -19 % at 1950 mV and $+43$ % at 2050 mV and the I_{SS} variations are -20 % at 1950 mV and $+13$ % at 2050 mV, as shown in fig. 4.17. Consequently the power consumption variation is -22 % at 1950 mV and $+27$ % at 2050 mV, as shown in fig. 4.18. Such a power consumption increase at 2050 mV is critical in the overall power budget of the AGILE payload.

As can be seen in fig. 4.19, the linearity curves show a saturation at 1900 mV (if $q \geq 1.5$ fC), at 1920 mV (if $q \geq 2.5$ fC) and at 1950 mV (if $q \geq 4$ fC) and a slope variation at 2050 mV (if 1.5 fC $\leq q \leq$ 2.5 fC). At the other voltage values no saturations are found but the dynamic range is smallest at 1980 mV and greatest at 2020 mV. All the output amplitude values corresponding to a 0.88 fC input charge (20 keV equivalent energy) are consistent within the errors in the voltage range from 1900 mV to 2050 mV, as shown in fig. 4.21. Furthermore, as can be seen in fig. 4.20, the offset and gain values are scattered without showing a definite slope.

As can be seen in fig. 4.18 and 4.20, in the range 1980 mV $\leq V_{DD} \leq$ 2020 mV the variation of power consumption, gain and offset is approximately linear as a function of the supply voltage. Applying a linear fit to the data in this range, the resulting variations are $(1.9 \pm 0.3) \cdot 10^{-3}$ mW $\cdot$ ch$^{-1} \cdot$ mV^{-1} for the power consumption, 3.2 ± 1.2 ADC $\cdot$ mV^{-1} for the offset and -4.0 ± 0.6 ADC $\cdot$ fC$^{-1} \cdot$ mV^{-1} for the gain.

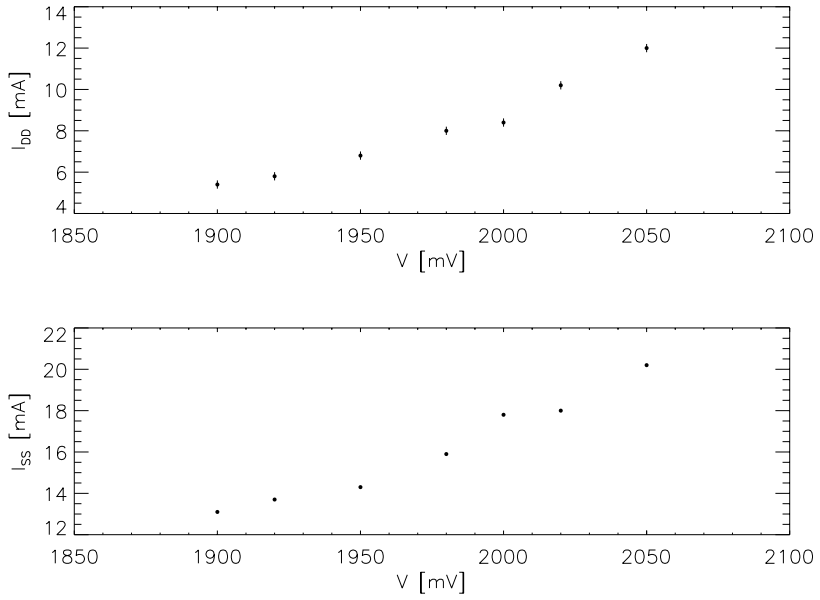

Figure 4.17: Supply currents I_{DD} (upper panel) and I_{SS} (lower panel) at different supply voltage values.

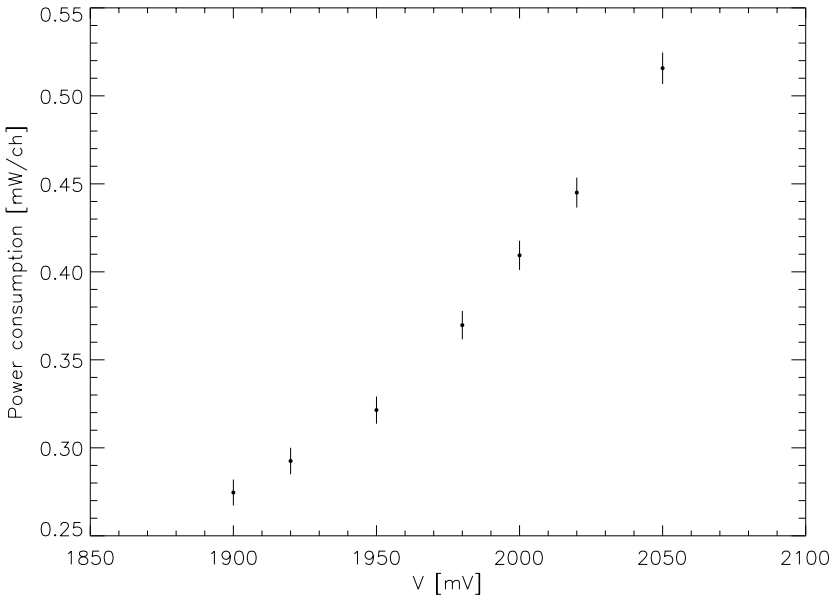

Figure 4.18: Power consumption at different supply voltage values

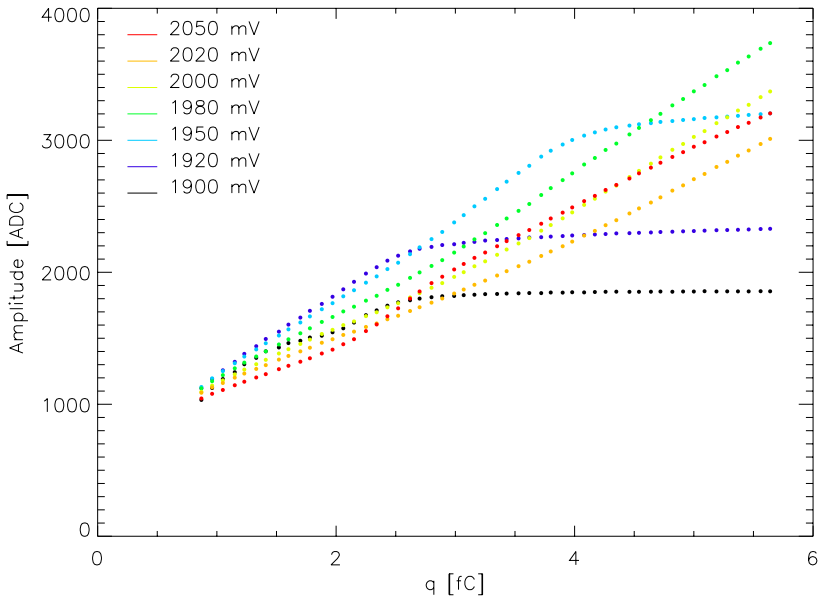

Figure 4.19: Superposition of linearity curves at different supply voltage values.

Both the address signals group and strip show variations depending on the supply voltage. The group signal (as in fig. 4.22) shows significant shifts on the scale of a 20 mV variation and, particularly, a group superposition is seen if the supply voltage changes of about 50 mV. A superposition of the strip signal in the first group is shown in fig. 4.23. As can be seen in the plot, the strip variation with supply voltage depends on the affected channel, being negligible between channel 10 and 20 and important under channel 5 and above channel 25. In this last case, as in the plot, a superposition in two consecutive channels can be seen if the supply voltage changes of about 50 mV.

4.6 Conclusions

In this chapter all the measurements performed on the XAA1.2 chip in order to study the uniformity level of its performances and its sensitivity to some of the peculiar features of the space environment are reported.

The results of the electronic calibrations show that the XAA1.2 chip is linear up to about 120 keV of equivalent energy signals. The uniformity of the output amplitude in the linearity curves is 5 % for the chip alone and 7 % for the XAA1.2 bonded to a 15 $\mathrm{pF} \cdot \mathrm{strip}^{-1}$ capacitance detector (CTM).

The offset and gain can be evaluated from the linear fit of the calibration curves. The offset uniformity is 7 % for the XAA1.2 alone and 22 % for the CTM and the gain uniformity is 6 % and 13 % respectively.

If considering as a threshold counting rate the limit background increased by 10 %

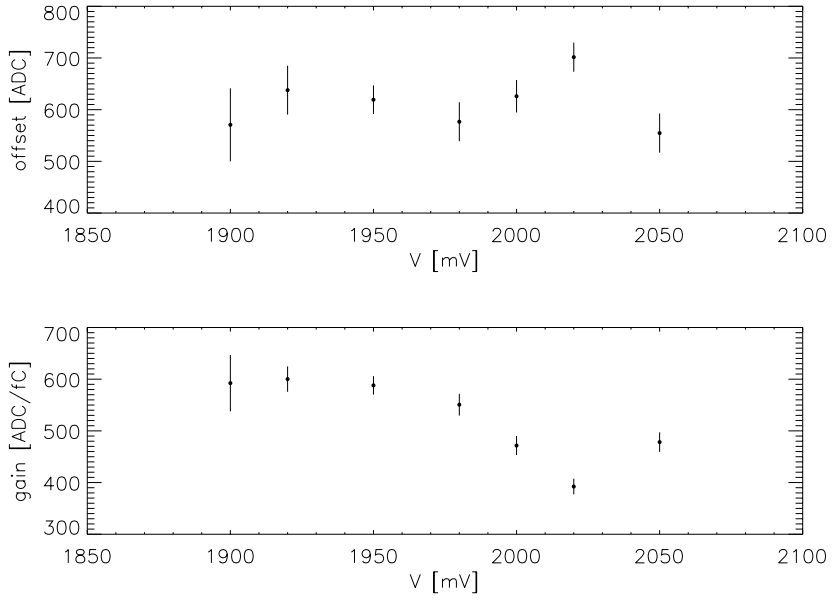

Figure 4.20: Offset (upper panel) and gain (lower panel) at different supply voltage values.

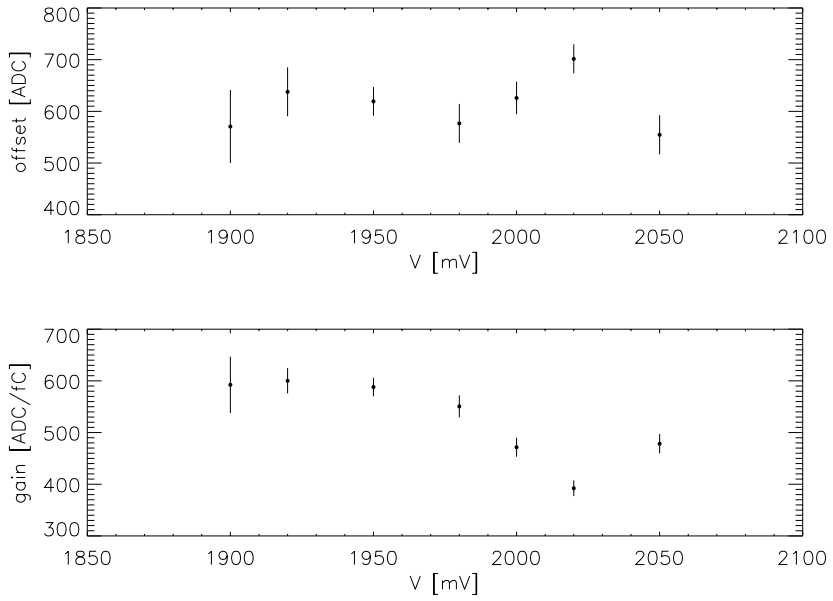

Figure 4.21: Output amplitude corresponding to a 0.88 fC test charge (equivalent to 20 keV) at different supply voltage values.

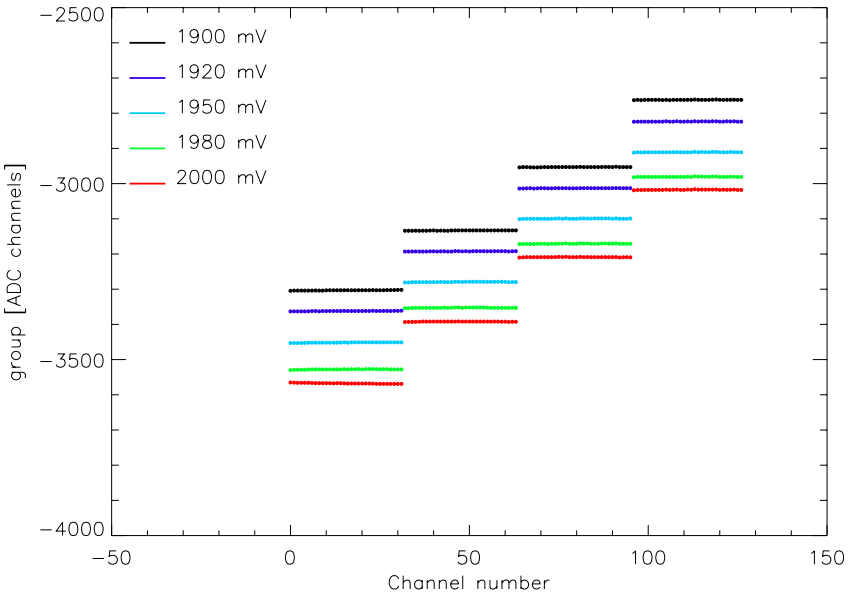

Figure 4.22: Superposition of the group signal at different voltage values.

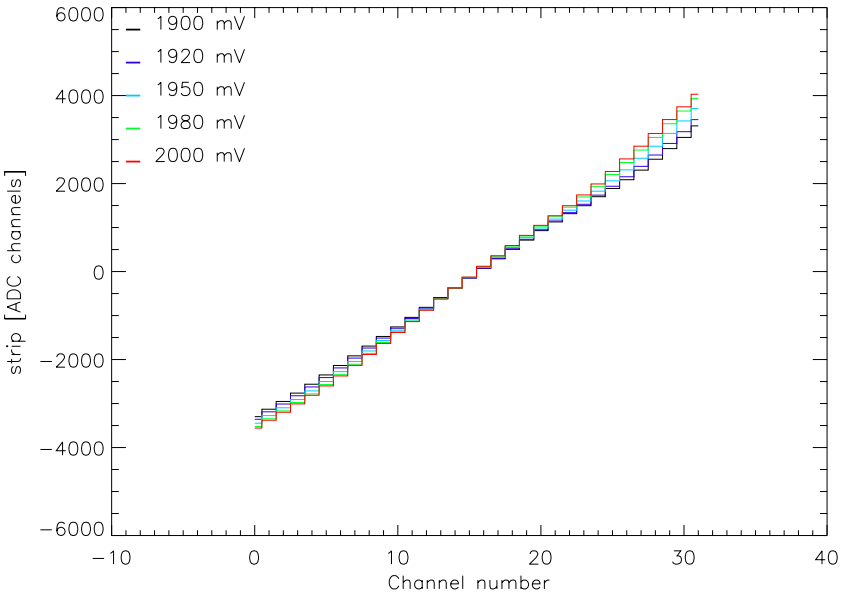

Figure 4.23: Superposition of the strip signal in the first group at different voltage values.

of SuperAGILE counting rate on orbit (0.1 cts $\cdot$ s^{-1} $\cdot$ strip^{-1}), 8.5 keV and 19.1 keV threshold values are found for the XAA1.2 alone and the CTM respectively. The uniformity of the measured threshold values is 11 % and 6 % respectively. Only 37 low noise channels can be considered in the analysis of the CTM measurements.

When the chip is bonded to the detector the linearity uniformity is lower than in the chip alone condition because of the noise introduced by the detector, increasing the amplitude spread among the channels. In the same way the detector noise affects also the spread of the gain and offset, evaluated from the linear fit of the output amplitude as a function of the input charge.

The XAA1.2 can be safely operated in a temperature range between -20° C and $+40^\circ$ C. In the measurements significant address shifts are seen with a temperature variation of about 10° C. Since four address conversion tables can be stored in the payload memory, a temperature variation range up to 40° C can be compensated without uploading different tables from the ground station, that is a time consuming operation and, due to the planned operating hours of the AGILE ground station (eight hours a day on five days a week), can introduce substantial delays from the diagnosis of the problem to the corrective action.

The XAA1.2 chip can be supplied without damage in the voltage range between 1900 mV and 2050 mV. The I_{DD} and I_{SS} supply currents, the power consumption, the offset and the gain (evaluated from the calibration curve linear fit) show significant variations as a function of the supply voltage while the output amplitude corresponding to a 0.88 fC input pulse does not show significant variations. Particularly, both address signals show significant shifts and a possible superposition corresponding to a 50 mV voltage variation. Such a voltage variation produces also a power consumption variation of the order $20 \div 30$ %.

To keep the gain variation below 1 % a maximum voltage variation of 2 mV can be tolerated. Such a stability keeps the power consumption variation under 3 % and prevents also the address shifts because of the supply variations.

Chapter 5

The XAA1.2 resistance to the cosmic rays interaction

5.1 Introduction

The selection of the electronic devices to be mounted on a satellite-borne experiment is a difficult and crucial task. In fact all the experiment components are exposed to the space environment peculiar conditions, mainly cosmic ray flux, temperature variations, high amplitude and peculiar frequency spectrum vibrations during the launch, and they cannot be substituted after the launch in case of damage. Considering also the tight mass and dimensions constraints that affect a space instrument, the average cost[1] to launch one kilogram is about $ 10000, it can be easily understood that all the electronic devices have to be carefully selected and tested.

Some of the electronic components are manufactured with "space qualified" properties, consisting in extended temperature range and high charged particles flux tolerance as the result of design and process improvements. An example is the MIL-STD-883 standard that establishes uniform methods, controls, and procedures for testing microelectronic devices suitable for use within Military and Aerospace electronic systems.

Generally "space qualified" components are selected to produce the electronic boards to be flown on satellite-borne experiments and all the devices without these properties must be tested to verify their compliance to the space environment. In this last case the so called "commercial-off-the-shelf" (COTS) components can be grouped (see Underwood and Oldfield (2000) for example), that are non MIL-STD-883 devices whose properties are specifically tested to verify their compliance to the space environment.

All SuperAGILE electronic components are selected with "space qualified" certification apart from the front-end electronic chips XAA1.2, that are custom devices and are not designed as radiation hard components, and the DAC AD8842. To study the resistance of the XAA1.2 chip to the cosmic rays interaction a sample consisting in three of them has been exposed to a heavy ion irradiation. The test has been performed at the SIRAD irradiation facility at the Laboratori Nazionali INFN of Legnaro. The test of

[1] see for example `www.futron.com/pdf/FutronLaunchCostWP.pdf`

the radiation-induced effects on the DAC AD8842 has been subcontracted to the French company Hirex[2].

In this chapter the measurements of the XAA1.2 resistance to the cosmic rays interaction is studied. In section 5.2 the phenomenology of the cosmic rays interaction effects in electronic circuits is summarized and section 5.3 is devoted to the description of the experimental set-up. In section 5.4 and 5.5 the results of the latch-up and SEU measurements respectively are shown while the total dose effects on the functionality and the performances of the XAA1.2 are in section 5.6. Section 5.7 discusses, as a possible application of the results, the evaluation of the expected latch-up and SEU rates and the total dose effects of the XAA1.2 chips on AGILE orbit. Finally in section 5.8 the conclusions of this work are given.

5.2 The interaction of cosmic rays in electronic devices

The earliest verified failure and damage in satellite-borne experiments due to the interaction of cosmic rays in electronic devices dates back in the literature to the beginning of the 1990's (Goka et al. (1991) and Adams et al. (1992)). In the first paper a three year long data acquisition is discussed and the occurrence of the effects is correlated with the solar activity. In the second paper a single failure recorded inside the South Atlantic Anomaly is later reproduced during a ground test irradiating the engineering model of the same instrument with a proton beam. In both papers it is stressed that the complementary metal oxide semiconductor (CMOS) technology, the same in the XAA1.2 chip, is particularly sensitive to the cosmic rays effects, as specified also in Liu et al. (2000).

The effects caused by the interaction of photons and charged particles in the electronic devices volume can be grouped in Single Event Effects (SEE), due to a single particle interaction, and Total Dose Effects, given by the integrated contribution of many low ionizing interactions. Among the SEE most extensively studied are the latch-up, which manifests itself as a sudden increase of the power supply current of a device, and the Single Event Upset (SEU), the bit flip in a digital element. The total dose produces an overall degradation of the device functionality and performance and its effects depend on the type of the affected component.

An extensive and detailed review about the latch-up in CMOS based integrated circuits can be found in Johnston (1996). The latch-up is caused by a parasitic circuit effect due to the *p-n-p-n* structure in which the middle junction is reverse biased and the other two junctions are forward biased. Typically the *p-n-p-n* regions are formed by parasitic bipolar devices, inherently present in most CMOS circuits, as shown in fig. 5.1. Considering for example a CMOS inverter (as shown in Cané et al. (1991)), if the bipolar circuit switches from its normally high impedance state to a low impedance state, a direct path between source and drain is generated. An equilibrium condition is then reached, in which all the three junctions are forward biased and a steady current can flow through the structure. This current flow can seriously damage or even destroy the

[2]Web site `http://www.hirexengineering.com/index1.htm`

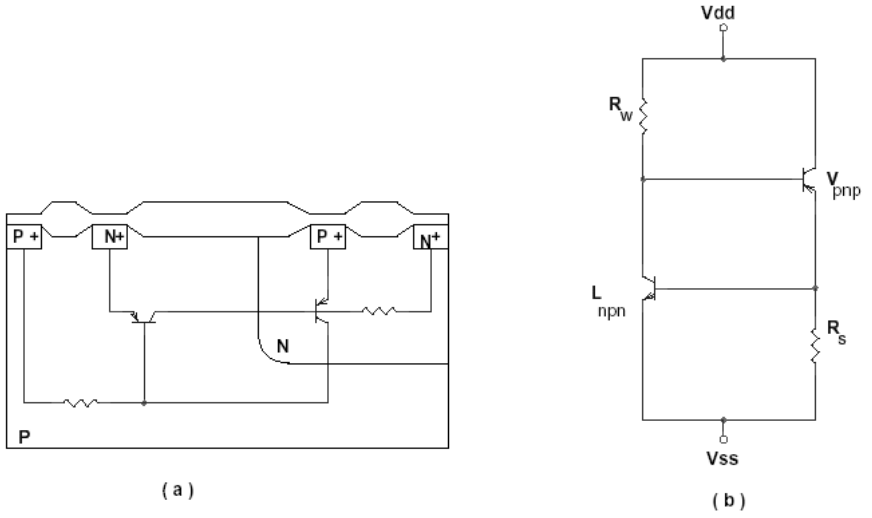

Figure 5.1: Example of a *p-n-p-n* structure (a) with its inherent parasitic circuit and of its first order (b) equivalent model, from Cané et al. (1991).

integrated circuit through Joule heating. To restore the device to the normal operation condition the power supply must be reduced or switched off.

The state change triggering the latch-up can be produced by the ionization of the silicon due to the interaction of photons (light, X-rays or gamma rays) and particles (protons or ions). The circuit is then said to be in latch-up if the high current state persists when the deviation from the normal condition is removed. Latch-up key parameters are the holding voltage and the holding current, that are the minimum conditions required to sustain latch-up once it is triggered, as described in McDaid et al. (1990).

The SEU is a bit flip in a digital element, caused by either the direct ionization from a traversing particle or by the ionization produced by charged particles and recoiling nuclei emitted from a nuclear reaction induced near the microcircuit element (see Belyakov et al. (2000)). The bit flip caused by the SEU modifies the stored digital information and can cause unpredictable changes in the device operation.

The spatial analysis in Johnston and Hughlock (1990) shows that in a CMOS structure the gathered charge and the collection regions of SEU and latch-up are different. The SEU is due to prompt charge collected within 3 μm from the surface while the latch-up is caused by charge gathered in the well-substrate junction, typically located $3 \div 6$ μm below the surface, and its funnelling region, extending about 2 μm below the depletion region.

Taking a macroscopic point of view, the electronic devices can be described in terms of sensitive volume to single event effects. In this scheme a latch-up or a SEU occurs if, and only if, an amount of energy above a given threshold is deposited within the

sensitive volume, as described in McNulty et al. (1993). The sensitive volume and the threshold energy for the latch-up are in general different than the corresponding SEU quantities.

The total dose effects to a CMOS integrated circuit are mainly caused by ionization charges trapped near or in the interface between the SiO_2 and the silicon bulk, as explained in Yokoyama et al. (2001). The trapped charge increases the noise, degrades the transconductance and shifts the threshold voltages. In particular, the carrier number fluctuation, due to the trapping and detrapping because of the near-interface oxide traps, increases the $1/f$ noise. The interaction between interface traps and carriers degrades the carriers mobility thus decreasing the transconductance and increasing the white noise. The charge of these oxide traps, depending on the position of the Fermi level, produces threshold voltage shifts in the devices.

The fabrication of integrated circuits on epitaxially grown layers, i.e. monocrystalline silicon thin layers deposited from the gas phase of a two gases chemical reaction on the surface of a silicon wafer (see Lutz (1999) for more details), reduces the devices latch-up sensitivity. In fact if the chip is built on an epitaxial substrate the holding voltage increases, reducing the latch-up susceptibility. When the holding voltage exceeds the supply voltage the device is immune to latch-up. Furthermore the intrinsic radiation hardness of CMOS integrated circuits depends on the gate-oxide thickness because a thinner oxide layer provides fewer ionization charges to be trapped near or within the SiO_2-Si bulk interface, thus making less serious the problems due to the trapped charges described above.

As described in sec. 3.3, the XAA1.2 chip is manufactured with a 0.8 μm CMOS technology on epitaxial layer. Currently devices with 0.35 μm CMOS technology are manufactured and a 0.25 μm CMOS technology is now under study.

5.3 Radiation-induced effects measurements

The sensitivity to radiation-induced effects of the electronic circuits to be flown on satellite-borne experiments is generally measured by irradiating the devices with protons or ions in an accelerator dedicated facility (see for example Koga (1996), Alessandro et al. (2002) and Grim et al. (2000)). In these tests incident particles with different atomic number and energy are selected, thus obtaining different linear energy transfer (LET) values.

The LET is a measure of the energy per unit length released by the particle in the silicon bulk through Coulomb forces between the ion positive charge and the negative charge of the orbital electrons within the absorber atoms (see Knoll (1989) for the definition). In measuring the LET the material thickness is usually divided by the material density and the resulting LET is given in units of $\mathrm{MeV} \cdot \mathrm{cm}^2 \cdot \mathrm{mg}^{-1}$.

The LET depends on the particle charge z as $LET \propto z^2$ and varies slowly with particle energy. The sensitivity of a device to SEE spans on more than one order of magnitude in LET. For these reason, to efficiently measure the SEE sensitivity scanning the LET values, particles of different charge z are selected with about the same energy and a

facility where ions of different charge are accelerated is needed. Thus measurements of SEE sensitivity are performed in particle accelerators, typically of tandem type, where ion sources are introduced as to produce a flux of about $10^2 \div 10^6$ ions $\cdot$ cm$^{-2} \cdot$ s^{-1} with energy $100 \div 400$ MeV. An example of SEE dedicated facility is the SIRAD experiment at the Laboratori Nazionali INFN of Legnaro in Italy.

5.3.1 The SIRAD irradiation facility

The SIRAD facility (see Wyss et al. (2001) for further details) is located at the $+70°$ line of the 15 MV Tandem accelerator at the Laboratori Nazionali INFN of Legnaro, near Padova in Italy. The accelerator can provide positive charged particles, from protons to ^{197}Au, at various energy values, ranging from about 30 MeV for protons to about 300 MeV for ^{197}Au. The facility is dedicated to radiation damage studies (bulk damage, total dose and SEE) induced by protons and heavy ions on semiconductor detectors, electronic devices and systems. A schematic of the SIRAD irradiation facility, from Wyss et al. (2001), is shown in fig. 5.2.

The facility is composed of a system of adjustable horizontal and vertical slits, a quadrupole doublet for focusing the beam down to millimetric spots, an electric rastering system for irradiating extended targets, a diagnostic chamber with a wire beam profiling monitor and an extractable Faraday cup, an irradiation chamber with a battery of small Faraday cups and a set of silicon diodes read by pulse counting electronics. The irradiation chamber has a volume of about 130 l and works under vacuum higher than $8 \cdot 10^{-6}$ mbar, obtained using a molecular pump (VARIAN Turbo-V 550) and monitored with a Penning probe. Two circular flanges of 160 mm diameter, one containing 16 BNC feed-throughs and the other containing two 50-pin Cannon connectors, are used to close the irradiation chamber.

The devices to be irradiated are fixed on a multiple sample holder, 30 cm long and 10 cm wide, together with a board containing four silicon diode detectors, described below. The experimental chamber contains a remote controlled motor drive that can vertically move the sample holder to change the device under test without opening the chamber. The motor drive allows only vertical movements.

The low ion flux required for SEE studies is obtained focusing the beam about 10 m before the target plane. On the target plane and inside a 2 cm-by-2 cm fiducial area, the beam has a circular shape and a typical uniformity of about 10 %. In this configuration the beam flux is monitored using two sets of four silicon diodes with sensitive area of about 0.16 cm^2 each and read by pulse counting electronics. One diode set is located upstream with respect to the target plane and monitors continuously the beam and the other set is fixed on the sample holder. Before starting the irradiation the diodes on the sample holder are put on target and the beam flux is measured. With a proper linear combination the flux measured by the upstream diodes is equalized to the flux measured on target. In this way when the device under test is irradiated the beam flux can be monitored using the upstream diodes.

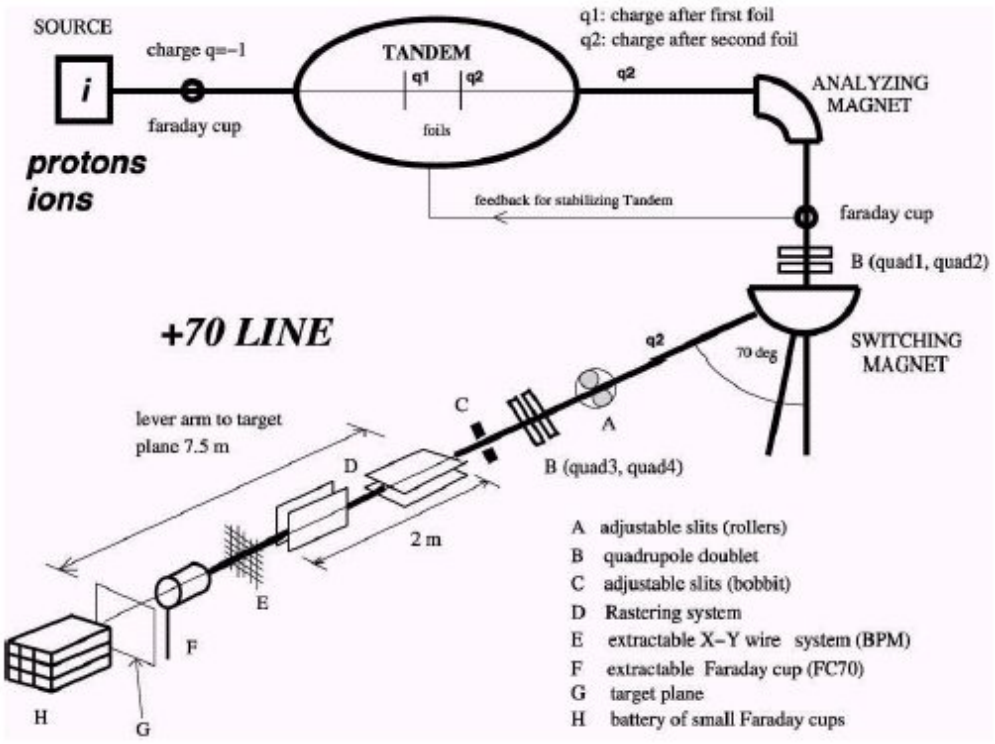

Figure 5.2: Schematic of the SIRAD irradiation facility, from Wyss et al. (2001).

5.3.2 XAA1.2 acquisition and control system

During the SEE measurements the XAA1.2 is interfaced to the XA-DAQ acquisition board, described in sec. 3.5.1. The LabView software of the acquisition board has been modified specifically for these measurements. In particular, a power supply monitor, interfaced to the board power supply circuit and used for the latch-up test and a configuration mask monitor, interfaced to the XA-DAQ digital configuration module and used for the SEU test, have been added to the code. A picture of the experimental set-up at SIRAD facility is shown in fig. 5.3.

The power supply monitor measures the I_{SS} and I_{DD} currents with a sampling time of about 0.3 s. A threshold is selected for each current and, since in case of a latch-up both currents suddenly increase, as soon as one of the two values exceeds the threshold the power supply is automatically switched off. During the irradiation we switch off the power supply less than 1 ms after a latch-up has been detected and we restart it after a programmable amount of time ($1 \div 10$ s). The values of the supply currents in steady conditions are $I_{SS} \simeq 24$ mA and $I_{DD} \simeq 14$ mA and, in case of a latch-up, both values exceed $50 \div 200$ mA.

Every 2 s during the irradiation the configuration bit stream is loaded in the chip memory registers and the previous configuration is present to the output and is read out. In case of a SEU, one or more bits in the memory registers change their polarity

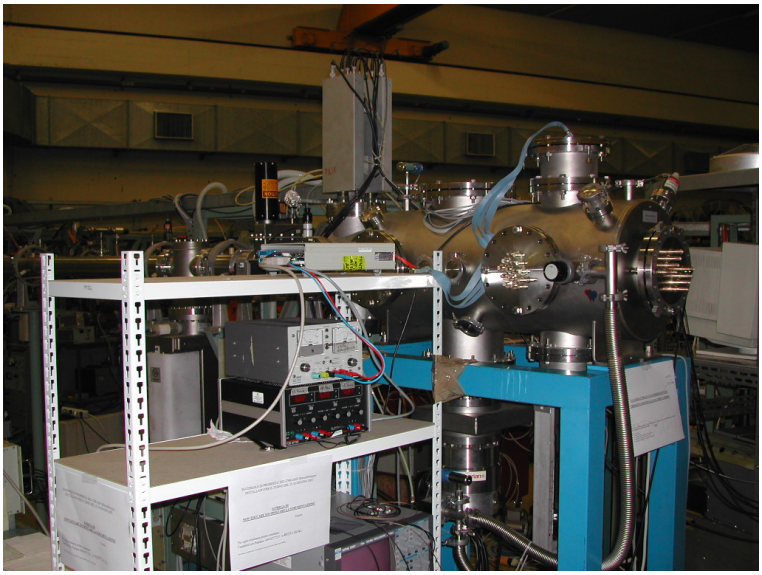

Figure 5.3: Experimental set-up: XA-DAQ acquisition board (top of the stand), power supply (under the XA-DAQ board) and SIRAD irradiation chamber (right of the picture).

state and the SEU occurrence is found simply by comparing the read out configuration mask with the input one.

5.3.3 Experimental set-up and strategy

A sample consisting in three XAA1.2 chips have been irradiated, each one mounted on its test PCB, with serial number 710-1-3, 710-1-12 and 710-1-25 respectively. Hereafter each chip is identified with the serial number of its board. Each board contains only one XAA1.2 which is the only active element. An aluminum layer about 1 mm thick with a rectangular window placed above the chip covers the boards preventing the incident ions from reaching the other components of the circuit different from the XAA1.2.

The test PCB containing the chips are fixed on the sample holder of the irradiation chamber together with the board containing the silicon diodes, fixed on the same plane of the test boards. Due to dimensional constraints, the sample holder can contain no more than two PCB. During all the irradiation the orientation of the test boards and of the counting diode detectors is kept normal to the incident ion beam. In fig. 5.4 two test PCB covered with the aluminum layers (left and center) and the diode set on the target plane (right) fixed on the sample holder inside the experimental chamber can be seen.

The XA-DAQ board is plugged to the external flange connector and to the acquisition PC. Since the flange contains only one 50-pin connector and each XAA1.2 chip requires a 50-pin connector, we can plug only one chip at a time. The device under test can be changed opening the experimental chamber, unplugging one chip from the flange and

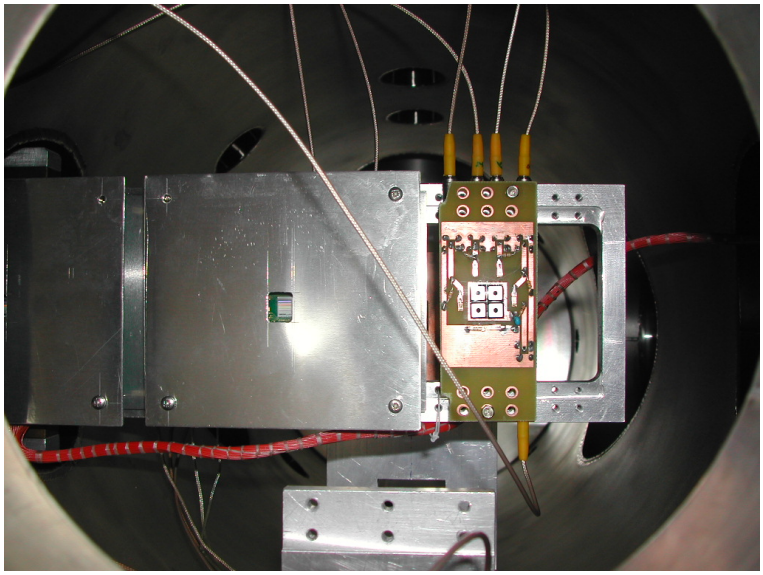

Figure 5.4: Experimental set-up: two test PCB covered with the aluminum layers (left and center) and the diode set on the target plane (right) fixed on the sample holder inside the experimental chamber.

connecting the other one.

The radiation damage measurements have been performed in two different runs 48 hours long. We select the ion species aiming to efficiently scan the LET values in silicon. In tab. 5.1 we show the ion species used to irradiate each XAA1.2 chip together with the values of energy, LET and range in silicon for the different ions. The LET is calculated using the SRIM software package (see Ziegler et al. (1985) for a full description of the calculation algorithms).

During the first run two chips have been irradiated, the number 710-1-25 and 710-1-3. The first chip has been irradiated with ion species with low (^{16}O, ^{28}Si and ^{32}S) and medium (^{46}Ti and ^{58}Ni) LET and with a single high LET ion (^{127}I) to test the so called "destructive latch-up", that can permanently damage a chip in a single interaction. During the test on chip 710-1-25, we start with a high fluence of small LET ions and we gradually increase the LET values (decreasing the fluence) from 2.85 MeV $\cdot$ cm^2 $\cdot$ mg^{-1} of the ^{16}O up to 61.80 MeV $\cdot$ cm^2 $\cdot$ mg^{-1} of the ^{127}I. In this way the chip absorbs a dose of about 235 krad during the initial irradiation with ^{16}O and ^{28}Si. The chip number 710-1-3 has been irradiated with some of the ions used for the 710-1-25 (^{32}S, ^{48}Ti and ^{58}Ni) to increase the data statistics, starting with high latch-up and SEU rate and low dose runs.

After the data analysis of the first run we used a second irradiation run to test the chip number 710-1-12 increasing the small LET ions statistics (^{16}O and ^{28}Si) and adding one ion at intermediate LET (^{79}Br). To compare these results with the previous irradiations we kept the two intermediate LET ions (^{48}Ti similar to ^{46}Ti and ^{58}Ni).

Table 5.1: Ion species used during the irradiation at SIRAD facility with energy, LET and range values in silicon, and serial number of the irradiated chip.

Ion species	E [MeV]	LET [MeV $\cdot$ cm^2 $\cdot$ mg^{-1}]	range [μm]	irradiated chip
^{16}O	108.68	2.85	109.49	710-1-25
^{16}O	58.18	4.15	45.15	710-1-12
^{28}Si	157.68	8.59	61.54	710-1-12, 710-1-25
^{32}S	171.68	10.96	54.44	710-1-3, 710-1-25
^{46}Ti/^{48}Ti	196.18	19.75	39.34	710-1-3, 710-1-12, 710-1-25
^{58}Ni	220.68	28.44	33.66	710-1-3, 710-1-12, 710-1-25
^{79}Br	255.68	38.49	32.90	710-1-12
^{107}Ag	273.78	54.65	28.14	710-1-12
^{127}I	276.68	61.80	27.90	710-1-12, 710-1-25
^{197}Au	275.68	81.74	23.40	710-1-12

Since with the first two chips we did not find any destructive latch-up we added two high LET ions (^{107}Ag and ^{197}Au) in this measurement.

The ion species selected for the irradiation are shown in tab. 5.3.3, 5.2 and 5.3 together with their LET, range in silicon, fluence (given by the product of the flux times the irradiation duration) and dose.

The fluence error in the tables is evaluated considering the flux uniformity during the measurement, evaluated during the pre-irradiation beam set-up considering the minimum F_{min} and maximum F_{max} flux values measured by the target-plane diodes. If $\bar{F}$ is the flux mean value and $\Delta F = (F_{max} - F_{min})/2$ is the flux dispersion, the flux percentage uniformity is given by $\Delta F/\bar{F}$.

5.4 Latch-up measurements

The latch-up occurrence is studied monitoring the power supply currents of the XAA1.2 chips during the irradiation and recording the number of times one of the two currents exceeds the monitor threshold. The sampling time of the current monitor is about 0.3 s and the current increase due to a latch-up is faster than this sampling time. This fact does not allow to study the temporal evolution of the currents variation.

An example of the currents values, recorded during a ^{46}Ti irradiation, can be seen in fig. 5.5. In the plot the values of the currents I_{SS} (upper panel) and I_{DD} (lower panel) as a function of time are shown. The vertical lines in the plot are the latch-up events and the dotted lines are the monitor current thresholds (30 mA for I_{SS} and 27 mA for I_{DD} respectively).

From the irradiation results we can calculate the probability and the cross section of the latch-up occurrence as a function of LET. If $N_{\mathrm{latch-up}}$ is the number of latch-up

Table 5.2: Ion selection for the irradiation of chip number 710-1-3. The fluence error is calculated basing on the beam non uniformity.

Ion species	LET [MeV · cm^2 · mg^{-1}]	range [μm]	Fluence [cm^{-2}]	Dose [krad]
^{32}S	10.96	54.4	$(8.6 \pm 0.3) \cdot 10^8$	151
^{46}Ti	19.75	39.3	$(3.0 \pm 0.2) \cdot 10^6$	1
^{58}Ni	28.44	33.7	$(2.1 \pm 0.2) \cdot 10^5$	0.1

Table 5.3: Ion selection for the irradiation of chip number 710-1-12. The fluence error is calculated basing on the beam non uniformity.

Ion species	LET [MeV · cm^2 · mg^{-1}]	range [μm]	Fluence [cm^{-2}]	Dose [krad]
^{16}O	4.15	45.2	$(5.2 \pm 0.3) \cdot 10^8$	34
^{28}Si	8.50	61.5	$(5.1 \pm 0.2) \cdot 10^9$	692
^{48}Ti	19.75	39.3	$(3.2 \pm 0.4) \cdot 10^6$	1
^{58}Ni	27.94	33.7	$(2.1 \pm 0.3) \cdot 10^5$	0.1
^{79}Br	38.49	32.9	$(5.1 \pm 0.5) \cdot 10^5$	0.3
^{107}Ag	54.65	28.1	$(1.3 \pm 0.1) \cdot 10^5$	0.1
^{127}I	61.80	27.9	$(2.3 \pm 0.2) \cdot 10^5$	0.3
^{197}Au	81.74	23.4	$(4.0 \pm 0.7) \cdot 10^5$	0.5

Table 5.4: Ion selection for the irradiation of chip number 710-1-25. The fluence error is calculated basing on the beam non uniformity.

Ion species	LET [MeV · cm^2 · mg^{-1}]	range [μm]	Fluence [cm^{-2}]	Dose [krad]
^{16}O	2.85	109.5	$(1.1 \pm 0.1) \cdot 10^8$	5
^{28}Si	8.59	61.5	$(2.3 \pm 0.2) \cdot 10^9$	373
^{32}S	10.96	54.4	$(2.0 \pm 0.1) \cdot 10^9$	348
^{46}Ti	19.75	39.3	$(5.1 \pm 0.5) \cdot 10^6$	2
^{58}Ni	28.44	33.7	$(5.2 \pm 0.9) \cdot 10^5$	0.2
^{127}I	61.80	27.9	$(1.1 \pm 0.1) \cdot 10^5$	0.1

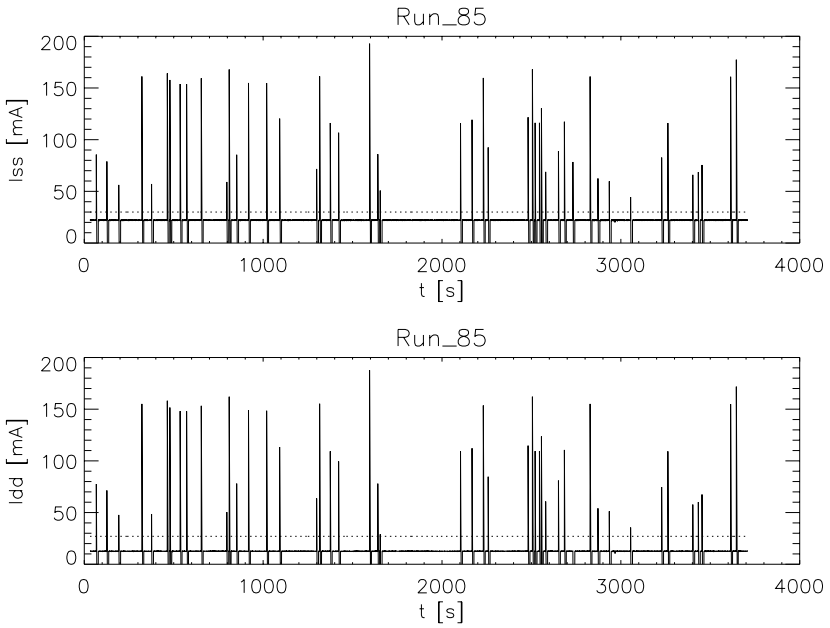

Figure 5.5: Values of the currents I_{SS} (upper panel) and I_{DD} (lower panel), recorded during a ^{46}Ti irradiation, as a function of time. The dotted lines are the monitor current thresholds (30 mA and 27 mA respectively).

events for a fixed LET, ϕ is the monitored incident flux (measured as in 5.3.1), $t_{\rm live}$ is the live time and S is the chip geometric surface (0.48 cm^2), the latch-up probability $P_{\rm latch-up}$ is

$$P_{\rm latch-up} = \frac{N_{\rm latch-up}}{(\phi \cdot t \cdot S)} \tag{5.1}$$

and the cross section $\sigma_{\rm latch-up}$ is given by

$$\sigma_{\rm latch-up} = \frac{N_{\rm latch-up}}{(\phi \cdot t)} = P_{\rm latch-up} \cdot S. \tag{5.2}$$

The latch-up probability and cross section for the three chips under test are shown in tab. 5.5, 5.6 and 5.7 and plotted in fig. 5.6.

The error associated to the latch-up probability and cross section is calculated considering the occurrence of the events distributed following a Poisson statistics and taking into account the flux uniformity. These two contributions are separated in tab. 5.5, 5.6 and 5.7. Since we do not find any event during the irradiation with ^{16}O (at both 2.85 and 4.15 MeV $\cdot$ cm^2 $\cdot$ mg^{-1} LET values) in tab. 5.5, 5.6 and 5.7 we show the upper limits for the probability and the cross section, calculated considering a confidence level of 99.7 %.

As can be seen from tab. 5.5, 5.6 and 5.7 and fig. 5.6, the 19.75 MeV $\cdot$ cm^2 $\cdot$ mg^{-1} (^{46}Ti) and 28.44 MeV $\cdot$ cm^2 $\cdot$ mg^{-1} (^{58}Ni) probability and cross section values are higher

in the chip number 710-1-25 than in the other chips. For both ions the dose absorbed by each chip before starting the irradiation is different. In fact ^{46}Ti is the first ion of the chip 710-1-3 irradiation and ^{48}Ti is the first ion of the 710-1-12 irradiation while, before starting the irradiation with ^{46}Ti, the chip 710-1-25 has been exposed to about 583 krad. Similarly, before starting the ^{58}Ni irradiation the dose is about 235 krad for 710-1-25, about 1 krad for 710-1-3 and about 150 krad for 710-1-12. The same logic does not seem to explain why the probability and cross section at 61.80 MeV $\cdot$ cm^2 $\cdot$ mg^{-1} (^{127}I) are consistent within the errors since the chip number 710-1-25 absorbed about 728 krad while the chip 710-1-12 about 1 krad before starting this irradiation.

The latch-up cross section $\sigma_{\mathrm{latch-up}}$ can be fitted as a function of LET using a Weibull function,

$$\sigma_{\mathrm{latch-up}} = \begin{cases} \sigma_\infty \left(1 - \exp\left[-\left(\frac{LET - LET_{\mathrm{thr}}}{W}\right)^S\right]\right) & \text{if } LET \geq LET_{\mathrm{thr}} \\ 0 & \text{if } LET < LET_{\mathrm{thr}} \end{cases} \tag{5.3}$$

where σ_∞ is the limiting or plateau cross section, LET_{thr} is the LET threshold (the maximum LET value that has a zero cross section), W and S are dimensionless shape parameters. The (5.3) is an empyrical function whose shape approximates the cross section as a function of LET and can be used to fit the data and particularly to evaluate the limiting cross section σ_∞ and the LET threshold LET_{thr} (see Petersen et al. (1992) for more information).

Applying the Weibull function to the latch-up data of the chip 710-1-12 we find that $\sigma_\infty = (1.7 \pm 0.1) \cdot 10^{-3}$ cm^2, $LET_{\mathrm{thr}} = (8.5 \pm 3.6)$ MeV $\cdot$ cm^2 $\cdot$ mg^{-1}, $W = (3.9 \pm 0.3) \cdot 10^{-2}$ and $S = (5.4 \pm 2.7)$. With the same function the parameters of the chip 710-1-25 data are $\sigma_\infty = (2.2 \pm 0.2) \cdot 10^{-3}$ cm^2, $LET_{\mathrm{thr}} = (4.2 \pm 1.7)$ MeV $\cdot$ cm^2 $\cdot$ mg^{-1}, $W = (4.0 \pm 0.2) \cdot 10^{-2}$ and $S = (9.5 \pm 1.5)$. The different values of the limiting cross section σ_∞ reflect the highest measured cross sections and the different LET threshold values LET_{thr} are mainly due to the cross section values at ^{46}Ti, ^{48}Ti and ^{58}Ni discussed above (see tab. 5.6 and 5.7).

5.5 SEU measurements

We study the SEU occurrence comparing the input configuration bit stream with the mask recorded in the chip memory registers. In case of a SEU one or more bit in the memory registers change their polarity state. The number of SEU events is recorded in the approximation that an ion interaction can change only a single bit of the configuration mask at a time.

As for the latch-up, we calculate the SEU probability and cross section as a function of the different LET values. If N_{SEU} is the number of SEU events for a fixed LET value, ϕ is the monitored incident flux (measured as in 5.3.1), t is the live time and S is the chip geometric surface, the probability P_{SEU} is

Table 5.5: Results of the irradiation for the latch-up measurements on the 710-1-3 chip. LET is the linear energy transfer, ϕ is the mean incident flux, t_{live} is the live time, $N_{\text{latch-up}}$ is the latch-up number and $P_{\text{latch-up}}$ is the latch-up probability. The first contribution in the probability error is the Poisson error and the second contribution is due to the flux non-uniformity.

LET $[\text{MeV} \cdot \text{cm}^{-2} \cdot \text{mg}^{-1}]$	ϕ $[\text{cm}^2 \cdot \text{s}^{-1}]$	t_{live} [s]	$N_{\text{latch-up}}$	$P_{\text{latch-up}}$
10.96	$(1.52 \pm 0.06) \cdot 10^5$	5629	4	$(9.7 \pm 4.9 \pm 0.4) \cdot 10^{-9}$
19.75	$(1.57 \pm 0.09) \cdot 10^3$	1849	36	$(2.6 \pm 0.4 \pm 0.2) \cdot 10^{-5}$
28.44	$(1.1 \pm 0.1) \cdot 10^2$	1499	80	$(1.0 \pm 0.1 \pm 0.1) \cdot 10^{-3}$

Table 5.6: Results of the irradiation for the latch-up measurements on the 710-1-12 chip. LET is the linear energy transfer, ϕ is the mean incident flux, t_{live} is the live time, $N_{\text{latch-up}}$ is the latch-up number and $P_{\text{latch-up}}$ is the latch-up probability. The first contribution in the probability error is the Poisson error and the second contribution is due to the flux non-uniformity.

LET $[\text{MeV} \cdot \text{cm}^{-2} \cdot \text{mg}^{-1}]$	ϕ $[\text{cm}^2 \cdot \text{s}^{-1}]$	t_{live} [s]	$N_{\text{latch-up}}$	$P_{\text{latch-up}}$
4.15	$(7.4 \pm 0.4) \cdot 10^4$	6950	0	$< 2.3 \cdot 10^{-8}$
8.50	$(9.9 \pm 0.4) \cdot 10^4$	51527	9	$(3.7 \pm 1.2 \pm 0.2) \cdot 10^{-9}$
19.75	$(8.7 \pm 1.1) \cdot 10^2$	3220	47	$(3.5 \pm 0.5 \pm 0.1) \cdot 10^{-5}$
27.94	$(1.2 \pm 0.1) \cdot 10^2$	1659	101	$(1.0 \pm 0.1 \pm 0.1) \cdot 10^{-3}$
38.49	$(1.4 \pm 0.1) \cdot 10^2$	2706	455	$(2.6 \pm 0.1 \pm 0.3) \cdot 10^{-3}$
54.65	$(7.5 \pm 0.4) \cdot 10^1$	1591	197	$(3.4 \pm 0.3 \pm 0.3) \cdot 10^{-3}$
61.80	$(7.9 \pm 0.9) \cdot 10^1$	2511	350	$(3.7 \pm 0.2 \pm 0.2) \cdot 10^{-3}$
81.74	$(6.9 \pm 1.2) \cdot 10^1$	3860	409	$(3.2 \pm 0.2 \pm 0.4) \cdot 10^{-3}$

Table 5.7: Results of the irradiation for the latch-up measurements on the 710-1-25 chip. LET is the linear energy transfer, ϕ is the mean incident flux, t_{live} is the live time, $N_{\text{latch-up}}$ is the latch-up number and $P_{\text{latch-up}}$ is the latch-up probability. The first contribution in the probability error is the Poisson error and the second contribution is due to the flux non-uniformity.

LET $[\text{MeV} \cdot \text{cm}^{-2} \cdot \text{mg}^{-1}]$	ϕ $[\text{cm}^2 \cdot \text{s}^{-1}]$	t_{live} [s]	$N_{\text{latch-up}}$	$P_{\text{latch-up}}$
2.85	$(1.5 \pm 0.2) \cdot 10^5$	710	0	$< 1.1 \cdot 10^{-7}$
8.59	$(1.1 \pm 0.1) \cdot 10^5$	20798	3	$(2.7 \pm 1.6 \pm 0.2) \cdot 10^{-9}$
10.96	$(2.4 \pm 0.1) \cdot 10^5$	8072	17	$(1.8 \pm 0.4 \pm 0.1) \cdot 10^{-8}$
19.75	$(1.2 \pm 0.1) \cdot 10^3$	3290	100	$(5.4 \pm 0.5 \pm 0.5) \cdot 10^{-5}$
28.44	$(1.6 \pm 0.3) \cdot 10^2$	1310	260	$(2.6 \pm 0.2 \pm 0.5) \cdot 10^{-3}$
61.80	$(3.3 \pm 0.3) \cdot 10^1$	2453	175	$(4.6 \pm 0.3 \pm 0.4) \cdot 10^{-3}$

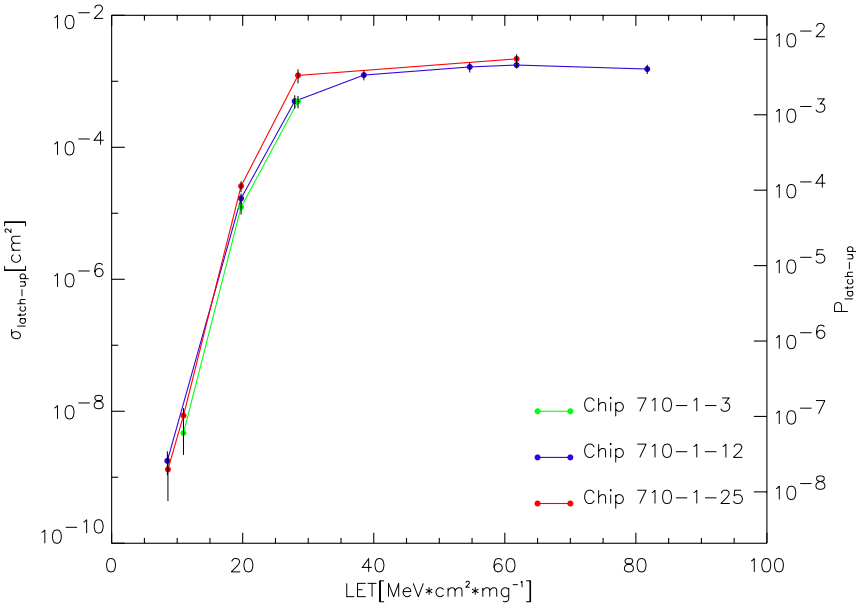

Figure 5.6: Results of the irradiation for the latch-up measurements on the three XAA1.2 chips. LET is the linear energy transfer, $P_{latch-up}$ is the latch-up probability and $\sigma_{latch-up}$ is the latch-up cross section.

$$P_{\mathrm{SEU}} = \frac{N_{\mathrm{SEU}}}{(\phi \cdot t \cdot S)} \tag{5.4}$$

while the cross section σ_{SEU} is given by

$$\sigma_{\mathrm{SEU}} = \frac{N_{\mathrm{SEU}}}{(\phi \cdot t)} = P_{\mathrm{SEU}} \cdot S. \tag{5.5}$$

The SEU probability and cross section for the three chips under test are shown in tab. 5.8, 5.9 and 5.10 and plotted in fig. 5.7.

The error associated to the SEU probability and cross section is calculated considering the occurrence of the SEU events distributed following a Poisson statistics and taking into account the flux uniformity. These two contributions are separated in tab. 5.8, 5.9 and 5.10. Since we do not find any event during the irradiation with ^{16}O at 2.85 MeV $\cdot$ cm^2 $\cdot$ mg^{-1} LET value, in tab. 5.8 and 5.10 we show the upper limits for the probability and the cross section, calculated considering a confidence level of 99.7 %.

The SEU probability and cross section values of the ^{28}Si and ^{58}Ni show significant differences among the three tested chips, as shown in tab. 5.8, 5.9 and 5.10 and plotted in fig. 5.7. For both the LET values the dose absorbed by the chips before starting each irradiation is different. In the ^{28}Si case the probability and cross section values are higher for the chip number 710-1-25 at about 235 krad than for the 710-1-12 at about

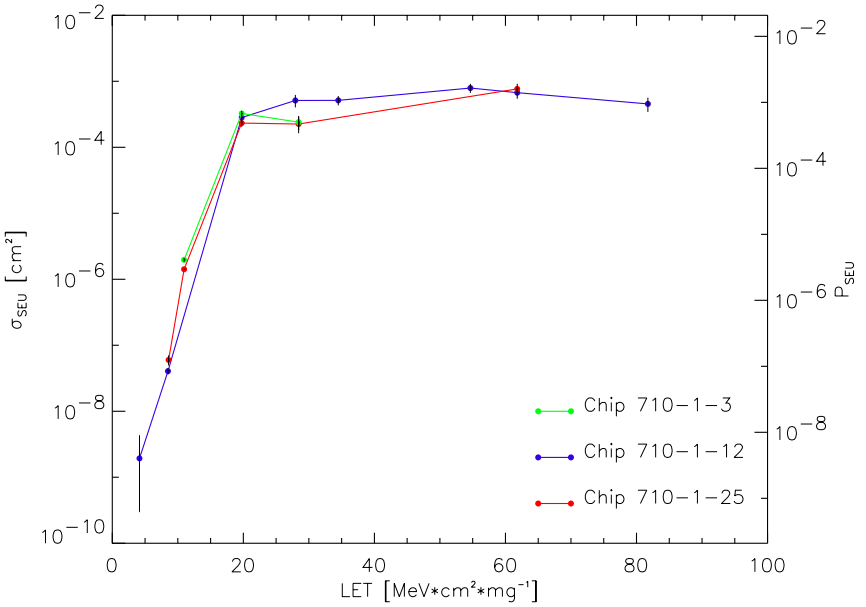

Figure 5.7: Results of the irradiation for the SEU measurements on the three XAA1.2 chips. LET is the linear energy transfer, P_{SEU} is the SEU probability and σ_{SEU} is the SEU cross section.

150 krad. In the ^{58}Ni case, however, the difference cannot be explained considering the dose absorbed by the chips before the irradiation with this ion because the cross sections of the chip number 710-1-3 (at about 1 krad) and 710-1-25 (at about 235 krad) values are consistent within the errors, while the cross section of the chip number 710-1-12 (at about 150 krad) is not.

The LET threshold for the SEU events can be defined as the maximum LET value that has a zero cross section. Since for the chip 710-1-12 we record an event at the smallest LET value (4.15 MeV $\cdot$ cm^2 $\cdot$ mg^{-1} at ^{16}O), we calculate the threshold basing only on the results of this chip. Using a linear extrapolation we find that the threshold is 3.9 ± 0.3 MeV $\cdot$ cm^2 $\cdot$ mg^{-1}.

5.6 Total Dose Effects measurements

During the irradiation at SIRAD facility we measured the degradation of the performance of the XAA1.2 chips due to the absorbed total dose, evaluated considering only the energy released in the active layer of the device, estimated to be about 10 μm thick.

From Knoll (1989), the absorbed dose is the amount of energy absorbed from any type of radiation per unit mass of the absorber. The historical unit of absorbed dose is the rad, such that 1 rad=100 erg/g. The dose d_{act} (measured in krad) absorbed in the ASIC active layer is calculated using the formula

Table 5.8: Results of the irradiation for the SEU measurements on the 710-1-3 chip. LET is the linear energy transfer, ϕ is the mean incident flux, t_{live} is the live time, N_{SEU} is the number of SEU events (in the approximation that one can ion can produce just one SEU a time) and P_{SEU} is the SEU probability. The first contribution in the probability error is the Poisson error and the second contribution is due to the flux non-uniformity.

LET [MeV $\cdot$ cm^{-2} $\cdot$ mg^{-1}]	ϕ [cm^2 $\cdot$ s^{-1}]	t_{live} [s]	N_{SEU}	P_{SEU}
10.96	$(1.52 \pm 0.06) \cdot 10^5$	5649	1693	$(4.1 \pm 0.1 \pm 0.2) \cdot 10^{-6}$
19.75	$(1.57 \pm 0.09) \cdot 10^3$	1885	965	$(6.8 \pm 0.2 \pm 0.4) \cdot 10^{-4}$
28.44	$(1.1 \pm 0.1) \cdot 10^2$	1929	50	$(5.0 \pm 0.7 \pm 0.5) \cdot 10^{-4}$

Table 5.9: Results of the irradiation for the SEU measurements on the 710-1-12 chip. LET is the linear energy transfer, ϕ is the mean incident flux, t_{live} is the live time, N_{SEU} is number of SEU events (in the approximation that one can ion can produce just one SEU a time) and P_{SEU} is the SEU probability. The first contribution in the probability error is the Poisson error and the second contribution is due to the flux non-uniformity.

LET [MeV $\cdot$ cm^{-2} $\cdot$ mg^{-1}]	ϕ [cm^2 $\cdot$ s^{-1}]	t_{live} [s]	N_{SEU}	P_{SEU}
4.15	$(7.4 \pm 0.4) \cdot 10^4$	6950	1	$< 4.0^{-3.2}_{+4.9} \cdot 10^{-9}$
8.50	$(9.9 \pm 0.4) \cdot 10^4$	51536	206	$(8.4 \pm 0.6 \pm 0.3) \cdot 10^{-8}$
19.75	$(8.7 \pm 1.1) \cdot 10^2$	3690	904	$(5.9 \pm 0.2 \pm 0.8) \cdot 10^{-4}$
27.94	$(1.2 \pm 0.1) \cdot 10^2$	1760	110	$(1.1 \pm 0.1 \pm 0.1) \cdot 10^{-3}$
38.49	$(1.4 \pm 0.1) \cdot 10^2$	4052	263	$(1.6 \pm 0.1 \pm 0.1) \cdot 10^{-3}$
54.65	$(7.5 \pm 0.4) \cdot 10^1$	1788	106	$(1.6 \pm 0.2 \pm 0.1) \cdot 10^{-3}$
61.80	$(7.9 \pm 0.9) \cdot 10^1$	2861	152	$(1.4 \pm 0.1 \pm 0.2) \cdot 10^{-3}$
81.74	$(6.9 \pm 1.2) \cdot 10^1$	5232	183	$(9.5 \pm 0.7 \pm 1.6) \cdot 10^{-4}$

Table 5.10: Results of the irradiation for the SEU measurements on the 710-1-25 chip. LET is the linear energy transfer, ϕ is the mean incident flux, t_{live} is the live time, N_{SEU} is number of SEU events (in the approximation that one can ion can produce just one SEU a time) and P_{SEU} is the SEU probability. The first contribution in the probability error is the Poisson error and the second contribution is due to the flux non-uniformity.

LET [MeV $\cdot$ cm^{-2} $\cdot$ mg^{-1}]	ϕ [cm^2 $\cdot$ s^{-1}]	t_{live} [s]	N_{SEU}	P_{SEU}
2.85	$(1.5 \pm 0.2) \cdot 10^5$	710	0	$< 1.1 \cdot 10^{-7}$
8.59	$(1.1 \pm 0.1) \cdot 10^5$	20828	137	$(1.2 \pm 0.1 \pm 0.1) \cdot 10^{-7}$
10.96	$(2.4 \pm 0.1) \cdot 10^5$	8102	2808	$(3.0 \pm 0.1 \pm 0.2) \cdot 10^{-6}$
19.75	$(1.2 \pm 0.1) \cdot 10^3$	4290	1176	$(4.8 \pm 0.1 \pm 0.4) \cdot 10^{-4}$
28.44	$(1.6 \pm 0.3) \cdot 10^2$	2979	117	$(4.7 \pm 0.4 \pm 0.8) \cdot 10^{-4}$
61.80	$(3.3 \pm 0.3) \cdot 10^1$	3354	85	$(1.6 \pm 0.2 \pm 0.1) \cdot 10^{-4}$

$$d_{\mathrm{act}} = \frac{LET \cdot \phi \cdot t}{6.24 \cdot 10^7} \tag{5.6}$$

where the LET is measured in $\mathrm{MeV} \cdot \mathrm{cm}^2 \cdot \mathrm{mg}^{-1}$, ϕ is the flux (measured as in 5.3.1) and t is the duration of the ion beam irradiation while $6.24 \cdot 10^7$ is a numerical conversion factor between the energy units.

During the irradiation I monitor the bias currents and the power supply currents of the XAA1.2 chip using the XA-DAQ board. From the supply currents $\mathrm{I_{SS}}$ and $\mathrm{I_{DD}}$ and from the voltages $\mathrm{V_{SS}}$ and $\mathrm{I_{DD}}$, I calculate the power consumption for each input channel from the (3.1).

The power consumption of the three XAA1.2 chips as a function of the total dose is shown in fig. 5.8. The supply voltages $\mathrm{V_{SS}}$ and $\mathrm{V_{DD}}$ are stable during the irradiation. From the figure we can see that the power consumption of the chips 710-1-3 and 710-1-25 increases when the dose absorbed in the active layer increases while the power consumption of the chip 710-1-12 decreases between 1 krad and 17 krad and then begins to increase. The amount of the variation depends on the particular chip considered.

The maximum expected dose absorbed by the chip on-orbit as part of the SuperAGILE front-end electronic is 3 krad. From a linear interpolation of the measured values we find that the power consumption at 3 krad is 0.47 mW/ch. for the chip number 710-1-3 (-2 % variation), 0.54 mW/ch. for the number 710-1-12 (no variation) and 0.60 mW/ch. for the chip number 710-1-25 ($+2$ % variation).

We have also studied the variation of the bias currents of the chip number 710-1-12 with the total dose. The bias currents have been defined in section 3.3. As can be seen in fig. 5.9, the *prebias*, *otabias*, *shabias*, *strbias* and *IbDAC* currents slightly increase linearly as a function of the dose in the active layer. Conversely the *Vfs* and the *Vfp* voltages do not show a significant variation as a function of the absorbed dose.

As a measure of the chip performance we can take into account the linearity curve of the chip number 710-1-25, produced using the internal test pulse generator. Considering that a hole-electron pair is created for every 3.62 eV absorbed inside the silicon detector, we fed every chip channel with 50 pulses per charge ranging from 0.41 fC (corresponding to 10 keV) to 5.64 fC (corresponding to 128 keV). The maximum pulse charge is well beyond the upper energy threshold of the SuperAGILE instrument. This fact allows to study the chip linearity and to verify the XAA1.2 performance in an extended energy range.

As shown in fig. 5.10, the linearity of the XAA1.2 chip does not show significant variations at a dose level of 1 krad, some linearity variations can be seen at a 173 krad level, orders of magnitude above the maximum expected dose, while the chip is not linear above 700 krad.

After analyzing the address signals provided by the XAA1.2, we find variations smaller than 5 % with the total dose for the two address signals and for the MGO. Only some sparse address values show variations of about 10 %. These results imply that the address signals emitted by the chips on-orbit do not need to be corrected because of the total dose.

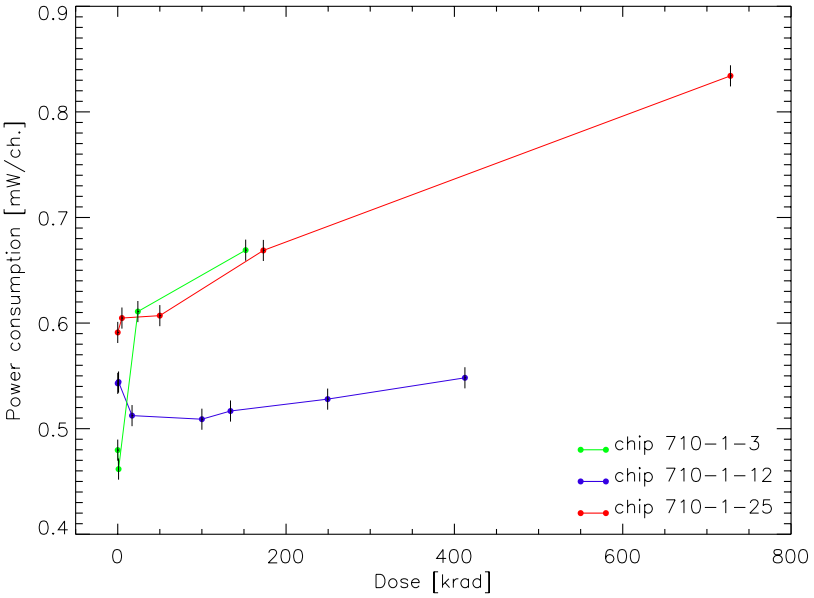

Figure 5.8: Power consumption for the three chips as a function of the total dose in the active layer.

5.7 The expected effects on-orbit and the recovery strategy

5.7.1 Heavy ions interactions

After the irradiation at the SIRAD facility I can estimate the radiation-induced effects in the environment of the AGILE spacecraft on-orbit. The expected rates are evaluated following the effective flux approach (described in Pickel (1996)) that takes a macroscopic viewpoint. In this scheme the chip is treated as a black box and the accelerator test data are used to predict a rate for the space environment on the basis of the measurements in the ground test, without detailed concern for the microscopic behaviour of the devices.

In our estimation the cosmic ray environment in the Earth magnetosphere is modeled using the CREME96 code (see Tylka et al. (1997) for the history and the details of the project), which evaluates the average flux of cosmic rays with atomic number from 1 to 92 for orbits of various altitudes and inclinations. The code allows also to evaluate the dose absorbed by the spacecraft electronic devices. Using CREME96 the flux can be evaluated after the transmission through an aluminum layer that models the spacecraft absorption of the cosmic rays. The code however does not take into account the detailed distribution of the spallation products generated by the protons interacting with the nuclei of the spacecraft shielding materials and the payload passive elements. With this restriction and considering that the protons LET is lower than the XAA1.2 latch-up and SEU threshold (the maximum LET of protons in silicon being 0.53 MeV $\cdot$ cm^2 $\cdot$ mg^{-1}) so

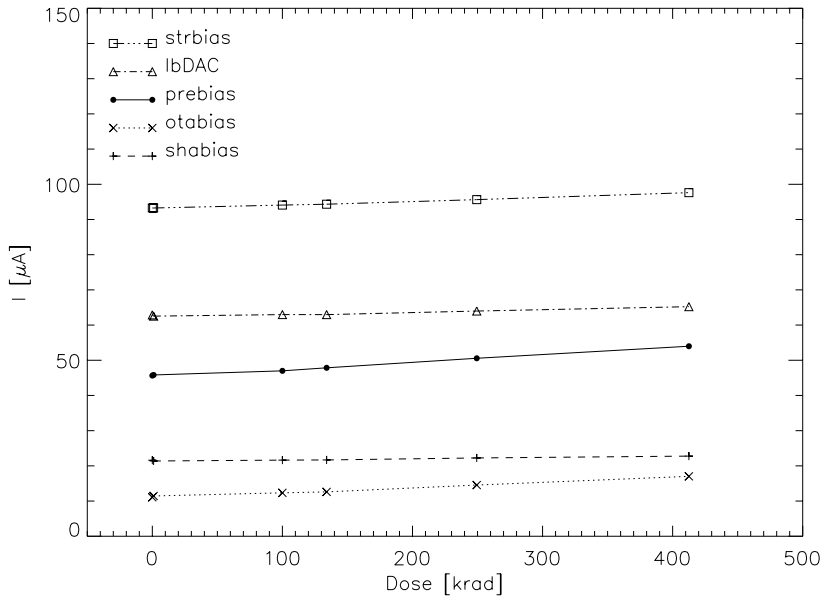

Figure 5.9: Values of the bias currents of the preamplifier (*prebias*), the discriminator (*otabias*), the shaper (*shabias*), the peak stetcher (*strbias*) and the current-voltage buffer converter (*IbDAC*) as a function of the total dose in the active layer.

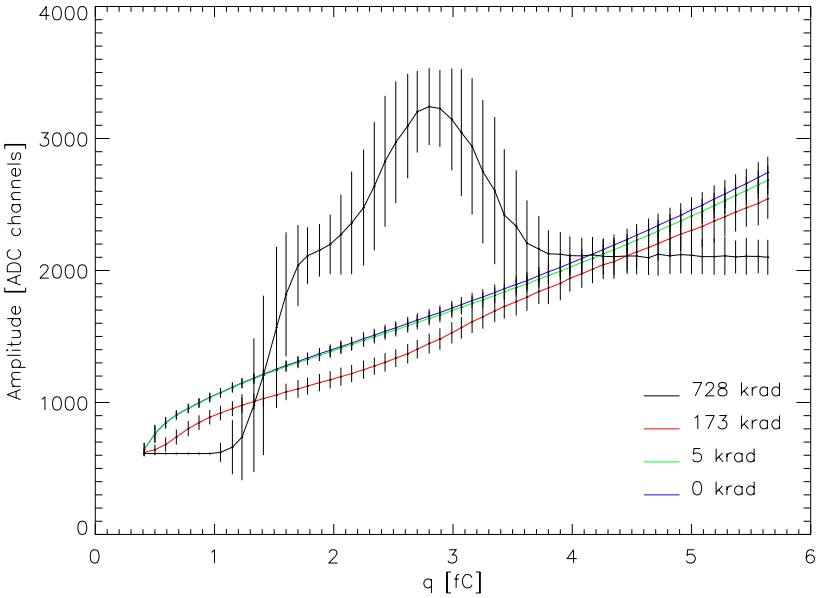

Figure 5.10: Amplitude (converted into ADC channels) of the output signal from the chip 710-1-25 as a function of the input charge for different dose values.

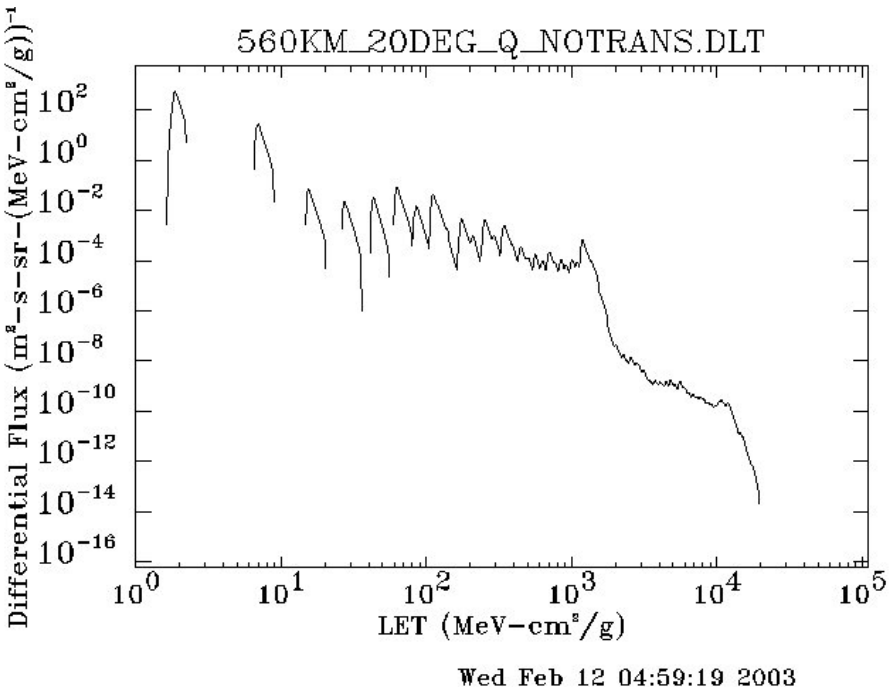

Figure 5.11: Cosmic rays differential flux simulated with CREME96 code at AGILE orbit.

they cannot produce directly SEE, using the CREME96 code only the ions contribution to the cosmic ray flux is evaluated, neglecting the protons.

The cosmic ray protons can indirectly produce SEE because heavy spallation and high LET fragments, produced for example from the interaction of these protons with the tungsten nuclei of the coded mask or collimator or with the bulk silicon nuclei of the chip itself, can hit the XAA1.2. An approximate analysis of this phenomenon is shown in the next subsection (5.7.2).

The planned orbit of the AGILE spacecraft is a circular low Earth orbit at an altitude of 550 km and with an inclination smaller than 10°. In my evaluation I assume a 20° inclination as a conservative approach since for a given altitude the flux of cosmic rays is lower the closer the orbit is to the magnetic equator. A plot of the cosmic rays differential flux simulated with CREME96 code at AGILE orbit can be seen in fig. 5.11.

After the evaluation we find that both the expected rates of latch-up and SEU events are about 10^{-10} events $\cdot$ year^{-1} $\cdot$ chip^{-1} taking into account the Solar steady flux in quiet conditions of the Earth magnetosphere and about $5 \cdot 10^{-6}$ events $\cdot$ year^{-1} $\cdot$ chip^{-1} in case a Solar storm is considered. In both cases less than one event during the entire life of the experiment (3 years) is expected.

Although in the estimation neither latch-up nor SEU events are expected in the XAA1.2 chip, to be conservative a latch-up protection system and a SEU recovery strategy have been designed to protect the SuperAGILE front-end electronic.

Since the latch-up causes a sudden increase in the chip supply currents, overloading the power supply and potentially damaging the chip itself and the wire bondings, we protect the system from this effect inserting a current discriminator in the supply circuit. The discriminator monitors the value of the positive supply current I_{DD} and switches off the power supply when this current exceeds a selected threshold. In the SuperAGILE front-end electronic design the chips are daisy chained in groups of three and the power supply is one for each daisy chain, so in case of a latch-up a whole daisy chain is switched off.

The main problem connected to the SEU events is the unpredictable changing of the chip configuration. To avoid this problem the configuration bit stream must be periodically restored inside the chip memory registers. In orbit we plan to perform at fixed time the so called "electronic calibrations", sending serially the test charge pulses to the input channels to check the value of the gain and the offset of each chain. During this operation the configuration mask is restored every time a channel is enabled to the pulse processing. Since the SEU expected rate is extremely low, by the periodic calibrations we expect to protect the XAA1.2 chips from this effect.

From the launcher properties and the orbital constraints for AGILE mission the expected dose absorbed by the electronic circuits of the payload is about 3 krad and it is mainly absorbed in the transfer orbit when the experiments are switched off. The AGILE hardest electronic components are thus selected to resist to a total dose of about 5 krad. Considering for the spacecraft the orbit specified above and a shielding of about 1 g/cm^2 of aluminum, we find from the CREME96 code that the expected dose absorbed by the electronic devices on-orbit is about $4 \cdot 10^{-4}$ krad $\cdot$ year^{-1}. As can be seen in fig. 5.8 and 5.10, the power consumption variation and the performances degradation of the XAA1.2 chip are not significant for a total dose value of about 5 krad, consequently we do not expect a dramatic variation of the SuperAGILE front-end electronic functionality and performance due to the total dose.

5.7.2 Proton interactions

The PROFIT model (see Calvel et al. (1996) for details) is an approximate evaluation of the proton induced SEE basing on the heavy ions data. The model basic assumption is that the inelastic collision of protons on the chip silicon atoms can produce ^{28}Si ions with most probable LET value about 15 MeV $\cdot$ cm^2 $\cdot$ mg^{-1}.

If Σ_{15}^{SEE} is the cross section of SEE at 15 MeV $\cdot$ cm^2 $\cdot$ mg^{-1} resulting from the interpolation of the irradiation data, taking into account the probability of the ^{28}Si production the resulting saturation cross section of SEE due to protons is

$$\Sigma_p^{SEE} \simeq \Sigma_{15}^{SEE} \cdot c \cdot N_{at} \cdot \overline{\Sigma}_{nuc} \tag{5.7}$$

where c is the thickness of the chip active part (estimated to be 10 μm), N_{at} is the density number of silicon atoms ($5 \cdot 10^{22}$ cm^{-3}) and $\overline{\Sigma}_{nuc} = 6 \cdot 10^{-26}$ cm^2 is the average cross section of the ^{28}Si spallation production by protons between 100 MeV and 200 MeV.

The latch-up interpolated cross section at 15 MeV $\cdot$ cm^2 $\cdot$ mg^{-1} is $\Sigma_{15}^{latch-up} = 7 \cdot 10^{-7}$ cm^2 so from the (5.7) the corresponding proton cross section is $\Sigma_p^{latch-up} \simeq 2 \cdot 10^{-12}$ MeV $\cdot$ cm^2 $\cdot$ mg^{-1}. The SEU interpolated cross section at 15 MeV $\cdot$ cm^2 $\cdot$ mg^{-1} is $\Sigma_{15}^{SEU} = 6.7 \cdot 10^{-6}$ cm^2 so from the (5.7) the corresponding proton cross section is $\Sigma_p^{SEU} \simeq 2 \cdot 10^{-11}$ MeV $\cdot$ cm^2 $\cdot$ mg^{-1}.

Basing on the estimated Σ_p^{SEE} values, the expected rate from protons can be written as

$$r_p^{SEE} \simeq \Sigma_p^{SEE} \cdot F \cdot \Omega \tag{5.8}$$

where F is the flux and Ω is the solid angle. If considering an upper limit $F \cdot \Omega \simeq$ 10 protons $\cdot$ cm^{-2} $\cdot$ s^{-1} (from Zombeck (1990)), the expected latch-up rate is $r_p^{latch-up} \simeq 6 \cdot 10^{-4}$ latch-up $\cdot$year^{-1} $\cdot$ chip^{-1} and the corresponding expected SEU rate is $r_p^{SEU} \simeq 6 \cdot 10^{-3}$ SEU $\cdot$ year^{-1} $\cdot$ chip^{-1}. Also in this case less than one event during the entire lifetime of the SuperAGILE instrument is expected.

5.8 Conclusions

The irradiation tests performed at the SIRAD facility of the 15 MV Tandem accelerator at the Laboratori Nazionali INFN of Legnaro show that the XAA1.2 chip, built with a 0.8 μm CMOS technology on epitaxial layer, can be safely used as a front-end chip for a satellite experiment although this device was not originally developed as a radiation resistant component for space applications.

The latch-up and SEU are two of the main Single Event Effects caused by the radiation environment on electronic circuits. From the accelerator test we evaluate the latch-up and SEU probability and cross section, shown in the figures 5.6 and 5.7 and in the tables from 5.5 to 5.10. We find that the mean LET threshold is 5.0 ± 1.5 MeV $\cdot$ cm^2 $\cdot$ mg^{-1} for the latch-up and 3.9 ± 0.3 MeV $\cdot$ cm^2 $\cdot$ mg^{-1} for the SEU.

Both the cross sections of latch-up and SEU are so small that the occurrence of these effects because of the cosmic ray ions can be excluded. In fact after modeling the cosmic ray environment on orbit using the code CREME96 we find that, considering both the Solar flux steady case and the Solar storm case, the expected rate in orbit due to the ions is less than one latch-up and one SEU event for the entire duration of the AGILE mission. Indeed these estimates might be optimistic because the code does not take into account the detailed distribution of the materials and the spallation products of the particles crossing the spacecraft shielding and the payload passive elements. An approximate estimation of the proton spallation contribution does not increase significantly these rate values.

Although the expected latch-up rate is extremely low, this effect is potentially dangerous because it can severely damage a chip because of overheating. We protect the SuperAGILE front-end electronic from the latch-up using power supply current discriminators. These devices monitor the chip supply currents and switch off the power supply in case of a latch-up. In the front-end electronic layout the power supply is common to

one daisy chain of three chips so we introduced one current discriminator for each daisy chain.

The configuration bit stream in the memory registers, that can be corrupted because of a SEU, is restored periodically during the "electronic calibrations" of the chip, performed using the internal test pulse generator. Since the SEU expected rate is low, this strategy is effective as a protection from this effect. In case of a SEU the data since the previous electronic calibration can be corrected or simply removed.

Furthermore the total dose is not important for the XAA1.2 chips in the SuperAGILE application. In fact, if considering 3 krad as an upper limit to the total dose absorbed by the active layer of the chips on-orbit, we can see that the functionality and the performance of the chips are not significantly affected by this dose value. Since we found that the chip is linear up to a dose of about 173 krad, the XAA1.2 can be safely used in satellite-borne experiments and also in High Energy Physics experiments in low-dose environments.

Chapter 6

The SuperAGILE data analysis programs

This chapter is devoted to the description of the data analysis programs developed during my research work in order to extract most of the information from the laboratory measurements and to produce significant results. Instead of explicitly showing program codes, in this chapter the most important problems connected to the data analysis and the algorithms developed in order to solve them are discussed. The algorithms description is aided by showing block diagrams and screen shots.

6.1 Purpose and requirements

The development and the laboratory tests of the different parts of the SuperAGILE instrument required the design and manufacturing of many different acquisition systems. The SAFEE test equipment (described in sec. 3.6) is developed to evaluate the SAFEE performances and has been used to test the electronic boards of the Simplified Engineering Model (SEM) and of the Proto-Flight Model (PFM). Similarly, the test of the SAIE electronic boards needed a specific SAIE test equipment (described in sec. 3.7) and the data handling unit of the whole payload (PDHU) required a custom PDHU test equipment.

The different test equipments are optimized for the specific electronics under test and also the format of the data that they produce is system specific. The data produced by each test equipment are archived by the DISCoS system, described in 6.2.1, both in binary format and converted into Flexible Image Transport System (FITS) format, a data standard widely used in Astronomy and defined in Hanisch et al. (2001).

A part of my research work involves the development of the software needed to analyse the data produced by the SAFEE and SAIE test equipments during the laboratory tests. Because of the big number of SuperAGILE pixels, the general requirement of the laboratory software is to perform most of the analysis automatically, without requiring the operator to modify the analysis parameters for the different pixels. For the same reason, the software needs to be fast and to produce summarized statistics reports of

the results in order to give a "global view" of the system under test, for example in terms of linearity and noise. All the SuperAGILE data analysis programs use the FITS format (selected for the data analysis software of the whole AGILE mission) as input and output standard format.

In order to satisfy the previously described requirements, the data analysis software has been developed under the RSI Interactive Data Language (IDL) environment[1], that provides various high level data manipulation and fitting procedures and that can be integrated with many programs developed and shared by the Astronomical Community, as for example the widely used Astronomy User's Library[2].

The format of the data produced by the SAFEE and SAIE test equipments is described in sec. 6.2 together with a short overview of the test equipment independent data format used for the photon acquisitions. The software developed to analyse the data produced during the measurements with the electronic pulse generator is described in sec. 6.3. The software developed to analyse the data produced during the photon acquisitions is described in sec. 6.4

The data analysis software is equipped with a Graphical User Interface (GUI) developed using the QT libraries[3]. The IDL programs are integrated within the GUI by means of the KDevelop[4] program interface. Since I am not involved in the development of this GUI, I will not describe this topic further. The package composed of the IDL analysis programs integrated with the GUI is the SuperAGILE Data Analysis Software (SADAS) that is described in sec. 6.5.

The general philosophy of SuperAGILE is to use the same software to analyse calibrations, simulations, laboratory tests and flight data. Therefore a large part of the programs developed during my research work will be integrated in the SuperAGILE standard data analysis software.

6.2 The SuperAGILE data architecture

The SuperAGILE data stream starts from the SAFEE boards, two of which are connected to one of the SAIE boards. The SAIE identifies the triggering daisy chain and provides the data to the PDHU. Some of the data processing, for example the address reconstruction and the images accumulation in case a burst trigger is detected, is performed on-board directly by the PDHU microprocessor. The data are then provided from the PDHU to the OBDH (bus computer) and from there to the telemetry.

Once per orbit the telemetry data are transmitted to the ASI Telemetry Station at the Broglio Space Center in Malindi (Kenya) using a radio link and after to the Telespazio Fucino station near Avezzano (Aq). From Fucino the stream is provided to the ASI Scientific Data Center (ASDC) where the quick-look analysis is performed.

In case a burst trigger is produced by the PDHU, the SuperAGILE image is ac-

[1]Web site `http://www.rsinc.com/idl/`

[2]Web site `http://idlastro.gsfc.nasa.gov/homepage.html`

[3]Web site `http://www.trolltech.com/products/qt/index.html`

[4]Web site `http://www.kdevelop.org`

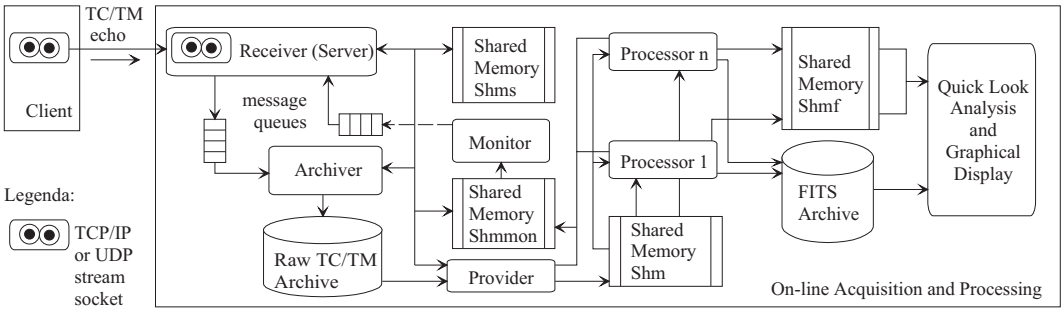

Figure 6.1: Block diagram of the DISCoS software architecture, from Gianotti and Trifoglio (2001).

cumulated and decoded directly on-board, in parallel to the usual photon by photon processing and transmission operations, in order to localize the burst position. The reconstructed coordinates are then transmitted to one of the ORBCOMM constellation satellites and from there to ground with a typical delay of one to ten minutes. This fast link allows the scientists to receive the burst alert information rapidly enough to repoint satellite-borne experiments and ground based telescopes in order to find the counterpart of the event at other wavelengths.

A summary of the main properties of SuperAGILE data and the most important software operations is reported in Lazzarotto et al. (2004).

6.2.1 The DISCoS archiving system

The binary data stream produced by the SAFEE and SAIE test equipments is converted in real time into the ESA packet telecommand (TC) and telemetry (TM) standard format. The use of the ESA TC/TM packets, the same managed by the Electrical Ground Segment Equipment (EGSE) that will be interfaced to the AGILE integrated payload during the tests, allows to develop the same data archiving and accessing architecture for the specific test equipments of each instrument and for the whole payload. For this reason no rewriting of the data archiving procedures is required.

The data telemetry packets are then transmitted via TCP/IP and are archived by means of the Detector Independent Science Console Subsystem (DISCoS), described in Gianotti and Trifoglio (2001). On the same archiving machine the data are stored in binary format (also known as "L0" data format for design purposes) and are also converted into FITS format (also known as "L1" data format for design purposes) by means of specific preprocessors. All the data analysis software then accesses the L1 FITS created archive. A block diagram of the DISCoS software architecture from Gianotti and Trifoglio (2001) is shown in fig. 6.1.

6.2.2 The SAFEE TE data format

The SAFEE TE data contain the same fields for photon acquisitions and electronic pulse measurements. A single SAFEE TE event in L1 format contains 25 fields of different byte length. The data are stored as the first binary extension of a FITS file. The field names and content of the L1 SAFEE TE data are showed in tab. 6.1.

In the electronic calibration data the configuration of the channel under test is encoded using 14 fields, indicating the configuration of a group of events, and called "running parameters". The running parameters are stored in the second binary extension of the FITS data file. Since during the measurement about $50 \div 500$ pulses share the same configuration, in order to reduce the file size the last field of the data table points to the running parameter line containing the configuration. The running parameters field names and content are shown in tab. 6.2, 6.3 and 6.4.

Table 6.1: Data type and format of SAFEE TE L1 output data.

data name	data type	data format
pack_time	packet time	double
time	time [μs] from start	double
count_v	V785 event counter	32-bit unsigned integer
count_b	Board4 event counter	32-bit unsigned integer
MGO_1	MGO of daisy chain 1 [ADC]	16-bit unsigned integer
Out_1	amplitude of daisy chain 1 [ADC]	16-bit unsigned integer
group_1	group of daisy chain 1 [ADC]	16-bit unsigned integer
strip_1	strip of daisy chain 1 [ADC]	16-bit unsigned integer
MGO_2	MGO of daisy chain 2 [ADC]	16-bit unsigned integer
Out_2	amplitude of daisy chain 2 [ADC]	16-bit unsigned integer
group_2	group of daisy chain 2 [ADC]	16-bit unsigned integer
strip_2	strip of daisy chain 2 [ADC]	16-bit unsigned integer
MGO_3	MGO of daisy chain 3 [ADC]	16-bit unsigned integer
Out_3	amplitude of daisy chain 3 [ADC]	16-bit unsigned integer
group_3	group of daisy chain 3 [ADC]	16-bit unsigned integer
strip_3	strip of daisy chain 3 [ADC]	16-bit unsigned integer
MGO_4	MGO of daisy chain 4 [ADC]	16-bit unsigned integer
Out_4	amplitude of daisy chain 4 [ADC]	16-bit unsigned integer
group_4	group of daisy chain 4 [ADC]	16-bit unsigned integer
strip_4	strip of daisy chain 4 [ADC]	16-bit unsigned integer
run_pointer	pointer to running parameters	32-bit unsigned integer
DCon_1	flag of event in daisy chain 1	bit
DCon_2	flag of event in daisy chain 2	bit
DCon_3	flag of event in daisy chain 3	bit
DCon_4	flag of event in daisy chain 4	bit

Table 6.2: Data type and format of the first SAFEE TE running parameter list (configuration of the channel in test).

parameter name	parameter type	parameter format
XA_SAFEE_ID	number of SAFEE	byte
XA_DC_ID	number of daisy chain	byte
XA_ID	number of chip	byte
XA_CHAN_ID	number of channel	8-bit integer
XA_FLAG	activation flag	bit

Table 6.3: Data type and format of the second SAFEE TE running parameter list (configuration of the test charge pulse).

parameter name	parameter type	parameter format
PLS_SAFEE_ID	number of SAFEE	byte
PLS_DC_ID	number of daisy chain	byte
PLS_AMP	pulse amplitude	8-bit integer
PLS_FLAG	activation flag	bit

Table 6.4: Data type and format of the third SAFEE TE running parameter list (configuration of the XAA1.2 DAC).

parameter name	parameter type	parameter format
SET_SAFEE_ID	number of SAFEE	byte
SET_DAC_ID	number of DAC to set	byte
SET_DAC_DIGVALUE	DAC digital value	byte
SET_DAC_ANVALUE	DAC analog value	float
SET_FLAG	activation flag	bit

6.2.3 The SAIE TE data format

The format of the output data from the SAIE test equipment depends on the measurement type. For this reason the dedicated field event_ID has been introduced, indicating the type of recorded data ($0 \div 2$ for photon acquisitions as explained below and 3 for pulse measurements).

During photon acquisitions the time tag is encoded as differential time (with respect to the previous event). If the SAIE does not receive any trigger in 8 ms, it delivers a "dummy event" (with event_ID=1) containing the information about the on-board absolute time. Moreover every 100 events (either photons or dummy events), the SAIE delivers an "absolute time event" (with event_ID=0) containing the information about the on-board time. The photon events are indicated with event_ID=2. In this way the time tag is synchronised with the on-board absolute time at least every 8 ms. The

Table 6.5: Data type and format of SAIE TE L1 photon acquisition output data. The calpulse_ID field is used during electronic pulse measurement and is dummy in this case.

data name	data type	data format
pack_time	packet time	double
event_ID	type of event $(0 \div 3)$	byte
calpulse_ID	number of pulse $(0 \div 3)$	byte
DC_ID	daisy chain number	byte
diff_time	differential time [μs]	16-bit unsigned integer
abs_time_s	absolute time [s]	32-bit unsigned integer
abs_time_us	absolute time [μs]	32-bit unsigned integer
group	group signal [ADC]	16-bit unsigned integer
strip	strip signal [ADC]	16-bit unsigned integer
energy	amplitude [ADC]	16-bit unsigned integer

Table 6.6: Data type and format of SAIE TE L1 electronic pulse output data.

data name	data type	data format
pack_time	packet time	double
event_ID	type of event $(0 \div 3)$	byte
calpulse_ID	number of pulse $(0 \div 3)$	byte
DC_ID	daisy chain number	byte
RealAddress	number of channel in test	16-bit unsigned integer
group	group signal [ADC]	16-bit unsigned integer
strip	strip signal [ADC]	16-bit unsigned integer
energy	amplitude [ADC]	16-bit unsigned integer

format of the SAIE photon data is shown in tab. 6.5.

During electronic pulse measurement the data do not contain time tag while they do contain dedicated fields showing the configuration of the recorded event: calpulse_ID showing the ordinal number of charge amplitude (from 0 to 3) and RealAddress showing the number of channel under test. Both data and configuration are stored in the same FITS binary table without creating additional running parameters table. The format of the electronic pulse data is shown in tab. 6.6.

6.2.4 The TE independent L2 data format

As explained in the previous sections, different test equipments produce data of different formats. In order to write a single set of programs to analyse the photon acquisitions performed with the different test equipments, a test equipment independent data format (called "L2" format being "L1" the specific output of each test equipment as stated above) has been defined. The fields and byte length of the L2 format are shown in tab. 6.7.

Table 6.7: Data type and format of the L2 test equipment independent output data.

data name	data type	data format
count	photon counter	32-bit unsigned integer
photon_id	photon ID	32-bit unsigned integer
time	photon time	32-bit unsigned integer
amplitude	pulse invariant	float
pos	photon address	16-bit integer
detector	detector number	byte

During the reduction process from L1 into L2 format, the strip and group values are converted by means of an address lookup table (LUT) into an address value showing the photon position on the detector and the amplitude is converted into a pulse invariant value by means of a gain LUT. More details about the address reconstruction and amplitude correction are shown in sec. 6.4.1 below. The amplitude correction reduces the spread on the amplitude values due to the non uniformity in the linearity parameters of the different analogue channels. The detector number ($1 \div 4$) field is added to the list to complete the address encoding.

6.3 Analysis of electronic pulse measurements

6.3.1 Analysis of electronic calibrations

The electronic calibrations (defined in sec. 3.3) are a fast and efficient way to measure the XAA1.2 linearity (in terms of offset and gain) and to identify the channels address (by means of the strip and group signals). The electronic calibrations are extensively performed in laboratory, to evaluate and optimize the XAA1.2 performances, and in orbit, to monitor the electronics stability and evaluate the correct chip parameters.

Because of the huge number of channels under test, the most serious requirement of the electronic calibrations analysis software is the capability of performing automatic operations without requiring parameters inserted by the operator. In order to simplify the data analysis tasks, a single program has been developed to process SAFEE TE and SAIE TE data. The block diagrams of the electronic pulse analysis subroutines are shown in fig. 6.2 (SAFEE TE) and fig. 6.3 (SAIE TE). All the parameters configuring the analysis, such as the channels and charge pulse ranges, are inserted at the session start using the GUI menu shown in fig. 6.4.

Because of the small statistics in the electronic calibrations (usually $100 \div 200$ pulses are distributed on about 100 ADC channels amplitude) it is not possible to apply the gaussian hypothesis and to perform a gaussian fit on the amplitude spectrum. The peak position and the sigma of the amplitude distribution are so evaluated by means of the barycenter and the standard deviation. The peak position and standard deviation are not evaluated in the underpopulated (with a small number of events because the charge amplitude is smaller than the threshold) and overpopulated (with additional

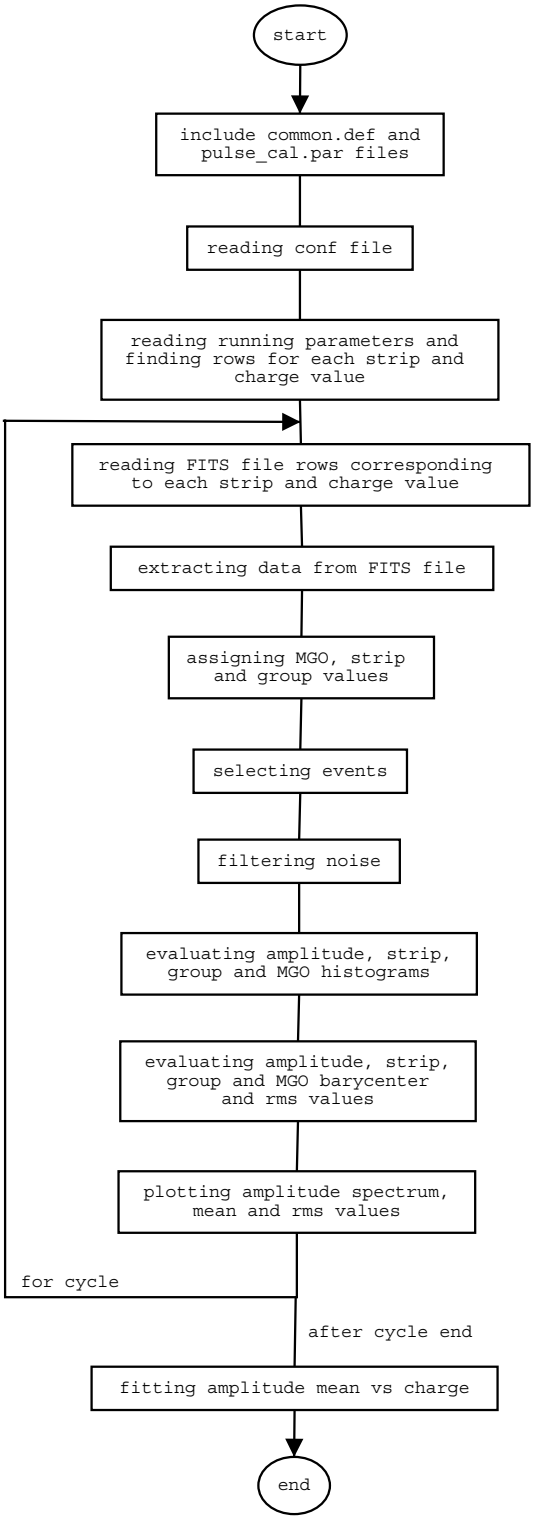

Figure 6.2: Block diagram of the SAFEE TE electronic calibration analysis software.

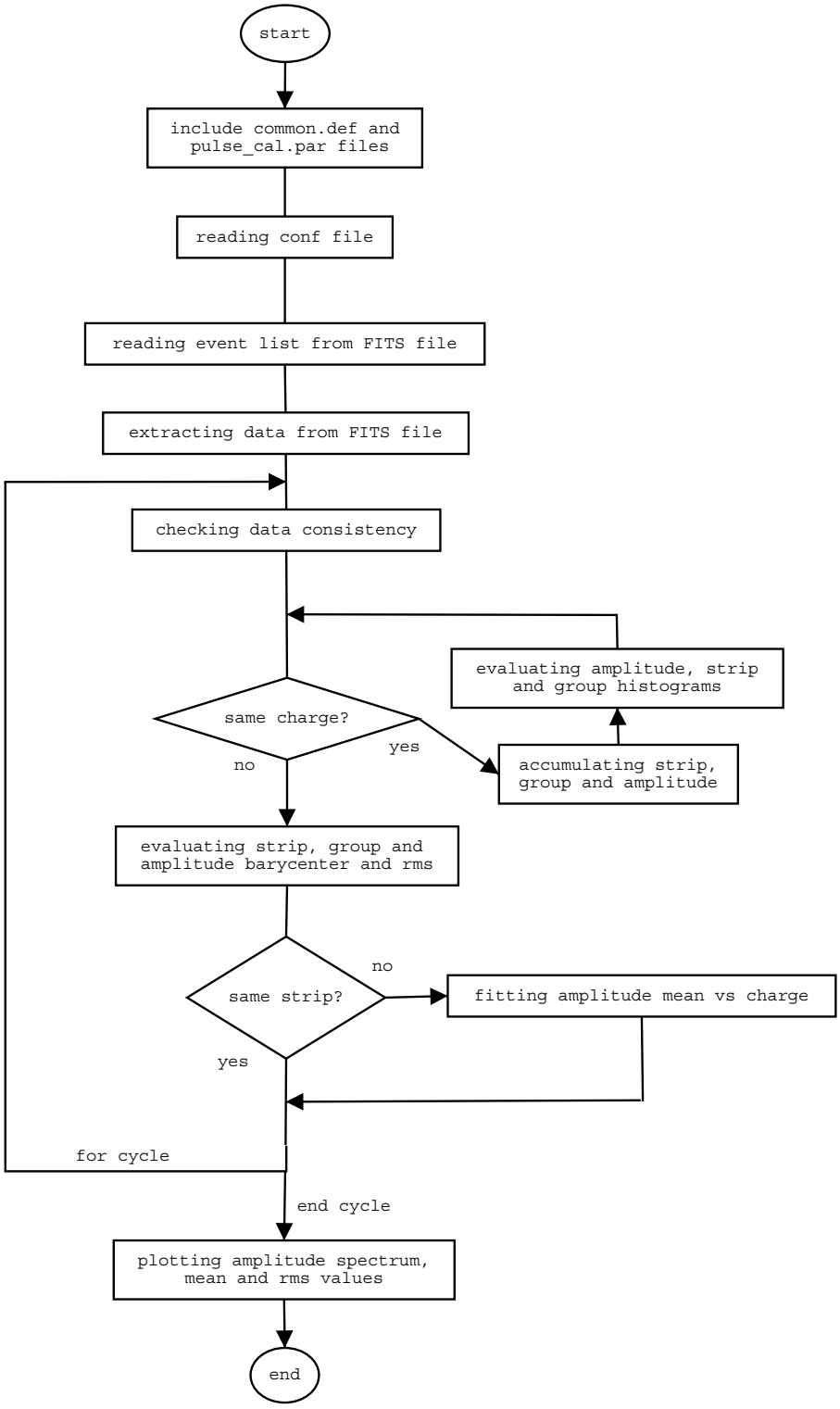

Figure 6.3: Block diagram of the SAIE TE electronic calibration analysis software.

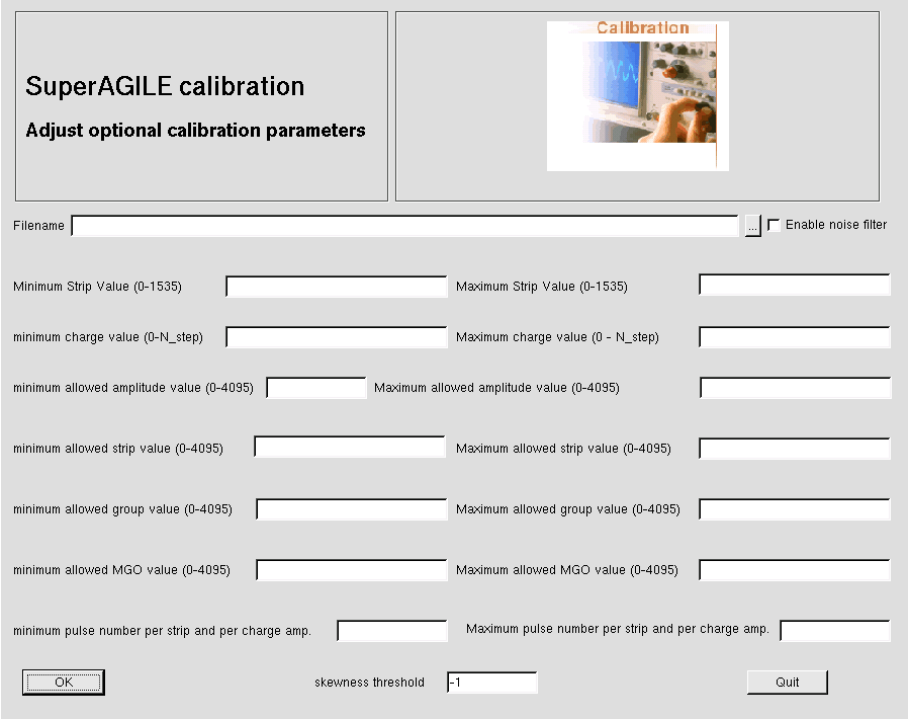

Figure 6.4: GUI menu to insert the electronic calibration parameters.

noise produced events) pulses. The range of the processed pulses population is fixed for all channels at the analysis start in the menu of fig. 6.4. The noise events at small amplitude are automatically removed from the sample using an iterative procedure based on the evaluation of the skewness of the amplitude distribution (the skewness limit is fixed for all channels in the menu of fig. 6.4). Of course skewness is not a maximum likelyhood estimator and, thence, is not the most efficient estimator in the statistical sense. But it is far the fastest we could find.

During the analysis the pulse amplitude spectra and the linear fit of each channel are plotted to a PostScript file. Furthermore the peak position and the FWHM noise of all the amplitudes are arranged in an array of 1536 rows and converted into FITS format. This file contains also the recorded number of pulses for each charge amplitude on each channel.

The peak position is then linearly fitted as a function of the input charge using as error the ratio $\sigma/\sqrt{N}$ where σ is the standard deviation and N is the number of recorded events. From this linear fit the offset and the gain of the selected input channels can be evaluated. The FWHM noise in ADC channels is calculated from the measured standard deviation of the amplitude distribution and is divided by the gain from the linear fit in order to be converted into keV.

The address signals strip and group and the multiplicity signal MGO (only from the SAFEE TE) of each input channel are accumulated and averaged. Since these signals

are fairly stable and do not show variations depending on the input pulse charge, no further analysis is needed. The histograms of the address signals of all the channels in a detector are written to a FITS file.

The analysis results are arranged in two arrays of 1536 rows then stored as FITS binary table extensions of two different files: one file containing the offset, the gain and the χ^2 of all the channels in a detector, the other file containing the strip, group and MGO averaged signals. From this last array the address lookup-table (LUT), associating the ADC channels with strip and group addresses, can be extracted and written to a different FITS file as shown in sec. 6.4.1.

The most important XAA1.2 performances, offset, gain, FWHM (both in ADC channels and keV), strip, group and MGO, are plotted into PostScript files for a single chip and for a whole daisy chain. All the plots contain an upper panel showing the histogram of the corresponding performance and a lower panel showing its value for the different channels.

All the analysis parameters and some ancillary parameters such as the date and the input TE are dumped to an ASCII log file. All the results of the analysis are dumped to a summary ASCII results file showing averaged values and spread of all the XAA1.2 performances discussed above. The average and spread results are shown for each chip and grouped for daisy chain.

6.3.2 Analysis of parameter scans

A parameter scan is a special measurement performed using the electronic pulse and changing the value of one bias during the measurement in order to evaluate the effect of this bias on the XAA1.2 performances. The bias value is changed for each pulse charge amplitude and each input channel. The bias change is obtained by programming the corresponding DAC.

The results of the parameter scan is given by the parameters offset and gain in the fit of the linearity curve (4.3) and the FWHM noise as a function of the bias values. This type of measurement is used to optimize the XAA1.2 performances selecting the circuit biases in order to maximize the signal to noise ratio, as explained in Del Monte et al. (2004).

Since the output signal from the XAA1.2 is processed by a peak stretcher, that extends the signal maximum, it is not possible to sample the output signal shape, as for example using an oscilloscope. To study the signal shape, after switching off the stretcher, a peculiar type of parameter scan can be used, that is the variation of the trigger delay (*TrigDelBias*). With this type of scan it is possible to detect the signal amplitude at different delays after the trigger, therefore sampling the signal shape. The *TrigDelBias* scan is used to study the variation of the output signal shape depending on the *prebias*, *shabias*, *Vfs* and *Vfp* biases during the optimization process.

6.3.3 Analysis of threshold scans

The threshold scan combines pulse measurements and background acquisition. The data analysis of this type of measurements involves both tasks of evaluating the reference voltage as a function of the input charge (a particular parameter scan in which is the reference voltage that is changed) and interpolating the background counting rate in order to find the actual threshold voltage.

The analysis of the reference voltage scan involves the automatic interpolation of the ratio N/N_0 between the detected pulse number N and the input pulse number N_0 for different reference voltage values in order to find the voltage value at which this ratio equals 1/2. No user provided parameter is needed. Then the interpolated reference voltage V is linearly fitted as a function of the input charge q,

$$V = c + d \cdot q. \tag{6.1}$$

During the fitting process, an iterative procedure is applied in order to exclude from the fit the points at small charge amplitude if they significantly increase the spread $(y-y_{fit})^2/(N-2)$ where y is the fit dependent variable input, y_{fit} is the fitted dependent variable and N is the number of y elements.

The results of the reference voltage scan are arranged as two FITS files each one containing one binary extension: one file contains the interpolated threshold voltage of all the pulse amplitudes for all the channels and the other contains the linear fit parameters (intercept and slope) for all the channels.

Once the reference voltage scan results are written to a FITS file, background acquisitions at different reference voltage are performed. The threshold voltage V_{thr} is then evaluated interpolating automatically the background counting rate (evaluated from the ratio of the detected number of events and the time read from the data) in order to find the voltage value such that the electronic noise increases the background counting rate of 0.01 $\text{cts} \cdot \text{s}^{-1} \cdot \text{strip}^{-1}$ (10 % of the SuperAGILE background on-orbit).

For each input channel, the threshold voltage V_{thr} resulting from the interpolation is converted into a threshold charge using the (6.1) and then into the energy threshold E_{thr} by means of the (3.2). In this way, combining background acquisitions and electronic pulse measurements, the energy threshold can be evaluated in each channel of the front-end electronics.

6.4 Analysis of photons acquisitions

Calibration X-ray sources are used at different stages of the SuperAGILE development in order to measure the spectral response and the position uniformity of the instrument. The list of X-ray sources used during the tests is shown in tab. 7.9.

The first step of the photon acquisition pipeline is the data reduction, consisting in the identification of the triggering detector and daisy chain, the following address reconstruction and amplitude correction and finally the rearrangement of the data in the L2 format (see tab. 6.7) and the storage to disk.

During my research work, I have developed programs to reduce the data as described above and to analyse the laboratory produced spectra as shown in sec. 6.4.2 below. Moreover I have collaborated in developing programs to deconvolve the laboratory produced detector images as described in sec. 6.4.3 below.

6.4.1 Address reconstruction and amplitude correction

After recorded, the photon list is reduced off-line in order to reconstruct the photon position and amplitude. Although the data reduction process does not depend on the input test equipment, some of the algorithms involved in the task are test equipment dependent since the data are arranged in different fields. For example the SAIE TE time tag is differential and needs to be reconstructed basing on the absolute time events while the SAFEE TE provides the time tag of the data which does not need to be reconstructed. Two different programs have been developed at this stage: `SFTE_photon_reduce` for the SAFEE TE data and `SITE_photon_reduce` for the SAIE TE data.

The address reconstruction is performed by means of an address LUT, where the address signals (strip and group) are recorded for all the channels in a detector. The address LUT is arranged as a table of 1536 rows (one per channel in a detector) and 7 columns (channel number, detector number, daisy chain number, strip signal minimum value, strip signal maximum value, group signal minimum value and group signal maximum value).

The first step of the address reconstruction is the daisy chain identification, directly provided by the SAIE and performed in the SAFEE TE data by searching which daisy chain delivered an MGO signal in the single event range (from 500 ADC to 2000 ADC). Then the row in the LUT is searched whose ranges of strip and group match both the photon address signals. Once the channel address is reconstructed, the photon amplitude is corrected converting the measured ADC channels into an equivalent energy basing on the offset and gain of the identified channel, by means of a gain LUT. The gain LUT is arranged as a table of 1536 rows (one per channel in a detector) and 5 columns (channel number, detector number, daisy chain number, offset value and gain value).

Both address and gain LUT are built from the output of the electronic calibration using the `address_gain_LUT` program and are then written to disk as the binary extension of two different FITS files. The address reconstruction and amplitude correction tasks convert the L1 data into the test equipment independent L2 format (specified in tab. 6.7). The L2 photon list is finally written to disk as the binary extension of a FITS file.

6.4.2 Analysis of spectra

As part of my research work I have developed the `spectral_analysis` program to process and analyse spectra produced in laboratory using X-ray sources. The spectral analysis is essential in order to study the linearity and the noise (in the form of the FWHM of the spectral lines) of the SuperAGILE flight model units and the results reported in sec. 7.5 are obtained using this program. The block diagram of the spectral

analysis pipeline can be seen in fig. 6.5.

The input to the spectral analysis process is the test equipment independent L2 photon list. After the L2 photon list has been loaded into memory, a quicklook of the data in the form of the spectrum, the detector image and the light curve of the whole dataset is provided. Basing on this quicklook the user can decide to process the whole set of data or to extract a subset selecting strip, amplitude and time ranges. Channels can be excluded from the data also by loading a detector image and selecting a significance level (usually 3σ) marking the noisy channels. In this way a particular dataset can be analysed or pathological subsets can be excluded from the data.

The spectrum of the selected subset is then accumulated with minimum amplitude, maximum amplitude and bin number (or bin size) provided as input from the user. The accumulated spectrum is written to disk in a PostScript file and as the binary extension of a FITS file in order to be recalled for later analysis.

The fit of the peak in the spectrum (produced by the photoelectric absorption) is performed using a gaussian function. In case the source emits two X-ray lines that SuperAGILE cannot resolve, like for example the ^{109}Cd (22.0 keV and 24.9 keV) or the Ba fluorescence source (32.1 keV and 36.4 keV), the fitting function is composed of two gaussian functions, whose integral is constrained by the source branching ratio and the silicon efficiency at the X-ray lines energy. Simple background models (constant or first order linear approximation) complement the fitting function.

The spectral fit provides the peak position, sigma and integral of the X-ray line. Depending on the selected function also the parameters modeling the noise are given. The fit results are written to disk as the binary extension of a FITS file and can be recalled to estimate the system linearity, which is the last stage of the spectral analysis process.

The linearity evaluation starts loading into memory the files containing the spectral fit results. The peak position is then linearly fitted as a function of the X-ray line energy using the peak sigma as an error estimation. The linear fit allows to estimate the offset and the gain of the detection unit independently of the electronic calibration.

For sake of simplicity, not all the pipeline has to be run sequentially but the analysis can be started also at the spectral fit stage (recalling an accumulated spectrum from file) or at the linearity stage (after reading the fit results from file).

The `all_spectra` program has been specifically developed in order to accumulate separately the spectrum of all the strips, because each one can be considered as an independent detector. This program allows also to investigate pathological strips since, for example, the output of a low-threshold strip is dominated by the electronic noise, whose spectrum is composed of a single line at about $10 \div 20$ keV equivalent energy and that is narrower than the spectral lines produced by X-ray sources in nominal-threshold strips.

6.4.3 Analysis of detector images

A detector image is produced from the histogram of the photon position, that is accumulating the counts of each strip in the detector. While the deconvolution of the

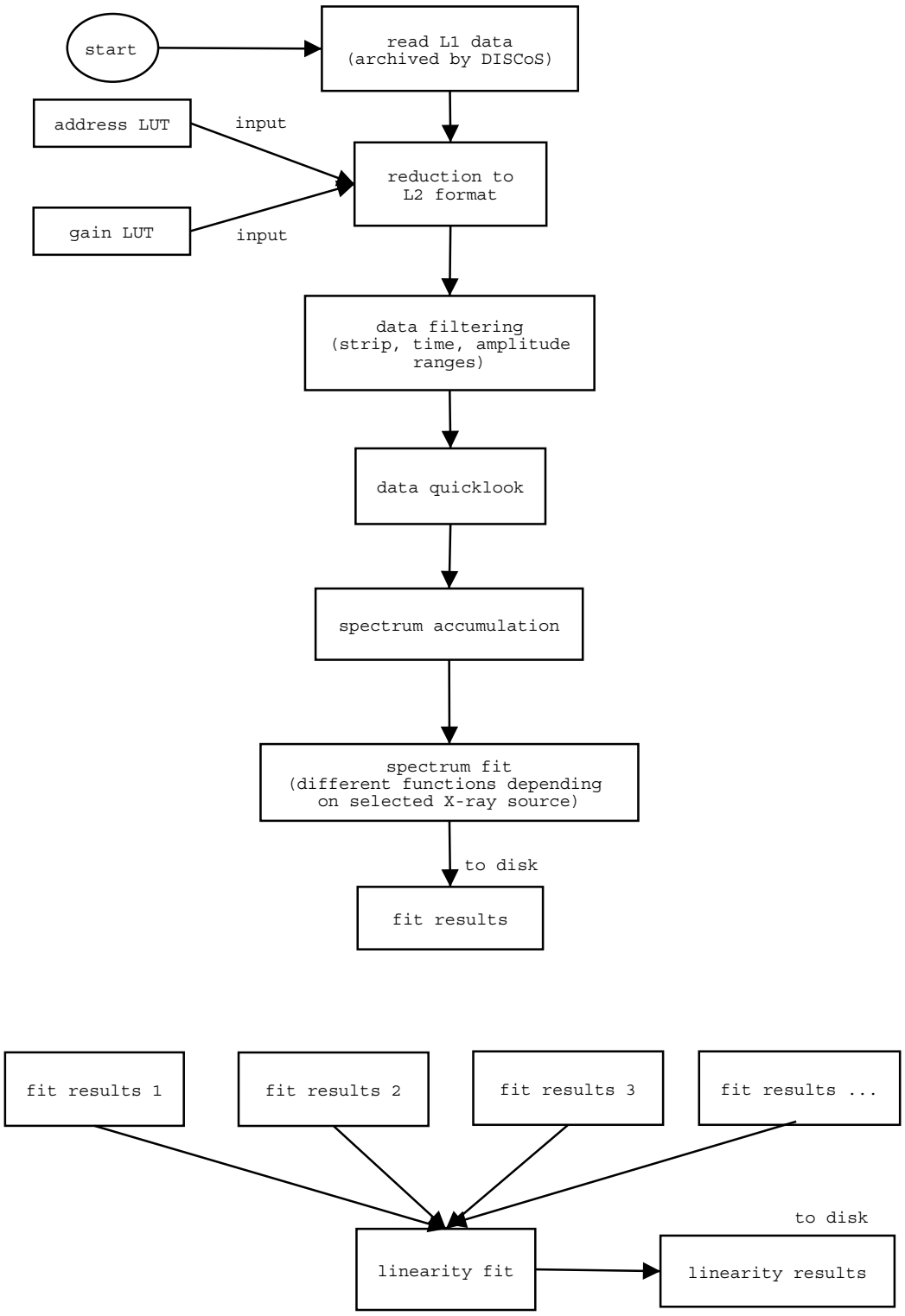

Figure 6.5: Block diagram of the SAFEE TE spectral analysis software.

detector images acquired by the detector coupled to the coded mask are used to evaluate the instrument point spread function, also the detector images acquired without the coded mask can give important information about the detector functionality and performances. I have written the specific `image_analysis` program in order to produce and analyse the detector images.

The program starts from the test equipment independent L2 photon list and produces the detector image of the whole dataset. From the image plot it is possible to check if all the strips are triggering correctly or if there are "dead pixels" (non triggering strips as described in sec. 3.9) or "hot pixels" (strips with an abnormally high counting rate as as described in sec. 3.9).

The search for "hot pixels" is automatically performed in the program while evaluating the strip average count number and standard deviation and extracting the strips whose counting rate is above a significance level inserted by the user (usually 3σ). The detector image is written as the binary extension of a FITS file containing for each strip in a detector the number of counts and the ratio between the distance from the average count number and the standard deviation. The average count number and standard deviation of the whole image are written in the file header.

6.5 The SADAS package

The `SADAS` package is an integrated software developed to process data from all the different test equipments connected to SuperAGILE in its development stages (SAFEE TE, SAIE TE and PDHU TE). In fact the general philosophy of SuperAGILE is to use the same software to analyse calibrations, simulations, laboratory tests and flight data. `SADAS` can perform analysis of electronic calibration with generation of intermediate products stored in FITS files, Postscript plots and results ASCII files, reduction of photon acquisition from L1 test equipment specific format to L2 test equipment independent format, and finally spectral analysis and image of photon acquisitions. Dedicated GUI allow usability even to people non developer of the instrument.

The `SADAS` software is organized with a client-server architecture allowing to control modules written in different programming languages (C++, Trolltech QT based GUI and IDL). Scientific operations are performed using Object Oriented libraries based on Root CERN package and RSI-IDL Astrolib. The distinctive features and the scientific performances of the SADAS package are reviewed in Lazzarotto and Del Monte (2004).

Chapter 7

The SAFEE performance measurements

7.1 Assembly and testing of the SuperAGILE proto-flight model

The assembly of the SuperAGILE proto-flight model (PFM) started at the end of August 2004 at the Mipot[1] company in Cormons, near Gorizia. At Mipot the passive components have been mounted on the SAFEE PCB, designed at IASF in Rome and produced by the German company ILFA[2], and the functionality of the assembled boards has been tested by us before mounting the XAA1.2 chips.

Six boards have been assembled to produce the four SuperAGILE detector modules. Four boards are selected as the SAFEE PFM units and one as a spare. Sorted from the first to be assembled, the boards are identified as PFM-A, PFM-B, PFM-C, PFM-D, and PFM-F. The sixth board (PFM-E) has some functionality problems and is discarded.

After verifying the functionality of all the ASIC in each board, the boards have been extensively tested using the electronic pulse generator and the SAFEE test equipment in order to evaluate their performances before the detector integration. Because of the big number of channels in the SAFEE, the tests aim to evaluate global properties of the boards without deepening the study of the single element performances. The results of these measurements are reported in sec. 7.2.

Then, the SAFEE boards underwent a ten days long burn-in process at a temperature of 75° C. During this process, required by the product assurance procedures, the operation at high temperature stabilizes the components characteristics and reveals defects (often referred to as "infant mortality"). No performance degradation is expected from this procedure. After the burn-in process, all the components showing defects are replaced and the other devices are expected not to show additional sudden failures. To be conservative, the temperature during the burn-in (75°C) is lower than the lowest

[1] Web site `http://www.mipot.com/`

[2] Web site `http://www.ilfa.de/leitseite.html`

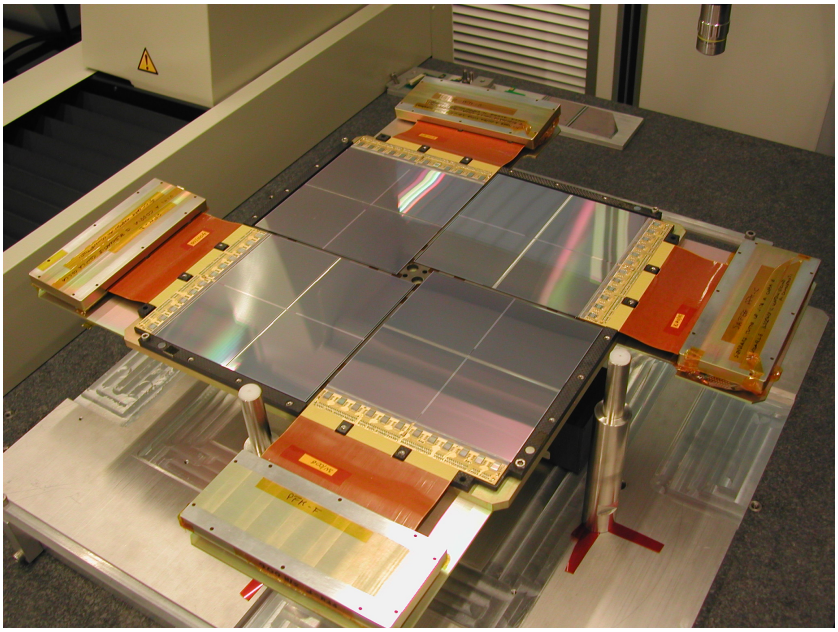

Figure 7.1: Picture of the SuperAGILE detector.

maximum operative temperature of the SAFEE components (80°C for the chip inductor KOA LPC4045).

After the burn-in the boards have been tested again with the electronic pulse generator to verify if the process produced some performance degradation and they have finally been integrated with the silicon microstrip detector. The stability of the SAFEE performances after the burn-in process is studied in sec. 7.3.

A picture of the SuperAGILE detector assembled with the SAFEE boards on the carbon fiber tray is shown in fig. 7.1 and the disposition of the four modules in the SuperAGILE detector is shown in fig. 7.2. The first board to be integrated is the PFM-B, becoming the Detection Unit 1, that did not undergo the burn-in process because of the tight schedule. The first board to be integrated with the detector after the burn-in is the PFM-C, becoming the Detection Unit 3, the Detection Unit 2 comes from the PFM-D, the Detection Unit 4 is integrated from the PFM-F and finally the spare Detection Unit 5 comes from the PFM-A.

As shown in fig. 7.2, SuperAGILE contains a total of four SAFEE boards, with twelve XAA1.2 chips each. The chips within each SAFEE are numbered from 1 to 12 and are grouped together in four daisy chains (DC), numbered from 1 to 4, of three XAA1.2 each.

After the detector integration, the SAFEE performances have been measured again using the electronic pulse generator (as reported in sec. 7.4) to evaluate the effect of the detector integration on the linearity, energy resolution and threshold. In this phase the first measurements with X-ray calibration sources have been performed, aiming to evaluate the SAFEE background uniformity and energy resolution, and are described in

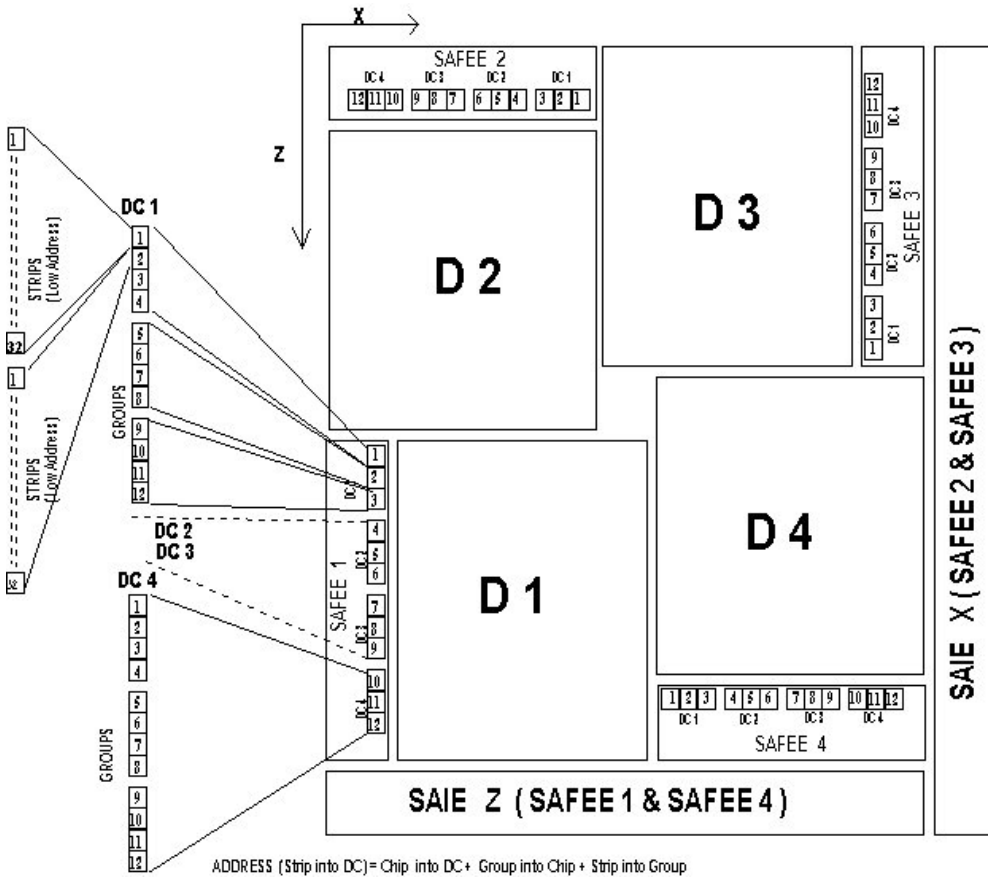

Figure 7.2: Disposition of the SAFEE and the four detection units (D1 ÷ D4) composing the SuperAGILE detector.

sec. 7.5.

The SAFEE performances can be optimized by means of the XAA1.2 bias parameters regulation, in order to decrease the system noise and the energy threshold, as described in sec. 7.6. The bias variation to reduce the noise affects the power consumption, which is the main constraint in this optimization technique.

Finally in sec. 7.7, the measured performances of the SuperAGILE flight model front-end electronics are summarized, the stability of the SAFEE performances after the burn-in process is verified, the performances as measured before and after the silicon microstrip detector integration are discussed and the conclusions are given.

7.2 Performances of the SAFEE before the detector integration

7.2.1 Linearity and electronic noise

The linearity of the SAFEE before the detector integration has been measured by means of the electronic calibration using the SAFEE test equipment. The measurements aim to evaluate the global properties of each SAFEE board in terms of mean values and standard deviation of offset, gain and energy resolution, given by the noise FWHM. The analysis of the electronic calibration is performed by a dedicated software as described in sec. 6.3.1.

In this section, particularly, the results of the electronic calibration of the PFM-B, the first SAFEE board to be integrated and bonded to the detector so becoming the Detection Unit 1, are reported. The XAA1.2 chips are fed with charge pulses from 0.5 fC (corresponding to about 11 keV) to 5 fC (corresponding to about 113 keV). Fifty pulses per amplitude and per channel are selected for the measurement. To reduce the acquisition duration, the electronic calibration is performed on a whole daisy chain (of three chips) at a time.

The offset f and the gain g are measured applying a linear fit to the amplitude as a function of the input charge q following the (4.3). The noise in the electronic calibration is evaluated as the standard deviation σ of the pulse spectra (measured in ADC channels) and is then converted into ΔE_{FWHM} (in keV) following the calibration curve,

$$\Delta E_{FWHM} = 2.35 \cdot \frac{\sigma}{g} \cdot E_0 \cdot \frac{q}{e} \tag{7.1}$$

where the conversion between charge and energy follows the (3.2) and 2.35 is the conversion factor between σ and ΔE_{FWHM} as in (3.5). Of each chip in the PFM board the offset, gain and ΔE_{FWHM} mean values and standard deviation are evaluated and are summarized in tab. 7.1.

The offset f, gain g and noise FWHM of the daisy chain 1 are plotted in fig. 7.3, 7.4 and 7.5 respectively.

The offset f, gain g and noise FWHM of the daisy chain 2 are plotted in fig. 7.6, 7.7 and 7.8 respectively.

The offset f, gain g and noise FWHM of the daisy chain 3 are plotted in fig. 7.9, 7.10 and 7.11 respectively.

The offset f, gain g and noise FWHM of the daisy chain 4 are plotted in fig. 7.12, 7.13 and 7.14 respectively.

As can be seen in the plots and in tab. 7.1, the gain mean values g in the electronic calibration of different daisy chains show variations because the I/V buffer conversion ranges of the SAFEE TE conditioning lines in the different daisy chains are not equalized. This lack of equalization produces a variation in the output amplitude of the same input charge value that reflects also in an offset f variation among the daisy chains. On the

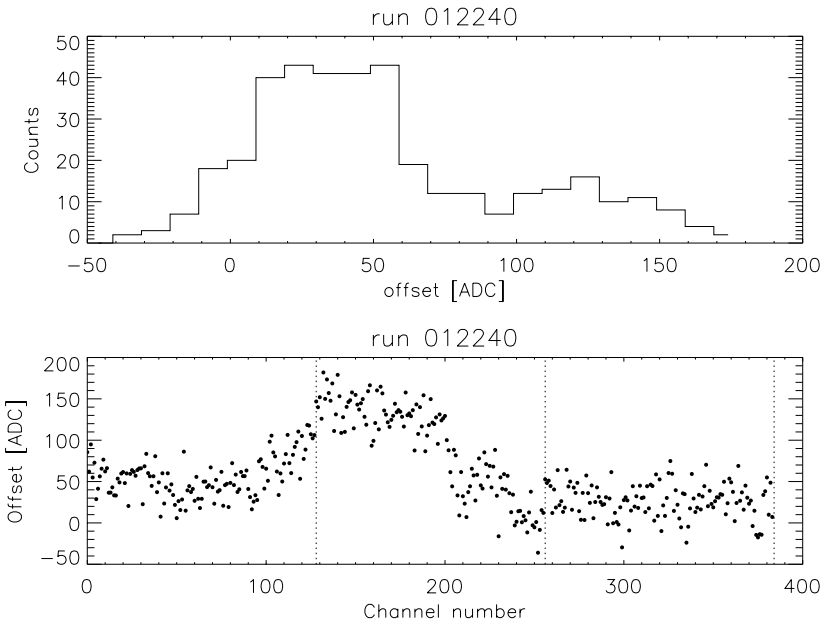

Figure 7.3: Histogram of the offset f from the daisy chain 1 calibration curve (upper panel) and offset value of each channel in the daisy chain (lower panel). The vertical dotted lines mark the chip boundaries within a daisy chain.

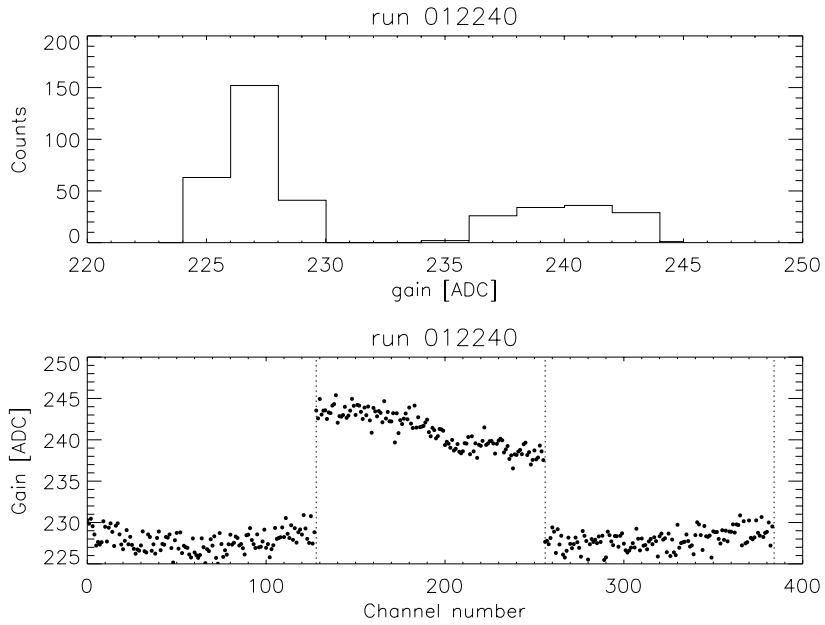

Figure 7.4: Histogram of the gain g from the daisy chain 1 calibration curve (upper panel) and gain value of each channel in the daisy chain (lower panel). The vertical dotted lines mark the chip boundaries within a daisy chain.

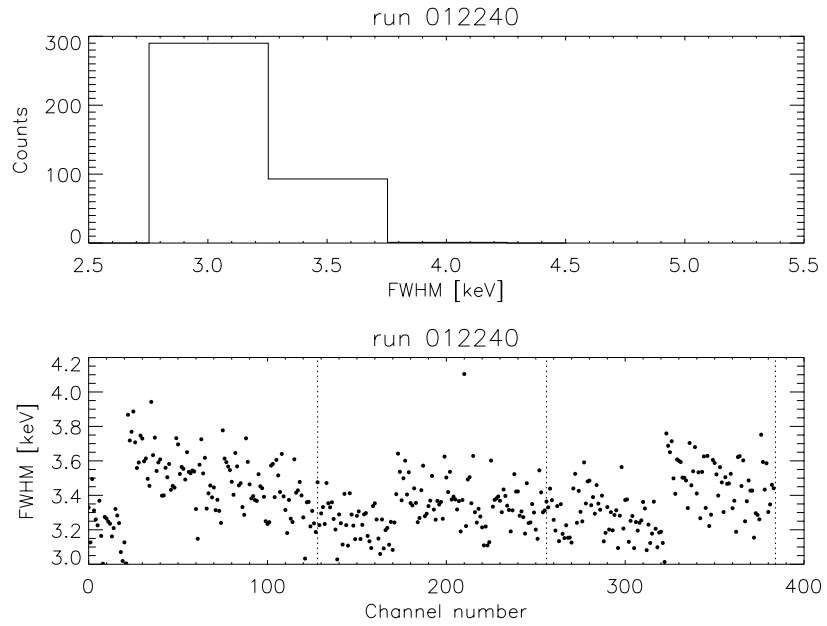

Figure 7.5: Histogram of the noise FWHM from the daisy chain 1 calibration curve (upper panel) and FWHM value of each channel in the daisy chain (lower panel). The vertical dotted lines mark the chip boundaries within a daisy chain.

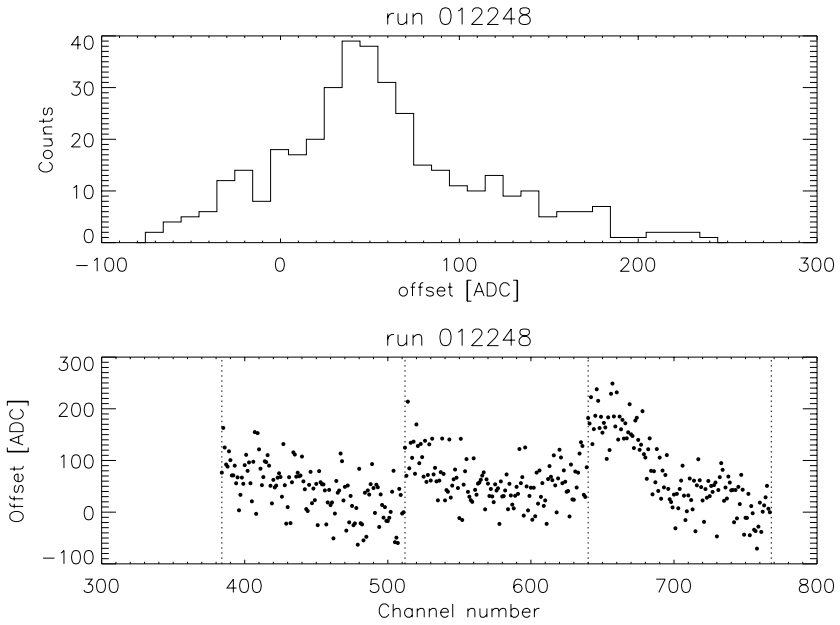

Figure 7.6: Histogram of the offset f from the daisy chain 2 calibration curve (upper panel) and offset value of each channel in the daisy chain (lower panel). The vertical dotted lines mark the chip boundaries within a daisy chain.

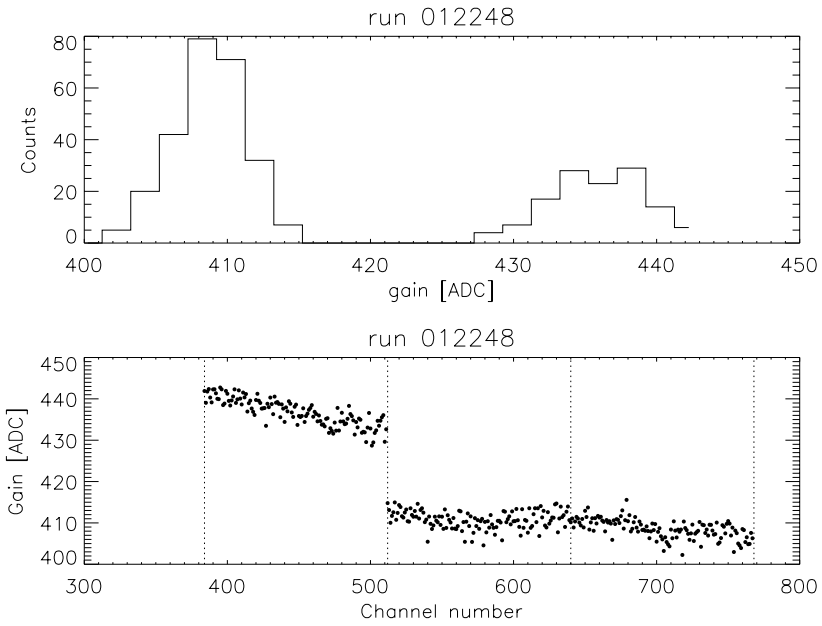

Figure 7.7: Histogram of the gain g from the daisy chain 2 calibration curve (upper panel) and gain value of each channel in the daisy chain (lower panel). The vertical dotted lines mark the chip boundaries within a daisy chain.

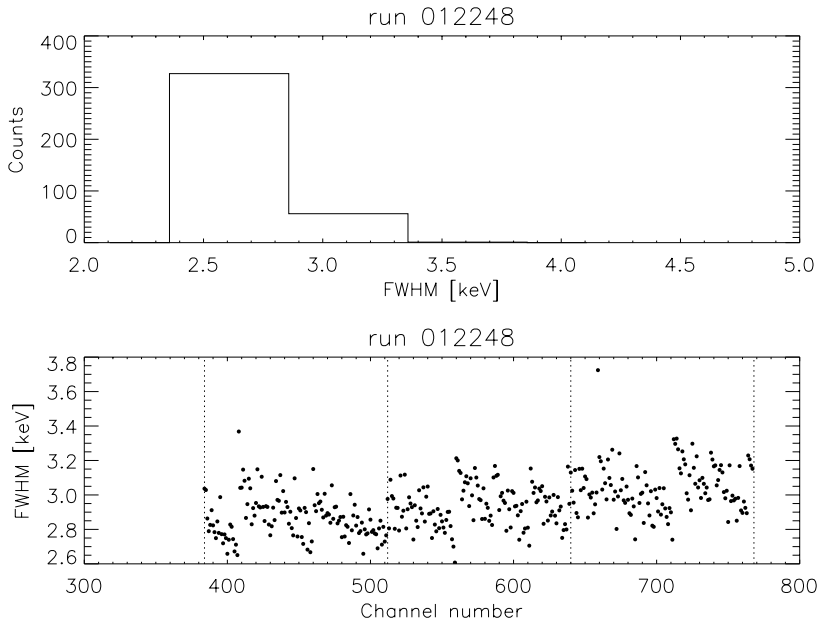

Figure 7.8: Histogram of the noise FWHM from the daisy chain 2 calibration curve (upper panel) and FWHM value of each channel in the daisy chain (lower panel). The vertical dotted lines mark the chip boundaries within a daisy chain.

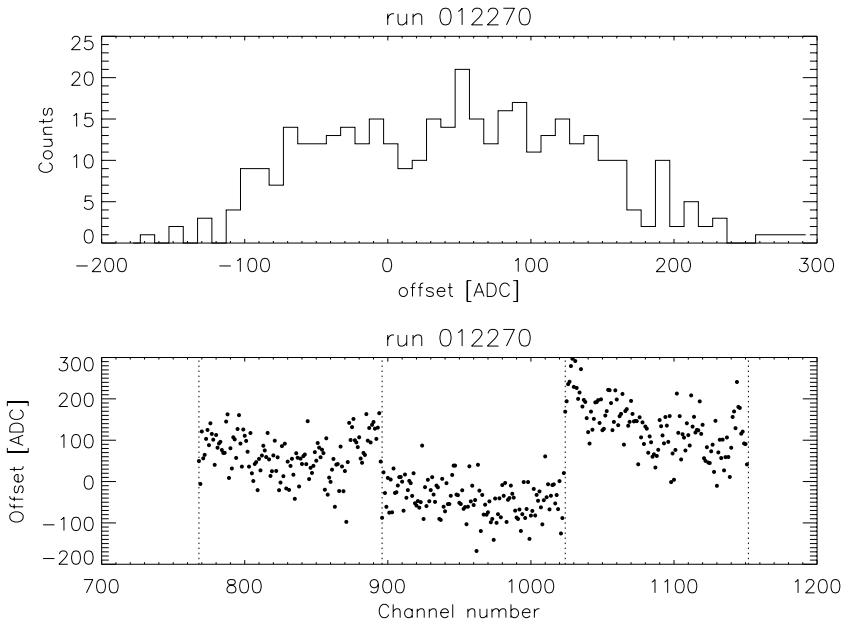

Figure 7.9: Histogram of the offset f from the daisy chain 3 calibration curve (upper panel) and offset value of each channel in the daisy chain (lower panel). The vertical dotted lines mark the chip boundaries within a daisy chain.

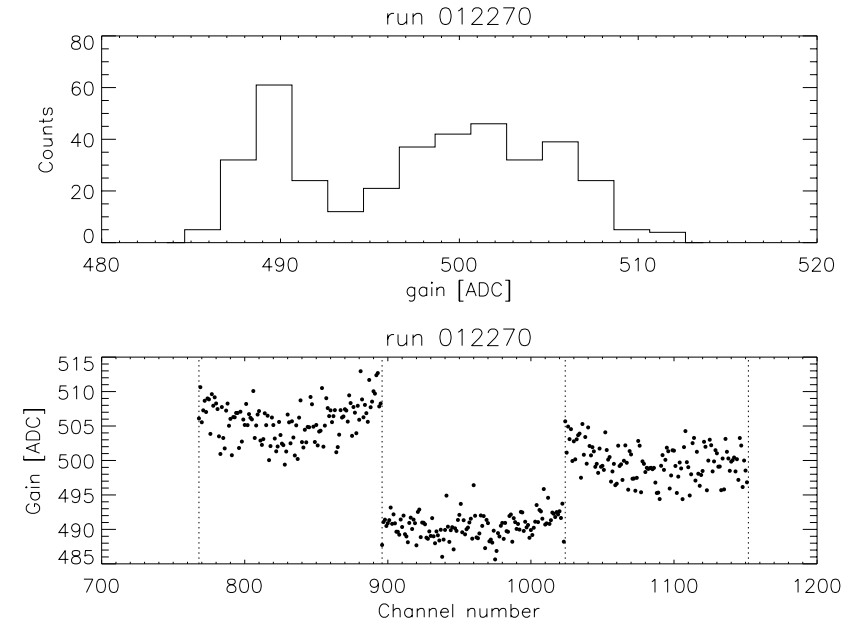

Figure 7.10: Histogram of the gain g from the daisy chain 3 calibration curve (upper panel) and gain value of each channel in the daisy chain (lower panel). The vertical dotted lines mark the chip boundaries within a daisy chain.

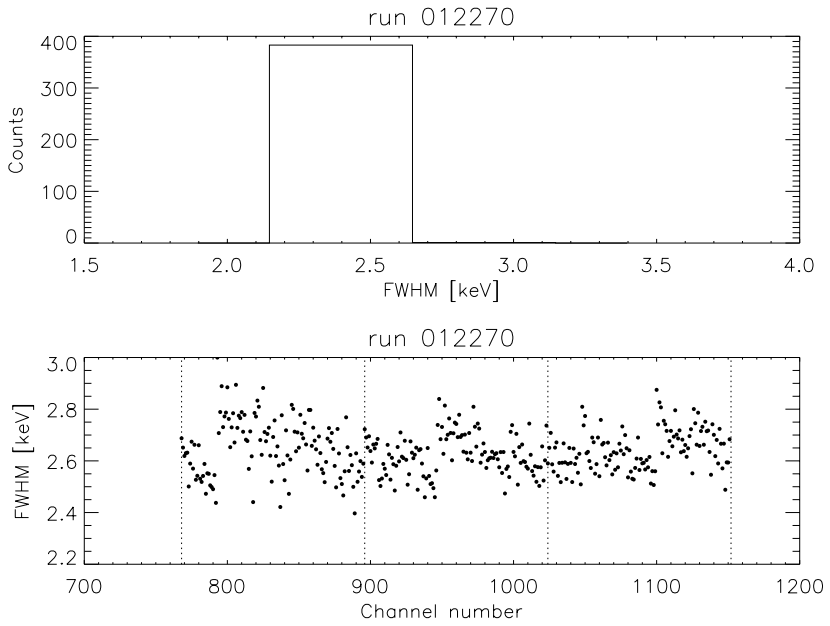

Figure 7.11: Histogram of the noise FWHM from the daisy chain 3 calibration curve (upper panel) and FWHM value of each channel in the daisy chain (lower panel). The vertical dotted lines mark the chip boundaries within a daisy chain.

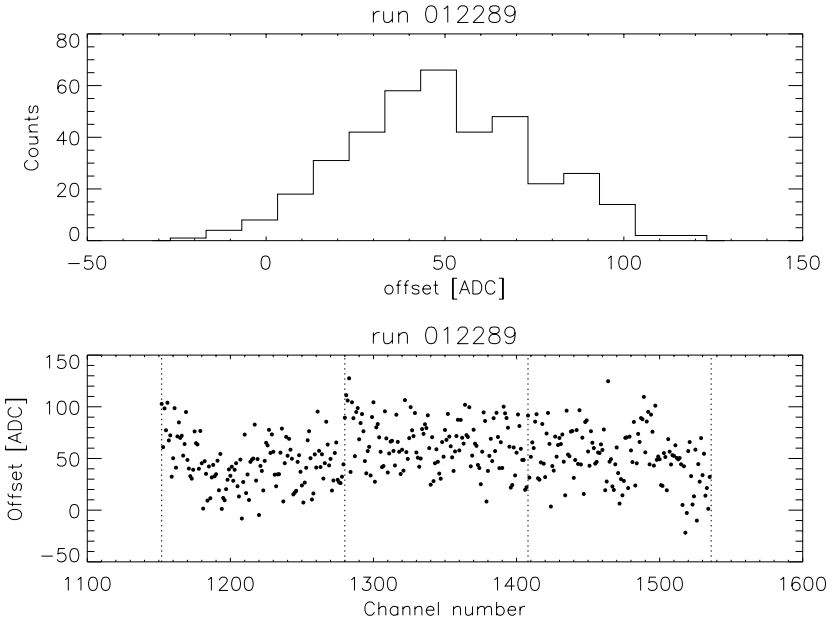

Figure 7.12: Histogram of the offset f from the daisy chain 4 calibration curve (upper panel) and offset value of each channel in the daisy chain (lower panel). The vertical dotted lines mark the chip boundaries within a daisy chain.

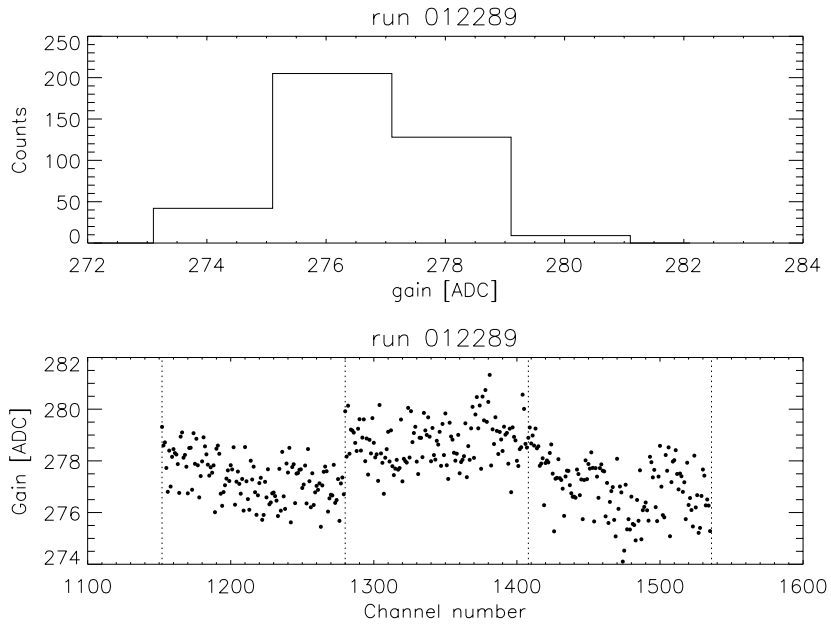

Figure 7.13: Histogram of the gain g from the daisy chain 4 calibration curve (upper panel) and gain value of each channel in the daisy chain (lower panel). The vertical dotted lines mark the chip boundaries within a daisy chain.

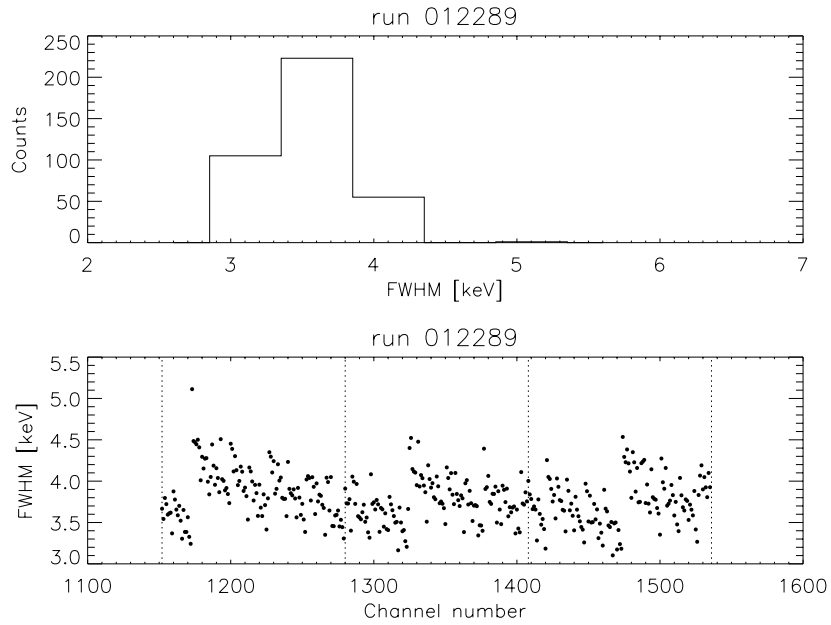

Figure 7.14: Histogram of the noise FWHM from the daisy chain 4 calibration curve (upper panel) and FWHM value of each channel in the daisy chain (lower panel). The vertical dotted lines mark the chip boundaries within a daisy chain.

Table 7.1: Detection Unit 1 electronic calibration before the detector integration. In the table $\bar{f}$ is the offset mean value, $\sigma(f)$ is the offset standard deviation, $\bar{g}$ is the gain mean value, $\sigma(g)$ is the gain standard deviation, $\overline{\Delta E}_{FWHM}$ is the FWHM mean value and $\sigma(\Delta E_{FWHM})$ is the FWHM standard deviation.

XA	DC	$\bar{f}$ [ADC]	$\sigma(f)$ [ADC]	$\bar{g}$ ADC/fC]	$\sigma(g)$ [ADC/fC]	$\overline{\Delta E}_{FWHM}$ [keV]	$\sigma(\Delta E_{FWHM})$ [keV]
1	1	55.5	24.8	227.8	1.3	3.4	0.2
2	1	92.0	55.4	241.1	2.2	3.3	0.1
3	1	27.0	21.0	227.9	1.1	3.4	0.2
4	2	43.7	49.0	436.8	3.3	2.9	0.1
5	2	61.7	43.4	410.8	2.2	2.9	0.1
6	2	76.5	74.9	408.6	2.3	3.0	0.1
7	3	64.5	51.0	505.8	2.8	2.7	0.1
8	3	-41.8	43.4	490.5	1.8	2.6	0.1
9	3	133.3	63.0	499.7	2.6	2.6	0.1
10	4	45.0	23.9	277.3	0.9	3.9	0.3
11	4	64.6	23.6	278.7	0.9	3.8	0.3
12	4	51.7	26.4	277.0	1.1	3.7	0.3

other hand the FWHM values, resulting from the ratio in (7.1), are closer and consistent at $3\,\sigma$ significance level.

The uniformity of the offset f, gain g and FWHM values can be evaluated from the results in tab. 7.1:

$$u(f) \equiv \frac{\sigma(f)}{|\bar{f}|} \tag{7.2}$$

$$u(g) \equiv \frac{\sigma(g)}{\bar{g}} \tag{7.3}$$

$$u(\Delta E_{FWHM}) \equiv \frac{\sigma(\Delta E_{FWHM})}{\overline{\Delta E}_{FWHM}} \tag{7.4}$$

and is shown in tab. 7.2. As can be seen in the table, the gain shows a uniformity level better than 1 % in all the 12 XAA1.2 chips, the noise FWHM uniformity ranges between 3.3 % and 8.1 % while the offset uniformity ranges between 37 % and 114 %.

The noise FWHM measured during the electronic calibration increases with the charge pulse amplitude. As an example, the plot of the FWHM mean values measured on the PFM-B daisy chain 2 at different pulse charge values is shown in fig. 7.15. After excluding the charge values $q \leq 2$ fC, where the pulse spectrum and consequently the noise FWHM are affected by the threshold, applying a linear fit to the measured $\overline{\Delta E}_{FWHM}$ values as a function of the input charge q,

$$\overline{\Delta E}_{FWHM} = a + b \cdot q \tag{7.5}$$

Table 7.2: Detection unit 1 uniformity before the detector integration. In the table $u(f)$ is the offset uniformity as in (7.2), $u(g)$ is the gain uniformity as in (7.3) and $u(\Delta E_{FWHM})$ is the FWHM noise uniformity as in (7.4).

XA	DC	$u(f)$ [%]	$u(g)$ [%]	$u(\Delta E_{FWHM})$ [%]
1	1	45	0.6	5.9
2	1	60	0.9	3.0
3	1	78	0.5	5.9
4	2	114	0.8	3.4
5	2	70	0.5	3.4
6	2	98	0.6	3.3
7	3	79	0.6	3.7
8	3	104	0.4	3.8
9	3	47	0.5	3.8
10	4	53	0.3	7.7
11	4	37	0.3	7.9
12	4	51	0.4	8.1

the fit parameters are $a = 2.85 \pm 0.02$ keV, $b = (3.5 \pm 0.6) \cdot 10^{-2}$ keV $\cdot$ fC^{-1}. The linear fit is superimposed in the plot as a dotted line. The increase in the FWHM noise can be explained with a noise contribution, introduced by the test equipment electronics, proportional to the charge pulse amplitude. In fact the quadratic difference between the maximum and minimum $\overline{\Delta E}_{FWHM}$ values gives 0.6 keV, corresponding to about 188 e$^-$, a measure of the extra noise introduced by the SAFEE TE.

7.2.2 The background and the threshold

The threshold of the flight model SAFEE is evaluated basing on the electronic pulse threshold scan and the background acquisition as in sec. 3.5.1. The measurements are analysed following the technique described in sec. 6.3.3 and the parameters c (intercept) and d (slope) of the linear fit in (6.1) are estimated.

The results of the threshold scan and the threshold mean values are summarized in tab. 7.3. In the tables the mean value and the standard deviation of the intercept ($\bar{c}$ and $\sigma(c)$ respectively) and the slope ($\bar{d}$ and $\sigma(d)$ respectively) of the threshold scan are reported. Because of schedule restriction, the threshold scan has been performed in a whole daisy chain at a time. Since the intercept and slope are evaluated basing on the detected number of pulses at different threshold voltage values, they are not affected by the equalization of the I/V converters among the different daisy chains and are much closer in different daisy chains for this reason.

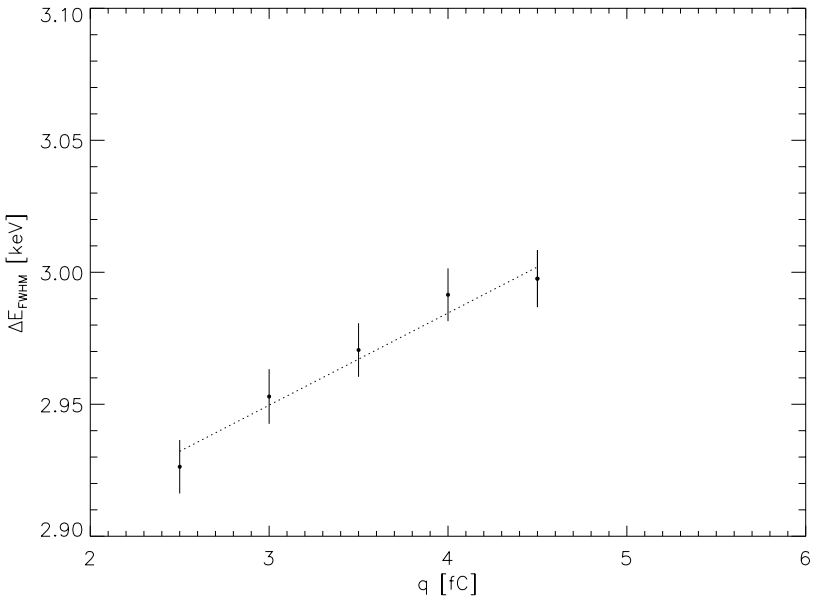

Figure 7.15: Plot of the FWHM measured on the PFM-B daisy chain 2 before the detector integration at different pulse charge values.

Table 7.3: SAFEE PFM-B (Detection unit 1) threshold before the detector integration.

DC	XA	$\bar{c}$ [mV]	$\sigma(c)$ [mV]	$\bar{d}$ [mV/fC]	$\sigma(d)$ [mV/fC]	V_{thr} [mV]	$\bar{E}_{thr}$ [keV]	$\sigma(E_{thr})$ [keV]
1	1, 2, 3	-72.4	24.9	309.4	8.6	4.25	8.7	1.6
2	4, 5, 6	-76.0	29.7	306.5	10.2	5.67	10.2	2.0
3	7, 8, 9	-59.4	26.3	308.0	8.3	4.25	7.8	1.8
4	10, 11, 12	-54.6	23.4	304.7	9.7	2.84	6.3	1.5

7.3 Verification of the performances stability after the burn-in process

The stability of the SAFEE performances in terms of gain g, noise ΔE_{FWHM} and threshold E_{thr} is verified on the PFM-C board before the detector integration that will make it the Detection Unit 3. The performances of this board as measured before the burn-in process are reported in tab. 7.4 and the performances after the burn-in are shown in tab. 7.5.

As can be seen comparing the data in tab. 7.4 and 7.5, the gain values are consistent within 1σ with the exception of the first and the sixth to ninth XA values, that are consistent at $2\,\sigma$, and the fifth chip, that ranges at $3\,\sigma$. The noise ΔE_{FWHM} values are consistent at $1\,\sigma$ significance level apart from the third XA value that is consistent at

Table 7.4: Performances of the SAFEE PFM-C before the burn-in process.

XA	DC	$\bar{g}$ [ADC/fC]	$\sigma(g)$ [ADC/fC]	$\overline{\Delta E}_{FWHM}$ [keV]	$\sigma(\Delta E_{FWHM})$ [keV]	$\bar{E}_{thr}$ [keV]	$\sigma(E_{thr})$ [keV]
1	1	178.8	1.0	4.5	0.5	8.1	1.9
2	1	196.8	1.7	4.3	0.5	10.2	2.0
3	1	182.9	0.8	4.0	0.2	12.3	5.2
4	2	633.5	19.5	2.9	0.4	5.0	1.2
5	2	599.2	2.6	2.8	0.1	5.4	1.9
6	2	603.9	3.4	2.9	0.3	4.6	1.1
7	3	436.0	2.2	3.2	0.4	8.8	2.0
8	3	425.1	1.9	3.0	0.1	7.8	1.8
9	3	416.7	2.5	3.1	0.2	8.5	1.9
10	4	262.5	1.3	4.4	0.4	7.6	1.5
11	4	270.8	1.0	4.2	0.4	7.0	1.7
12	4	259.1	1.4	4.2	0.4	6.9	1.3

Table 7.5: Performances of the SAFEE PFM-C after the burn-in process.

XA	DC	$\bar{g}$ [ADC/fC]	$\sigma(g)$ [ADC/fC]	$\overline{\Delta E}_{FWHM}$ [keV]	$\sigma(\Delta E_{FWHM})$ [keV]	$\bar{E}_{thr}$ [keV]	$\sigma(E_{thr})$ [keV]
1	1	180.4	1.1	5.0	0.3	8.1	2.4
2	1	198.6	1.8	5.1	0.3	10.4	4.3
3	1	184.1	0.9	4.9	0.3	10.2	2.1
4	2	635.9	17.7	3.1	0.2	4.0	1.3
5	2	604.8	2.7	3.0	0.2	6.1	1.1
6	2	610.6	2.4	3.1	0.1	3.6	1.1
7	3	440.4	2.2	3.1	0.3	8.7	1.8
8	3	428.7	2.0	2.9	0.1	6.0	1.8
9	3	419.5	2.1	3.0	0.2	7.3	1.8
10	4	262.7	1.2	4.3	0.3	5.2	2.0
11	4	270.9	1.5	4.0	0.4	7.7	2.0
12	4	260.5	1.3	4.1	0.3	6.5	2.0

$3\,\sigma$. Finally all the threshold values before and after the burn-in process are consistent at $1\,\sigma$ significance level.

As a conclusion, the burn-in process affects marginally the XAA1.2 gain while its effects on the noise FWHM and the threshold can be neglected.

7.4 Performances of the SAFEE after the detector bonding measured with the electronic calibration

This section deals with the measurements of the SAFEE performances after the detector integration and bonding using the electronic pulse generator. Particularly, the measured performances of the Detection Unit 1 and the comparison with the performances before the detector integration are reported. Because of schedule restrictions, this SAFEE board has not been subjected to the burn-in process.

As explained in sec. 4.2, the capacitance of the silicon microstrip detector produces a charge division between the preamplifier feedback capacitance (0.2 pF) and the detector capacitance (30 pF $\cdot$ strip^{-1}) producing a decrease in the output amplitude for the same input charge value. The main result connected to this phenomenon is the gain decrease after the detector integration. The SAFEE linearity and energy resolution have been measured after the detector integration and the results are summarized in sec. 7.4.1.

The detector connection to the front-end electronics produces also an increase in the overall noise because of the various noise contributions of the detector itself, as estimated in sec. 3.4. For this reason the SAFEE background and threshold have been evaluated after the detector integration and the results are described in sec. 7.4.2.

7.4.1 Linearity and electronic noise

After the detector integration, the SAFEE board linearity is measured again by means of the electronic calibration. The XAA1.2 are fed with charge pulses from 0.5 fC (corresponding to about 11 keV) to 5.5 fC (corresponding to about 124 keV). Fifty pulses per amplitude and per channel are selected for the measurement. Also in this case, to reduce the acquisition time the electronic calibration is performed on a whole daisy chain at a time. The linearity measurements results are shown in tab. 7.6. Channels with gain smaller than $3\,\sigma$ or noise FWHM bigger than $3\,\sigma$ are considered as pathological and are excluded from the analysis.

The offset f, gain g and noise FWHM of the daisy chain 1 are plotted in fig. 7.16, 7.17 and 7.18 respectively.

The offset f, gain g and noise FWHM of the daisy chain 2 are plotted in fig. 7.19, 7.20 and 7.21 respectively.

The offset f, gain g and noise FWHM of the daisy chain 3 are plotted in fig. 7.22, 7.23 and 7.24 respectively.

The offset f, gain g and noise FWHM of the daisy chain 4 are plotted in fig. 7.25, 7.26 and 7.27 respectively.

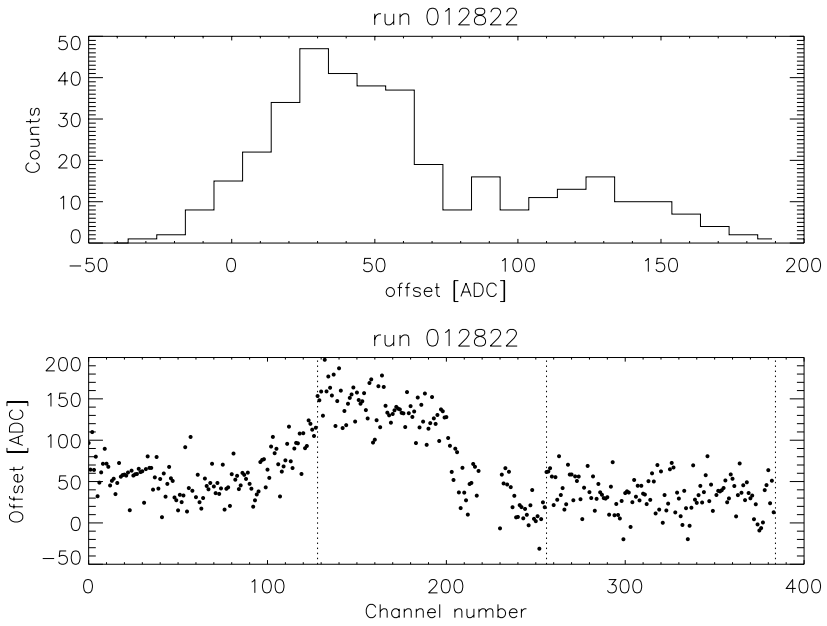

Figure 7.16: Histogram of the offset f from the daisy chain 1 calibration curve (upper panel) and offset value of each channel in the daisy chain (lower panel) after the detector integration and bonding. The vertical dotted lines mark the chip boundaries within a daisy chain.

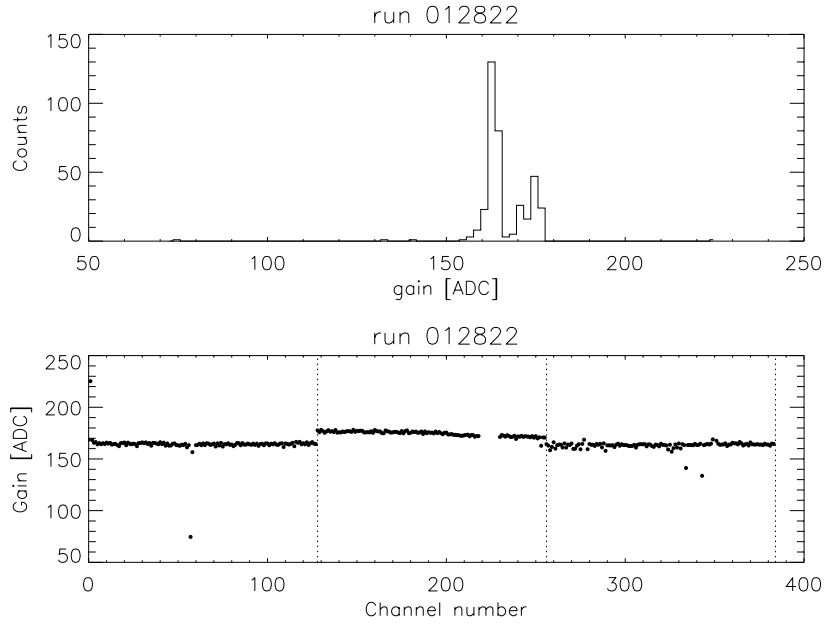

Figure 7.17: Histogram of the gain g from the daisy chain 1 calibration curve (upper panel) and gain value of each channel in the daisy chain (lower panel) after the detector integration and bonding. The vertical dotted lines mark the chip boundaries within a daisy chain.

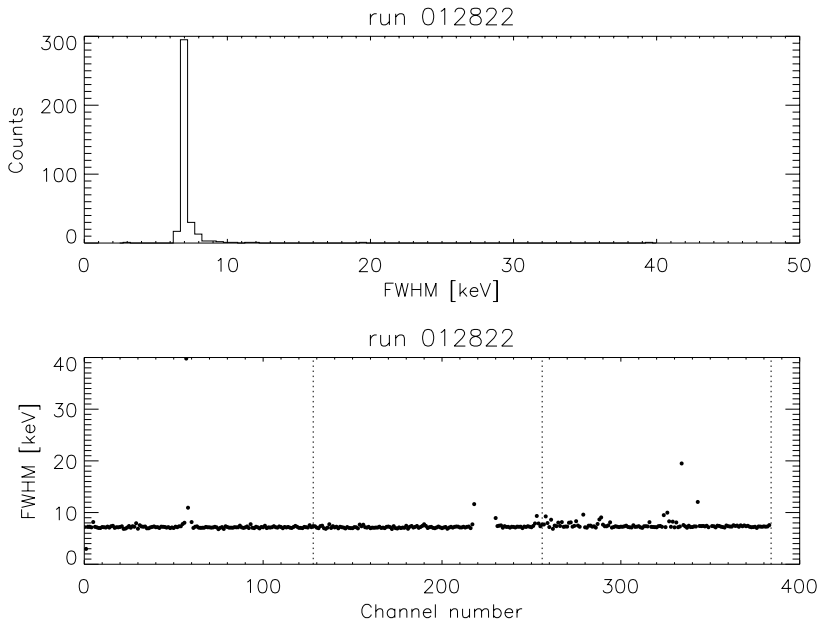

Figure 7.18: Histogram of the noise FWHM from the daisy chain 1 calibration curve (upper panel) and FWHM value of each channel in the daisy chain (lower panel) after the detector integration and bonding. The vertical dotted lines mark the chip boundaries within a daisy chain.

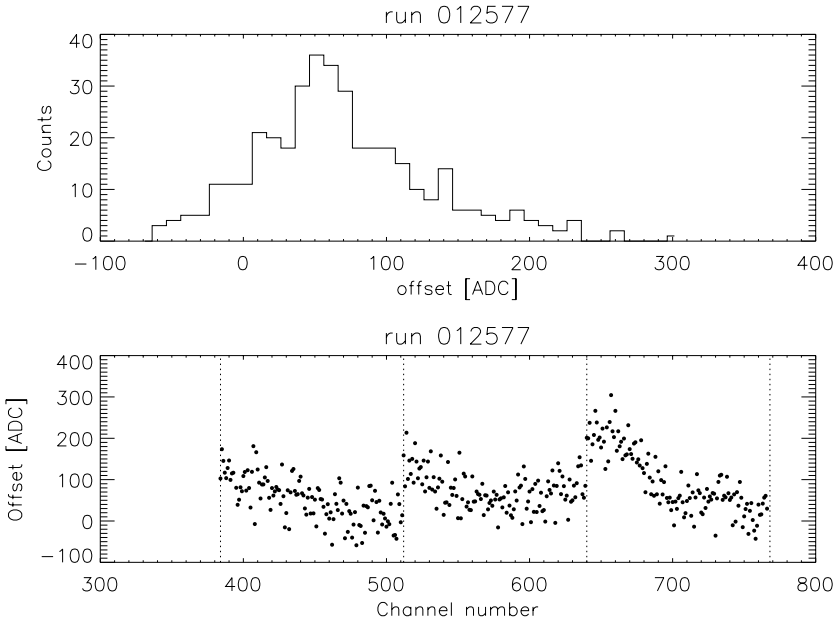

Figure 7.19: Histogram of the offset f from the daisy chain 2 calibration curve (upper panel) and offset value of each channel in the daisy chain (lower panel) after the detector integration and bonding. The vertical dotted lines mark the chip boundaries within a daisy chain.

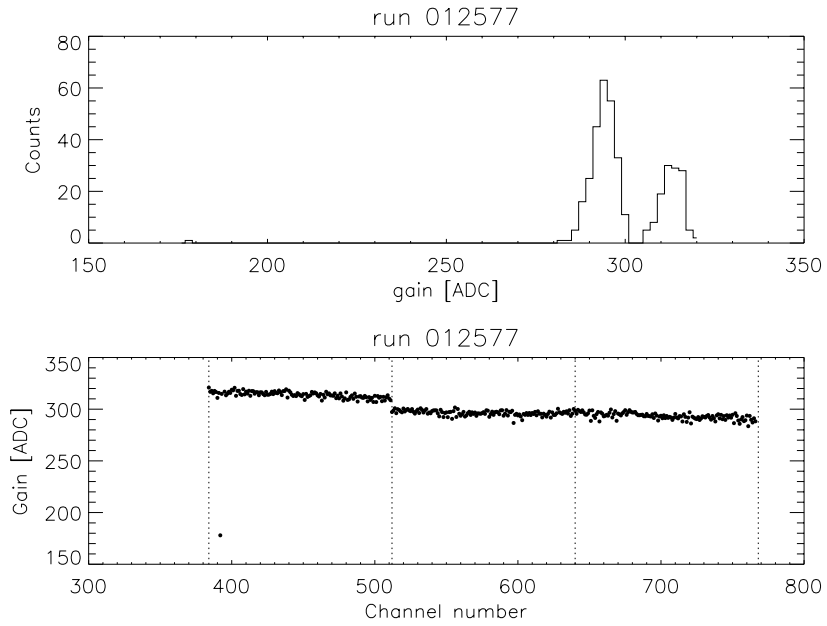

Figure 7.20: Histogram of the gain g from the daisy chain 2 calibration curve (upper panel) and gain value of each channel in the daisy chain (lower panel) after the detector integration and bonding. The vertical dotted lines mark the chip boundaries within a daisy chain.

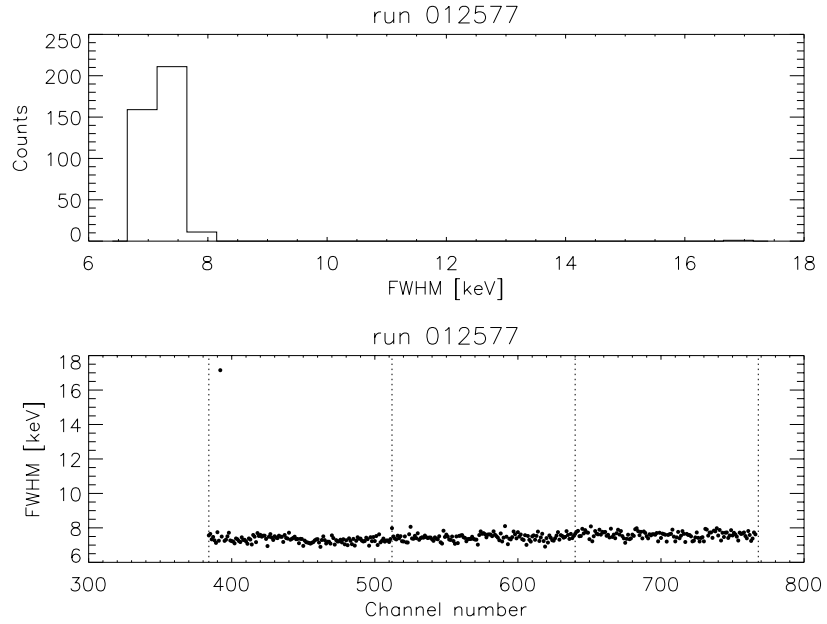

Figure 7.21: Histogram of the noise FWHM from the daisy chain 2 calibration curve (upper panel) and FWHM value of each channel in the daisy chain (lower panel) after the detector integration and bonding. The vertical dotted lines mark the chip boundaries within a daisy chain.

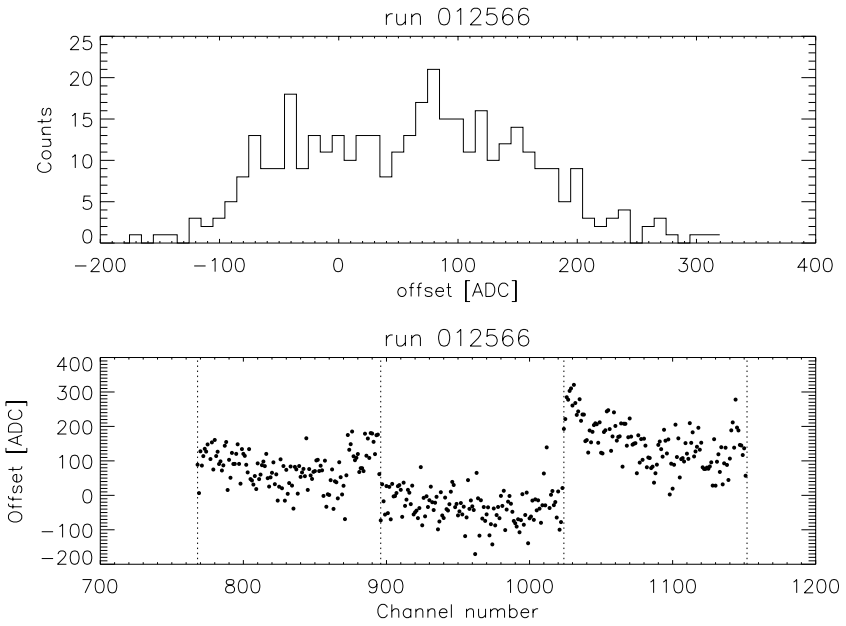

Figure 7.22: Histogram of the offset f from the daisy chain 3 calibration curve (upper panel) and offset value of each channel in the daisy chain (lower panel) after the detector integration and bonding. The vertical dotted lines mark the chip boundaries within a daisy chain.

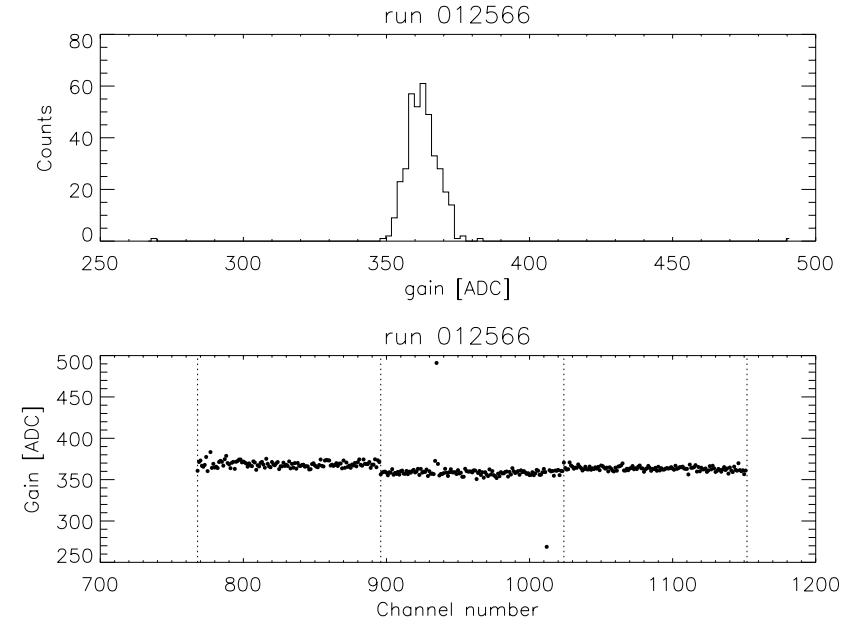

Figure 7.23: Histogram of the gain g from the daisy chain 3 calibration curve (upper panel) and gain value of each channel in the daisy chain (lower panel) after the detector integration and bonding. The vertical dotted lines mark the chip boundaries within a daisy chain.

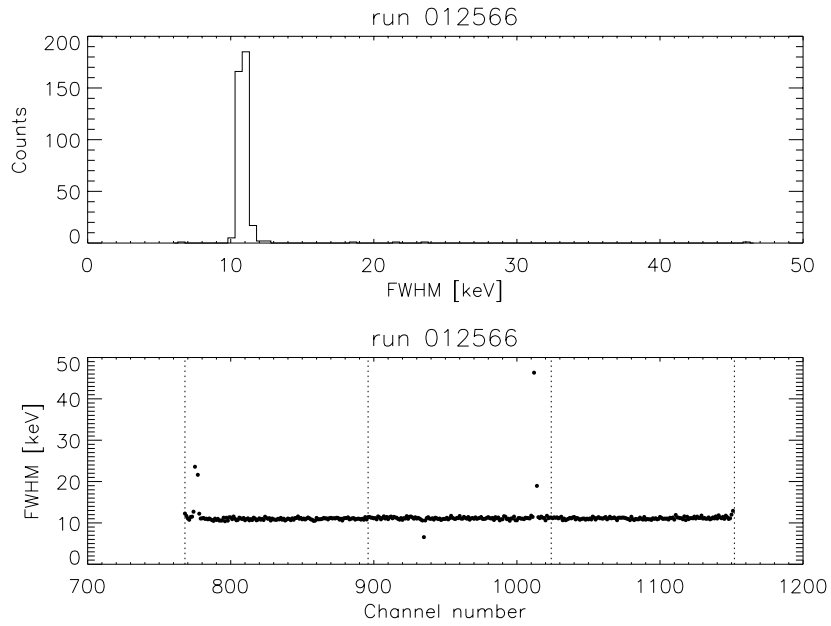

Figure 7.24: Histogram of the noise FWHM from the daisy chain 3 calibration curve (upper panel) and FWHM value of each channel in the daisy chain (lower panel) after the detector integration and bonding. The vertical dotted lines mark the chip boundaries within a daisy chain.

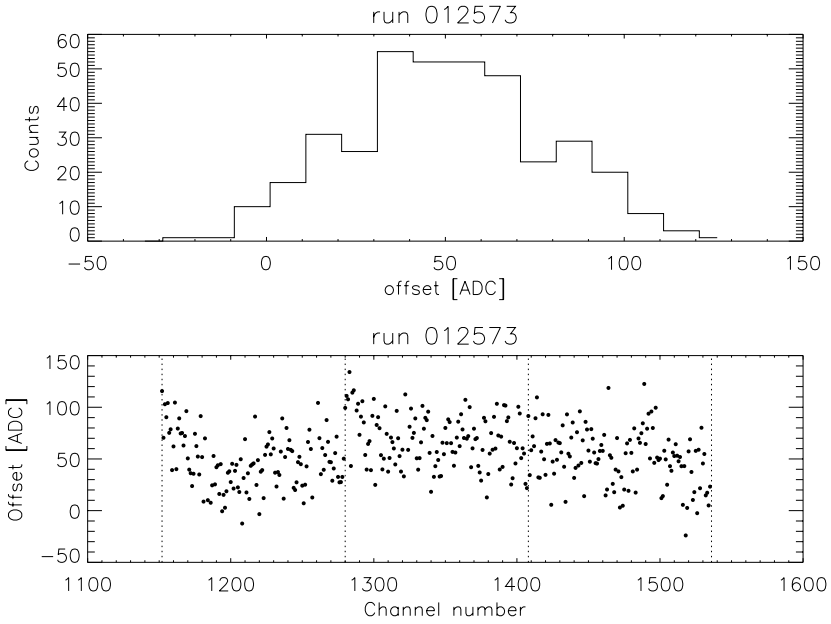

Figure 7.25: Histogram of the offset f from the daisy chain 4 calibration curve (upper panel) and offset value of each channel in the daisy chain (lower panel) after the detector integration and bonding. The vertical dotted lines mark the chip boundaries within a daisy chain.

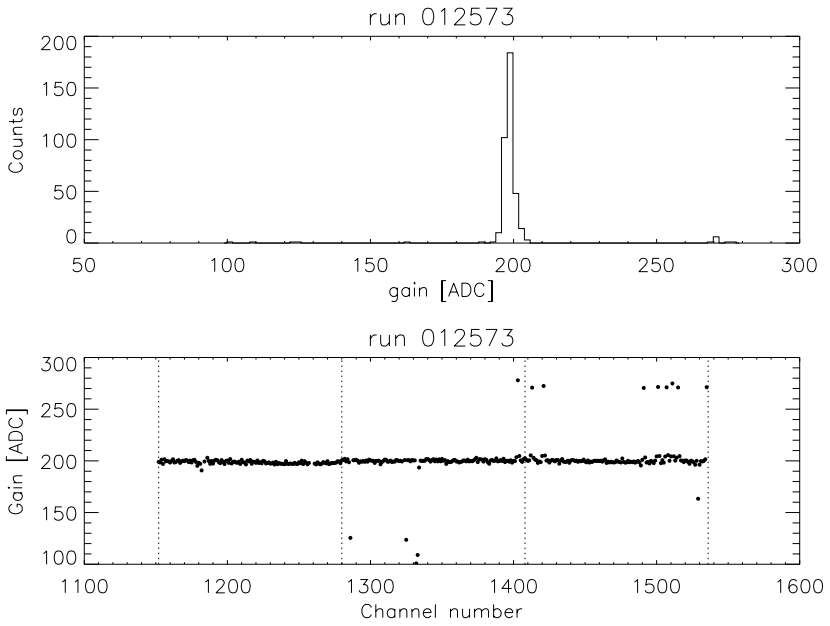

Figure 7.26: Histogram of the gain g from the daisy chain 4 calibration curve (upper panel) and gain value of each channel in the daisy chain (lower panel) after the detector integration and bonding. The vertical dotted lines mark the chip boundaries within a daisy chain.

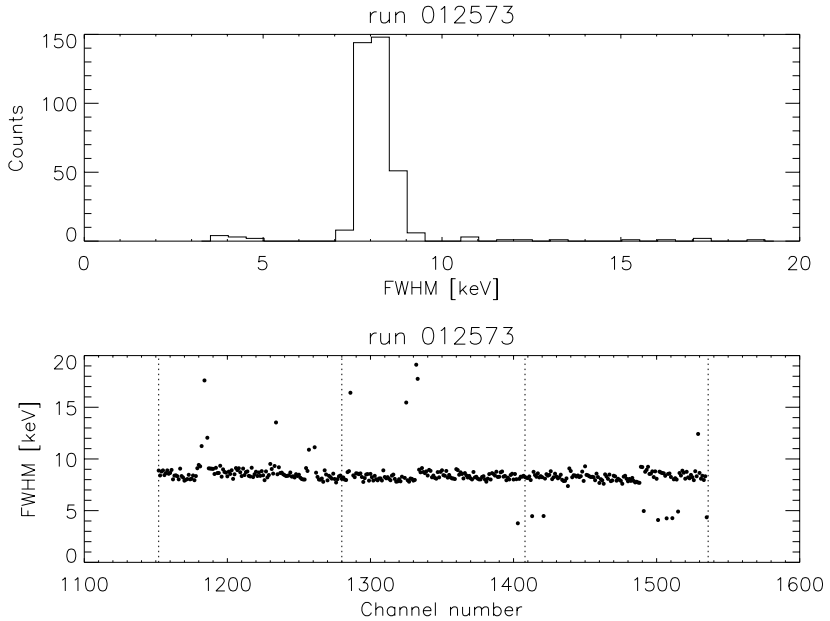

Figure 7.27: Histogram of the noise FWHM from the daisy chain 4 calibration curve (upper panel) and FWHM value of each channel in the daisy chain (lower panel) after the detector integration and bonding. The vertical dotted lines mark the chip boundaries within a daisy chain.

Table 7.6: Detection unit 1 electronic calibration after the detector integration. In the table $\bar{f}$ is the offset mean value, $\sigma(f)$ is the offset standard deviation, $\bar{g}$ is the gain mean value, $\sigma(g)$ is the gain standard deviation, $\overline{\Delta E}_{FWHM}$ is the FWHM mean value and $\sigma(\Delta E_{FWHM})$ is the FWHM standard deviation. Channels with gain smaller than $3\,\sigma$ or noise FWHM bigger than $3\,\sigma$ are considered as pathological and are excluded from the analysis.

XA	DC	$\bar{f}$ [ADC]	$\sigma(f)$ [ADC]	$\bar{g}$ ADC/fC]	$\sigma(g)$ [ADC/fC]	$\overline{\Delta E}_{FWHM}$ [keV]	$\sigma(\Delta E_{FWHM})$ [keV]
1	1	59.3	25.6	164.9	5.6	7.2	0.8
2	1	100.5	56.6	174.6	2.5	7.3	0.5
3	1	34.8	21.5	163.2	3.2	7.5	0.5
4	2	51.0	52.2	313.9	3.0	7.3	0.2
5	2	74.3	44.8	296.4	2.5	7.5	0.2
6	2	96.9	76.7	293.3	3.2	7.6	0.2
7	3	78.5	52.8	368.5	3.4	11.0	0.3
8	3	-33.8	45.0	359.6	12.2	11.1	0.3
9	3	151.0	65.9	363.5	2.6	11.1	0.3
10	4	48.4	25.9	198.5	1.6	8.6	0.5
11	4	68.1	25.2	200.1	1.3	8.3	0.3
12	4	51.3	27.1	200.0	1.9	8.3	0.4

As before the detector integration, the noise FWHM measured during the electronic calibration increases with the charge pulse amplitude. The plot of the FWHM average value measured on the daisy chain 2 at different pulse charge values is shown in fig. 7.28. After excluding the charge values $q \leq 2.5$ fC, where the pulse spectrum and consequently the noise FWHM are affected by the threshold, and applying the linear fit in (7.5) to the measured $\overline{\Delta E}_{FWHM}$ values as a function of the input charge q, the resulting parameters are $a = 7.11 \pm 0.05$ keV and $b = (1.1 \pm 0.1) \cdot 10^{-1}$ keV $\cdot$ fC^{-1}. The fit is superimposed as a dotted line in fig. 7.28. The quadratic difference between the maximum and minimum $\overline{\Delta E}_{FWHM}$ values, a measure of the noise introduced by the SAFEE TE, gives 1.7 keV, corresponding to about 480 e$^-$.

The uniformity of the offset f and gain g values can be evaluated from the results in tab. 7.6 and is shown in tab. 7.7. The parameters of the electronic calibration before and after the detector integration can be compared evaluating the ratio of the offset f and the gain g and the FWHM as shown in tab. 7.8.

As can be seen in tab. 7.8, all the offset values are consistent within $1\,\sigma$ before and after the detector integration. The detector produces a gain variation due to the charge division between the preamplifier feedback capacitance (0.2 pF) and the detector capacitance (30 pF $\cdot$ strip^{-1}). The noise FWHM increases after the detector integration because of the noise contributions introduced by the detector itself, as explained in sec. 3.4.

Table 7.7: Detection unit 1 uniformity after the detector integration. In the table $u(f)$ is the offset uniformity as in (7.2), $u(g)$ is the gain uniformity as in (7.3) and $u(\Delta E_{FWHM})$ is the FWHM noise uniformity as in (7.4).

XA	DC	$u(f)$ [%]	$u(g)$ [%]	$u(\Delta E_{FWHM})$ [%]
1	1	43	3.3	11.1
2	1	56	1.4	6.8
3	1	62	2.0	6.7
4	2	102	1.0	2.7
5	2	60	0.8	2.7
6	2	79	1.1	2.6
7	3	67	0.9	2.7
8	3	133	3.4	2.7
9	3	44	0.7	2.7
10	4	54	0.8	5.8
11	4	37	0.6	3.6
12	4	53	1.0	4.8

Table 7.8: Comparison of the SAFEE performances before and after the detector integration as estimated using the electronic calibration. In the table f_{ratio} is the ratio between the offset after the detector integration (from tab. 7.6) and before the detector integration (from tab. 7.1), g_{ratio} is the ratio between the gain after the detector integration (from tab. 7.6) and before the detector integration (from tab. 7.1) and finally ΔE_{ratio} is the ratio between the noise FWHM after the detector integration (from tab. 7.6) and before the detector integration (from tab. 7.1).

XA	$\bar{f}_{ratio}$	$\sigma(f_{ratio})$	$\bar{g}_{ratio}$	$\sigma(g_{ratio})$	$\overline{\Delta E}_{ratio}$	$\sigma(\Delta E_{ratio})$
1	1.1	0.7	0.724	0.05	2.12	0.06
2	1.1	0.9	0.724	0.02	2.21	0.03
3	1.3	0.8	0.716	0.03	2.21	0.04
4	1.2	1.3	0.719	0.02	2.52	0.02
5	1.2	0.8	0.722	0.01	2.59	0.02
6	1.3	1.3	0.719	0.02	2.53	0.02
7	1.2	0.8	0.724	0.01	4.07	0.01
8	0.8	1.7	0.733	0.05	4.27	0.01
9	1.1	0.6	0.727	0.01	4.27	0.01
10	1.1	0.7	0.716	0.01	2.21	0.04
11	1.1	0.5	0.718	0.01	2.18	0.04
12	1.0	0.7	0.722	0.01	2.24	0.04

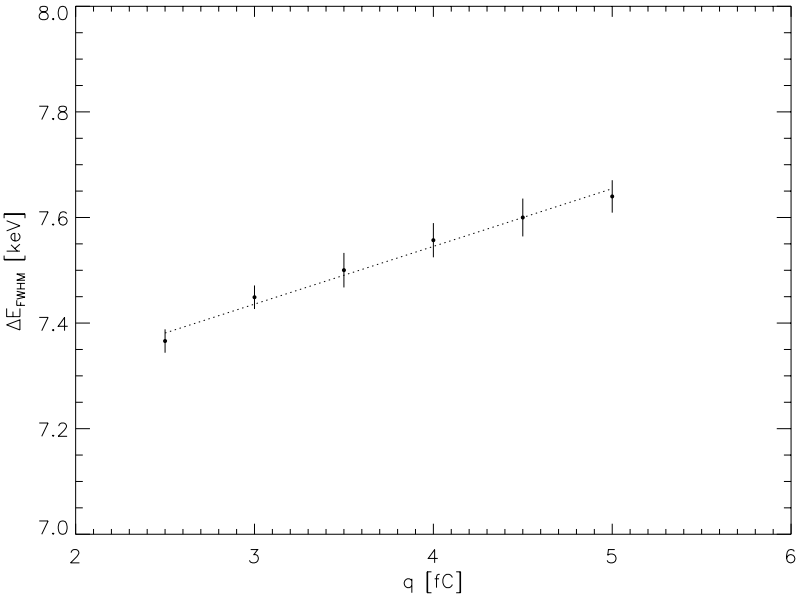

Figure 7.28: Plot of the FWHM measured on the Detection Unit 1 daisy chain 2 at different pulse charge values.

7.4.2 The background and the threshold

Threshold measurements of the Detection Unit 1 are available only on the second daisy chain. Also in this case the measurements are analysed following the technique described in sec. 6.3.3. The parameters of the linear fit in (6.1) of the whole daisy chain are $\bar{c} = -38.9$ mV, $\sigma(c) = 26.9$ mV, $\bar{d} = 209.9$ mV/fC and $\sigma(d) = 8.8$ mV/fC.

The background counting rate as a function of the energy threshold is plotted in fig. 7.29. As explained in sec. 6.3.3, the threshold is fixed at the energy value such that the limiting background counting rate is increased of 0.01 $\text{cts} \cdot \text{s}^{-1} \cdot \text{strip}^{-1}$ (being 10 % of the expected SuperAGILE background on-orbit). As can be seen in the plot, in such interpolation a threshold mean value of 19.0 keV with a standard deviation of 2.7 keV results.

The histogram of the interpolated threshold energy values is plotted in the upper panel of fig. 7.29 and the threshold value of each channel is plotted in the lower panel of the same plot. As can be seen in the plot, the threshold values are rather high and will be reduced by means of the XAA1.2 optimization described in sec. 7.6.

7.5 SuperAGILE "first light"

The first SuperAGILE photon acquisition has been performed on the daisy chain number 2 of the Detection Unit 1. The measurement aims to verify the uniformity in the background counting rate of the pixels in the detector and is an independent way to

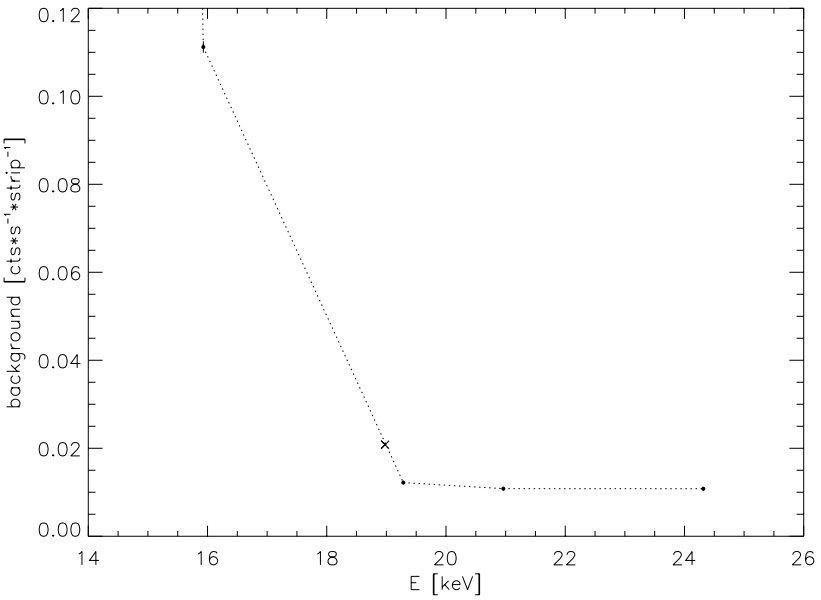

Figure 7.29: Background counting rate as a function of the threshold measured on the second daisy chain of the Detection Unit 1. The cross in the plot marks the interpolated energy threshold value.

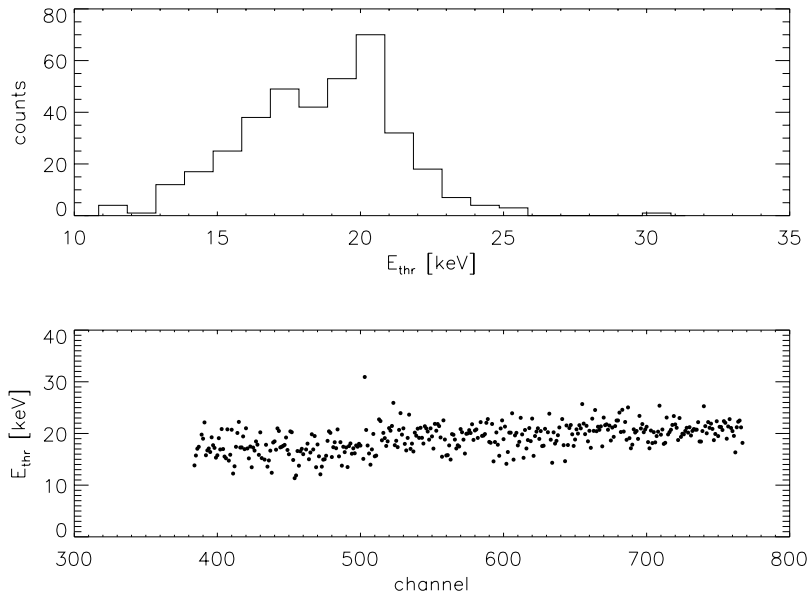

Figure 7.30: Histogram of the energy threshold in the different channels of the second daisy chain of the Detection Unit 1 (upper panel) and energy threshold value in each channel (lower panel).

evaluate the linearity and energy resolution of the three chips under test.

Initially a background detector image is accumulated in order to estimate the counting rate of each strip and to verify if hot pixels are present. In fact, as explained in sec. 6.4.3, the search of noisy pixels is performed basing on the standard deviation of the background counts among the detector pixels. Since the threshold equalization algorithm is not yet firmly stated, the threshold has not been equalized in this measurement.

After finding the noisy pixels, four measurement have been performed on the daisy chain number 2, each one using a different X-ray calibration source: custom Ba fluorescence source that emits X-rays from the Ba K-shell ($K\alpha 2$ at 31.8 keV, $K\alpha 1$ at 32.2 keV, $K\beta 1$ at 36.4 keV, $K\beta 3$ at 36.6 keV and $K\beta 2$ at 37.3 keV), ^{241}Am (59.5 keV line), ^{109}Cd (88.0 keV line) and ^{57}Co (122.1 keV line). The most important properties of the X-ray sources used during the tests are summarized in tab. 7.9.

7.5.1 Identification of hot pixels

A 45 minutes long background acquisition with 19.0 keV mean energy threshold has been performed on the second daisy chain in order to evaluate the counting rate of each pixel and to search if hot pixels are present. The threshold is not equalized adjusting the 3-bit DAC in this measurement. The detector image of this acquisition is shown in fig. 7.31. The image consists in the number of counts accumulated on each pixel. The vertical dotted lines in the plot show the boundaries of each daisy chain, the horizontal dashed black line marks the counts mean value ($\bar{N}$) and the horizontal dashed red line marks the counts mean value increased of three times the standard deviation ($\bar{N} + 3\,\sigma$).

As can be seen in the plot, two groups are missing because their group address value is smaller than the minimum voltage in the ADC range and their position cannot be reconstructed using the address LUT. Moreover the accumulated counts in two pixels (number 437 and 521) exceeds the $3\,\sigma$ limit above the mean value being $11\,\sigma$ and $14\,\sigma$ respectively.

The background spectra of a noisy pixel (number 437) can be seen in fig. 7.32. The background spectrum of a non noisy pixel is plotted in fig. 7.33 for comparison. As can be seen in the plots, the noisy pixel shows a counting rate about two orders of magnitude greater than the other one with a narrow line at low amplitude values (about 20 PHA) in the spectrum and due to the electronic noise, while the non noisy pixel has an almost flat spectrum, dominated by the X-ray background from the environment.

The spectral features exhibited by the pixel number 437 and 521 are produced by a high counting rate of electronic noise events. Since the same pixels do not show any pathological feature during the electronic calibration, the high background counting rate can be explained with a lower threshold compared to the other strips in the detector. For this reason the two pixels have been excluded from the following spectral analysis but are not considered as pathological.

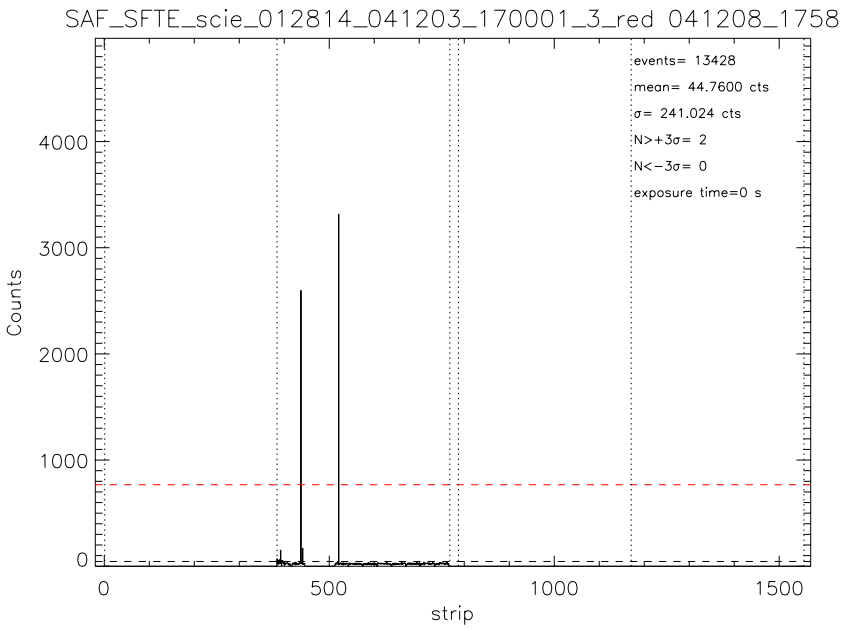

Figure 7.31: First background detector image accumulated on the second daisy chain of the Detection Unit 1.

7.5.2 Analysis of the X-ray sources spectra

The acquisition of X-ray sources is used to measure the Detection Unit performances in terms of linearity (offset and gain) and energy resolution (estimated by means of the noise FWHM). Four X-ray lines are used in the measurements on the Detection Unit 1 and their features are summarized in tab. 7.9.

In the measurements the spectrum of a single source is accumulated on one Detection Unit. In this process, photons of different strips, with different offset and gain values, are accumulated together and a broadening in the X-ray lines can occur. To avoid this phenomenon, during the data reduction process, described in sec. 6.4.1, the address of each detected photon is reconstructed basing on the address LUT and the amplitude is corrected converting the measured amplitude (in ADC channels) into an equivalent energy (in PHA) using the offset and the gain measured on the identified channel during the electronic calibration and stored in the gain LUT. Since the amplitude correction avoids the line broadening because of the difference in offset and gain among the strips, this technique allows to accumulate the spectrum on a big number of strips (up to one detector) so reducing the acquisition exposure time.

The spectral lines are then fitted to evaluate the peak position (indicated with m in the tables) and the line width (measured with σ and then converted into ΔE_{FWHM}). The linear fit of the peak position as a function of the input energy is an independent method to evaluate the Detection Unit linearity parameters (offset and gain) and will be extensively used during the SuperAGILE on-ground calibration to obtain the instrument

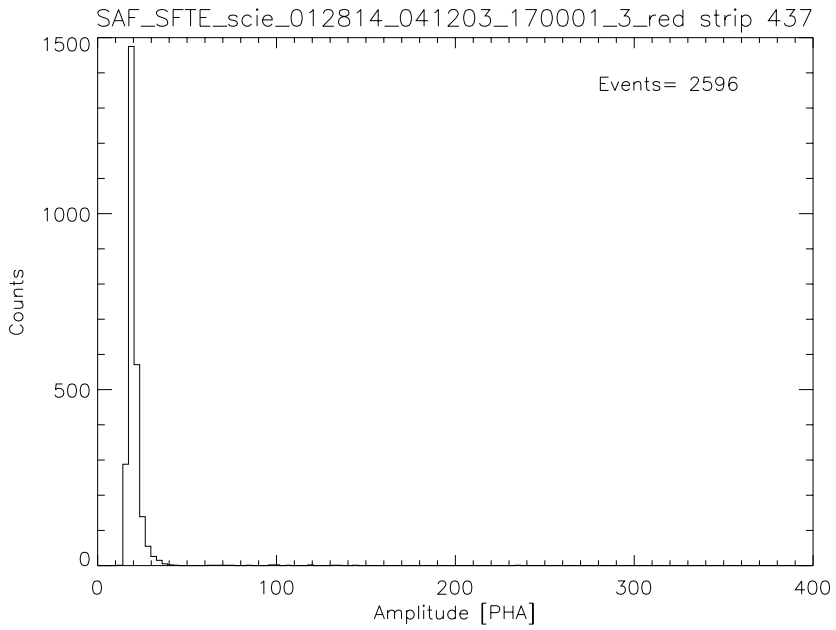

Figure 7.32: Background spectrum of the noisy pixel 437.

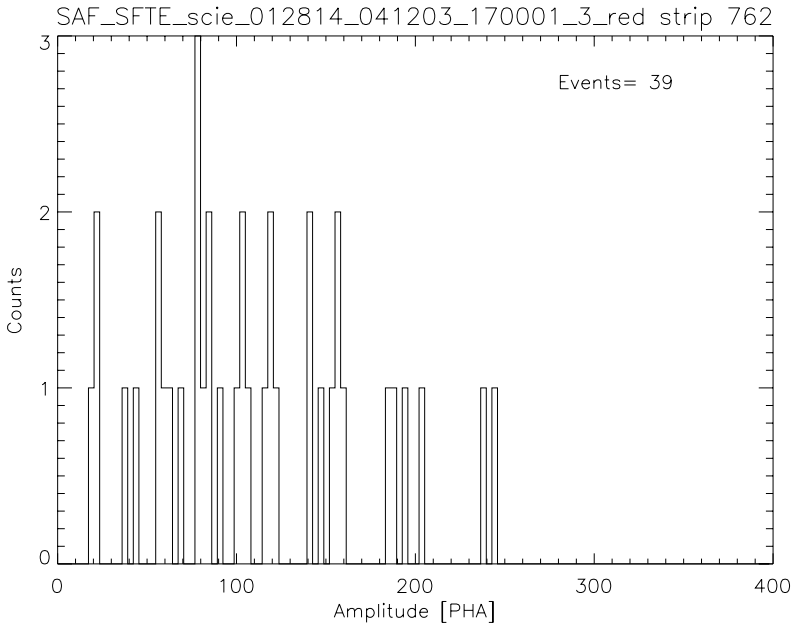

Figure 7.33: Background spectrum of the non noisy pixel 762.

Table 7.9: List of the X-ray sources used during tests. In the table I_γ is the gamma ray line intensity, from Chu et al. (1999), and ε_{photo} is the photoelectric absorption efficiency in silicon, evaluated from the absorption coefficients in Berger et al. (1999). For the Ba fluorescence source I_γ is the fluorescence yield.

source name	E [keV]	activity [μCi]	I_γ [%]	ε_{photo}
^{109}Cd	22.0	11.5	85.2	25.3
Ba fluorescence	32.1	1.4	76.9	8.6
^{241}Am	59.5	9.8, 10.9	35.9	1.3
^{109}Cd	88.0	11.5	3.6	0.4
^{57}Co	122.1	55.9	85.6	0.1

offset, gain and energy resolution.

A schematic of the Ba fluorescence source is shown in fig. 7.34. The two ^{241}Am sources, located in the bottom, emit upward X-rays of 59.5 keV that are absorbed with photoelectric effect by the atoms in the BaF_2 crystal on top and electrons are ejected from the inner shells, creating vacancies. As the atom returns to its stable condition, electrons from the outer shells are transferred to the inner shells and in the process give off a characteristic fluorescence X-ray whose energy is the difference between the two binding energies of the corresponding shells. The Ba atoms disexcitation produces fluorescence X-ray lines at 31.8 and 32.1 keV ($K\alpha$ shell) and 36.4, 36.6 and 37.3 keV ($K\beta$ shell). The source is contained in an aluminum frame and the ^{241}Am direct emission is shielded by two lead flat pieces.

The spectrum of the Ba fluorescence source can be seen in fig. 7.35. The main fluorescence line (32.1 keV) is the highest peak at around 30 PHA amplitude. The features below about 25 PHA are due to the electronic noise and the threshold and are excluded from the fit. The bump around 50 PHA, that is not consistent with the ^{241}Am line at 59.5 keV, can be explicated as produced by photons scattered by the source aluminum frame and walls.

The spectrum can be fitted using three gaussian functions (the first two representing the Ba fluorescence lines at 32.1 keV and 36.4 keV respectively and the third one modeling the scattering feature around 50 keV), whose sum is superimposed on the spectrum as a solid red line. A constant background is added to the fit model. The spectral fit parameters are $m = 33.06 \pm 0.04$ PHA, $\sigma = 3.09 \pm 0.05$ PHA and $\chi^2 = 1.282$.

The spectrum of the ^{241}Am line at 59.5 keV can be seen in fig. 7.36. From left to right in the plot the electronic noise peak superimposed on the 26.3 keV X-ray line (between about 15 PHA and about 35 PHA amplitude) and the 59.5 keV line (ranging from about 55 PHA to above 70 PHA amplitude) can be seen. The bump between the two lines (at about $50 \div 60$ PHA) is due to the backscattering, i.e. photons diffused by Compton effect in the materials surrounding the detector and absorbed by photoelectric effect in the detector itself (see Knoll (1989) for details).

The backscattering feature produces a broadening of the spectral line left side. Since the backscattering is extremely difficult to model, the ^{241}Am line is fitted with a gaussian

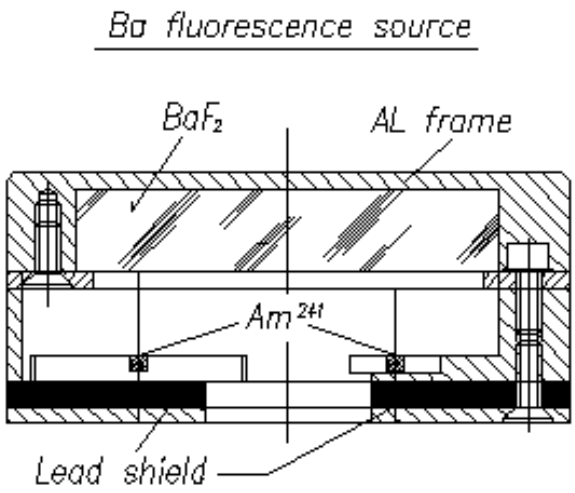

Figure 7.34: Schematic of the Ba fluorescence source. The two ^{241}Am sources, located in the bottom, emit upward X-rays of 59.5 keV that are absorbed with photoelectric effect by the atoms in the BaF_2 crystal on top. The Ba atoms disexcitation produces fluorescence X-ray lines at 32.1 keV and 36.4 keV.

function on the peak and the right side while the left FWHM is estimated using a linear interpolation at half maximum on the line left side. Only the σ estimated on the right side is taken into account to evaluate the Detection Unit energy resolution. A constant background is added to the fit model. The parameters of the ^{241}Am line fit are $m = 61.97 \pm 0.02$ PHA, $\sigma = 3.61 \pm 0.03$ PHA and the fit model is superimposed on the spectrum as a solid red line.

Since the performances in the Detection Unit 1 are not yet optimized, the threshold at 19.0 keV does not allow to fit the ^{109}Cd line at 22.0 keV. In fact this line is superimposed on the threshold and the peak position cannot be fitted. The spectrum of the ^{109}Cd line at 88.0 keV is shown in fig. 7.38. In the plot, apart from the photopeak of the 88.0 keV line, the backscattering feature between about 55 keV and about 80 keV can be seen.

The spectrum of the ^{109}Cd line at 88.0 keV is fitted using a gaussian model and a linear background (first order approximation). The fit is shown as a solid red line in fig. 7.38 and the fit parameters are $m = 92.6 \pm 0.2$ PHA, $\sigma = 3.9 \pm 0.1$ PHA and $\chi^2 = 1.237$ per degree of freedom.

The last measurement performed is the acquisition of the ^{57}Co 122.1 keV line, shown in fig. 7.37. This source emits a line at 14.4 keV, whose energy is lower than the threshold, that cannot be seen in the plot, an intense line at 122.1 keV, between 120 PHA and 140 PHA in the plot, and a faint line (about nine times smaller than the previous one) at 136.5 keV, ranging between 140 PHA and 160 PHA. The feature that can be seen around 40 PHA superimposed on the electronic noise peak in the plot is due

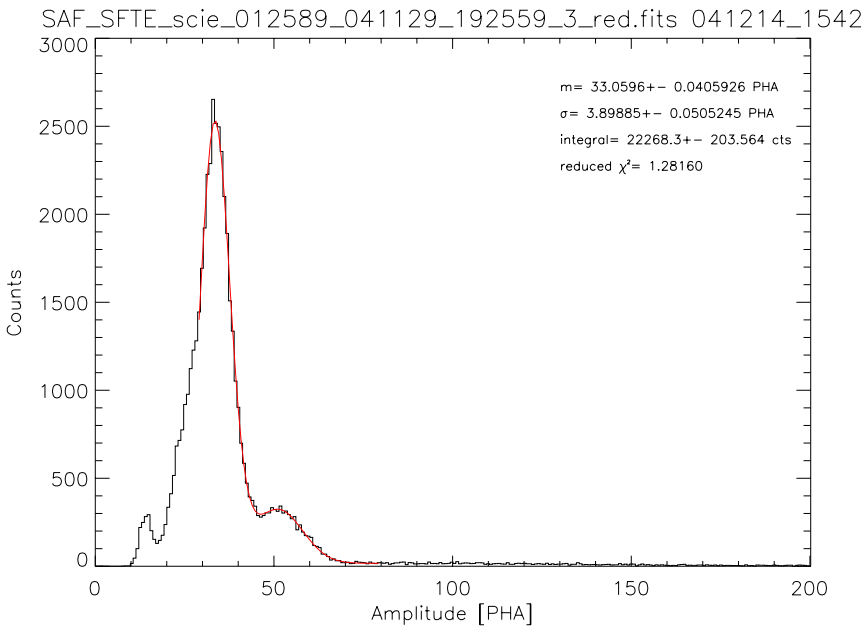

Figure 7.35: First spectrum of the custom Ba fluorescence source (32.1 keV and 36.4 keV lines) with a gaussian fit superimposed (in red).

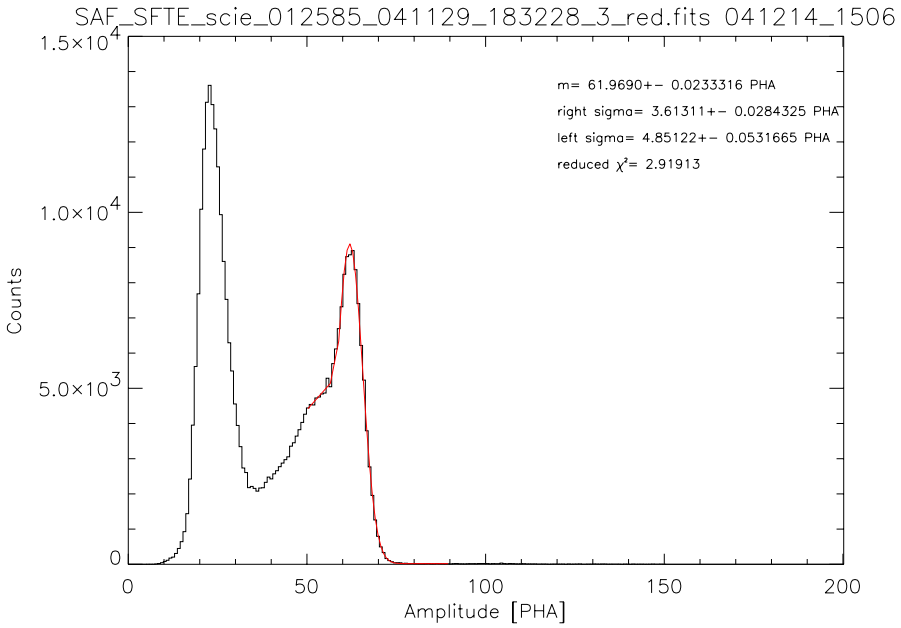

Figure 7.36: First spectrum of the ^{241}Am source (59.5 keV line) with superimposed a gaussian fit on the right side and a linear interpolation to find the FWHM on the left side (in red).

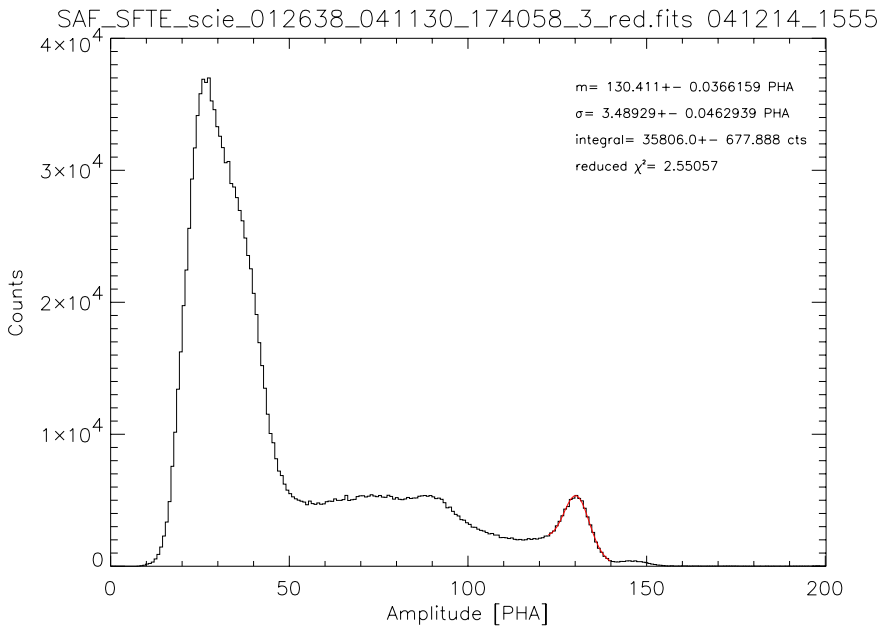

Figure 7.37: First spectrum of the ^{57}Co source (122.1 keV line) with a gaussian fit superimposed (in red).

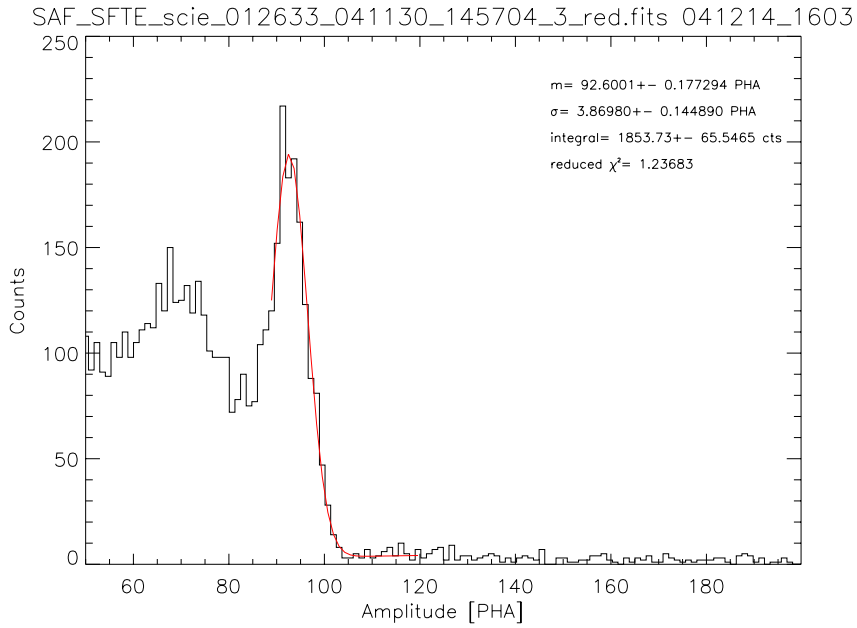

Figure 7.38: First spectrum of the ^{109}Cd source (88.0 keV line) with a gaussian fit superimposed (in red).

Table 7.10: Fit results of the SuperAGILE "first light" with m peak position and ΔE_{FWHM} full-width at half maximum of the X-ray line.

Source	E [keV]	$m \pm \sigma(m)$ [PHA]	$\Delta E_{FWHM} \pm \sigma(\Delta E_{FWHM})$ [keV]
Ba fluorescence	32.1	32.95±0.05	8.7±0.1
^{241}Am	59.5	61.91±0.03	7.89±0.09
^{109}Cd	88.0	92.5±0.2	9.3±0.4
^{57}Co	122.1	130.15±0.04	8.0±0.1

to the photons of 122.1 keV energy absorbed by Compton effect in the detector and the bump around $80 \div 90$ PHA is produced by the backscattering of 122.1 keV and 136.5 keV photons. The Compton effect of the photons in the same two lines produces the high level of background that can be seen throughout the spectrum, for example in the left side of the 122.1 keV line in the plot.

The spectrum fit model contains the 122.1 keV X-ray line and a linear background (first order approximation) and is superimposed on the plot as a solid red line. The fit parameters are $m = 130.41 \pm 0.04$ PHA, $\sigma = 3.49 \pm 0.05$ PHA, $\chi^2 = 2.551$ per degree of freedom.

The reduced χ^2 of all the fits shown in this section is rather high because the fitting model are not yet optimized. The improvement of the fitting functions, especially to model all the spectral features produced by the Compton effect, allows to reduce the fit χ^2.

The calibration of the fitted peak position from the spectra as a function of the source energy is shown in fig. 7.39 and the fit parameters are shown in tab. 7.10. The parameters of the linear fit in (4.3) are $f = -2.36 \pm 0.05$ PHA and $g = 1.0848 \pm 0.0007$ PHA/keV. The gain measured using X-ray sources increases of about 9 % with respect to the gain measured using the electronic pulse generator. The variation can be explained considering that, during the electronic calibration, the XAA1.2 chip is fed with voltage pulses, that are converted into charge signals in a capacitor (0.5 pF) internal to the chip. If the internal capacity differs from the nominal 0.5 pF value, a pulse of slightly different charge can be produced, thus giving a different output amplitude resulting in a variation in the fitted gain.

The FWHM values from the fit range between 7.89±0.09 keV (at 59.5 keV) and 9.3± 0.4 keV (at 88.0 keV) and are in rather good agreement with the 7.5 keV FWHM mean value (with 0.5 keV standard deviation) measured from the electronic calibration. The plot of the noise ΔE_{FWHM} as a function of the X-ray line energy is shown in fig. 7.40. As can be seen in the plot, no trend of the ΔE_{FWHM} as a function of energy can be seen. The correlation coefficient is $r = -0.161$, consistent with a lack of correlation between the measured ΔE_{FWHM} and the input energy. The lack of correlation between the noise ΔE_{FWHM} and the input energy strengthens the explication of the ΔE_{FWHM} increase in the electronic calibrations (see sec. 7.2.1 and 7.4.1) as due to a noise contribution, introduced by the test equipment electronics, proportional to the charge pulse amplitude.

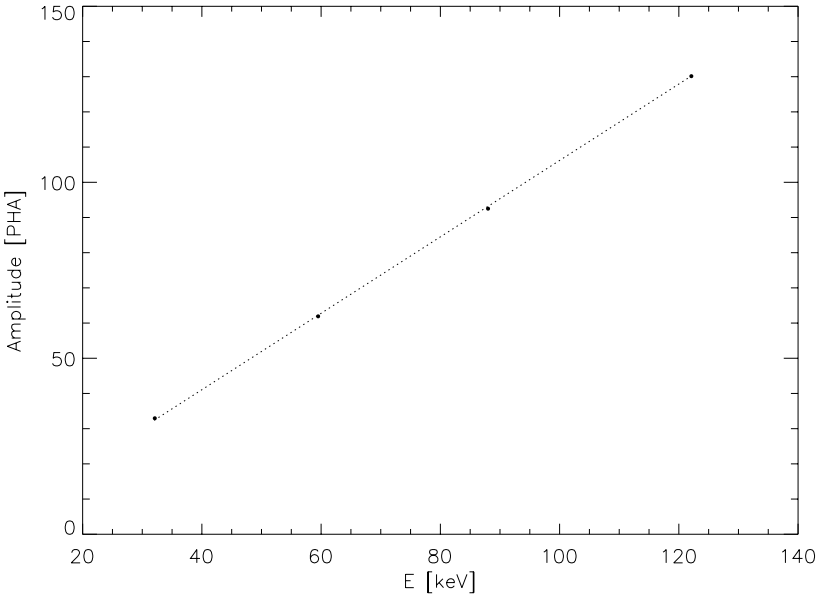

Figure 7.39: First linear fit from the peak position of the spectra in fig. 7.35, 7.36, 7.38 and 7.37 as a function of the X-ray line energy.

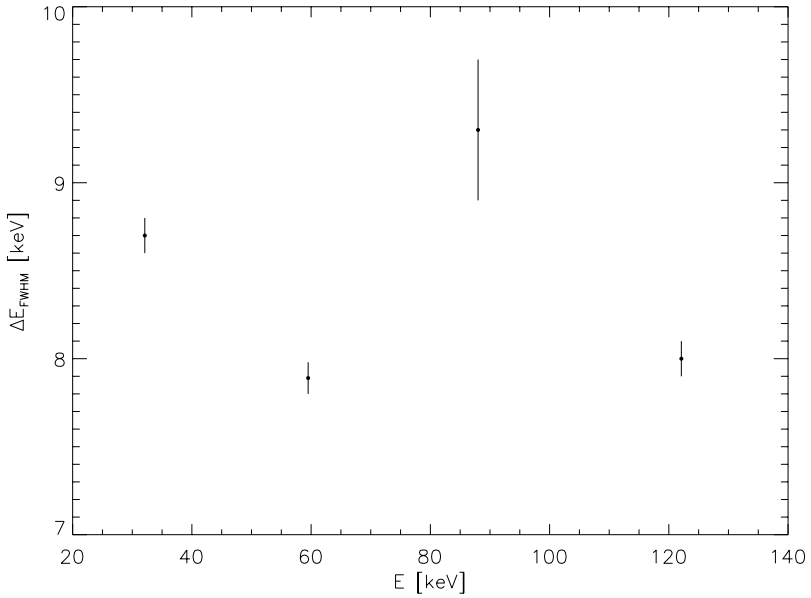

Figure 7.40: Noise ΔE_{FWHM} of the spectra in fig. 7.35, 7.36, 7.38 and 7.37 as a function of the X-ray line energy.

7.6 Optimization method of the SAFEE performances

Some of the XAA1.2 parameters, fed to the chip as bias voltages and currents, affect the performances in terms of electronic noise. Among all the biases described in sec. 3.3, particularly the *prebias*, *Vfp*, *shabias* and *Vfs* affect the output signal shape and consequently the electronic noise.

The transistor channel noise can be reduced increasing the transconductance by means of an increase in the *prebias*, that produces also a reduction in the peaking time, affecting the shot noise, the thermal noise in the bias resistors and the noise due to the metal strips, all depending on the peaking time as reported in sec. 3.4. In order to control the peaking time also the *shabias*, the *Vfp* and the *Vfs* have to be adjusted. The main constraint to the *prebias* value is the chip power consumption. For example an increase from 50 μA to 100 μA produces a power consumption increase from about 0.4 mW/ch to about 0.55 mW/ch.

The SAFEE test equipment allows to perform an electronic calibration changing the value of one bias during the measurement in order to evaluate the effect of this bias on the XAA1.2 performances. The bias value is changed for each pulse charge and each input channel. As a result, the linearity curve parameters (offset and gain) and the FWHM noise are evaluated as a function of the bias values as described in Del Monte et al. (2004).

Unfortunately the bias optimization by means of the electronic pulse generator does not apply to the X-ray measurements because the output signal shape slightly differs if the XAA1.2 is fed with the electronic pulse generator or with charge pulses from a detector. For this reason the SAFEE energy resolution has to be optimized adjusting the biases, accumulating spectra from at least three X-ray sources, fitting the spectra to find the peak position and FWHM and evaluating the linearity as shown in sec. 7.5. It is an iterative procedure that has to be repeated until the energy resolution is optimized.

7.7 Discussion and conclusions

In this chapter the measurement of the performances of the SAFEE is reported with particular emphasis on the global properties, given using mean values and standard deviations.

As summarized in tab. 7.2 and 7.7, the XAA1.2 gain shows a high degree of uniformity ranging between 0.8 % (for the XAA1.2 chip alone) and 3.4 % (after the detector integration). Lower uniformity levels are characteristic of the noise FWHM (between 8.1 % and 11.1 % for the XAA1.2 alone and after the detector integration respectively) and of the offset (from 114 % to 133 % for the XAA1.2 alone and after the detector integration respectively).

The burn-in process, required by the product assurance procedures and performed at 75° C for ten days before the detector integration, does not affect the SAFEE performances in terms of linearity, noise and threshold. As can be seen comparing the data in tab. 7.4 and 7.5, before and after the burn-in process all the threshold values and most

of the gain and noise FWHM values are consistent at $1\,\sigma$ significance level, with some exceptions consistent at $2\,\sigma$ or $3\,\sigma$.

The detector integration and bonding produces a gain reduction due to the amplitude decrease for the same input charge because of the charge division between the preamplifier feedback capacitance (0.2 pF) and the detector strip capacitance (30 $\mathrm{pF} \cdot \mathrm{strip}^{-1}$). As can be seen in tab. 7.8, all the offset values are consistent within $1\,\sigma$ before and after the detector integration while, after the detector integration, the gain decreases of about 28 % because of the charge division effect and the noise FWHM increases of at least a factor of two because of the noise contributions introduced by the detector itself.

The mean noise FWHM measured with the electronic pulse generator on the second daisy chain of the Detection Unit 1 board (where also X-ray acquisitions are available) is 7.5 keV with a standard deviation of 0.5 keV. As can be seen in sec. 3.4, this value is in extremely good agreement with the estimated FWHM from all the noise contributions in the XAA1.2 chip connected to the SuperAGILE silicon microstrip detector. The FWHM measured from the X-ray photon acquisitions is slightly higher because the XAA1.2 bias parameters are not yet optimized. The iterative optimization method described in sec. 7.6 can reduce the electronic noise drawing this value near the electronic calibration one.

The spectral analysis of photon acquisitions, described in sec. 7.5, will be used during the on-ground calibration to evaluate the SuperAGILE linearity and energy resolution. Moreover during the on-ground calibration also the instrument efficiency, required to build the response matrix, will be measured by means of X-ray acquisitions from the same sources listed in tab. 7.9.

Chapter 8

Impact of the SAFEE features on the SuperAGILE scientific performances

8.1 Introduction

This chapter deals with the estimation of the effects produced by the non uniformity of some of the SuperAGILE front-end electronics features on the instrument scientific performances. In particular, among the SuperAGILE criticalities, the impact of the threshold non uniformity on the instrument background and consequently on the imaging capabilities is studied.

Because of their large field of view, coded aperture systems are background dominated instruments. The background is not modulated by the coded mask and most of it is suppressed as average level during the decoding procedure but its fluctuations around this zero level are the noise, which is the sum of a statistic term (square rooted half of the total number of counts on the detector) and a coding term (due to the image deconvolution algorithm). Since the sources detection is performed by selecting a significance level and setting a threshold given by the significance level times the sky image standard deviation (usually $5\,\sigma$), any phenomenon affecting the sky images standard deviation has a serious impact on the sources detection.

In SuperAGILE instrument the most important non uniformity in the detector performances is due to the threshold. A measure of the SuperAGILE threshold uniformity, performed on the Detection Unit 1, is reported in sec. 8.2. Since the instrument background, mainly due to the Cosmic Diffuse X-ray Background, is integrated from the threshold up to the maximum energy, the threshold non uniformity among the pixels results in a non uniformity in the background accumulated on the detector images. The effect of the threshold non uniformity on the SuperAGILE imaging can be estimated from the statistics of the background images. An overview on the nature of the various components producing the SuperAGILE background is given in sec. 8.3. Since the threshold effect can be appreciated for exposure times above 10^4 s and the simulations

using Monte Carlo codes are severely time consuming, in that section a semi-analytic technique to produce detector images and apply the perturbations due to the threshold non uniformity is introduced.

The coded aperture imaging principle, requiring a position sensitive detector and a coded mask composed of a pattern of pixels transparent and opaque to the electromagnetic radiation under study, is a technique to produce images without a focusing device and is a two step process. First the source casts the shadow of the mask pattern on the detector and the number of photons accumulated on each pixel are recorded, so producing the detector image. The detector image cannot be observed directly since it contains a peak for each transparent element in the mask. Dedicated algorithms are applied to the detector image in order to extract the sources image (or sky image) from the correlation with the mask pattern. An overview of the coded mask instrument imaging algorithms with attention to the SuperAGILE decoding technique is given in sec. 8.4.

In order to evaluate the effect of the threshold non uniformity on the SuperAGILE imaging, in sec. 8.5 background detector images are simulated taking into account the effect of the measured thresholds. Three models of thresholds are considered in the background generation: replica of a permutation of the measured values, background integration only above a fixed energy value and finally XAA1.2 threshold equalization using the internal 3-bit DAC.

The first statistical analysis of the threshold non uniformity effect is performed directly on the detector images. Then the images are deconvolved, applying the SuperAGILE imaging algorithm, and the statistical analysis is performed also on the sky images, estimating the effect of the three threshold equalization models.

Finally, the efficiency of the different threshold equalization methods is discussed in sec. 8.6, where the conclusions of this study are given.

8.2 Measurement of the threshold non uniformity

The SuperAGILE threshold uniformity can be evaluated from the measurements on the daisy chain 2 of the Detection Unit 1, reported in sec. 7.4.2. The statistics of the parameters in the linear fit (6.1) is: $\bar{c} = -38.9$ mV, $\sigma(c) = 26.9$ mV, $\bar{d} = 109.9$ mV/fC and $\sigma(d) = 8.8$ mV/fC. Consequently the uniformity of the fit parameters is

$$\frac{\sigma(c)}{|\bar{c}|} = 69.2\ \% \tag{8.1}$$

$$\frac{\sigma(d)}{|\bar{d}|} = 4.2\ \% \tag{8.2}$$

and a histogram of the fit parameters c (upper panel) and d (lower panel) is shown in fig. 8.1.

If considering, for example, a 15 keV mean threshold, from the parameters c and d it is possible to evaluate the distribution and uniformity of the energy threshold values: if $\bar{E}_{thr} = 15$ keV, $\sigma(E_{thr}) = 2.6$ keV and $\sigma(E_{thr})/\bar{E}_{thr} = 17$ %. A histogram of the threshold values evaluated imposing $\bar{E}_{thr} = 15$ keV is shown in fig. 8.2. A small number

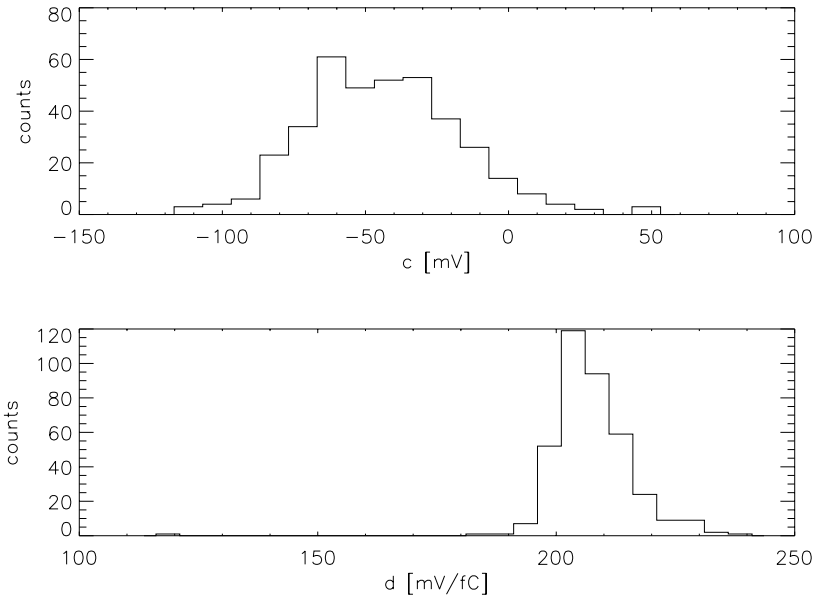

Figure 8.1: Histogram of the threshold fit parameters c (upper panel) and d (lower panel).

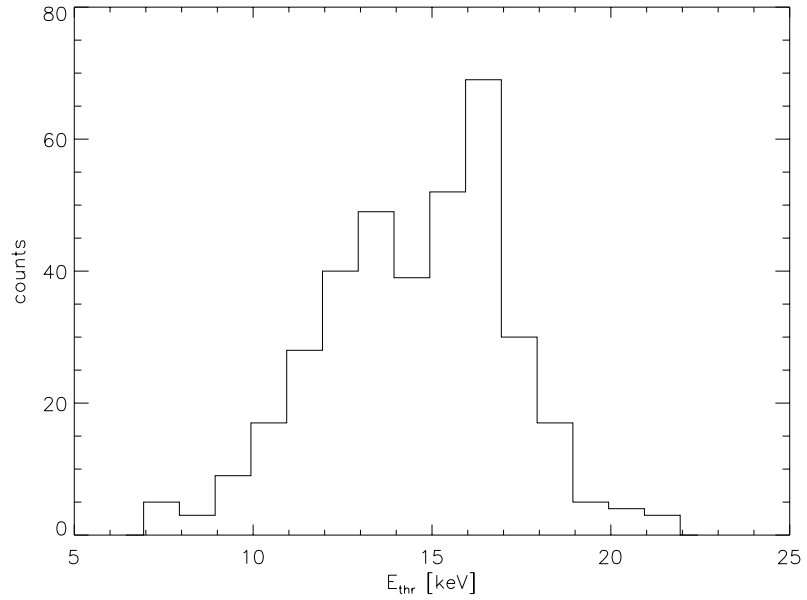

Figure 8.2: Histogram of the energy threshold values imposing $\bar{E}_{thr} = 15$ keV.

of channels in the plot show abnormally low threshold values (below 12 keV), given by a high value of the c parameter, while some noisy channels show extremely high threshold values (above 20 keV). At this stage the measurement aims only to estimate the energy threshold uniformity and more reliable threshold values will be measured after the SAFEE optimization process.

8.3 The SuperAGILE background

The SuperAGILE background is composed of two different types of events: the X-ray background photons, impinging on the detector within the field of view delimited by the collimator, and the instrumental background, composed of all the other processes producing counts in the detector and conditioned by the electronics.

The X-ray photon background is mainly composed of the Cosmic Diffuse X-Ray Background (DXRB) that is isotropic and with a spectrum given by

$$B(E) = \begin{cases} 8.5 \cdot E^{-1.4} \text{ photons} \cdot \text{cm}^{-2} \cdot \text{s}^{-1} \cdot \text{keV}^{-1} \cdot \text{srad}^{-1} & \text{E} < 20.88 \text{ keV} \\ 167 \cdot E^{-2.38} \text{ photons} \cdot \text{cm}^{-2} \cdot \text{s}^{-1} \cdot \text{keV}^{-1} \cdot \text{srad}^{-1} & \text{E} \geq 20.88 \text{ keV} \end{cases} \tag{8.3}$$

as shown in Zombeck (1990). A plot of the DXRB spectrum between 10 keV and 100 keV can be seen in fig. 8.3.

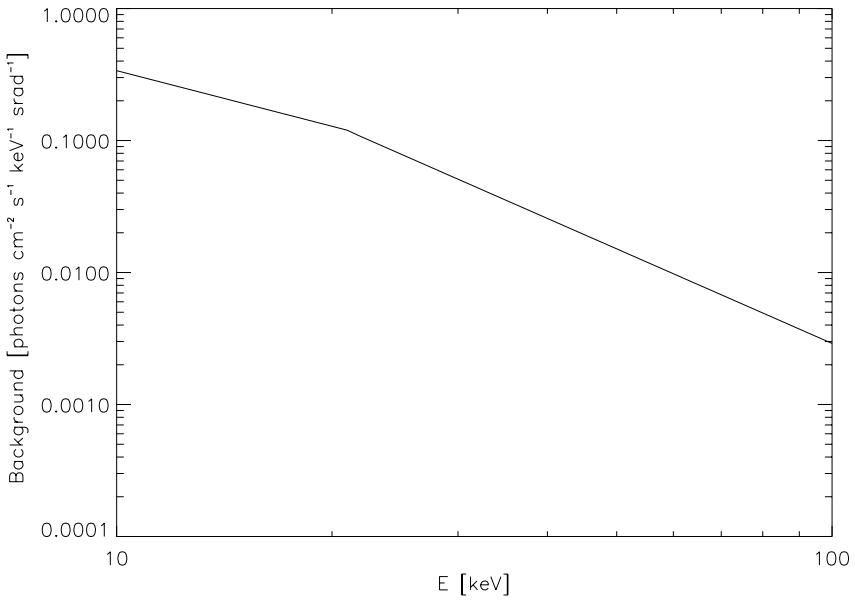

Figure 8.3: Power laws fitting the spectrum of the Cosmic Diffuse X-Ray Background from Zombeck (1990).

Diffuse X-ray background fluxes have been observed since the beginning of the rocket-borne X-ray observations, as shown for example in Seward et al. (1967). Recently, a significant fraction of the X-ray background has been identified with discrete extragalactic sources, mainly AGN (see Hasinger (1998) for ROSAT observations between 0.5 keV and 2 keV, Mushotzky et al. (2000) for the analysis from 2 keV to 10 keV and finally Comastri et al. (1995) for the hardest background between 8 keV and 50 keV). Following recent papers, for example Sołtan (2003), a small fraction (about $3 \div 4$ %) of the X-ray background, especially at energies below 1 keV, can be produced by the emission of Warm-Hot Intergalactic Medium.

For comparison the spectrum of the Crab Nebula, considered as the standard flux in X-ray experiments, can be approximated by a power law,

$$F(E) = 10 \cdot E^{-2.05} \cdot e^{-\sigma_T n_H} \text{ photons} \cdot \text{cm}^{-2} \cdot \text{s}^{-1} \cdot \text{keV}^{-1} \tag{8.4}$$

as reported in Zombeck (1990), where $\sigma_T = 0.665 \cdot 10^{-24}$ cm^2 is the Thomson scattering cross section and $n_H \simeq 3 \cdot 10^{21}$ cm^{-2} is the equivalent hydrogen column density (representing the integrated X-ray absorption of the matter along the line of sight), that can be neglected for galactic sources if E $>$ 10 keV. A plot of the power law in (8.4) fitting the spectrum of the Crab nebula in the same energy band ($10 \div 100$ keV) is shown in fig. 8.4.

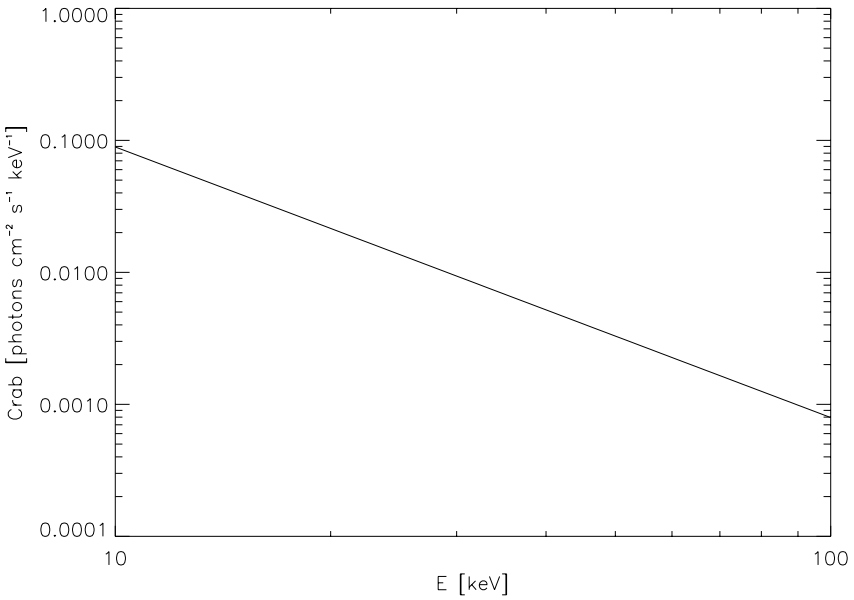

Figure 8.4: Power law fitting the spectrum of the Crab Nebula from Zombeck (1990).

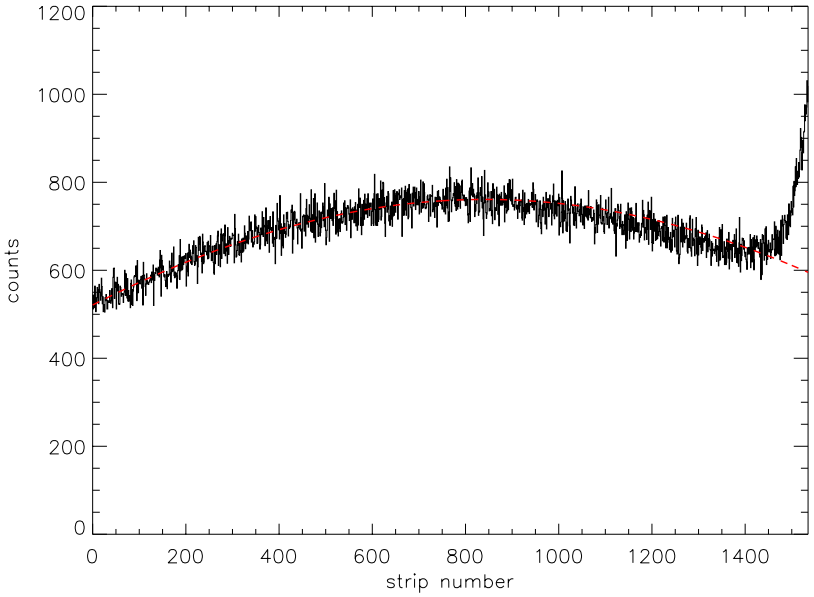

Figure 8.5: Image of the Monte Carlo simulated SuperAGILE background on one detector in 10^4 s observation time. The cosine fit in (8.5) is the dotted red curve.

8.3.1 Monte Carlo simulation of the SuperAGILE background features

A plot of the Monte Carlo simulation of the Cosmic Diffuse X-Ray Background as seen by SuperAGILE in one detector with $5 \cdot 10^4$ s of observation time is shown in fig. 8.5. As can be seen in the plot, the main feature in the image is the central bump, due to geometrical effects, and the right side excess, due to the non perfect tungsten shield of the collimator walls.

Excluding the right side excess, that is in part suppressed by further absorbers not yet introduced in the simulation, the left half of the simulated detector image can be fitted using a cosine function,

$$B(x) = A \cdot \cos(\alpha \cdot x + \phi) \tag{8.5}$$

where x is the strip number and the fit parameters are $A = 761 \pm 4$ cts, $\alpha = (98 \pm 3) \cdot 10^{-5}$ and $\phi = -0.817 \pm 0.005$ with reduced $\chi^2 = 1.001$ on 766 degrees of freedom. The cosine fit is superimposed in red to the plot in fig. 8.5.

Since part of the count excess distorts also the left half of the image, the fitted phase produces different count values at the detector boundaries, as can be seen in fig. 8.5. For this reason the phase has been corrected imposing the background counts to be equal at the boundaries producing the equation

$$\tan(\phi) = \frac{\cos(\beta) - 1}{\sin(\beta)} \tag{8.6}$$

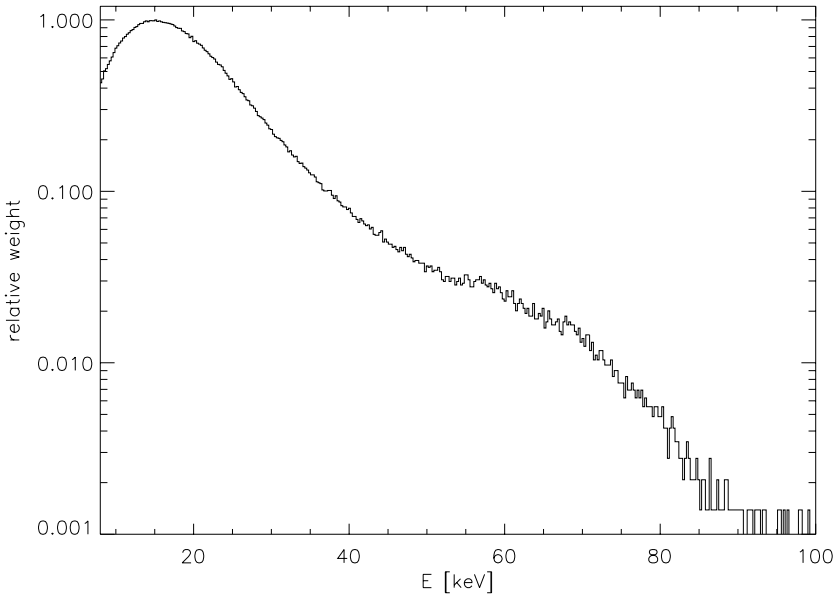

Figure 8.6: Relative weight in the spectrum of the simulated SuperAGILE background between 8 keV and 100 keV.

where $\beta \equiv \alpha \cdot 1535 = 1.504$ thus giving $\phi = -0.752$. The cosine feature will be fitted and removed from the SuperAGILE background performing a so called "flat field correction".

The spectrum of the simulated SuperAGILE background, smoothed using an approximated FWHM value of 8 keV as measured in the SuperAGILE flight model (see sec. 7.5 for the detailed analysis), can be seen in fig. 8.6. Since the mass model used in the simulation is roughly approximated, the spectrum normalization is poorly reliable and it can be used only to find the relative weight at the different energy values. A better approximated normalization will be applied later using an improved mass model.

The background contribution to each detector pixel is given by the integration of the background spectrum $B(E)$ from the lower energy E_{min} to the upper boundary E_{max},

$$B = \int_{E_{min}}^{E_{max}} B(E)dE\,. \tag{8.7}$$

To estimate the relative variation of the background with respect to the threshold, I have integrated the background spectrum $B(E)$ at different threshold values,

$$B(E_{thr}) = \int_{E_{thr}}^{E_{max}} B(E)dE \tag{8.8}$$

where $E_{max} = 40$ keV and E_{thr} ranges between 12 keV and 20 keV. The nominal value $B(15)$ is integrated between 15 keV and 40 keV. The relative variation as a function of the energy threshold E_{thr} is given in terms of the ratio $B(E_{thr})/B(15)$, shown in tab. 8.1 and in fig. 8.7.

Table 8.1: Relative variation of the integrated SuperAGILE background $B(E_{thr})/B(15)$ depending on the lower energy threshold E_{thr}.

E_{thr} [keV]	$B(E_{thr})/B(15)$
12	1.28
13	1.18
14	1.09
15	1.00
16	0.91
17	0.82
18	0.74
19	0.66
20	0.59

The ratio $B(E_{thr})/B(15)$ can be linearly fitted as a function of the threshold energy E_{thr},

$$\frac{B(E_{thr})}{B(15)} = \gamma + \delta \cdot E_{thr} \tag{8.9}$$

giving as parameters $\gamma = 2.30 \pm 0.02$ and $\delta = -0.086 \pm 0.001$. The linear fit is the dotted line superimposed on the data in fig. 8.7.

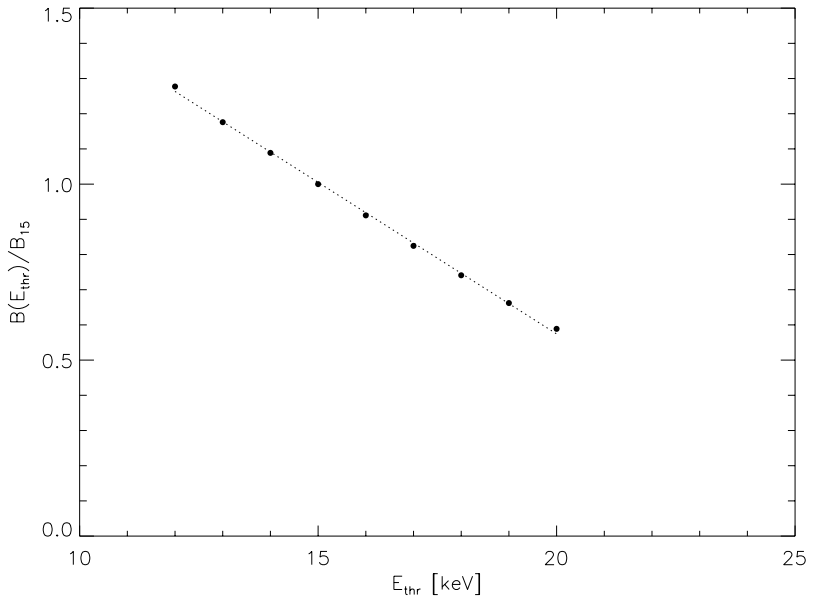

Figure 8.7: Percentage variation of the integrated SuperAGILE background depending on the lower energy threshold E_{thr}.

8.3.2 Semi-analytic background estimations

One of the major drawbacks of the SuperAGILE Monte Carlo code is the computation time currently needed for a high statistics background simulation, about 20 s for 1 s of exposure time. Since the effect of the threshold non uniformity on the background can be appreciated only with long exposures, from 10^4 s to 10^6 s, complete simulations of such exposures cannot be afforded. Thus the background can be estimated using semi-analytic techniques, taking into account the background most important features, simulated by Monte Carlo method.

The semi-analytic technique starts from the simulated average background counting rate, about 0.1 $\mathrm{cts} \cdot \mathrm{s}^{-1} \cdot \mathrm{pixel}^{-1}$. The cosine factor due to the geometrical effects is not added because it is supposed to be easily fitted and removed from SuperAGILE background data. The background counts are modified taking into account the threshold non uniformity. To each pixel an energy threshold value is assigned following three methods, that will be discussed in sec. 8.5 below. Depending on the assigned threshold, the background counts variation in each pixel follows the (8.1). Finally, the Poisson statistics is applied adding to each bin of counts N an indetermination $\sigma(N) = \sqrt{N}$ multiplied by a random number with normal distribution.

8.4 Overview of the imaging algorithm

Since SuperAGILE contains one-dimension coded masks and position sensitive detectors, the detector images are accumulated as one-dimension arrays, every elements containing the counts in the corresponding pixel. At this stage each detector can be considered as an independent instrument.

An example of the Crab simulated on-axis detector image with 10^4 s exposure is shown in fig. 8.8. As shown in the plot, the detector image contains only a succession of "full" and "empty" pixels reproducing the mask pattern.

The next step is is the decoding of the sky image, i.e. the extraction of the sources distribution in the Sky that best matches the image accumulated on the detector given the mask pattern. Basically, as explained in Lapshov (2004), the detection process can be described by

$$\vec{d} = \mathbf{T} \otimes \vec{s} + \vec{n} \tag{8.10}$$

where the $\vec{d}$ is the detector image (array containing the histogram of the "full" and "empty" pixels), $\vec{s}$ is the sky image (array containing the reconstructed position of the sources), $\vec{n}$ is the background detector image, $\mathbf{T}$ is the transition matrix depending on the mask pattern and $\otimes$ is the convolution mathematical operator.

The reconstruction of the sky image requires the inversion of the transition matrix $\mathbf{T}$,

$$\vec{s} = (\vec{d} - \vec{n}) \otimes \mathbf{T^{-1}} = \vec{d} \otimes \mathbf{T^{-1}} - \vec{n} \otimes \mathbf{T^{-1}} \tag{8.11}$$

but $\mathbf{T}$ may contain null elements and cannot be inverted. For this reason the problem belongs to a class of Ill-Conditioned problems.

Neither method can give exact and true solution to (8.11) because of the origin of the problem. In case of a coded mask aperture system, the transition matrix is simple and consists only of 1 (for the transparent pixels) and 0 (for the opaque pixels).

It is possible to define the reconstructed sky image $\vec{s}_r$ as

$$\vec{s}_r = \vec{d} \otimes \mathbf{R} = \vec{s} \otimes (\mathbf{T} \otimes \mathbf{R}) + \vec{n} \otimes \mathbf{R} \tag{8.12}$$

where $\mathbf{R}$ is a reconstruction matrix such that $\mathbf{T} \otimes \mathbf{R} = \delta_{ij}$. Particularly, to cancel the noise in the reconstruction,

$$\mathbf{R_{ij}} = \begin{cases} 1 & \text{if } \mathbf{T_{ij}} = 1 \\ -1 & \text{if } \mathbf{T_{ij}} = 0 \end{cases} \tag{8.13}$$

is the definition of the reconstruction operator.

The convolution $\otimes$ is a mathematical operation which takes two functions, $s(x)$ and $t(x)$, and produces as output $d(x)$ such that

$$d(x) = s(x) \otimes t(x) = \int_{-\infty}^{+\infty} s(\tau) \cdot t(x - \tau) d\tau \tag{8.14}$$

and $t(x)$ is referred to as the *filter*. The integral only needs to be evaluated over the range where $t(x - \tau) \neq 0$, that is the *support* of the *filter*.

Mathematically, the convolution operation in the spatial domain equals to the multiplication operation in the Fourier (frequency) domain and from the (8.10) and (8.12) we obtain

$$\mathcal{F}_t(\vec{d}_r) = \mathcal{F}_t(\vec{s}) \cdot \mathcal{F}_t(\mathbf{T}) \tag{8.15}$$

$$\mathcal{F}_t(\vec{s}_r) = \mathcal{F}_t(\vec{d}) \cdot \mathcal{F}_t(\mathbf{R}) \tag{8.16}$$

respectively, where $\mathcal{F}_t(\vec{d})$ and $\mathcal{F}_t(\vec{s})$ are the Fourier Transform of the detector and sky array respectively and $\mathcal{F}_t(\mathbf{R})$ and $\mathcal{F}_t(\mathbf{T})$ are the Fourier Transform of the reconstruction and transition matrices respectively. For this reason, the Fast Fourier Transform (FFT) is widely used in coded aperture imaging algorithms, included SuperAGILE.

Finally, the reconstructed sky image of each detector is obtained from the inverse Fourier Transform $\mathcal{F}_t^{-1}$ of the (8.16),

$$\vec{s}_r = \mathcal{F}_t^{-1}(\mathcal{F}_t(\vec{s}_r)) = \mathcal{F}_t^{-1}(\mathcal{F}_t(\vec{d}) \cdot \mathcal{F}_t(\mathbf{R})) \tag{8.17}$$

and the resulting sky image of the on-axis Crab simulation with 10^4 s exposure is shown in fig. 8.9. The central peak is the source reconstructed direction and the baseline fluctuations are produced by the noise introduced by the reconstruction algorithm ("coding noise"). As can be seen in the plot, the image fluctuations decrease off-axis because the exposed area decreases for geometrical reasons and thus the accumulated flux does decrease.

At this stage the four SuperAGILE detector modules produce four independent images, two of them coding the Sky in the x direction and two in the z direction (see the disposition of the detector modules in fig. 7.2 for reference). Then a balancing algorithm is applied to the sky images coded in the same direction, aimed to suppress the coding noise, i.e. the modulation induced by the mask pattern on the sky images. After this procedure, two one-dimension images are obtained, corresponding to the x and z coding directions respectively, without most of the coding noise.

8.5 Analysis of the SuperAGILE images and correction techniques

In this section the impact of the measured threshold non uniformity on the SuperAGILE background and consequently on the imaging is estimated by simulating background detector images and by evaluating the statistics in the detector and sky images.

Background detector images at different exposure times, ranging from 10^2 s to 10^6 s, are simulated with the semi-analytic technique described in sec. 8.3.2 above. The cosine geometrical factor is not introduced in the images because it is supposed to be easily fitted and removed in the SuperAGILE background.

In the background generation different threshold equalization models are taken into account: replica to the whole instrument of a permutation of the measured threshold values (in sec. 8.5.1), simple cut-off technique consisting in the integration of the background only above a fixed threshold (see sec. 8.5.2) and finally XAA1.2 threshold equalization using the 3-bit DAC fine regulation (in sec. 8.5.3).

The images are then decoded using the imaging algorithm developed for SuperAGILE and the standard deviation of the sky images is evaluated and compared to the value resulting from images with a pure Poisson statistics. Depending on the threshold equalization model, the standard deviation of the sky images shows significant variations, estimated by means of the ratio to the standard deviation of the images with only the Poisson statistics. The efficiency of the different threshold equalization models is then discussed in sec. 8.6 where the conclusions of this study are given.

8.5.1 Replica of the measured threshold values

The first threshold model applied in the background generation is the replica of the measured threshold values (described in sec. 8.2). After excluding from the whole dataset the 73 abnormally high or low threshold values, 311 elements with 12 keV $\leq E_{thr} \leq$ 20 keV are considered.

As a basic threshold pattern 384 values, corresponding to the number of channels in a daisy chain of three XAA1.2 chips, are considered. In order to take into account a threshold distribution closest to the measured one, the 73 missing values are filled by duplicating, using a uniformly distributed random variable, some of the 311 measured values.

The basic pattern of 384 threshold values is then replicated in order to assign a

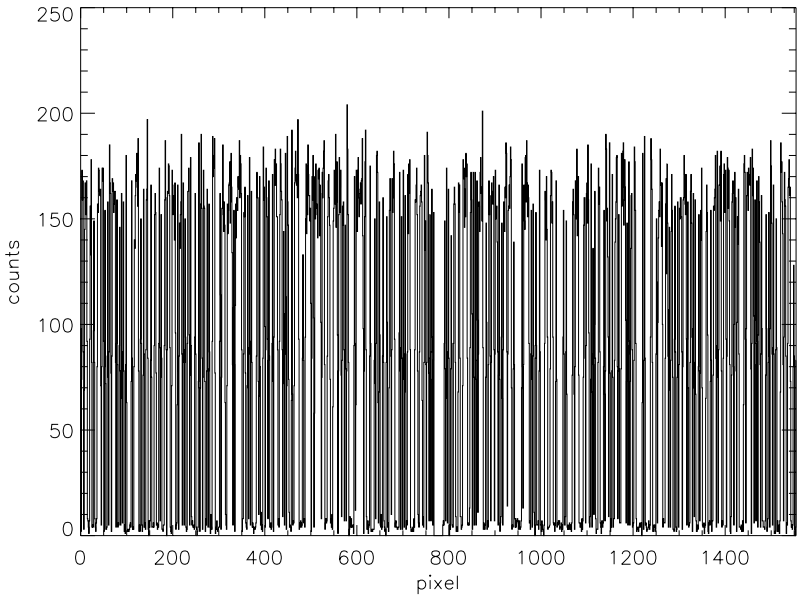

Figure 8.8: Crab simulated on-axis detector image with 10^4 s exposure.

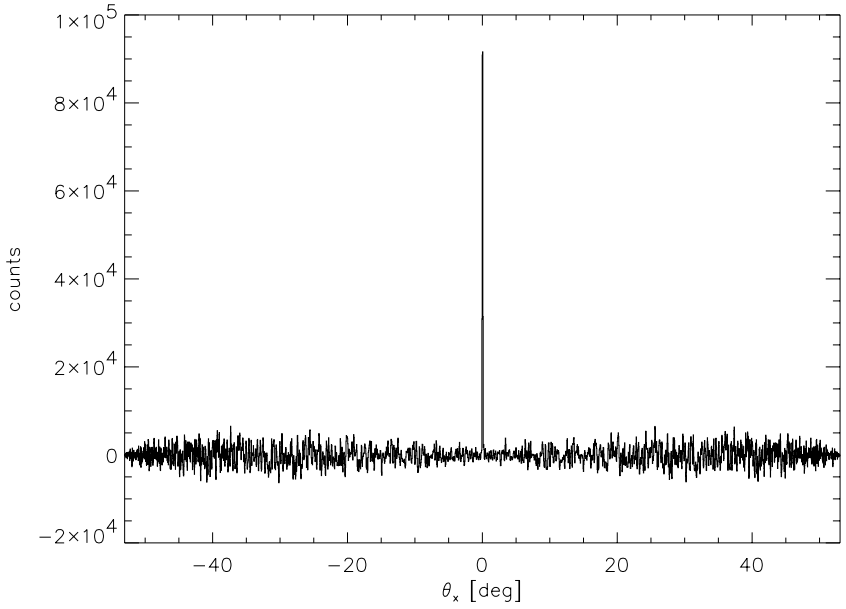

Figure 8.9: Crab simulated on-axis sky image with 10^4 s exposure.

Table 8.2: Energy threshold basic subset permutations

detector module 1:		detector module 2:	
daisy chain 1	$\{d,\ c,\ a,\ b\}$	daisy chain 1	$\{b,\ c,\ d,\ a\}$
daisy chain 2	$\{a,\ b,\ c,\ d\}$	daisy chain 2	$\{d,\ b,\ a,\ c\}$
daisy chain 3	$\{c,\ d,\ b,\ a\}$	daisy chain 3	$\{c,\ a,\ b,\ d\}$
daisy chain 4	$\{b,\ a,\ d,\ c\}$	daisy chain 4	$\{a,\ d,\ c,\ b\}$
detector module 3:		detector module 4:	
daisy chain 1	$\{b,\ c,\ a,\ d\}$	daisy chain 1	$\{d,\ c,\ b,\ a\}$
daisy chain 2	$\{a,\ d,\ b,\ c\}$	daisy chain 2	$\{a,\ d,\ c,\ b\}$
daisy chain 3	$\{c,\ a,\ d,\ b\}$	daisy chain 3	$\{b,\ a,\ d,\ c\}$
daisy chain 4	$\{d,\ b,\ c,\ a\}$	daisy chain 4	$\{c,\ b,\ a,\ d\}$

Table 8.3: Statistics of background detector images simulated applying a pure Poisson statistics.

t [s]	$\bar{B}$ [cts]	$\sigma(B)$ [cts]	$\sigma(B)/\bar{B}$
10^2	10.01 ± 0.04	3.20 ± 0.08	0.320 ± 0.008
10^3	100.2 ± 0.3	10.0 ± 0.3	0.997 ± 0.003
10^4	999.5 ± 0.5	31.9 ± 0.4	0.0319 ± 0.0004
10^5	10000 ± 1	101.4 ± 0.2	0.01014 ± 0.00002
10^6	99995 ± 10	999 ± 16	0.00315 ± 0.00005

threshold to all the 6144 SuperAGILE pixels. Since the imaging deconvolution algorithm is based on the FFT and is extremely sensitive to the spatial frequency, the threshold assignment is performed by dividing the 384 threshold datasets into four subsets of 96 values each and by assigning to each daisy chain a different permutation of these four subsets.

Considering the basic pattern of 384 thresholds as formed of four subsets in the permutation $\{a,\ b,\ c,\ d\}$, in the construction of the threshold pattern for a detector the repetition of the same subset (a, b, c or d) in the same position is avoided in order not to introduce spatial frequencies. The threshold pattern in each daisy chain of the four detector modules is shown in tab. 8.2 and the threshold values are plotted in fig. 8.10. The measured standard deviation of the threshold pattern is $\sigma(E_{thr}) = 1.9$ keV.

After simulating the background detector images, the mean value $\bar{B}$ and the standard deviation $\sigma(B)$ at different exposure times are evaluated and the results are reported in tab. 8.4. For comparison, the same computation for a background distributed following a pure Poisson statistics is shown in tab. 8.3. The detector image relative dispersion, estimated using the ratio $\sigma(B)/\bar{B}$ is plotted in fig. 8.4 as a function of the exposure time, where the same ratio for the Poisson statistics is plotted for comparison.

As can be seen in the table and in the figure, the relative dispersion in the background

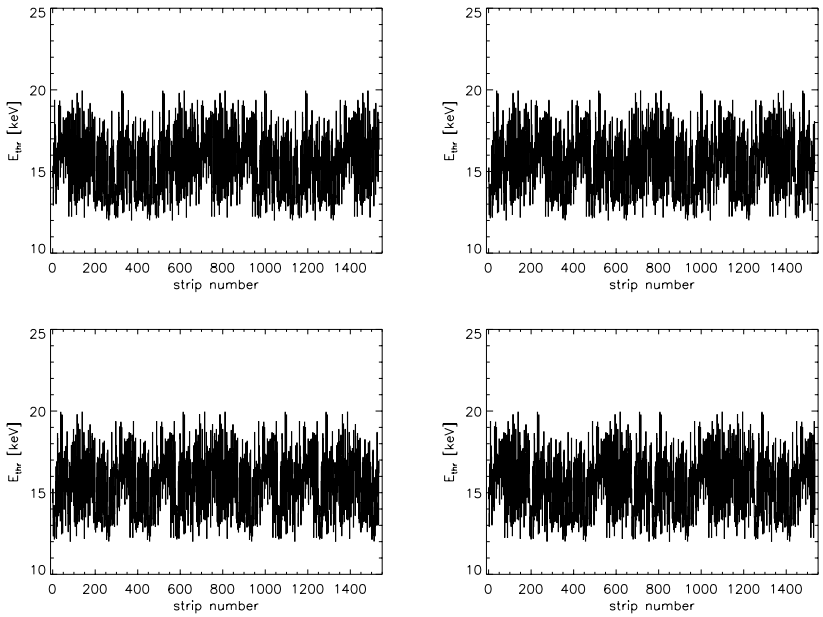

Figure 8.10: Energy threshold in the SuperAGILE four detectors from the permutation of the basic pattern as explained in tab. 8.2.

Table 8.4: Statistics of the background detector images simulated applying the replica of the energy threshold pattern.

t [s]	$\bar{B}$ [cts]	$\sigma(B)$ [cts]	$\sigma(B)/\bar{B}$
10^2	9.49 ± 0.08	3.13 ± 0.07	0.335 ± 0.008
10^3	95.7 ± 0.1	18.6 ± 0.1	0.194 ± 0.001
10^4	956.5 ± 0.7	165 ± 1	0.172 ± 0.001
10^5	9563 ± 5	1617 ± 1	0.1691 ± 0.0001
10^6	95660 ± 7	16162 ± 7	0.16895 ± 0.00007

Table 8.5: Statistics of the background sky images from the simulation applying the replica of the energy threshold pattern.

t [s]	$\sigma(S)$ [cts]	$\sigma(S_{Poisson})$ [cts]	$\sigma(S)/\sigma(S_{Poisson})$
10^2	132 ± 3	122.6 ± 0.8	1.08 ± 0.02
10^3	787 ± 4	425 ± 12	1.85 ± 0.05
10^4	7221 ± 14	1940 ± 13	3.72 ± 0.03
10^5	70317 ± 304	14747 ± 44	4.77 ± 0.03
10^6	702684 ± 884	143650 ± 36	4.89 ± 0.01

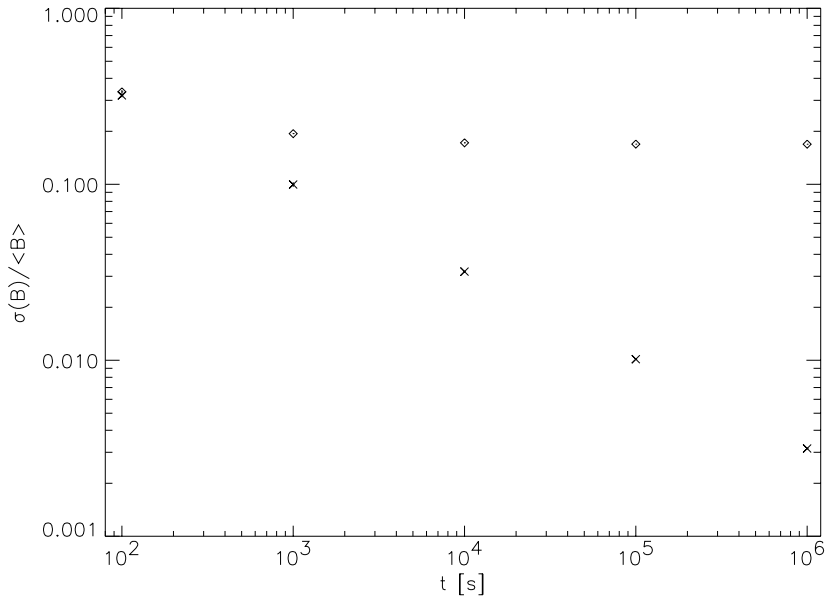

Figure 8.11: Relative dispersion $\sigma(B)/\bar{B}$ as a function of the exposure time from the background detector images simulated applying the replica of the energy threshold pattern (diamonds) compared with the relative dispersion of the background detector images simulated applying the pure Poisson statistics (crosses).

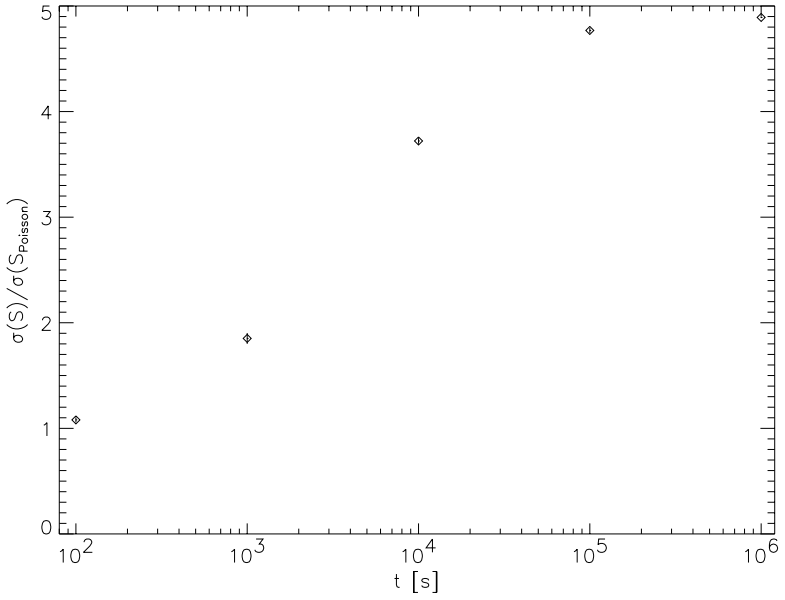

Figure 8.12: Ratio $\sigma(S)/\sigma(S_{Poisson})$ as a function of the exposure time of the standard deviation in the sky images of the background simulated applying the replica of the energy threshold pattern to the standard deviation of the sky images of the background simulated applying a pure Poisson statistics.

detector images shows a limit value around 0.169 at 10^6 s exposure time. The relative dispersion is already about 0.172 at 10^4 s exposure. This fact has a serious effect on the SuperAGILE imaging capabilities because the detector image indetermination does not decrease if the exposure time is increased above 10^4 s.

After decoding the detector images, two sky images (one along the x direction and the other along the orthogonal z direction) are produced. The statistic of the background sky images is shown in tab. 8.5 where the same estimation in case of a pure Poisson statistics background is considered as a comparison. The ratio $\sigma(S)/\sigma(S_{Poisson})$ of the sky image standard deviation with the pattern energy threshold model and the sky image standard deviation with a pure Poisson statistics is plotted in fig. 8.12.

As can be seen in the table and in the figure, the sky image standard deviation increases with respect to the Poisson statistics model (considered as a reference) and the amount of variation increases with the exposure time. This fact can be neglected in case of short duration observations, for example about 10^2 s in case of a Gamma Ray Burst, but it has serious consequences on the SuperAGILE performances at long exposures, for example observing faint sources, as the blazars, for 10^6 s. Particularly, at 10^6 s the sky image standard deviation is about five times above the standard deviation in a background with a pure Poisson statistics.

8.5.2 Threshold cut-off technique

The simplest method to decrease the threshold non uniformity is the background integration only above a fixed energy, for example 15 keV. In pixels where the threshold is lower than 15 keV, only events at energy equal to 15 keV or above are acquired while, in pixels where the threshold is greater, all the events are integrated. This correction method decreases the threshold non uniformity from $\sigma(E_{thr}) = 1.9$ keV to $\sigma(E_{thr}) = 1.3$ keV at the expense of a source signal loss that can be significant since the spectrum of the X-ray sources is generally a power-law with spectral index near 2.

The statistics of the background detector images simulated considering $E_{thr} \geq 15$ keV is reported in tab. 8.6. The relative dispersion $\sigma(B)/\bar{B}$ is plotted as a function of the exposure time in fig. 8.13, where the relative dispersion in case of images simulated only with the Poisson statistics is plotted for comparison. Also in this case, as can be seen in the table and in the figure, the detector image relative dispersion $\sigma(B)/\bar{B}$ shows a limit value (around 0.119) as a function of time.

After decoding the detector images, the sky images statistics is evaluated and reported in tab. 8.7. If compared to the result shown in tab. 8.5, the sky image standard deviation is about three times above the standard deviation computed in the reference images (simulated with the Poisson statistics only) at 10^6 s, smaller then the value without correction (see tab. 8.5 and fig. 8.12 for comparison) but still high to observe faint source with long exposures.

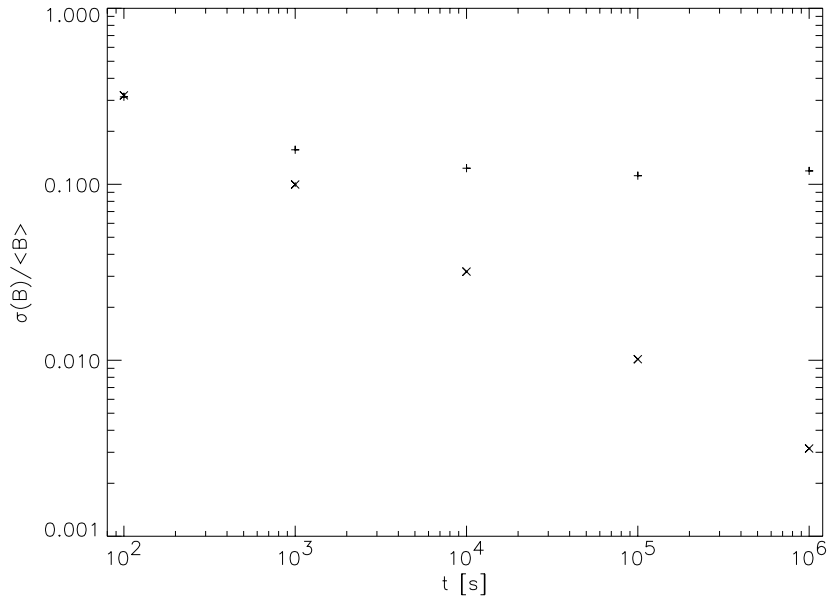

Figure 8.13: Relative dispersion $\sigma(B)/\bar{B}$ as a function of the exposure time from the background detector images simulated applying the cut-off technique $E_{thr} \geq 15$ keV (plus signs) compared with the relative dispersion of the background detector images simulated applying the pure Poisson statistics (crosses).

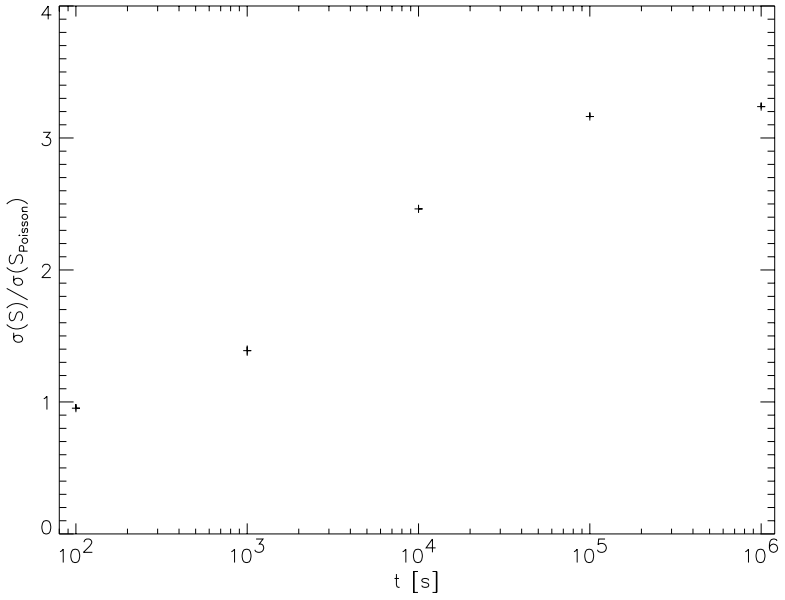

Figure 8.14: Ratio $\sigma(S)/\sigma(S_{Poisson})$ as a function of the exposure time of the standard deviation in the sky images of the background simulated applying the cut-off technique $E_{thr} \geq 15$ keV to the standard deviation of the sky images of the background simulated applying a pure Poisson statistics.

Table 8.6: Statistics of the background detector images simulated applying the correction $E_{thr} \geq 15$ keV.

t [s]	$\bar{B}$ [cts]	$\sigma(B)$ [cts]	$\sigma(B)/\bar{B}$
10^2	9.07 ± 0.03	2.85 ± 0.04	0.314 ± 0.005
10^3	90.7 ± 0.1	14.2 ± 0.2	0.127 ± 0.002
10^4	909.3 ± 0.5	112.2 ± 0.2	0.1234 ± 0.0002
10^5	9089 ± 2	1087 ± 2	0.1196 ± 0.0002
10^6	90891 ± 6	10828 ± 8	0.11914 ± 0.00009

Table 8.7: Statistics of the background sky images from the simulation applying the correction $E_{thr} \geq 15$ keV.

t [s]	$\sigma(S)$ [cts]	$\sigma(S_{Poisson})$ [cts]	$\sigma(S)/\sigma(S_{Poisson})$
10^2	117 ± 2	122.6 ± 0.8	0.953 ± 0.02
10^3	590 ± 4	425 ± 12	1.389 ± 0.04
10^4	4778 ± 34	1940 ± 13	2.463 ± 0.02
10^5	46639 ± 139	14747 ± 44	3.163 ± 0.01
10^6	465062 ± 2427	143650 ± 36	3.237 ± 0.02

8.5.3 Threshold digital fine regulation technique

The XAA1.2 chip contains a digital fine regulation of the threshold, performed using a 3-bit DAC. The threshold voltage of a single channel can be changed of three positive and three negative steps (the eighth step in the DAC produces no variations). The major drawback of this threshold equalization method is that the sum of the all the variation steps has to equal zero unless a variation of the threshold mean value in the whole XAA1.2 is produced. Using the digital fine regulation an equalization at a level $\sigma(E_{thr}) = 0.4$ keV has been measured by Uberti and Soffitta (2005) on a sample of 39 channels with average threshold value about 22 keV. Since the digital equalization affects only the threshold dispersion and not the average value, this method produces no losses in the Sky sources signal.

Introducing $\sigma(E_{thr}) = 0.4$ keV in the background simulations, although this value can be rather optimistic and needs to be estimated on a bigger sample, the results in tab. 8.8 are obtained. With $\sigma(E_{thr}) = 0.4$ keV the limit value of the detector images relative dispersion $\sigma(B)/\bar{B}$ is about 0.035, as can be seen plotted as a function of time in fig. 8.15.

After decoding the detector images and evaluating the statistics of the sky images, the standard deviation in the resulting sky image is smaller than 1.4 times the reference value (of the images from a Poisson statistics distributed background) at the 10^6 s maximum exposure time. This is an important result since such an standard deviation value allows to observe faint sources, as for example the blazars, with long exposures.

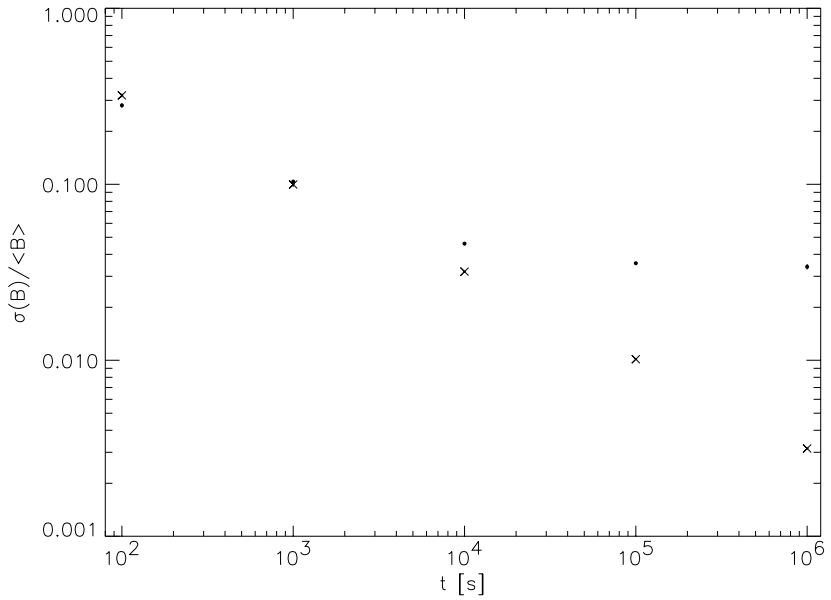

Figure 8.15: Relative dispersion $\sigma(B)/\bar{B}$ as a function of the exposure time from the background detector images simulated applying the threshold equalization $\sigma(E_{thr} = 0.4$ keV (dots) compared with the relative dispersion of the background detector images simulated applying the pure Poisson statistics (crosses).

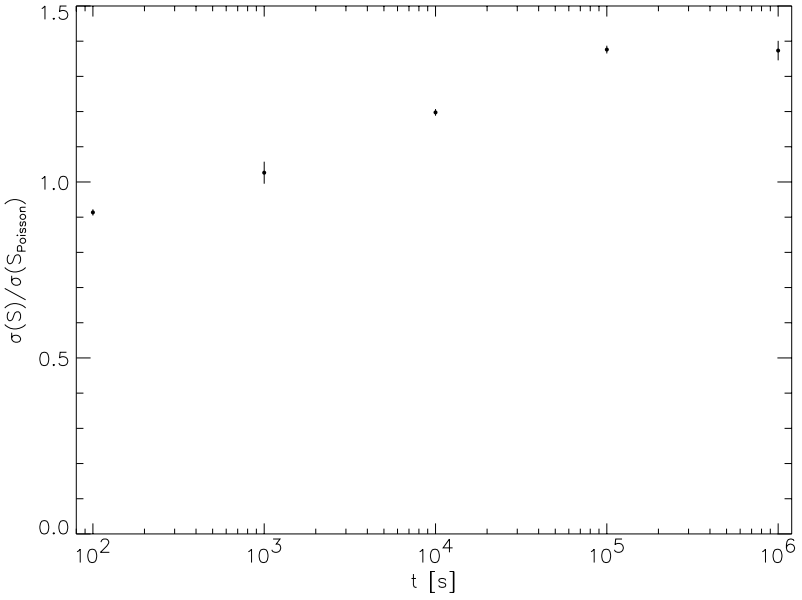

Figure 8.16: Ratio $\sigma(S)/\sigma(S_{Poisson})$ as a function of the exposure time of the standard deviation in the sky images of the background simulated applying the digital fine threshold equalization to the standard deviation of the sky images of the background simulated applying a pure Poisson statistics.

Table 8.8: Statistics of the background detector images simulated applying the digital fine regulation of the threshold resulting in $\sigma(E_{thr}) = 0.4$ keV.

t [s]	$\bar{B}$ [cts]	$\sigma(B)$ [cts]	$\sigma(B)/\bar{B}$
10^2	10.04 ± 0.08	2.82 ± 0.08	0.281 ± 0.008
10^3	100.7 ± 0.2	10.42 ± 0.09	0.1036 ± 0.0009
10^4	1007 ± 2	47 ± 1	0.046 ± 0.001
10^5	10073 ± 5	358 ± 2	0.0356 ± 0.0002
10^6	100724 ± 89	3447 ± 125	0.034 ± 0.001

Table 8.9: Statistics of the background sky images from the simulation applying the digital fine regulation of the threshold resulting in $\sigma(E_{thr}) = 0.4$ keV.

t [s]	$\sigma(S)$ [cts]	$\sigma(S_{Poisson})$ [cts]	$\sigma(S)/\sigma(S_{Poisson})$
10^2	112.0 ± 0.7	122.6 ± 0.8	0.914 ± 0.009
10^3	436 ± 6	425 ± 12	1.03 ± 0.03
10^4	2324 ± 9	1940 ± 13	1.198 ± 0.009
10^5	20294 ± 151	14747 ± 44	1.38 ± 0.01
10^6	197280 ± 3976	143650 ± 36	1.37 ± 0.03

8.6 Discussion and conclusions

The threshold uniformity is a key parameter in background dominated wide field of view instruments, especially coded mask aperture systems and in this chapter the impact of the measured threshold uniformity on SuperAGILE imaging is evaluated.

The semi-analytic technique described in sec. 8.3.2 allows to easily and rapidly produce background detector images overcoming the computation time needed by Monte Carlo simulation codes. All the major perturbations of the background among the different pixels are introduced.

The effect of the threshold uniformity on the relative dispersion $\sigma(B)/\bar{B}$ of the background detector images is estimated considering different threshold models: a replica of the 384 measured threshold values, by using a permutation of four subsets of 96 values each in order to avoid spatial frequencies in the threshold pattern of the SuperAGILE detector modules, a simple cut-off technique by integrating the background events only above 15 keV and finally the threshold equalization by means of the 3-bit XAA1.2 DAC fine regulation. As can be seen in the summary plot in fig. 8.18, in all cases the relative dispersion $\sigma(B)/\bar{B}$ of the background detector images shows a limit value as a function of the exposure time. While, in case of the threshold pattern replica, the limit value (about 0.169) is big compared to the relative dispersion at the same exposure in background images simulated with only the Poisson statistics contribution (around 0.001), the value slightly decreases if considering the cut-off method $E_{thr} \geq 15$ keV (down to

0.119) and finally is the smallest (about 0.034) if the background is simulated with the threshold equalized using the 3-bit DAC.

After decoding the detector images and producing the sky images using the SuperAGILE imaging algorithm, the background sky images standard deviation is evaluated for the different threshold cases. Particularly, the ratio of the background sky images standard deviation in the different threshold models with respect to the pure Poisson statistics standard deviation (considered as a reference) is evaluated in order to estimate how the threshold non uniformity increases the sky image dispersion.

If considering the threshold pattern replica, a ratio around 5 of the sky image standard deviation to the Poisson statistics value is found at 10^6 s exposure and, if not corrected, this fact does not allow to observe faint sources, as the blazar, with SuperAGILE. The ratio slightly decreases down to about 3 in case the cut-off technique of integrating the background only above 15 keV is considered, but this value is still too high to efficiently observe faint sources with SuperAGILE. Finally, the 3-bit DAC fine regulation of the thresholds allows to reduce the ratio down to about 1.4, a very promising value. The ratio of the sky images standard deviation with respect of the Poisson statistics value in the different cases is plotted as a function of time in fig. 8.18.

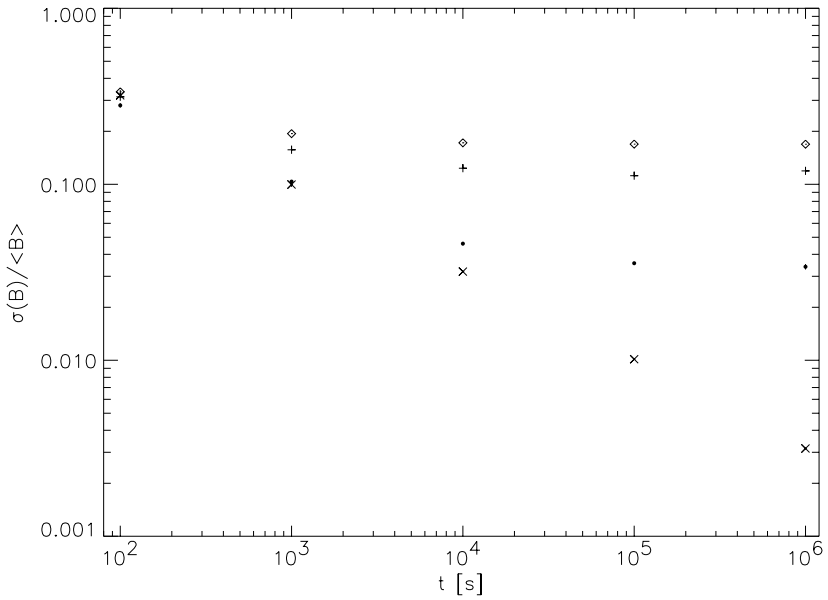

Figure 8.17: Comparison of the relative dispersion $\sigma(B)/\bar{B}$ as a function of the exposure time from the background detector images simulated with the different threshold models: replica of the measured threshold pattern (diamonds), cut-off technique $E_{thr} \geq 15$ keV (plus signs), digital threshold equalization (dots) and reference background with pure Poisson statistics (crosses).

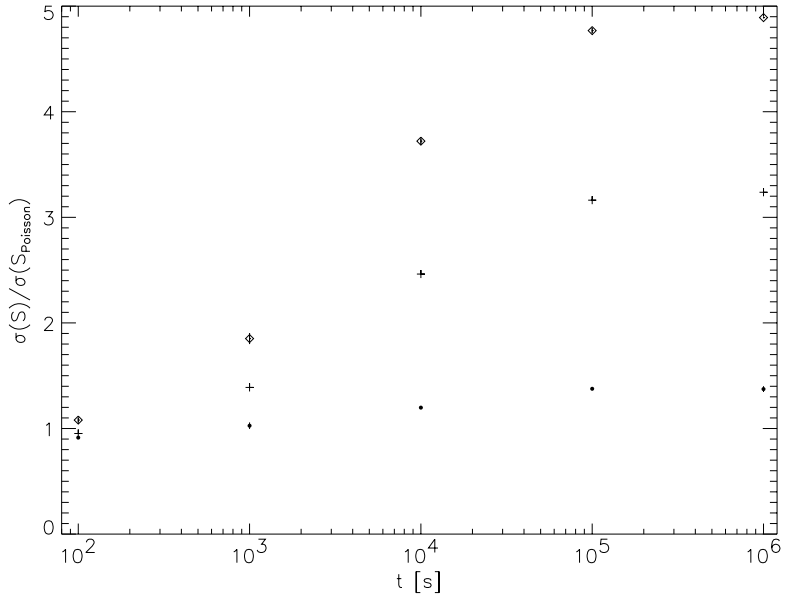

Figure 8.18: Comparison of the ratio $\sigma(S)/\sigma(S_{Poisson})$ as a function of the exposure time in the sky images of the background simulated with the different threshold models: replica of the measured threshold pattern (diamonds), cut-off technique $E_{thr} \geq 15$ keV (plus signs), and digital threshold equalization (dots).

Conclusions and future perspectives

This thesis describes the study of the performances of the SuperAGILE instrument, with a particular attention to the most important criticalities of the front-end electronics. The research work has been developed in the "Astrofisica delle Alte Energie e Tecnologie Relative" research group of the Istituto di Astrofisica Spaziale e Fisica Cosmica (IASF) CNR (now INAF) in Rome.

SuperAGILE is the hard X-ray monitor of the AGILE satellite mission, the first small scientific mission of the Agenzia Spaziale Italiana (ASI), devoted to the observation of the Sky in the $15 \div 40$ keV and 30 MeV $\div$ 50 GeV energy bands, whose launch is foreseen in late 2005. It is the first time that a gamma ray sensitive mission is equipped with a hard X-ray monitor, playing an important role in the scientific objectives and observing strategy. Because of the required wide field of view and high angular resolution and due to the energy band, SuperAGILE is designed as a coded aperture instrument, with a silicon microstrip detector and a tungsten coded mask.

The study of the sources in the High Energy Astrophysics proves that joint observations in the X-ray and gamma ray energy bands can add significant clues to the knowledge of the emission mechanisms and sources nature. This is the case of some classes of compact galactic sources, for example the microquasars, that are accreting black holes emitting moderately relativistic jets, intense in X-rays and expected to emit gamma rays, where the X-ray observations can be used to "single out" the faint gamma ray emission. Another important example concerns the blazar, a class of Active Galactic Nuclei characterized by two intense jets, one pointing along the line of sight, whose spectral energy distribution contains two peaks, one in the infrared to X-ray band and the other in the gamma rays. Finally in the Gamma Ray Burst, transients sources bright in hard X-rays and whose emission in gamma rays has been detected only in few events by EGRET, the X-ray flux can be used to locate the transient, constraint the possible gamma ray detection and deliver the coordinates to optical, infrared and radio observers so allowing a rapid and efficient follow-up.

SuperAGILE is an innovative instrument under many points of view: it is the first space instrument for X-rays based on a silicon microstrip detector, the coded mask has one of the smallest pixel size ever manufactured and the main front-end electronics peculiarity is a high signal to noise ratio with a small power consumption.

The research work contained in this thesis deals with some of the most important criticalities of the SuperAGILE instrument: the thermal stability of the front-end electronics circuit and the stability with respect of the supply voltage variations, the effects produced by the cosmic rays interaction in integrated circuits on orbit, the uniformity of the linearity parameters and of the energy threshold and finally the effect of the measured front-end electronics performances on the SuperAGILE imaging.

The thermal stability of the XAA1.2 read-out chip, especially of the address signals, has serious consequences on the SuperAGILE performances. In fact the reconstruction of the photon position on the detector, the first step of the imaging process in coded aperture instruments, is performed by means of two address signals, delivered by the front-end electronics circuit at every trigger. The values of the address signals for each pixel are stored in a look-up table, where they are extracted to reconstruct the photons position. Any variation in the address signals must be corrected in order to efficiently reconstruct the sources position in the Sky. Last but not least, if the position error exceeds one bit the whole imaging can be seriously compromised.

As described in chapter 4, the address signals are measured feeding the XAA1.2 with an electronic charge pulse generator and show significant shifts corresponding to temperature variations on the scale of 10° C. Since four such address conversion tables can be stored in the payload memory, a temperature variation range up to 40° C can be compensated without uploading different tables from the ground station, that is a time consuming operation.

Although only large supply voltage variations (50 mV) produce significant shifts in the XAA1.2 address signals, smaller variations affect the read-out chip gain and power consumption, as reported in chapter 4. Particularly the power consumption variations are critical since the total AGILE power budget is only 122 W, of which 11 W allocated to SuperAGILE. The measurements show that the gain and power consumption variations constraint the voltage stability down to 2 mV.

All the electronic devices, and particularly the integrated circuits built using the CMOS technology as the XAA1.2, are affected by the interaction of the cosmic rays on orbit. These interactions can produce single particle effects, such as the latch-up, that is the sudden increase of the supply currents and can permanently damage the chip because of the overheating, the Single Event Upset (SEU), a bit flip in the chip memory producing unpredictable changes in the device operations, and finally integrated effects known as total ionizing dose, degrading the overall chip performances.

Since the XAA1.2 is not designed as a radiation-resistant chip for space applications, its sensitivity to latch-up, SEU and total ionizing dose has been measured in my research work at the dedicated SIRAD facility of the Laboratori Nazionali INFN in Legnaro near Padova in Italy. As described in chapter 5, the circuit is exposed at ions of different linear energy transfer (the key parameter describing the energy released by the charged particle in the silicon bulk) and the latch-up and SEU cross sections are measured. The test results are very promising since the XAA1.2 shows a reduced sensitivity to latch-up and SEU and is tolerant to the total ionizing dose up to more than 100 krad.

To estimate the expected rate of latch-up and SEU from cosmic rays on AGILE, the measured cross sections are convolved with the cosmic ray flux at the AGILE or-

bit, estimated using the CREME96 code. An approximated technique considering the spallation of high energy protons in the silicon bulk is taken into account to evaluate the rate of proton induced effects. As reported in chapter 5, no latch-up or SEU events are expected and the effects of the total dose are negligible. These results are very important since they prevent the SuperAGILE front-end electronics from damages and loss of configuration when on orbit. In order to be conservative, a latch-up monitor and a SEU prevention strategy are introduced anyway in the electronics design.

My research work involves the development of data analysis programs in order to efficiently process the data produced during the laboratory measurements. The most important requirement of the analysis software, as described in chapter 6, is the capability to process data from a big number of pixels, each one considered as an independent detector. For this reason, in both the analysis of electronic pulse measurements and photon acquisitions, automatic fitting procedures without the parameter introduction for each single pixel from the user are developed and functions to evaluate the global properties of the system under test are introduced. Part of the programs developed during my research work will be integrated in the SuperAGILE data analysis software.

The assembly of the SuperAGILE proto-flight model started at the end of August 2004 and is presently in progress. As explained in chapter 4, the front-end electronics is the heart of a solid state detector based instrument and affects all its scientific performances. For this reason, a great effort is made in measuring the front-end electronic performances during all the stages of the instrument development.

Chapter 7 contains the measurements of the front-end electronics performances before the detector integration, after the burn-in process (with the SAFEE boards supplied and programmed in nominal conditions at 75° C for 240 hours long) and finally after the detector integration and bonding. No performance degradation is measured after the burn-in process. As a result, the system energy resolution, dominated by the electronic noise in the read-out circuit, is 7.5 keV FWHM as measured with the electronic pulse generator on the first complete detector module. The measured value is in good agreement with the estimations of the noise components in chapter 4 and is rather well confirmed by fitting the spectra of X-ray calibration sources. Actually the measured threshold is about 19 keV and is expected to decrease applying an optimization technique to the XAA1.2 circuit parameters.

Coded aperture systems are wide field of view instruments and are background dominated. For this reason any instrumental feature affecting the background uniformity among the pixels has serious effects on the background accumulation and thus on the imaging capabilities. In chapter 8 the study of the effect of the measured threshold non uniformity on SuperAGILE imaging is described.

Since a complete Monte Carlo simulation would be extremely time consuming, background detector images are produced using a semi-analytic technique applying different threshold uniformity models. Applying to the whole instrument a replica of the measured threshold values, with permutations of the elements in order to avoid spatial frequencies, has serious effects on the imaging at exposure times about 10^6 s and prevents the observation of faint sources as the blazar. Even integrating the background only above a fixed threshold this effect is reduced but not eliminated. Only applying the

threshold equalization, by means of the XAA1.2 3-bit digital fine regulation, uniformity levels allowing to integrate at 10^6 s and to observe faint sources can be reached.

The proto-flight model assembly is foreseen to be completed in spring 2005. After that time, SuperAGILE will be extensively calibrated at the Istituto di Astrofisica Spaziale e Fisica Cosmica (IASF) CNR (now INAF) in Rome. At the beginning the SuperAGILE detector will be calibrated using X-ray sources (^{109}Cd, ^{241}Am and ^{57}Co) and an X-ray tube facility of the Istituto di Struttura della Materia (ISM) CNR to measure the detector efficiency, linearity and energy resolution. Then the coded mask will be aligned and integrated and the complete SuperAGILE instrument will be calibrated with the same X-ray sources and the X-ray tube facility to measure the detector efficiency, linearity, energy resolution and point spread function (from the images) on-axis and at different angles off-axis. After the SuperAGILE integration in the AGILE payload (with the Anti-Coincidence system and all the payload blankets), the instrument efficiency will be measured using the X-ray sources (^{109}Cd, ^{241}Am and ^{57}Co).

Acknowledgements

The research work described in this thesis has been developed at the IASF CNR in Rome within the "Astrofisica delle Alte Energie e Tecnologie Relative" research group. I am indebted with all the members of the research group and the SuperAGILE team, researchers, technicians and students and I want to express my thanks to all of them. A special acknowledgement goes to my supervisor Enrico Costa for useful suggestions and discussions about all the topics of this thesis.

AGILE is a project funded by ASI, CNR/INAF, INFN and CIFS. I would like to thank AGILE Principal Investigator Marco Tavani, especially for his explanations about the High Energy sources that AGILE will observe.

Many persons provided me useful information about the instruments in the AGILE payload. Among them I want to thank Andrea Argan (IASF Milano), Claudio Labanti (IASF Bologna), Bettj Schena and Giacinto De Paris (IASF Roma).

Many persons are involved in the design and manufacturing of the SuperAGILE front-end electronics and test equipments. From them, especially Ennio Morelli (IASF Bologna), Geiland Porrovecchio and Alda Rubini (IASF Roma) and Marcello Mastropietro (ISC Roma), I received many explanations about the SuperAGILE electronics. I received useful explanation and discussions about the SuperAGILE mechanical design and structure from Massimo Rapisarda (ENEA Frascati) and Massimo Frutti (IASF Roma). Moreover I want to thank Bjørn Sundal (Ideas ASA) for its useful discussions about the XAA1.2 ASIC chip.

In performing all the laboratory measurements described in this thesis I received useful suggestions and discussion from many members of the SuperAGILE team. Among them I want to thank especially Paolo Soffitta, Marco Feroci and Luigi Pacciani. Their suggestions deeply affect also the development of the data analysis software.

Many suggestions in planning the radiation damage tests, in designing the experimental set-up and in discussing the results have been given by Michela Prest (Università dell'Insubria), Erik Vallazza (INFN Trieste), Scott Barthelmy and Ray Ladbury (GSFC NASA). Furthermore I am grateful to the SIRAD facility team at the Laboratori Nazionali INFN of Legnaro, especially Andrea Candelori and Jeffery Wyss, for their essential help during the irradiation tests and to the ion beam operators for collaboration and patience.

With Francesco Lazzarotto I shared the development of the `SADAS` data analysis software and I received from him explanations and suggestions about the SuperAGILE software architecture and design.

In the study of the threshold non uniformity on the SuperAGILE imaging I have benefited greatly from discussions with Igor Lapshov (HEAD IKI), Imma Donnarumma (IASF Rome) and Barbara Preger (INFN Frascati), all people involved in the SuperAGILE Monte Carlo simulations and imaging software development.

Last but not least, I would like to thank the NASA Astrophysics Data System[1] for their on-line abstract and scanned article services.

[1] `http://adswww.harvard.edu/`

Appendix A

Selected list of publications

A.1 The AGILE mission and the SuperAGILE instrument

1. 2. V. Cocco, M. Tavani, G. Barbiellini, A. Argan, N. Auricchio, A. Bulgarelli, P. Caraveo, E. Celesti, A. Chen, E. Costa, E. Del Monte, G. Di Cocco, G. Fedel, M. Feroci, M. Fiorini, T. Froysland, M. Galli, F. Gianotti, A. Giuliani, C. Labanti, I. Lapshov, F. Lazzarotto, P. Lipari, F. Longo, E. Mattaini, S. Mereghetti, E. Morelli, A. Morselli, L. Pacciani, A. Pellizzoni, F. Perotti, P. Picozza, C. Pittori, C. Pontoni, G. Porrovecchio, B. Preger, M. Prest, M. Rapisarda, E. Rossi, A. Rubini, P. Soffitta, M. Trifoglio, E. Vallazza, S. Vercellone, D. Zanello,
"The Science of AGILE: Part I",
Nuclear Physics B, ***113****, 231-238 (2002)*;

2. C. Pittori, M. Tavani, G. Barbiellini, A. Argan, N. Auricchio, A. Bulgarelli, P. Caraveo, E. Celesti, A. Chen, E. Costa, V. Cocco, E. Del Monte, G. Di Cocco, G. Fedel, M. Feroci, M. Fiorini, T. Froysland, M. Galli, F. Gianotti, A. Giuliani, C. Labanti, I. Lapshov, F. Lazzarotto, P. Lipari, F. Longo, E. Mattaini, S. Mereghetti, E. Morelli, A. Morselli, L. Pacciani, A. Pellizzoni, F. Perotti, P. Picozza, C. Pontoni, G. Porrovecchio, B. Preger, M. Prest, M. Rapisarda, E. Rossi, A. Rubini, P. Soffitta, M. Trifoglio, E. Vallazza, S. Vercellone, D. Zanello,
"The Science of AGILE: Part II",
Nuclear Physics B, ***113****, 239-246 (2002)*;

3. M. Feroci, E. Costa, L. Barbanera, E. Del Monte, G. Di Persio, I. Donnarumma, M. Frutti, I. Lapshov, F. Lazzarotto, M. Mastropietro, E. Morelli, L. Pacciani, G. Porrovecchio, B. Preger, M. Rapisarda, A. Rubini, P. Soffitta, G. Sabatino,
"The Engineering Model of the SuperAGILE Experiment",
Proceedings of the SPIE, Volume 5488, pp. 165-176 (2004);

4. L. Pacciani, G. Porrovecchio, L Barbanera, E. Costa, E. Del Monte, G. Di Persio, I. Donnarumma, M. Feroci, F. Lazzarotto, O. Uberti, A. Rubini, P. Soffitta, A. Bulgarelli, F. Gianotti, E. Morelli, M. Trifoglio, M. Mastropietro,

"Instrumentation for Ground Test of SuperAgile Detectors and Front-End Electronics",
Proceedings of the SPIE, Volume 5488, pp. 719-730 (2004);

5. M. Feroci, E. Costa, L. Barbanera, E. del Monte, G. di Persio, M. Frutti, I. Lapshov, F. Lazzarotto, M. Mastropietro, E. Morelli, L. Pacciani, G. Porrovecchio, B. Preger, M. Rapisarda, A. Rubini, P. Soffitta, M. Tavani, A. Argan, G. Ghirlanda, S. Mereghetti, A. Pellizzoni, S. Vercellone, G. Barbiellini, F. Longo, M. Prest, E. Vallazza
"SuperAGILE: The Hard X-ray Imager of AGILE",
"Gamma-Ray Bursts: 30 Years of Discovery", (Edited by E. E. Fenimore and M. Galassi), AIP Conference Proceedings, Vol. 727, p. 696-699 (2004);

6. M. Tavani, G. Barbiellini, A. Argan, A. Bulgarelli, P. Caraveo, E. Celesti, A. Chen, V. Cocco, E. Costa, E. Del Monte, G. di Cocco, G. Di Persio, I. Donnarumma, M. Feroci, M. Fiorini, T. Froysland, M. Frutti, M. Galli, F. Gianotti, A. Giuliani, C. Labanti, I. Lapshov, F. Lazzarotto, F. Liello, P. Lipari, F. Longo, L. Marisaldi, M. Matropietro, A. Mauri, S. Mereghetti, E. Morelli, A. Morselli, L. Pacciani, A. Pellizzoni, F. Perotti, P. Picozza, C. Pittori, C. Pontoni, G. Porrovecchio, B. Preger, M. Prest, M. Rapisarda, E. Rossi, A. Rubini, P. Soffitta, A. Traci, M. Trifoglio, E. Vallazza, S. Vercellone, D. Zanello,
"The AGILE Mission: X-Ray and Gamma-Ray Astrophysics of Galactic Sources",
"Fourth AGILE Science Workshop" (M. Tavani, A. Pellizzoni, S. Vercellone editors), p. 3 (2003);

7. E. Costa, E. Del Monte, I. Donnarumma, M. Feroci, I. Lapshov, E. Morelli, L. Pacciani, B. Preger, M. Rapisarda, P. Soffitta, M. Tavani, S. Mereghetti, S. Vercellone, G. Barbiellini, M. Prest, E. Vallazza,
"Galactic Sources and AGILE: Observations and Multifrequency Programs",
"Fourth AGILE Science Workshop" (M. Tavani, A. Pellizzoni, S. Vercellone editors), p. 229 (2003);

8. M. Feroci, E. Costa, E. Del Monte, I. Lapshov, F. Lazzarotto, L. Pacciani, B. Preger, M. Rapisarda, P. Soffitta,
"Gamma-Ray Burst Localization with SuperAGILE",
"Third Rome Workshop on Gamma-Ray Bursts in the Afterglow Era" (M. Feroci, F. Frontera, N. Masetti, L .Piro eds.), ASP Conference Series, vol. 312, p. 509-512 (2004);

9. M. Tavani, G. Barbiellini, A. Argan, N. Auricchio, A. Bernabeo, A. Bulgarelli, P. Caraveo, E. Celesti, A. Chen, V. Cocco, E. Costa, E. Del Monte, G. De Paris, G. Di Cocco, G. Fedel, M. Feroci, M. Fiorini, T. Froysland, M. Galli, F. Gianotti, A. Giuliani, C. Labanti, I. Lapshov, F. Lazzarotto, P. Lipari, F. Longo, M. Mastropietro, E. Mattaini, A. Mauri, S. Mereghetti, E. Morelli, A. Morselli, L. Pacciani,

A. Pellizzoni, F. Perotti, P. Picozza, C. Pittori, C. Pontoni, G. Porrovecchio, B. Preger, M. Prest, M. Rapisarda, E. Rossi, A. Rubini, E. Sant'Ambrogio, P. Soffitta, L. Soli, A. Traci, M. Trifoglio, E. Vallazza, S. Vercellone, A. Zambra, D. Zanello,
"The AGILE Instrument",
Proceedings of the SPIE "X-Ray and Gamma-Ray Telescopes and Instruments for Astronomy" (Truemper J. E., Tananbaum H. D. editors), vol. 4851, p. 1151 (2003);

10. M. Feroci, E. Costa, E. Del Monte, I. Lapshov, M. Mastropietro, E. Morelli, M. Rapisarda, A. Rubini, P. Soffitta, G. Barbiellini, F. Longo, M. Prest, E. Vallazza, A. Argan, S. Mereghetti, M. Tavani, S. Vercellone, A. Morselli,
"SuperAGILE: the X-ray monitor of the AGILE gamma-ray mission",
"the Fourth INTEGRAL Workshop" (Gimenez A., Reglero V, Winkler C. editors), p. 569 (2001) and astro-ph/0101154;

11. M. Rapisarda, L. Barbanera, E. Costa, E. Del Monte, G. di Persio, M. Feroci, M. Frutti, I. Lapshov, B. Martino, M. Mastropietro, E. Morelli, A. Rubini, P. Soffitta, M. Tavani, S. Mereghetti, S. Vercellone, P. Caraveo, F. Perotti, G. Barbiellini, G. Budini, F. Longo, M. Prest, E. Vallazza, A. Morselli, P. Picozza, V. Cocco, C. Pittori, G. di Cocco, C. Labanti,
"SuperAGILE, the X-ray monitor of AGILE (presented by M. Rapisarda)",
"Frontier Objects in Astrophysics and Particle Physics", (F. Giovannelli and G. Mannocchi editors), p. 539 (2001);

12. I. Lapshov, L. Barbanera, E. Costa, E. Del Monte, M. Feroci, G. Porrovecchio, M. Mastropietro, L. Pacciani, A. Rubini, P. Soffitta, E. Morelli, M. Rapisarda, G. Barbiellini, F. Longo, M. Prest, E. Vallazza, A. Argan, S. Mereghetti, M. Tavani, S. Vercellone, A. Morselli,
"SuperAGILE: the X-ray Monitor on-board of AGILE",
"Gamma-Ray Astrophysics 2001" (Edited by Steven Ritz, Neil Gehrels, and Chris R. Shrader), AIP Conference Proceedings, vol. 587, p. 769 (2001);

13. M. Feroci, E. Costa, E. Del Monte, I. Lapshov, M. Rapisarda, P. Soffitta, G. Barbiellini, M. Prest, E. Vallazza, S. Mereghetti, M. Tavani, S. Vercellone, A. Morselli, F. Longo,
"Gamma-ray bursts with SuperAGILE",
"Gamma Ray Burst in the Afterglow Era" (Costa E., Frontera F., Hjorth J. editors), p. 368 (2001);

A.2 The XAA1.2 ASIC performances

1. E. Del Monte, E. Costa, G. Di Persio, M. Feroci, M. Mastropietro, E. Morelli, L. Pacciani, G. Porrovecchio, A. Rubini, P. Soffitta,

"Laboratory tests and scientific performances of the XAA1.2 front-end chip for space applications",
Proceedings of the SPIE, Volume 5488, pp. 648-659 (2004);

A.3 Radiation-induced effects on ASIC

1. E. Del Monte, L. Pacciani, G. Porrovecchio, P. Soffitta, E. Costa, G. Di Persio, M. Feroci, M. Mastropietro, E. Morelli, M. Rapisarda, A. Rubini, D. Bisello, A. Candelori, A. Kaminski, J. Wyss,
"Radiation-induced effects on the XAA1.2 ASIC chip for space application",
*Nucl. Instr. and Meth. A, **538**, 465-482 (2005)*;

2. E. Del Monte, L. Pacciani, G. Porrovecchio, P. Soffitta, E. Costa, G. Di Persio, M. Feroci, M. Mastropietro, E. Morelli, M. Rapisarda, A. Rubini, D. Bisello, A. Candelori, A. Kaminski, J. Wyss,
"Heavy Ion Irradiation of the XAA1.2 ASIC Chip for Space Application",
Proceedings of the 2^{ND} SIRAD Workshop, LNL-INFN (REP) - 203/2004, p. 67-70 (2005)

3. E. Del Monte, E. Costa, G. Di Persio, M. Feroci, M. Mastropietro, E. Morelli, L. Pacciani, G. Porrovecchio, A. Rubini, P. Soffitta, D. Bisello, A. Candelori, A. Kaminski, J. Wyss,
"Radiation damage studies of XAA1.2 ASIC chip for the SuperAGILE experiment on board of AGILE",
Proceedings of the SPIE "X-Ray and Gamma-Ray Telescopes and Instruments for Astronomy" (Truemper J. E., Tananbaum H. D. editors), vol. 4851, p. 1029 (2003);

A.4 Software for SuperAGILE Data Analysis

1. F. Lazzarotto, E. Del Monte, M. Feroci,
"Data model applications for the SuperAGILE detection system",
Ground-based Telescopes. Edited by Oschmann, Jacobus M., Jr. Proceedings of the SPIE, Volume 5493, pp. 126-136 (2004);

2. F. Lazzarotto and E. Del Monte,
"SADAS: an integrated software system for the data of the SuperAGILE experiment",
2004, in press on Proceedings of the ADA III, Sorrento (NA), Apr 28-May 01 2004;

3. F. Lazzarotto, E. Costa, E. Del Monte, M. Feroci,
"Modeling and Developing the Information System for the SuperAGILE Experiment",
ASP Conf. Ser. 314: Astronomical Data Analysis Software and Systems (ADASS) XIII, p. 464 (2004);

Appendix B

List of acronyms and abbreviations

ADC	Analog Digital Converter
AGN	Active Galactic Nucleus
ASI	Agenzia Spaziale Italiana
ASIC	Application Specific Integrated Circuit
CMOS	Complementary Metal Oxide Semiconductor
CNR	Consiglio Nazionale delle Ricerche
CTM	Constructive Technical Model
DAC	Digital Analog Converter
DC	Daisy Chain
DISCoS	Detector Independent Science Console Subsystem
DXRB	Diffuse X-Ray Background
ENC	Equivalent Noise Charge
FEE	Front-End Electronics
FITS	Flexible Image Transport System
FWHM	Full-Width at Half Maximum
FFT	Fast Fourier Transform
GRB	Gamma Ray Burst
GRID	Gamma Ray Imaging Detector
GUI	Graphical User Interface
HMXB	High Mass X-ray Binary
IDL	Interactive Data Language

INAF	Istituto Nazionale di Astrofisica
INFN	Istituto Nazionale di Fisica Nucleare
LET	Linear Energy Transfer
LMXB	Low Mass X-ray Binary
LUT	Look-Up Table
LSB	Least Significant Bit
MGO	Multiplicity Generator Output
MSB	Most Significant Bit
PC	Personal Computer
PCB	Printed Circuit Board
PDHU	Payload Data Handling Unit
PFM	Proto-Flight Model
PHA	Pulse Height Amplitude
PSU	Power Supply Unit
RMS	Root Mean Squared
SAIE	SuperAGILE Inteface Electronics
SAFEE	SuperAGILE Front-End Electronics
SEE	Single Event Effect
SEM	Simplified Engineering Model
SEU	Single Event Upset
TE	Test Equipment
VLSI	Very Large Scale Integration

List of Figures

1.1 Final map showing the location in galactic coordinates of the 2704 GRB recorded with BATSE experiment. 3
1.2 Source flux with time in the 2-10 keV range from Costa et al. (1997). . . 4
1.3 Histogram of the GRB duration T_{90} from Horváth (2002). 6
1.4 Final map showing the location in galactic coordinates of the 271 sources recorded in the Third EGRET catalog (from Hartman et al. (1999)). The unidentified sources are plotted with open circles 14
1.5 Simulation of an AGILE observation of the Vela pulsar from Pellizzoni et al. (2004). Timing analysis with resolution $10 \div 50\,\mu$s can reveal possible microstructures within the peaks of the light curve. 16
1.6 Principal classes of AGN (from Urry and Padovani (1995)). 18
1.7 A schematic diagram of the current paradigm for radio-loud AGN (not to scale) from Urry and Padovani (1995). 20
1.8 Reconstructed light curve of a simulated flare of PKS 1622-297 (similar to the 1995 event reported in Mattox et al. (1997)). 22
1.9 Reconstructed light curve of the 3C 279 AGILE simulated observation with two possible models (steady emission, dashed blue line and flaring emission, solid red line) from Vercellone et al. (2003). 23
1.10 AGILE energy bands superimposed on the Spectral Energy Distribution of several blazars 24
1.11 Example of simultaneous gamma ray and hard X-ray observations of known AGN by AGILE. 25
1.12 Average diffuse gamma ray spectrum of the inner Galaxy region, ($300° < l < 60°$, $|b| \leq 10°$), from Hunter et al. (1997). 26

2.1 Schematic of the AGILE payload. 32
2.2 Schematic view of the Silicon Tracker assembly. 33
2.3 Schematic view of the Mini-Calorimeter assembly from Celesti et al. (2004). 35
2.4 A comparison between the effective areas of AGILE, EGRET and COMPTEL at different inclinations off axis, from Tavani et al. (2004). 36
2.5 A comparison between the angular resolution of AGILE (in red) and EGRET (in blue), from Tavani et al. (2003). 37
2.6 Picture of the SuperAGILE coded mask. 40
2.7 Picture of the SuperAGILE collimator. 40

2.8 Section of the silicon microstrip detector together with a schematic view of its working principle from Peisert (1992). 41
2.9 Picture of the SuperAGILE field of view. The region between $-30°$ and $+30°$ is fully coded while in the remaining four "wings" only one coordinate is coded. 42
2.10 Plot of the SuperAGILE effective area below 60 keV. 44
2.11 On-axis sensitivity curves for SuperAGILE with $5 \cdot 10^4$ s integration time at 5σ significance level in units of photons $\cdot$ cm$^{-2} \cdot$ s$^{-1} \cdot$ keV^{-1}. 45
2.12 On-axis sensitivity curves for SuperAGILE with $5 \cdot 10^4$ s integration time at 5σ significance level in units of mCrab. 45

3.1 Block diagram of the SAFEE board. 51
3.2 Picture of the SAFEE PCB. 52
3.3 Microscopy picture of the ceramic pitch adapter. 52
3.4 Schematic of a XAA1.2 analogue channel. From left the preamplifier, the shaper, the peak stretcher and the discriminator. 54
3.5 Screen capture of the XA-DAQ software main menu. 59
3.6 Simplified scheme of the SAFEE TE from Pacciani et al. (2004). 60
3.7 Example of the SAFEE TE quicklook screen capture. 62
3.8 Block diagram of the SAIE board. 63
3.9 Main functions of the PDHU. 64

4.1 Linearity curve of the XAA1.2 chip non bonded to the detector. 71
4.2 Linearity curve of the CTM. 71
4.3 Histogram of the XAA1.2 offset (upper panel) and offset value of each input channel (lower panel). 73
4.4 Histogram of the XAA1.2 gain (upper panel) and gain value of each input channel (lower panel). 73
4.5 Histogram of the CTM offset (upper panel) and offset value of the 37 less noisy input channel (lower panel). 74
4.6 Histogram of the CTM gain (upper panel) and gain value of the 37 less noisy input channel (lower panel). 74
4.7 Histogram of the 0.88 fC output amplitude (corresponding to 20 keV energy) acquired with the XAA1.2 alone (upper panel) and output amplitude value of each input channel (lower panel). 76
4.8 Histogram of the 0.88 fC output amplitude (corresponding to 20 keV energy) acquired with the CTM (upper panel) and output amplitude value of the 37 less noisy input channel (lower panel). 76
4.9 Histogram of the intercept a in the XAA1.2 threshold scan (upper panel) and intercept value of each input channel (lower panel). 78
4.10 Histogram of the slope b in the XAA1.2 threshold scan (upper panel) and intercept value of each input channel (lower panel). 78
4.11 Histogram of the intercept a in the CTM threshold scan (upper panel) and intercept value of the 37 less noisy input channels (lower panel). . . 79

4.12 Histogram of the slope b in the CTM threshold scan (upper panel) and slope value of the 37 less noisy input channels (lower panel). 79
4.13 Histogram of the XAA1.2 energy threshold (upper panel) and energy threshold value of the input channels (lower panel). 80
4.14 Histogram of the CTM energy threshold (upper panel) and energy threshold value of the input channels (lower panel). 80
4.15 Superposition of group signals at different temperatures between $-20°$ C and $+40°$ C. 83
4.16 Superposition of strip signals in the first group at different temperatures between $-20°$ C and $+40°$ C. 83
4.17 Supply currents I_{DD} (upper panel) and I_{SS} (lower panel) at different supply voltage values. 85
4.18 Power consumption at different supply voltage values 85
4.19 Superposition of linearity curves at different supply voltage values. . . . 86
4.20 Offset (upper panel) and gain (lower panel) at different supply voltage values. 87
4.21 Output amplitude corresponding to a 0.88 fC test charge (equivalent to 20 keV) at different supply voltage values. 87
4.22 Superposition of the group signal at different voltage values. 88
4.23 Superposition of the strip signal in the first group at different voltage values. 88

5.1 Example of a p-n-p-n structure (a) with its inherent parasitic circuit and of its first order (b) equivalent model, from Cané et al. (1991). 93
5.2 Schematic of the SIRAD irradiation facility, from Wyss et al. (2001). . . 96
5.3 Experimental set-up: XA-DAQ acquisition board (top of the stand), power supply (under the XA-DAQ board) and SIRAD irradiation chamber (right of the picture). 97
5.4 Experimental set-up: two test PCB covered with the aluminum layers (left and center) and the diode set on the target plane (right) fixed on the sample holder inside the experimental chamber. 98
5.5 Values of the currents I_{SS} (upper panel) and I_{DD} (lower panel), recorded during a ^{46}Ti irradiation, as a function of time. 101
5.6 Results of the irradiation for the latch-up measurements on the three XAA1.2 chips. LET is the linear energy transfer, $P_{latch-up}$ is the latch-up probability and $\sigma_{latch-up}$ is the latch-up cross section. 104
5.7 Results of the irradiation for the SEU measurements on the three XAA1.2 chips. LET is the linear energy transfer, P_{SEU} is the SEU probability and σ_{SEU} is the SEU cross section. 105
5.8 Power consumption for the three chips as a function of the total dose in the active layer. 108

5.9 Values of the bias currents of the preamplifier (*prebias*), the discriminator (*otabias*), the shaper (*shabias*), the peak stetcher (*strbias*) and the current-voltage buffer converter (*IbDAC*) as a function of the total dose in the active layer. 109
5.10 Amplitude (converted into ADC channels) of the output signal from the chip 710-1-25 as a function of the input charge for different dose values. 109
5.11 Cosmic rays differential flux simulated with CREME96 code at AGILE orbit. 110

6.1 Block diagram of the DISCoS software architecture, from Gianotti and Trifoglio (2001). 117
6.2 Block diagram of the SAFEE TE electronic calibration analysis software. 122
6.3 Block diagram of the SAIE TE electronic calibration analysis software. . 123
6.4 GUI menu to insert the electronic calibration parameters. 124
6.5 Block diagram of the SAFEE TE spectral analysis software. 129

7.1 Picture of the SuperAGILE detector. 132
7.2 Disposition of the SAFEE and the four detection units (D1 $\div$ D4) composing the SuperAGILE detector. 133
7.3 Histogram of the offset f from the daisy chain 1 calibration curve (upper panel) and offset value of each channel in the daisy chain (lower panel). 135
7.4 Histogram of the gain g from the daisy chain 1 calibration curve (upper panel) and gain value of each channel in the daisy chain (lower panel). . 135
7.5 Histogram of the noise FWHM from the daisy chain 1 calibration curve (upper panel) and FWHM value of each channel in the daisy chain (lower panel). 136
7.6 Histogram of the offset f from the daisy chain 2 calibration curve (upper panel) and offset value of each channel in the daisy chain (lower panel). 136
7.7 Histogram of the gain g from the daisy chain 2 calibration curve (upper panel) and gain value of each channel in the daisy chain (lower panel). . 137
7.8 Histogram of the noise FWHM from the daisy chain 2 calibration curve (upper panel) and FWHM value of each channel in the daisy chain (lower panel). 137
7.9 Histogram of the offset f from the daisy chain 3 calibration curve (upper panel) and offset value of each channel in the daisy chain (lower panel). 138
7.10 Histogram of the gain g from the daisy chain 3 calibration curve (upper panel) and gain value of each channel in the daisy chain (lower panel). 138
7.11 Histogram of the noise FWHM from the daisy chain 3 calibration curve (upper panel) and FWHM value of each channel in the daisy chain (lower panel). 139
7.12 Histogram of the offset f from the daisy chain 4 calibration curve (upper panel) and offset value of each channel in the daisy chain (lower panel). 139
7.13 Histogram of the gain g from the daisy chain 4 calibration curve (upper panel) and gain value of each channel in the daisy chain (lower panel). . 140

7.14 Histogram of the noise FWHM from the daisy chain 4 calibration curve (upper panel) and FWHM value of each channel in the daisy chain (lower panel). 140
7.15 Plot of the FWHM measured on the PFM-B daisy chain 2 before the detector integration at different pulse charge values. 143
7.16 Histogram of the offset f from the daisy chain 1 calibration curve (upper panel) and offset value of each channel in the daisy chain (lower panel) after the detector integration and bonding. 146
7.17 Histogram of the gain g from the daisy chain 1 calibration curve (upper panel) and gain value of each channel in the daisy chain (lower panel) after the detector integration and bonding. 146
7.18 Histogram of the noise FWHM from the daisy chain 1 calibration curve (upper panel) and FWHM value of each channel in the daisy chain (lower panel) after the detector integration and bonding. 147
7.19 Histogram of the offset f from the daisy chain 2 calibration curve (upper panel) and offset value of each channel in the daisy chain (lower panel) after the detector integration and bonding. 147
7.20 Histogram of the gain g from the daisy chain 2 calibration curve (upper panel) and gain value of each channel in the daisy chain (lower panel) after the detector integration and bonding. 148
7.21 Histogram of the noise FWHM from the daisy chain 2 calibration curve (upper panel) and FWHM value of each channel in the daisy chain (lower panel) after the detector integration and bonding. 148
7.22 Histogram of the offset f from the daisy chain 3 calibration curve (upper panel) and offset value of each channel in the daisy chain (lower panel) after the detector integration and bonding. 149
7.23 Histogram of the gain g from the daisy chain 3 calibration curve (upper panel) and gain value of each channel in the daisy chain (lower panel) after the detector integration and bonding. 149
7.24 Histogram of the noise FWHM from the daisy chain 3 calibration curve (upper panel) and FWHM value of each channel in the daisy chain (lower panel) after the detector integration and bonding. 150
7.25 Histogram of the offset f from the daisy chain 4 calibration curve (upper panel) and offset value of each channel in the daisy chain (lower panel) after the detector integration and bonding. 150
7.26 Histogram of the gain g from the daisy chain 4 calibration curve (upper panel) and gain value of each channel in the daisy chain (lower panel) after the detector integration and bonding. 151
7.27 Histogram of the noise FWHM from the daisy chain 4 calibration curve (upper panel) and FWHM value of each channel in the daisy chain (lower panel) after the detector integration and bonding. 151
7.28 Plot of the FWHM measured on the Detection Unit 1 daisy chain 2 at different pulse charge values. 154

7.29 Background counting rate as a function of the threshold measured on the second daisy chain of the Detection Unit 1. 155
7.30 Histogram of the energy threshold in the different channels of the second daisy chain of the Detection Unit 1 (upper panel) and energy threshold value in each channel (lower panel). 155
7.31 First background detector image accumulated on the second daisy chain of the Detection Unit 1. 157
7.32 Background spectrum of the noisy pixel 437. 158
7.33 Background spectrum of the non noisy pixel 762. 158
7.34 Schematic of the Ba fluorescence source. 160
7.35 First spectrum of the custom Ba fluorescence source (32.1 keV and 36.4 keV lines) with a gaussian fit superimposed (in red). 161
7.36 First spectrum of the ^{241}Am source (59.5 keV line) with superimposed a gaussian fit on the right side and a linear interpolation to find the FWHM on the left side (in red). 161
7.37 First spectrum of the ^{57}Co source (122.1 keV line) with a gaussian fit superimposed (in red). 162
7.38 First spectrum of the ^{109}Cd source (88.0 keV line) with a gaussian fit superimposed (in red). 162
7.39 First linear fit from the peak position of the spectra in fig. 7.35, 7.36, 7.38 and 7.37 as a function of the X-ray line energy. 164
7.40 Noise ΔE_{FWHM} of the spectra in fig. 7.35, 7.36, 7.38 and 7.37 as a function of the X-ray line energy. 164

8.1 Histogram of the threshold fit parameters c (upper panel) and d (lower panel). 169
8.2 Histogram of the energy threshold values imposing $\bar{E}_{thr} = 15$ keV. . . . 169
8.3 Power laws fitting the spectrum of the Cosmic Diffuse X-Ray Background from Zombeck (1990). 170
8.4 Power law fitting the spectrum of the Crab Nebula from Zombeck (1990). 171
8.5 Image of the Monte Carlo simulated SuperAGILE background on one detector in 10^4 s observation time. The cosine fit in (8.5) is the dotted red curve. 172
8.6 Relative weight in the spectrum of the simulated SuperAGILE background between 8 keV and 100 keV. 173
8.7 Percentage variation of the integrated SuperAGILE background depending on the lower energy threshold E_{thr}. 174
8.8 Crab simulated on-axis detector image with 10^4 s exposure. 178
8.9 Crab simulated on-axis sky image with 10^4 s exposure. 178
8.10 Energy threshold in the SuperAGILE four detectors from the permutation of the basic pattern as explained in tab. 8.2. 180

8.11 Relative dispersion $\sigma(B)/\bar{B}$ as a function of the exposure time from the background detector images simulated applying the replica of the energy threshold pattern (diamonds) compared with the relative dispersion of the background detector images simulated applying the pure Poisson statistics (crosses). 181
8.12 Ratio $\sigma(S)/\sigma(S_{Poisson})$ as a function of the exposure time of the standard deviation in the sky images of the background simulated applying the replica of the energy threshold pattern to the standard deviation of the sky images of the background simulated applying a pure Poisson statistics. 181
8.13 Relative dispersion $\sigma(B)/\bar{B}$ as a function of the exposure time from the background detector images simulated applying the cut-off technique $E_{thr} \geq 15$ keV (plus signs) compared with the relative dispersion of the background detector images simulated applying the pure Poisson statistics (crosses). 183
8.14 Ratio $\sigma(S)/\sigma(S_{Poisson})$ as a function of the exposure time of the standard deviation in the sky images of the background simulated applying the cut-off technique $E_{thr} \geq 15$ keV to the standard deviation of the sky images of the background simulated applying a pure Poisson statistics. 183
8.15 Relative dispersion $\sigma(B)/\bar{B}$ as a function of the exposure time from the background detector images simulated applying the threshold equalization $\sigma(E_{thr} = 0.4$ keV (dots) compared with the relative dispersion of the background detector images simulated applying the pure Poisson statistics (crosses). 185
8.16 Ratio $\sigma(S)/\sigma(S_{Poisson})$ as a function of the exposure time of the standard deviation in the sky images of the background simulated applying the digital fine threshold equalization to the standard deviation of the sky images of the background simulated applying a pure Poisson statistics. . 185
8.17 Comparison of the relative dispersion $\sigma(B)/\bar{B}$ as a function of the exposure time from the background detector images simulated with the different threshold models. 188
8.18 Comparison of the ratio $\sigma(S)/\sigma(S_{Poisson})$ as a function of the exposure time in the sky images of the background simulated with the different threshold models. 188

List of Tables

3.1 Nominal values of the XAA1.2 bias currents and voltages. I_{bias} is the bias current while V_{bias} is the bias voltage. 54

4.1 XAA1.2 bias values fixed during the test 84

5.1 Ion species used during the irradiation at SIRAD facility with energy, LET and range values in silicon, and serial number of the irradiated chip. 99
5.2 Ion selection for the irradiation of chip number 710-1-3. The fluence error is calculated basing on the beam non uniformity. 100
5.3 Ion selection for the irradiation of chip number 710-1-12. The fluence error is calculated basing on the beam non uniformity. 100
5.4 Ion selection for the irradiation of chip number 710-1-25. The fluence error is calculated basing on the beam non uniformity. 100
5.5 Results of the irradiation for the latch-up measurements on the 710-1-3 chip. 103
5.6 Results of the irradiation for the latch-up measurements on the 710-1-12 chip. 103
5.7 Results of the irradiation for the latch-up measurements on the 710-1-25 chip. 103
5.8 Results of the irradiation for the SEU measurements on the 710-1-3 chip. 106
5.9 Results of the irradiation for the SEU measurements on the 710-1-12 chip. 106
5.10 Results of the irradiation for the SEU measurements on the 710-1-25 chip. 106

6.1 Data type and format of SAFEE TE L1 output data. 118
6.2 Data type and format of the first SAFEE TE running parameter list (configuration of the channel in test). 119
6.3 Data type and format of the second SAFEE TE running parameter list (configuration of the test charge pulse). 119
6.4 Data type and format of the third SAFEE TE running parameter list (configuration of the XAA1.2 DAC). 119
6.5 Data type and format of SAIE TE L1 photon acquisition output data. The calpulse_ID field is used during electronic pulse measurement and is dummy in this case. 120
6.6 Data type and format of SAIE TE L1 electronic pulse output data. . . . 120

6.7 Data type and format of the L2 test equipment independent output data. 121

7.1 Detection Unit 1 electronic calibration before the detector integration . 141
7.2 Detection unit 1 uniformity before the detector integration. 142
7.3 SAFEE PFM-B (Detection unit 1) threshold before the detector integration. 143
7.4 Performances of the SAFEE PFM-C before the burn-in process. 144
7.5 Performances of the SAFEE PFM-C after the burn-in process. 144
7.6 Detection unit 1 electronic calibration after the detector integration . . 152
7.7 Detection unit 1 uniformity after the detector integration. 153
7.8 Comparison of the SAFEE performances before and after the detector integration as estimated using the electronic calibration. 153
7.9 List of the X-ray sources used during tests. 159
7.10 Fit results of the SuperAGILE "first light" with m peak position and ΔE_{FWHM} full-width at half maximum of the X-ray line. 163

8.1 Relative variation of the integrated SuperAGILE background $B(E_{thr})/B(15)$ depending on the lower energy threshold E_{thr}. 174
8.2 Energy threshold basic subset permutations 179
8.3 Statistics of background detector images simulated applying a pure Poisson statistics. 179
8.4 Statistics of the background detector images simulated applying the replica of the energy threshold pattern. 180
8.5 Statistics of the background sky images from the simulation applying the replica of the energy threshold pattern. 180
8.6 Statistics of the background detector images simulated applying the correction $E_{thr} \geq 15$ keV. 184
8.7 Statistics of the background sky images from the simulation applying the correction $E_{thr} \geq 15$ keV. 184
8.8 Statistics of the background detector images simulated applying the digital fine regulation of the threshold resulting in $\sigma(E_{thr}) = 0.4$ keV. . . . 186
8.9 Statistics of the background sky images from the simulation applying the digital fine regulation of the threshold resulting in $\sigma(E_{thr}) = 0.4$ keV. . 186

Bibliography

Adams, L., Daly, E. J., Harboe-Sorensen, R., Nickson, R., Haines, J., Schafer, W., Conrad, M., Griech, H., Merkel, J., Schwall, T., dec 1992. A verified proton induced latch-up in space [CMOS SRAM]. IEEE Trans. Nucl. Sci. 39 (6), 1804–1808.

Alessandro, B., S. Beolé, S., G. Bonazzola, G., Crescio, E., De Witt, J., Giubellino, P., Idzik, M., Marzari-Chiesa, A., Masera, M., Prino, F., Ramello, L., Rato Mendes, P., Riccati, L., Sitta, M., jan 2002. Observation of radiation induced latchup in the readout electronics of NA50 multiplicity detector. Nucl. Instr. and Meth. A 476 (3), 758–764.

Amati, L., Frontera, F., Tavani, M., in't Zand, J. J. M., Antonelli, A., Costa, E., Feroci, M., Guidorzi, C., Heise, J., Masetti, N., Montanari, E., Nicastro, L., Palazzi, E., Pian, E., Piro, L., Soffitta, P., Jul. 2002. Intrinsic spectra and energetics of BeppoSAX Gamma-Ray Bursts with known redshifts. Astron. Astrophys. 390, 81–89.

Andersen, M. I., Hjorth, J., Pedersen, H., Jensen, B. L., Hunt, L. K., Gorosabel, J., Møller, P., Fynbo, J., Kippen, R. M., Thomsen, B., Olsen, L. F., Christensen, L., Vestergaard, M., Masetti, N., Palazzi, E., Hurley, K., Cline, T., Kaper, L., Jaunsen, A. O., Dec. 2000. VLT identification of the optical afterglow of the gamma-ray burst GRB 000131 at z=4.50. Astron. Astrophys. 364, L54–L61.

Band, D., Matteson, J., Ford, L., Schaefer, B., Palmer, D., Teegarden, B., Cline, T., Briggs, M., Paciesas, W., Pendleton, G., Fishman, G., Kouveliotou, C., Meegan, C., Wilson, R., Lestrade, P., Aug. 1993. BATSE observations of gamma-ray burst spectra. I - Spectral diversity. Astrophys. J. 413, 281–292.

Barichello, G., Cervera-Villanueva, A., Daniels, D. C., do Couto e Silva, E., Dumps, L., M. Ellis, M., D. Ferrère, D., Gomez-Cadenas, J. J., Gouanère, M., Hernando, J. A., Huta, W., Jimenez, J. M., Kokkonen, J., Kuznetsov, V. E., Linssen, L., Lisowski, B., Runolfsson, Ö., Soler, F. J. P., Steele, D., Stipčević, M., Veltri, M., aug 1998. Performance of long modules of silicon microstrip detectors. Nucl. Instr. and Meth. A. 413 (1), 17–30.

Begelman, M. C., Blandford, R. D., Rees, M. J., Apr. 1984. Theory of extragalactic radio sources. Reviews of Modern Physics 56, 255–351.

Beilicke, M., Ouchrif, M., Rowell, G., Schlenker, S., Mar. 2004. Discovery of PSR 1259-63 in VHE Gamma-Rays with H.E.S.S. The Astronomer's Telegram 249, 1–+.

Belyakov, V. V., Chumakov, A. I., Nikiforov, A. Y., Pershenkov, V. S., Skorobogatov, P. K., Sogoyan, A. V., dec 2000. IC's radiation effects modeling and estimation. Microel. Rel. 40 (12), 1997–2018.

Berger, M. J., Hubbell, J. H., Seltzer, S. M., Coursey, J. S., Zucker, D. S., 1999. XCOM: Photon Cross Section Database (version 1.2). [Online] Available: http://physics.nist.gov/xcom [2004, December 27]. National Institute of Standards and Technology, Gaithersburg, MD.

Bertsch, D. L., Dame, T. M., Fichtel, C. E., Hunter, S. D., Sreekumar, P., Stacy, J. G., Thaddeus, P., Oct. 1993. Diffuse Gamma-Ray Emission in the Galactic Plane from Cosmic-Ray, Matter, and Photon Interactions. Astrophys. J. 416, 587–+.

Bhat, P. N., Gupta, S. K., Murthy, P. V. R., Sreekantan, B. V., Tonwar, S. C., Viswanath, P. R., Jan. 1980. Pulsed high energy gamma rays from VELA pulsar. Astron. Astrophys. 81, L3–L5.

Bignami, G. F., Hermsen, W., 1983. Galactic gamma-ray sources. Ann. Rev. Astron. Astrophys. 21, 67–108.

Bloemen, H., 1989. Diffuse Galactic gamma-ray emission. Ann. Rev. Astron. Astrophys. 27, 469–516.

Bloom, J. S., Berger, E., Kulkarni, S. R., Djorgovski, S. G., Frail, D. A., Mar. 2003. The Redshift Determination of GRB 990506 and GRB 000418 with the Echellete Spectrograph Imager on Keck. Astron. J. 125, 999–1005.

Bloom, J. S., Djorgovski, S. G., Kulkarni, S. R., Jun. 2001. The Redshift and the Ordinary Host Galaxy of GRB 970228. Astrophys. J. 554, 678–683.

Boella, G., Butler, R. C., Perola, G. C., Piro, L., Scarsi, L., Bleeker, J. A. M., Apr. 1997a. BeppoSAX, the wide band mission for X-ray astronomy. Astron. Astrophys. Suppl. Ser. 122, 299–307.

Boella, G., Chiappetti, L., Conti, G., Cusumano, G., del Sordo, S., La Rosa, G., Maccarone, M. C., Mineo, T., Molendi, S., Re, S., Sacco, B., Tripiciano, M., Apr. 1997b. The medium-energy concentrator spectrometer on board the BeppoSAX X-ray astronomy satellite. Astron. Astrophys. Suppl. Ser. 122, 327–340.

Boller, T., Voges, W., Frontera, F., Costa, E., Piro, L., Pedersen, H., Benetti, S., Turatto, M., Goudfrooij, P., Marconi, A., Jablonka, P., Palazzi, E., Heise, J., Studt, J., Castro-Tirado, A. J., Mar. 1997. GRB 970228. IAU Circ. 6580, 1–+.

Briggs, M. S., Paciesas, W. S., Pendleton, G. N., Meegan, C. A., Fishman, G. J., Horack, J. M., Brock, M. N., Kouveliotou, C., Hartmann, D. H., Hakkila, J., Mar. 1996.

BATSE Observations of the Large-Scale Isotropy of Gamma-Ray Bursts. Astrophys. J. 459, 40–+.

Budtz-Jørgensen, C., Lund, N., Westergaard, N. J., Brandt, S., Hornstrup, A., Rasmussen, I., Laursen, S., Pedersen, S. M., Kristansen, R. E., Mogensen, P. B., Andersen, K. H., Rasmussen, I., Polny, J., Jensen, P. A., Oxborrow, C. A., Chenevez, J., Omoe, K., Kämäräinen, V. J., Andersson, T., Vilhu, O. R., Huovelin, J., Costa, E., Feroci, M., Rubini, A., Morelli, E., Morbidini, A., Frontera, F., Pelliciari, C., Loffredo, G., Zavattini, G., Carassiti, V., Morawski, M., Juchnikowski, G., Reglero, V., Peris, J., Collado, V., Rodrigo, J. M., Perez, F., Requena, J., Larsson, S., Svensson, R., Zdziarski, A., Castro-Tirado, A. J., Schnopper, H. W., Feb. 2004. JEM-X: the x-ray monitor on INTEGRAL. In: X-Ray and Gamma-Ray Instrumentation for Astronomy XIII. Edited by Flanagan, Kathryn A.; Siegmund, Oswald H. W. Proceedings of the SPIE, Volume 5165, pp. 139-150 (2004). pp. 139–150.

Cairns, I. H., Aug. 2004. Properties and Interpretations of Giant Micropulses and Giant Pulses from Pulsars. Astrophys. J. 610, 948–955.

Calvel, P., Barillot, C., Lamothe, P., Escoffet, R., dec 1996. An Empirical Model for Predicting Proton Induced Upset. IEEE Trans. Nucl. Sci. 43 (6), 2827–2832.

Cané, C., Lozano, M. L., Cabruja, E., Anguita, J., Lora-Tamayo, E., Serra-Mestres, F., aug 1991. Latch-up Characterization Using Novel Test Structures and Instruments. IEEE Trans. Semic. Manuf. 4 (3), 199–205.

Castro, S., Galama, T. J., Harrison, F. A., Holtzman, J. A., Bloom, J. S., Djorgovski, S. G., Kulkarni, S. R., Mar. 2003. Keck Spectroscopy and Hubble Space Telescope Imaging of GRB 000926: Probing a Host Galaxy at z = 2.038. Astrophys. J. 586, 128–134.

Castro-Tirado, A. J., Brandt, S., Lund, N., Lapshov, I., Sunyaev, R. A., Shlyapnikov, A. A., Guziy, S., Pavlenko, E. P., Jun. 1994. Discovery and observations by watch of the X-ray transient GRS 1915+105. Astrophys. J., Suppl. Ser. 92, 469–472.

Cavaliere, A., D'Elia, V., May 2002. The Blazar Main Sequence. Astrophys. J. 571, 226–233.

Celesti, E., Bulgarelli, A., Di Cocco, G., Galli, M., Gianotti, F., Labanti, C., Marisaldi, M., Mauri, A., Rossi, E., Traci, A., Trifoglio, M., Tavani, M., Argan, A., 2004. AGILE, a satellite for high energy gamma-ray astrophysics: prospects for the Mini-Calorimeter. New Astronomy Reviews 48, 315–320.

Charles, P. A., Seward, F. D., 1995. Exploring the X-ray Universe. Cambridge University Press.

Chu, S., Ekström, L., Firestone, R., 1999. Www table of radioactive isotopes. Database version 2/28/1999 from URL http://nucleardata.nuclear.lu.se/nucleardata/toi/.

Citterio, O., Conti, G., Mattaini, E., Santambrogio, E., Sacco, B., 1986. Optics for X-ray concentrators on board of the Astronomy Satellite SAX. In: X-ray instrumentation in astronomy; Proceedings of the Meeting, Cannes, France, December 2-4, 1985 (A87-19722 07-35). Bellingham, WA, Society of Photo-Optical Instrumentation Engineers, 1986, p. 102-110. pp. 102–110.

Cline, T. L., Hurley, K. C., Barthelmy, S., Butterworth, P., Feroci, M., Frontera, F., Golenetskii, S., Mazets, E., Trombka, J., 2001. The IPN I: From the Past to the Future. In: Gamma-ray Bursts in the Afterglow Era. pp. 375–+.

Collmar, W., Reimer, O., Bennett, K., Bloemen, H., Hermsen, W., Lichti, G. G., Ryan, J., Schönfelder, V., Steinle, H., Williams, O. R., Böttcher, M., Feb. 2000. A large high-energy gamma-ray flare from the blazar 3C 273. Astron. Astrophys. 354, 513–521.

Comastri, A., Setti, G., Zamorani, G., Hasinger, G., Apr. 1995. The contribution of AGNs to the X-ray background. Astron. Astrophys. 296, 1–+.

Costa, E., Frontera, F., dal Fiume, D., Amati, L., Cinti, M. N., Collina, P., Feroci, M., Nicastro, L., Orlandini, M., Palazzi, E., Rapisarda, M., Zavattini, G., Oct. 1998. The gamma-ray bursts monitor onboard SAX. Advances in Space Research 22, 1129–1132.

Costa, E., Frontera, F., Heise, J., Feroci, M., in 't Zand, J., Fiore, F., Cinti, M. N., dal Fiume, D., Nicastro, L., Orlandini, M., Palazzi, E., Rapisarda, M., Zavattini, G., Jager, R., Parmar, A., Owens, A., Molendi, S., Cusumano, G., Maccarone, M. C., Giarrusso, S., Coletta, A., Antonelli, L. A., Giommi, P., Muller, J. M., Piro, L., Butler, R. C., 1997. Discovery of an X-ray afterglow associated with the gamma-ray burst of 28 February 1997. Nature 387, 783–785.

D'Amico, N., Kaspi, V. M., Manchester, R. N., Camilo, F., Lyne, A. G., Possenti, A., Stairs, I. H., Kramer, M., Hobbs, G., Bell, J. F., 2001. The Parkes Multibeam Pulsar Survey and the Discovery of New Energetic Radio Pulsars. In: AIP Conf. Proc. 587: Gamma 2001: Gamma-Ray Astrophysics. pp. 555–+.

Davidson, K., Ostriker, J. P., Jan. 1973. Neutron-Star Accretion in a Stellar Wind: Model for a Pulsed X-Ray Source. Astrophys. J. 179, 585–598.

Del Monte, E., Costa, E., Di Persio, G., Feroci, M., Lapshov, I., Martino, B., Mastropietro, M., Morelli, E., Prest, M., Rubini, A., Soffitta, P., Vallazza, E., Dec. 2000. Performances of XA1.3 ASIC chip for the SuperAGILE experiment on board of AGILE. In: Proc. SPIE Vol. 4140, p. 584-594, X-Ray and Gamma-Ray Instrumentation for Astronomy XI, Kathryn A. Flanagan; Oswald H. Siegmund; Eds. pp. 584–594.

Del Monte, E., Costa, E., Di Persio, G., Feroci, M., Mastropietro, M., Morelli, E., Pacciani, L., Porrovecchio, G., Rubini, A., Soffitta, P., Oct. 2004. Laboratory tests and scientific performances of the XAA1.2 front-end chip for space applications. In: Proceedings of the SPIE, Volume 5488, pp. 648-659 (2004). pp. 648–659.

Fenimore, E. E., Cannon, T. M., Feb. 1978. Coded aperture imaging with uniformly redundant arrays. Appl. Opt. 17, 337–347.

Fishman, G. J., Meegan, C. A., Wilson, R. B., Parnell, T. A., Paciesas, W. S., Pendleton, G. N., Hudson, H. S., Matteson, J. L., Peterson, L. E., Cline, T. L., Teegarden, B. J., Schaefer, B. E., Mar. 1989. The BATSE Experiment for the GRO - Solar Flare Hard X-Ray and Gamma-Ray Capabilities. Bull. Am. Astron. Soc. 21, 860–+.

Frail, D. A., Kulkarni, S. R., Nicastro, S. R., Feroci, M., Taylor, G. B., 1997. The radio afterglow from the gamma-ray burst of 8 May 1997. Nature 389, 261–263.

Friedman, A. S., Bloom, J. S., Aug. 2004. Towards a More Standardized Candle Using GRB Energetics and Spectra. ArXiv Astrophysics e-prints.

Frontera, F., Costa, E., dal Fiume, D., Feroci, M., Nicastro, L., Orlandini, M., Palazzi, E., Zavattini, G., Apr. 1997. The high energy instrument PDS on-board the BeppoSAX X–ray astronomy satellite. Astron. Astrophys. Suppl. Ser. 122, 357–369.

Ghosh, K. K., Ramsey, B. D., Sivaram, C., Jun. 1999. Origin of MeV gamma-ray emissions from blazars. Astroparticle Physics 11, 69–71.

Gianotti, F., Trifoglio, M., 2001. DISCoS—Detector-Independent Software for On-Ground Testing and Calibration of Scientific Payloads Using the ESA Packet Telemetry and Telecommand Standards. In: ASP Conf. Ser. 238: Astronomical Data Analysis Software and Systems X. pp. 245–+.

Goka, T., Kuboyama, S., Shimano, Y., Kawanishi, T., dec 1991. The on-orbit measurement of single event phenomena by ETS-V spacecraft. IEEE Trans. Nucl. Sci 38 (6), 1693–1699.

Grim, G. P., Bishai, M., Gay, C., Hill, C., Nahn, S., Pellett, D. E., Pope, G., Shepard, P. F., Slaughter, A. J., Wester III, W. C., jun 2000. Measurement of SEU cross sections in the CDF SVX3 ASIC using 63 MeV protons. Nucl. Instr. and Meth. A 447 (1-2), 160–166.

Grove, J. E., Tavani, M., Purcell, W. R., Johnson, W. N., Kurfess, J. D., Strickman, M. S., Arons, J., Jul. 1995. Evidence for Shock Acceleration in the Binary Pulsar System PSR B1259-63. Astrophys. J., Lett. 447, L113+.

Gursky, H., Giacconi, R., Gorenstein, P., Waters, J. R., Oda, M., Bradt, H., Garmire, G., Sreekantan, B. V., Jun. 1966a. A Measurement of the Angular Size of the X-Ray Source SCO X-1. Astrophys. J. 144, 1249–+.

Gursky, H., Giacconi, R., Gorenstein, P., Waters, J. R., Oda, M., Bradt, H., Garmire, G., Sreekantan, B. V., Oct. 1966b. A Measurement of the Location of the X-Ray Source SCO X-1. Astrophys. J. 146, 310–316.

Hanisch, R. J., Farris, A., Greisen, E. W., Pence, W. D., Schlesinger, B. M., Teuben, P. J., Thompson, R. W., Warnock, A., Sep. 2001. Definition of the Flexible Image Transport System (FITS). Astron. Astrophys. 376, 359–380.

Hankins, T. H., Sep. 1992. Ultra-high Time Resolution Measurements of the Crab "Giant" Radio Pulses. Bulletin of the American Astronomical Society 24, 1277–+.

Hartman, R. C., Bertsch, D. L., Bloom, S. D., Chen, A. W., Deines-Jones, P., Esposito, J. A., Fichtel, C. E., Friedlander, D. P., Hunter, S. D., McDonald, L. M., Sreekumar, P., Thompson, D. J., Jones, B. B., Lin, Y. C., Michelson, P. F., Nolan, P. L., Tompkins, W. F., Kanbach, G., Mayer-Hasselwander, H. A., Mücke, A., Pohl, M., Reimer, O., Kniffen, D. A., Schneid, E. J., von Montigny, C., Mukherjee, R., Dingus, B. L., Jul. 1999. The Third EGRET Catalog of High-Energy Gamma-Ray Sources. Astrophys. J., Suppl. Ser. 123, 79–202.

Hasinger, G., 1998. The X-ray background and the AGN X-ray luminosity function. Astronomische Nachrichten 319, 37–+.

Hirayama, M., Nagase, F., Tavani, M., Kaspi, V. M., Kawai, N., Arons, J., Dec. 1996. Post-Periastron ASCA Observation of the PSR B1259-63 System. Publ. Aston. Soc. Jpn. 48, 833–840.

Horváth, I., Sep. 2002. A further study of the BATSE Gamma-Ray Burst duration distribution. Astron. Astrophys. 392, 791–793.

Hunter, S. D., Bertsch, D. L., Catelli, J. R., Dame, T. M., Digel, S. W., Dingus, B. L., Esposito, J. A., Fichtel, C. E., Hartman, R. C., Kanbach, G., Kniffen, D. A., Lin, Y. C., Mayer-Hasselwander, H. A., Michelson, P. F., von Montigny, C., Mukherjee, R., Nolan, P. L., Schneid, E., Sreekumar, P., Thaddeus, P., Thompson, D. J., May 1997. EGRET Observations of the Diffuse Gamma-Ray Emission from the Galactic Plane. Astrophys. J. 481, 205–+.

Hurley, K. C., Cline, T. L., Barthelmy, S., Butterworth, P., Feroci, M., Frontera, F., Montanari, E., Golenetskii, S., Mazets, E., Trombka, J., 2001. One Year of Rapid, Precise Gamma-Ray Burst Localizations by the Interplanetary Network. In: Gamma-ray Bursts in the Afterglow Era. pp. 378–+.

in't Zand, J. J. M., 1992. A coded-mask imager as monitor of Galactic X-ray sources. Ph.D. thesis, University of Utrecht.

Jager, R., Mels, W. A., Brinkman, A. C., Galama, M. Y., Goulooze, H., Heise, J., Lowes, P., Muller, J. M., Naber, A., Rook, A., Schuurhof, R., Schuurmans, J. J., Wiersma, G., Nov. 1997. The Wide Field Cameras onboard the BeppoSAX X-ray Astronomy Satellite. Astron. Astrophys. Suppl. Ser. 125, 557–572.

Johnston, A. H., apr 1996. The Influence of VLSI Technology Evolution on Radiation-Induced Latchup in Space Systems. IEEE Trans. Nucl. Sci. 43 (2), 505–521.

Johnston, A. H., Hughlock, B. W., dec 1990. Latchup in cmos from single particles. IEEE Trans. Nucl. Sci. 37 (6), 1886–1893.

Jones, B. B., Bertsch, D. L., Dingus, B. L., Esposito, J. E., Fichtel, C. E., Fierro, J. M., Hartman, R. C., Hunter, S. D., Kanbach, G., Kniffen, D. A., Lin, Y. C., Mayer-Hasselwander, H. A., Mattox, J. R., Michelson, P. F., von Montigny, C., Nolan, P. L., Pohl, M., Schneid, E. J., Sreekumar, P., Thompson, D. J., Tompkins, W. F., Willis, T. D., Jun. 1996. Possible EGRET Gamma-Ray Burst Detection Independent of BATSE Triggering. Astrophys. J. 463, 565–569.

Kaaret, P., Cottam, J., May 1996. Do the Unidentified EGRET Sources Lie in Star-forming Regions? Astrophys. J., Lett. 462, L35+.

Kaspi, V. M., Tavani, M., Nagase, F., Hirayama, M., Hoshino, M., Aoki, T., Kawai, N., Arons, J., Nov. 1995. X-Ray Detection of PSR B1259-63 at Periastron. Astrophys. J. 453, 424–+.

Klebesadel, R. W., Strong, I. B., Olson, R. A., Jun. 1973. Observations of Gamma-Ray Bursts of Cosmic Origin. Astrophys. J. 182, L85+.

Knoll, G. F., 1989. Radiation detection and measurement, 2nd Edition. John Wiley & Sons.

Koga, R., apr 1996. Single-Event Effect Ground Test Issues. IEEE Trans. Nucl. Sci. 43 (2), 661–670.

Kouveliotou, C., Meegan, C. A., Fishman, G. J., Bhat, N. P., Briggs, M. S., Koshut, T. M., Paciesas, W. S., Pendleton, G. N., Aug. 1993. Identification of two classes of gamma-ray bursts. Astrophys. J., Lett. 413, L101–L104.

Krawczynski, H., Coppi, P. S., Maccarone, T., Aharonian, F. A., Dec. 2001. An X-ray/TeV gamma-ray study of Mkn 501 during its extraordinary outburst of 1997. AIP Conf. Proc. 599: X-ray Astronomy: Stellar Endpoints, AGN, and the Diffuse X-ray Background 599, 694–697.

Lapshov, I., april 2004. Image Deconvolution and IROS.

Lazzarotto, F., Del Monte, E., 2004. SADAS: an integrated software system for the data of the *SuperAGILE* experiment.

Lazzarotto, F., Del Monte, E., Feroci, M., Sep. 2004. Data model applications for the SuperAGILE detection system. In: Ground-based Telescopes. Edited by Oschmann, Jacobus M., Jr. Proceedings of the SPIE, Volume 5493, pp. 126-136 (2004). pp. 126–136.

Liu, J., Hou, M. D., Li, B. Q., Liu, C. L., Wang, Z. G., Cheng, S., Sun, Y. M., Jin, Y. F., Lin, Y. L., Cai, J. R., Wang, S. J., Ye, Z. H., Zhu, G. W., Du, H., Ren, Q. Y., Wu, W., Mao, X. M., Sun, Y. Q., Guo, R., apr 2000. Experimental studies of single-event effects induced by heavy ions. Nucl. Instr. and Meth. B 164-165, 973–978.

Longo, F., Argan, A., Auricchio, N., Barbiellini, G., Bulgarelli, A., Caraveo, P., Celesti, E., Chen, A., Cocco, V., Costa, E., Di Cocco, G., Fedel, G., Feroci, M., Fiorini, M., Froysland, T., Galli, M., Gianotti, F., Giuliani, A., Labanti, C., Lapshov, I., Lazzarotto, F., Lipari, P., Mauri, A., Marisaldi, M., Mereghetti, S., Morelli, E., Morselli, A., Pacciani, L., Paladin, F., Pellizzoni, A., Perotti, F., Picozza, P., Pittori, C., Pontoni, C., Porrovecchio, G., Preger, B., Prest, M., Rapisarda, M., Rossi, E., Rubini, A., Soffitta, P., Tavani, M., Traci, A., Trifoglio, M., Vallazza, E., Vercellone, S., Zanello, D., 2003. AGILE and Gamma-Ray Astrophysics. Nucl. Phys. Proc. Suppl. 125, 222–229.

Lundgren, S. C., Cordes, J. M., Ulmer, M., Matz, S. M., Lomatch, S., Foster, R. S., Hankins, T., Nov. 1995. Giant Pulses from the Crab Pulsar: A Joint Radio and Gamma-Ray Study. Astrophys. J. 453, 433–+.

Lutz, G., 1999. Semiconductor Radiation Detectors. Springer-Verlag.

Lyutikov, M., Blackman, E. G., Feb. 2001. Gamma-ray bursts from unstable Poynting-dominated outflows. Mon. Not. R. Astron. Soc. 321, 177–186.

Mao, P. H., Harrison, F. A., Platonov, Y. Y., Broadway, D., Degroot, B., Christensen, F. E., Craig, W. W., Hailey, C. J., Oct. 1997. Development of grazing incidence multilayer mirrors for hard x-ray focusing telescopes. In: Proc. SPIE Vol. 3114, p. 526-534, EUV, X-Ray, and Gamma-Ray Instrumentation for Astronomy VIII, Oswald H. Siegmund; Mark A. Gummin; Eds. pp. 526–534.

Maraschi, L., Cavaliere, A., 1977. Highlights of Astronomy. Vol. 4 part I. Reidel, Dordrecht, p. 127.

Mattox, J. R., Wagner, S. J., Malkan, M., McGlynn, T. A., Schachter, J. F., Grove, J. E., Johnson, W. N., Kurfess, J. D., Feb. 1997. An Intense Gamma-Ray Flare of PKS 1622-297. Astrophys. J. 476, 692–+.

McDaid, L., Hall, S., Marsland, J., Eccleston, W., Alderman, J., Cook, K., Bunyan, R., Uren, M., Oct. 1990. A simple model to predict the holding voltage for SOI MOSFETs operating in the latch state. In: SOS/SOI Technology Conference, 1990., 1990 IEEE. pp. 19–20.

McNulty, P. J., Abdel-Kader, W. G., Beauvais, W. G., Adams, L., Daly, E. J., Harboe-Sorensen, R., dec 1993. Simple model for proton-induced latch-up. IEEE Trans. Nucl. Sci. 40 (6), 1947–1951.

Meegan, C. A., Fishman, G. J., Wilson, R. B., Horack, J. M., Brock, M. N., Paciesas, W. S., Pendleton, G. N., Kouveliotou, C., Jan. 1992. Spatial distribution of gamma-ray bursts observed by BATSE. Nature 355, 143–145.

Mel'Nik, A. M., Efremov, Y. N., Jan. 1995. A new list of OB associations in our galaxy. Astronomy Letters 21, 10–26.

Metzger, M. R., Djorgovski, S. G., Kulkarni, S. R., Steidel, C. C., Adelberger, K. L., Frail, D. A., Costa, E., Frontera, F., 1997. Spectral constraints on the redshift of the optical counterpart to the gamma-ray burst of 8 May 1997. Nature 387, 879–+.

Morselli, A., Argan, A., Costa, E., Feroci, M., Labanti, C., Picozza, P., Prest, M., Salamon, A., Soffitta, P., Tavani, M., Vallazza, E., Dec. 2000. Data handling system of the gamma-ray space detector AGILE. In: Proc. SPIE Vol. 4140, p. 493-499, X-Ray and Gamma-Ray Instrumentation for Astronomy XI, Kathryn A. Flanagan; Oswald H. Siegmund; Eds. pp. 493–499.

Mukherjee, R., Bertsch, D. L., Dingus, B. L., Kanbach, G., Kniffen, D. A., Sreekumar, P., Thompson, D. J., Mar. 1995. On the nature of the unidentified EGRET sources: Are they Geminga-like pulsars? Astrophys. J., Lett. 441, L61–L64.

Mushotzky, R. F., Cowie, L. L., Barger, A. J., Arnaud, K. A., Mar. 2000. Resolving the extragalactic hard X-ray background. Nature 404, 459–464.

Mushotzky, R. F., Done, C., Pounds, K. A., 1993. X-ray spectra and time variability of active galactic nuclei. Ann. Rev. Astron. Astrophys. 31, 717–761.

Nolan, P. L., Fierro, J. M., Lin, Y. C., Michelson, P. F., Bertsch, D. L., Dingus, B. L., Esposito, J. A., Fichtel, C. E., Hartman, R. C., Hunter, S. D., von Montigny, C., Mukherjee, R., Ramanamurthy, P. V., Thompson, D. J., Kniffen, D. A., Schneid, E., Kanbach, G., Mayer-Hasselwander, H. A., Merck, M., Nov. 1996. EGRET observations of pulsars. Astron. Astrophys. Suppl. Ser. 120, C61+.

Pacciani, L., Porrovecchio, G., Barbanera, L., Costa, E., Del Monte, E., Di Persio, G., Donnarumma, I., Feroci, M., Lazarotto, F., Uberti, O., Rubini, A., Soffitta, P., Bulgarelli, A., Gianotti, F., Morelli, E., Trifoglio, M., Mastropietro, M., Oct. 2004. Instrumentation for ground test of SuperAgile detectors and front-end electronics. In: Proceedings of the SPIE, Volume 5488, pp. 719-730 (2004). pp. 719–730.

Paciesas, W. S., Meegan, C. A., Pendleton, G. N., Briggs, M. S., Kouveliotou, C., Koshut, T. M., Lestrade, J. P., McCollough, M. L., Brainerd, J. J., Hakkila, J., Henze, W., Preece, R. D., Connaughton, V., Kippen, R. M., Mallozzi, R. S., Fishman, G. J., Richardson, G. A., Sahi, M., Jun. 1999. The Fourth BATSE Gamma-Ray Burst Catalog (Revised). Astrophys. J., Suppl. Ser. 122, 465–495.

Paczynski, B., 1998. Gamma-Ray Bursts as Hypernovae. In: American Institute of Physics Conference Series. pp. 783–+.

Pareschi, G., Frontera, F., de Chiara, P., Ferrara, G., Costa, E., Jul. 1997. New reflecting materials for the construction of hard x-ray focusing telescopes based on Bragg diffraction. In: Proc. SPIE Vol. 3113, p. 275-284, Grazing Incidence and Multilayer X-Ray Optical Systems, Richard B. Hoover; Arthur B. Walker; Eds. pp. 275–284.

Parmar, A. N., Martin, D. D. E., Bavdaz, M., Favata, F., Kuulkers, E., Vacanti, G., Lammers, U., Peacock, A., Taylor, B. G., Apr. 1997. The low-energy concentrator spectrometer on-board the BeppoSAX X-ray astronomy satellite. Astron. Astrophys. Suppl. Ser. 122, 309–326.

Peisert, A., 1992. Instrumentation on High energy Physics. World Scientific Publishing Co., Ch. Silicon microstrip detectors.

Pellizzoni, A., Chen, A., Conti, M., Giuliani, A., Mereghetti, S., Tavani, M., Vercellone, S., 2004. Prospects for high energy studies of pulsars with the AGILE γ-ray telescope. Advances in Space Research 33, 625–629.

Petersen, E. L., Pickel, J. C., Adams Jr., J. H., Smith, E. C., dec 1992. Rate Prediction for Single Event Effects – a Critique. IEEE Trans. Nucl. Sci. 39 (6), 1577–1599.

Pickel, J. C., apr 1996. Single-Event Effects Rate Prediction. IEEE Trans. Nucl. Sci. 43 (2), 483–495.

Piran, T., 1997. Unsolved Problems in Astrophysics (J. N. Bahcall and J. P. Ostriker Editors). Princeton University Press, Ch. 18, pp. 343–377.

Piran, T., 2000. Gamma-ray bursts - a puzzle being resolved. Phys. Rep. 333, 529–553.

Piro, L., Scarsi, L., Butler, R. C., Oct. 1995. SAX: the wideband mission for x-ray astronomy. In: Proc. SPIE Vol. 2517, p. 169-181, X-Ray and EUV/FUV Spectroscopy and Polarimetry, Silvano Fineschi; Ed. pp. 169–181.

Piron, F., Djannati-Atai, A., Punch, M., Tavernet, J.-P., Barrau, A., Bazer-Bachi, R., Chounet, L.-M., Debiais, G., Degrange, B., Dezalay, J.-P., Espigat, P., Fabre, B., Fleury, P., Fontaine, G., Goret, P., Gouiffes, C., Khelifi, B., Malet, I., Masterson, C., Mohanty, G., Nuss, E., Renault, C., Rivoal, M., Rob, L., Vorobiov, S., Aug. 2001. Temporal and spectral gamma-ray properties of Mkn 421 above 250 GeV from CAT observations between 1996 and 2000. Astron. Astrophys. 374, 895–906.

Prest, M., Barbiellini, G., Bordignon, G., Fedel, G., Liello, F., Longo, F., Pontoni, C., Vallazza, E., mar 2003. The AGILE silicon tracker: an innovative γ-ray instrument for space. Nucl. Instr. and Meth. A 501 (1), 280–287.

Ramanamurthy, P. V., Bertsch, D. L., Fichtel, C. E., Kanbach, G., Kniffen, D. A., Mayer-Hasselwander, H. A., Nolan, P. L., Sreekumar, P., Thompson, D. J., Sep. 1995. A Long-Term Study of High-Energy Gamma-Ray Emission from the Vela, Geminga, and Crab Pulsars. Astrophys. J. 450, 791–+.

Ricker, G. R., HETE Science Team, May 2001. HETE-2 Status: New Gamma-ray Burst Results and Future Prospects. Bulletin of the American Astronomical Society 33, 833–+.

Ritz, S., Michelson, P. F., Meegan, C., Grindlay, J., GLAST Mission, Dec. 2004. The Gamma-ray Large Area Space Telescope (GLAST) Mission. Bulletin of the American Astronomical Society 205, 606–+.

Sakamoto, T., Lamb, D. Q., Graziani, C., Donaghy, T. Q., Suzuki, M., Ricker, G., Atteia, J.-L., Kawai, N., Yoshida, A., Shirasaki, Y., Tamagawa, T., Torii, K., Matsuoka, M., Fenimore, E. E., Galassi, M., Tavenner, T., Doty, J., Vanderspek, R., Crew, G. B., Villasenor, J., Butler, N., Prigozhin, G., Jernigan, J. G., Barraud, C., Boer, M., Dezalay, J.-P., Olive, J.-F., Hurley, K., Levine, A., Monnelly, G., Martel, F., Morgan, E., Woosley, S. E., Cline, T., Braga, J., Manchanda, R., Pizzichini, G., Takagishi, K., Yamauchi, M., Feb. 2004. High Energy Transient Explorer 2 Observations of the Extremely Soft X-Ray Flash XRF 020903. Astrophys. J. 602, 875–885.

Schneid, E. J., Bertsch, D. L., Dingus, B. L., Fichtel, C. E., Hartman, R. C., Hunter, S. D., Kanbach, G., Kniffen, D. A., Lin, Y. C., Mattox, J. R., Mayer-Hasselwander, H. A., Michelson, P. F., von Montigny, C., Nolan, P. L., Sreekumar, P., Thompson, D. J., Nov. 1995. EGRET Measurements of Energetic Gamma Rays from the Gamma-Ray Bursts of 1992 June 22 and 1994 March 1. Astrophys. J. 453, 95–99.

Seward, F., Chodil, G., Mark, H., Swift, C., Toor, A., Dec. 1967. Diffuse Cosmic X-Ray Background Between 4 and 40 KEV. Astrophys. J. 150, 845–+.

Soffitta, P., Costa, E., Del Monte, E., Feroci, M., Lapshov, I., Mastropietro, M., Morelli, E., Rapisarda, M., Rubini, A., Barbiellini, G., Longo, F., Mereghetti, S., Morselli, A., Prest, M., Tavani, M., Vallazza, E., Vercellone, S., Dec. 2000. Instrumental and astrophysical performances of SuperAGILE on-board AGILE Gamma-Ray mission. In: Proc. SPIE Vol. 4140, p. 283-292, X-Ray and Gamma-Ray Instrumentation for Astronomy XI, Kathryn A. Flanagan; Oswald H. Siegmund; Eds. pp. 283–292.

Sołtan, A. M., Sep. 2003. The diffuse X-ray background. Astron. Astrophys. 408, 39–42.

Stacy, J. G., Vestrand, W. T., Sreekumar, P., Nov. 2003. The Gamma-Ray Blazar PKS 0208-512 from MeV to GeV Energies. Astrophys. J. 598, 216–231.

Staelin, D. H., Reifenstein, E. C., 1968. Pulsating radio sources near the Crab Nebula. Science 162, 1481–1483.

Sundal, B. M., june 1999. The VA-DAQ 1.2 test and readout system for the VA/TA chip sets.

Sundal, B. M., 2001. private communication.

Tavani, M., Arons, J., Mar. 1997. Theory of High-Energy Emission from the Pulsar/Be Star System PSR 1259-63. I. Radiation Mechanisms and Interaction Geometry. Astrophys. J. 477, 439–+.

Tavani, M., Barbiellini, G., Argan, A., Auricchio, N., Bernabeo, A. R., Bulgarelli, A., Caraveo, P. A., Celesti, E., Chen, A., Cocco, V., Costa, E., Del Monte, E., De Paris,

G., Di Cocco, G., Fedel, G., Feroci, M., Fiorini, M., Froysland, T., Galli, M., Gianotti, F., Giuliani, A., Labanti, C., Lapshov, I., Lazzarotto, F., Lipari, P., Longo, F., Mastropietro, M., Mattaini, E., Mauri, A., Mereghetti, S., Morelli, E., Morselli, A., Pacciani, L., Pellizzoni, A., Perotti, F., Picozza, P., Pittori, C., Pontoni, C., Porrovecchio, G., Preger, B., Prest, M., Rapisarda, M., Rossi, E., Rubini, A., Sant'Ambrogio, E., Soffitta, P., Soli, L., Traci, A., Trifoglio, M., Vallazza, E., Vercellone, S., Zambra, A., Zanello, D., Mar. 2003. The AGILE instrument. In: X-Ray and Gamma-Ray Telescopes and Instruments for Astronomy. Edited by Joachim E. Truemper, Harvey D. Tananbaum. Proceedings of the SPIE, Volume 4851, pp. 1151-1162 (2003). pp. 1151–1162.

Tavani, M., Barbiellini, G., Argan, A., Caraveo, P. A., Chen, A., Cocco, V., Costa, E., Del Monte, E., Di Cocco, G., Donnarumma, I., Feroci, M., Fiorini, M., Froysland, T., Galli, M., Gianotti, F., Giuliani, A., Labanti, C., Lapshov, I., Lazzarotto, F., Liello, F., Lipari, P., Longo, F., Marisaldi, M., Mauri, A., Mereghetti, S., Morelli, E., Morselli, A., Pacciani, L., Pellizzoni, A., Perotti, F., Picozza, P., Pittori, C., Pontoni, C., Prest, M., Rapisarda, M., Rossi, E., Rubini, A., Soffitta, P., Traci, A., Trifoglio, M., Vallazza, E., Vercellone, S., Zanello, D., Jul. 2004. The AGILE mission: Gamma-Ray Astrophysics of Galactic Sources. In: M. Tavani, A. P., Vercellone, S. (Eds.), X-Ray and Gamma-Ray Astrophysics of Galactic Sources. pp. 3–22.

Tavani, M., Grove, J. E., Purcell, W., Hermsen, W., Kuiper, L., Kaaret, P., Ford, E., Wilson, R. B., Finger, M., Harmon, B. A., Zhang, S. N., Mattox, J., Thompson, D., Arons, J., Dec. 1996. High-energy emission from the PSR B1259-63 system near periastron. Astron. Astrophys. Suppl. Ser. 120, C221+.

Thompson, D. J., Bertsch, D. L., Fichtel, C. E., Hartman, R. C., Hofstadter, R., Hughes, E. B., Hunter, S. D., Hughlock, B. W., Kanbach, G., Kniffen, D. A., Lin, Y. C., Mattox, J. R., Mayer-Hasselwander, H. A., von Montigny, C., Nolan, P. L., Nel, H. I., Pinkau, K., Rothermel, H., Schneid, E. J., Sommer, M., Sreekumar, P., Tieger, D., Walker, A. H., Jun. 1993. Calibration of the Energetic Gamma-Ray Experiment Telescope (EGRET) for the Compton Gamma-Ray Observatory. Astrophys. J., Suppl. Ser. 86, 629–656.

Torres, D. F., Nuza, S. E., Jan. 2003. Possible New γ-Ray Pulsar Detections by the AGILE and GLAST Missions: An Outer Gap Model Look at the Parkes Pulsar Catalog. Astrophys. J., Lett. 583, L25–L29.

Tylka, A. J., Adams Jr, J. H., Boberg, P. R., Brownstein, B., Dietrich, W. F., Flueckiger, E. O., Petersen, E. L., Shea, M. A., Smart, D. F., Smith, E. C., dec 1997. CREME96: A Revision of the Cosmic Ray Effects on Micro-Electronics Code. IEEE Trans. Nucl. Sci. 44 (6), 2150–2160.

Uberti, O., Soffitta, P., 2005. private communication.

Ubertini, P., Lebrun, F., Di Cocco, G., Bazzano, A., Bird, A. J., Broenstad, K., Goldwurm, A., La Rosa, G., Labanti, C., Laurent, P., Mirabel, I. F., Quadrini, E. M.,

Ramsey, B., Reglero, V., Sabau, L., Sacco, B., Staubert, R., Vigroux, L., Weisskopf, M. C., Zdziarski, A. A., Nov. 2003. IBIS: The Imager on-board INTEGRAL. Astron. Astrophys. 411, L131–L139.

Underwood, C. I., Oldfield, M. K., Jun. 2000. Observations on the reliability of COTS-device-based solid state data recorders operating in low-Earth orbit. IEEE Trans. Nucl. Sci. 47 (3), 647–653.

Urry, C. M., Padovani, P., Sep. 1995. Unified Schemes for Radio-Loud Active Galactic Nuclei. Publ.. Astron. Soc. Pac. 107, 803–+.

van Paradijs, J., Groot, P. J., Galama, T., Kouveliotou, C., Strom, R. G., Telting, J., Rutten, R. G. M., Fishman, G. J., Meegan, C. A., Pettini, M., Tanvir, N., Bloom, J., Pedersen, H., Nordgaard-Nielsen, H. U., Linden-Vornle, M., Melnick, J., van der Steene, G., Bremer, M., Naber, R., Heise, J., in 't Zand, J., Costa, E., Feroci, M., Piro, L., Frontera, F., Zavattini, G., Nicastro, L., Palazzi, E., Bennet, K., Hanlon, L., Parmar, A., 1997. Transient optical emission from the error box of the gamma-ray burst of 28 February 1997. Nature 386, 686–689.

Vedrenne, G., Roques, J.-P., Schönfelder, V., Mandrou, P., Lichti, G. G., von Kienlin, A., Cordier, B., Schanne, S., Knödlseder, J., Skinner, G., Jean, P., Sanchez, F., Caraveo, P., Teegarden, B., von Ballmoos, P., Bouchet, L., Paul, P., Matteson, J., Boggs, S., Wunderer, C., Leleux, P., Weidenspointner, G., Durouchoux, P., Diehl, R., Strong, A., Cassé, M., Clair, M. A., André, Y., Nov. 2003. SPI: The spectrometer aboard INTEGRAL. Astron. Astrophys. 411, L63–L70.

Vercellone, S., Argan, A., Auricchio, N., Barbiellini, G., Caraveo, P., Celesti, E., Chen, A., Cocco, V., Costa, E., di Cocco, G., Fedel, G., Feroci, M., Fiorini, M., Froysland, T., Galli, M., Gianotti, F., Giuliani, A., Labanti, C., Lapshov, I., Lipari, P., Longo, F., Mauri, A., Merenghetti, S., Morelli, E., Morselli, A., Pacciani, L., Pellizzoni, A., Perotti, F., Picozza, P., Pittori, C., Pontoni, C., Porrovecchio, J., Preger, B., Prest, M., Rapisarda, M., Rossi, E., Rubini, A., Soffitta, P., Tavani, M., Traci, A., Trifoglio, M., Vallazza, E., Zanello, D., 2003. Blazars: the View from AGILE (Invited Talk). In: ASP Conf. Ser. 299: High Energy Blazar Astronomy. pp. 19–+.

Vietri, M., Stella, L., Dec. 1999. Supranova Events from Spun-up Neutron Stars: an Explosion in Search of an Observation. Astrophys. J., Lett. 527, L43–L46.

Walker, K. C., Schaefer, B. E., Fenimore, E. E., Jul. 2000. Gamma-Ray Bursts Have Millisecond Variability. Astrophys. J. 537, 264–269.

Wallace, P. M., Griffis, N. J., Bertsch, D. L., Hartman, R. C., Thompson, D. J., Kniffen, D. A., Bloom, S. D., Sep. 2000. A Systematic Search for Short-Term Variability of EGRET Sources. Astrophys. J. 540, 184–191.

Walter, R., Rodriguez, J., Foschini, L., de Plaa, J., Corbel, S., Courvoisier, T. J.-L., den Hartog, P. R., Lebrun, F., Parmar, A. N., Tomsick, J. A., Ubertini, P., Nov. 2003.

INTEGRAL discovery of a bright highly obscured galactic X-ray binary source IGR J16318-4848. Astron. Astrophys. 411, L427–L432.

Winkler, C., Courvoisier, T. J.-L., Di Cocco, G., Gehrels, N., Giménez, A., Grebenev, S., Hermsen, W., Mas-Hesse, J. M., Lebrun, F., Lund, N., Palumbo, G. G. C., Paul, J., Roques, J.-P., Schnopper, H., Schönfelder, V., Sunyaev, R., Teegarden, B., Ubertini, P., Vedrenne, G., Dean, A. J., Nov. 2003. The INTEGRAL mission. Astron. Astrophys. 411, L1–L6.

Woosley, S. E., Taam, R. E., Sep. 1976. Gamma-ray bursts from thermonuclear explosions on neutron stars. Nature 263, 101–103.

Wyss, J., Bisello, D., Pantano, D., apr 2001. SIRAD: an irradiation facility at the LNL Tandem accelerator for radiation damage studies on semiconductor detectors and electronic device and systems. Nucl. Instr. and Meth. A 462 (3), 426–434.

Yokoyama, M., Aihara, H., Hazumi, M., Ishino, H., Kaneko, J., Li, Y., Marlow, D., Mikkelsen, S., Nygård, E., Tajima, H., Talebi, J., Varner, G., Yamamoto, H., jun 2001. Radiation Hardness of VA1 Submicron Process Technology. IEEE Trans. Nucl. Sci. 48 (3), 440–443.

Ziegler, J. F., Biersack, J. P., Littmark, U., 1985. The Stopping and Range of Ions in Solids. Pergamon Press.

Ziólkowski, J., 2003. Black hole candidates. In: Giovannelli, F., Mannocchi, G. (Eds.), Frontier Objects in Astrophysics and Particle Physics. pp. 411–440.

Zombeck, M. V., 1990. Handbook of Astronomy and Astrophysics, 2nd Edition. Cambridge, UK: Cambridge University Press.